Decision '08: Where Obama and McCain Stand on Science Page 518

24 October 2008 | $10

Science

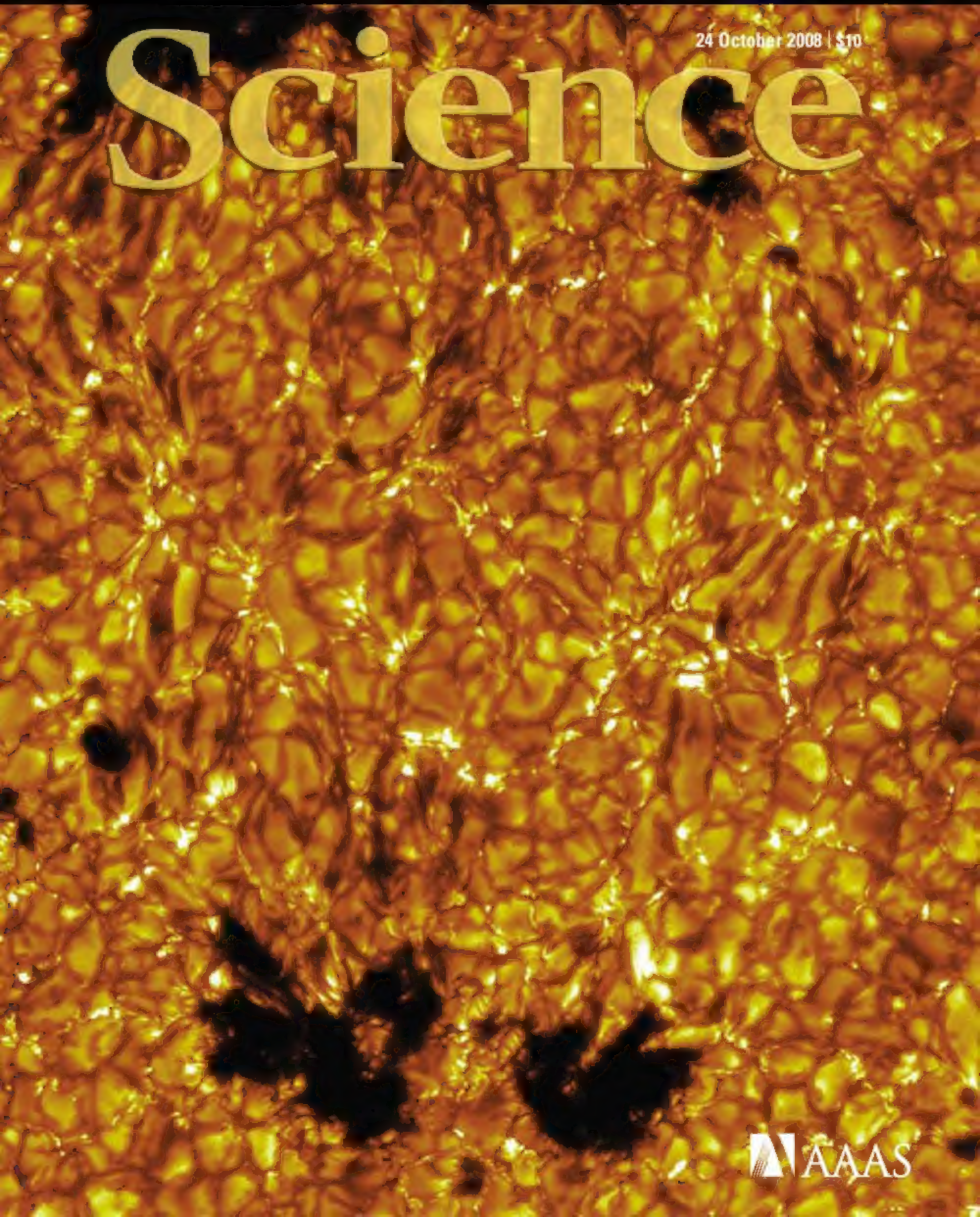

AAAS

CONTENTS

Volume 322, Issue 5901

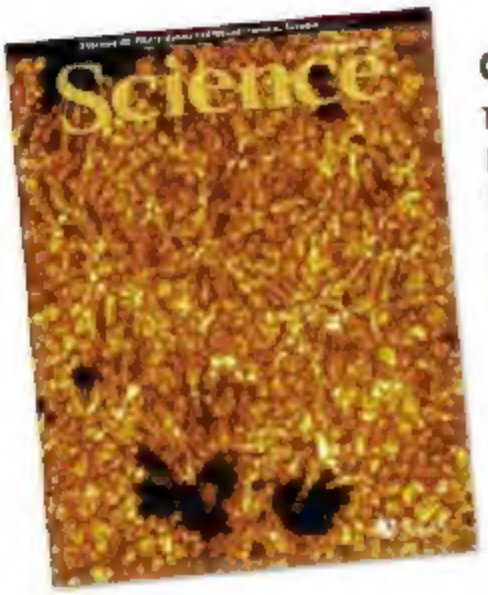

COVER

The surface of the Sun shows rapidly changing patterns due to convection, as well as global oscillations of very low amplitude. The CoRoT (Convection Rotation and Planetary Transits) satellite, launched in December 2006, has now measured both phenomena in other stars. See page 558.

Image: Thomas Berger; ISP/Royal Swedish Academy of Sciences

DEPARTMENTS

EDITORIAL

NEWS OF THE WEEK

>> Science Online Feature, see p. 499

NEWS FOCUS

U.S. Presidential Election 2008

518

LETTERS

BOOKS *ET AL.*

POLICY FORUM

530

PERSPECTIVES

ASSOCIATION AFFAIRS

CONTENTS continued >>

Science

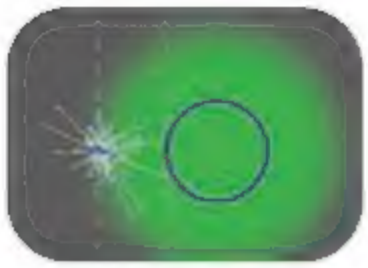

SCIENCE EXPRESS

www.sciencexpress.org

BREVIA

RESEARCH ARTICLE

RESEARCH ARTICLE

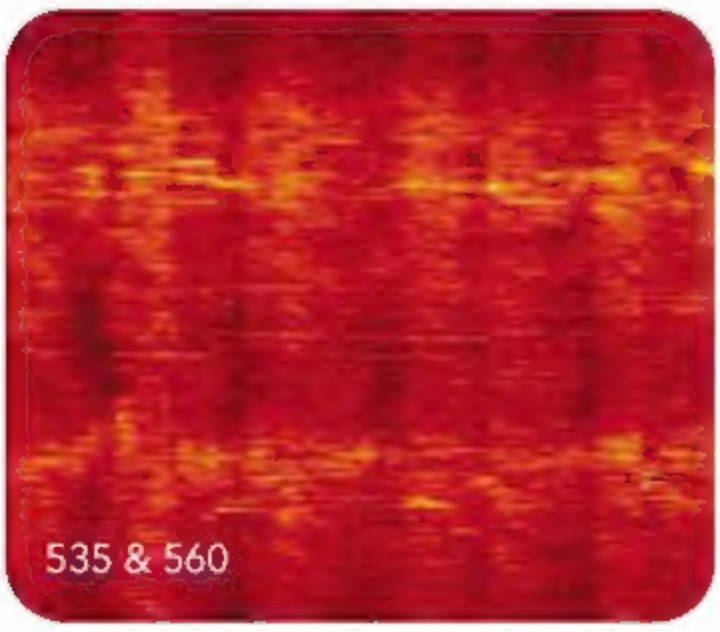

REPORTS

CONTENTS continued >>

Science

REPORTS *CONTINUED...*

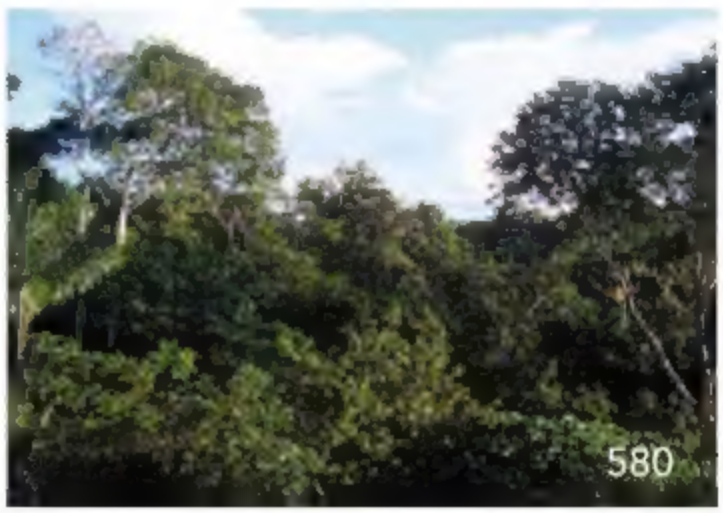

AAAS
ADVANCING SCIENCE, SERVING SOCIETY

SCIENCE (ISSN 0036-8075) is published weekly on Friday, except the last week in December, by the American Association for the Advancement of Science, 1200 New York Avenue, NW, Washington, DC 20005. Periodicals Mail postage (publication No. 484460) paid at Washington, DC, and additional mailing offices. Domestic individual membership and subscription (51 issues): $144 ($74 allocated to subscription). Domestic institutional subscription (51 issues): $770; Foreign postage extra: Mexico, Caribbean (surface mail) $55; other countries (air assist delivery) $85. First class, airmail, student, and emeritus rates on request. Canadian rates with GST available upon request, GST #1254 88122. Publications Mail Agreement Number 1069624. SCIENCE is printed on 30 percent post-consumer recycled paper. **Printed in the U.S.A.**

Change of address: Allow 4 weeks, giving old and new addresses and 8-digit account number. **Postmaster:** Send change of address to AAAS, P.O. Box 96178, Washington, DC 20090-6178. **Single-copy sales:** $10.00 current issue, $15.00 back issue prepaid includes surface postage; bulk rates on request. **Authorization to photocopy material** for internal or personal use under circumstances not falling within the fair use provisions of the Copyright Act is granted by AAAS to libraries and other users registered with the Copyright Clearance Center (CCC) Transactional Reporting Service, provided that $20.00 per article is paid directly to CCC, 222 Rosewood Drive, Danvers, MA 01923. The identification code for *Science* is 0036-8075. *Science* is indexed in the *Reader's Guide to Periodical Literature* and in several specialized indexes.

Printed on 30% post-consumer recycled paper.

CONTENTS continued >>

SCIENCENOW

www.sciencenow.org

HIGHLIGHTS FROM OUR DAILY NEWS COVERAGE

Hallucinogenic Hand-Me-Downs
Ancient Caribbean families appeared to share drug paraphernalia across generations.

Monster Tag Team
Gigantic black holes threw their weight around in the early universe.

The Grunter Gets the Worm
Scientists think they have figured out why low-pitched sounds drive earthworms above.

Signaling networks as digital circuits.

SCIENCE SIGNALING

www.sciencesignaling.org

THE SIGNAL TRANSDUCTION KNOWLEDGE ENVIRONMENT

EDITORIAL GUIDE: From Input to Output—Are All Paths Equal?
N. R. Gough
The consequences of various input signals must first be understood to gain a systems-level explanation of signaling networks.

PERSPECTIVE: Systems- and Molecular-Level Elucidation of Signaling Processes Through Chemistry
K. P. Chiang and T. W. Muir
New techniques take advantage of chemistry to investigate signal transduction mechanisms in the cell.

PERSPECTIVE: A Scaffold Makes the Switch
H. G. Dohlman
The location of a scaffolding protein determines whether activation of MAPK signaling in yeast will produce a graded or binary response.

PERSPECTIVE: Probing Pathways Periodically
T. C. Elston
Monitoring the response to periodic input signals reveals dynamic properties of a MAPK pathway.

RESEARCH ARTICLE: Fault Diagnosis Engineering of Digital Circuits Can Identify Vulnerable Molecules in Complex Cellular Pathways
A. Abdi, M. B. Tahoori, E. S. Emamian
An engineering approach reveals the weakest links in cellular signaling networks.

CREDITS: (SCIENCE CAREERS) PHOTODISC; (SCIENCE SIGNALING) CHRIS BICKEL/SCIENCE; (SCIENCE ONLINE FEATURE) KATRIEN KOLENBERG

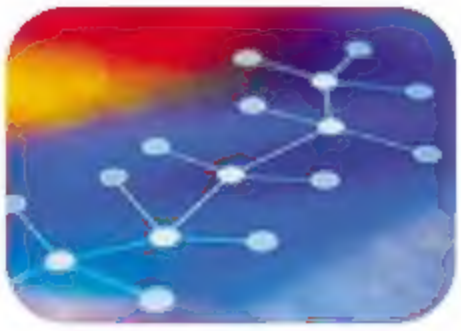

Online networking to help your career.

SCIENCE CAREERS

www.sciencecareers.org/career_development

FREE CAREER RESOURCES FOR SCIENTISTS

Tooling Up: Enhance Your Job Search Online
D. Jensen
Online professional networking Web sites can advance your job search.

Social Networking Grows Up
L. Laursen
New resources lend a social dimension to online research and publishing tools.

The Toilet Technologist
A. Levine
A Ph.D. chemist found a rewarding career designing toilets.

From the Archives: Of Noble Descent
D. van Vlooten
There are ways of getting elite positions without being nobility or going to the "right" university.

SCIENCE ONLINE FEATURE

THE GONZO SCIENTIST: Flunking Spore
An article and video explore the computer game Spore and how it scores on its scientific themes.

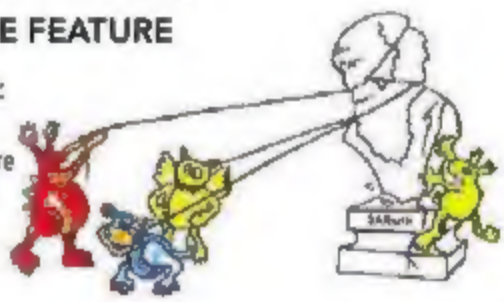

>> News story p. 517
www.sciencemag.org/sciext/gonzoscientist/

SCIENCEPODCAST

www.sciencemag.org/multimedia/podcast

FREE WEEKLY SHOW

Download the 24 October *Science* Podcast to hear how physical warmth promotes interpersonal warmth, measuring pulsing stars, science and the U.S. presidential election, and more.

Separate individual or institutional subscriptions to these products may be required for full-text access.

EDITED BY STELLA HURTLEY

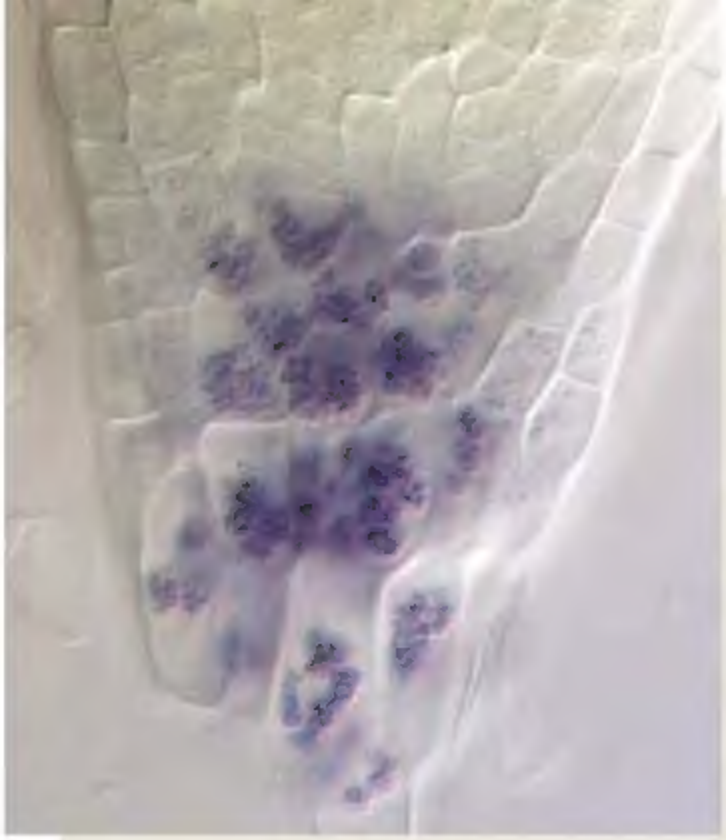

<< Lateral Root Regulation

Control of cell division patterns is essential for normal development. **De Smet *et al.*** (p. 594) looked in living tissues at the early stages of the formation of lateral roots in the model plant, *Arabidopsis thaliana*. The cells that give rise to lateral roots responded to a key receptor-like kinase, ACR4, which was also required to maintain stem cells at the root tip meristem. Although sharing a kinase, these processes remain distinct because, while the root tip meristem is a permanent organ, lateral roots are generated only when required during development.

Ring Out, Bright Star

Helioseismology is the study of the oscillations and surface convection patterns, or granulation, of the Sun. From these measurements, internal structure can be inferred. **Michel *et al.*** (p. 558; see the Perspective by **Montgomery**; see the cover) used data gathered by the CoRoT satellite from three other stars in the same class as the Sun. These suns were hotter and had much finer granulation than ours and, in addition, the amplitudes of their global oscillations were about 1.5-fold greater, although less than theoretical estimates. Thus, helioseismology may represent a promising approach to learning about the structure and evolution of more distant suns, as well as our own.

Chlorine Gets Grounded

Reactions of halide atoms with hydrogen are simple to probe with extreme precision and have thus become test cases for understanding the implications of quantum mechanics to chemical reactions. **Wang *et al.*** (p. 573) performed highly controlled collision studies between crossed beams of H_2 and Cl in the gas phase and found that electronic excitation plays only a minor role in the reaction forming HCl and H. This finding resolves a long-standing controversy about the general applicability of the Born-Oppenheimer approximation that separates nuclear from electronic rearrangements.

Mixing It Up

The transition of matter between an ordered state, such as found in a crystal, and a disordered state, such as found in a liquid, is fairly easy to visualize and is a common occurrence. Transitions between two disordered states are much less common, and it can be hard to understand how two liquids of the same material can both be disordered but nevertheless have a different internal structure. **Greaves *et al.*** (p. 566) have now been able to observe a first-order liquid-liquid transition in an yttrium oxide–aluminum oxide melt. By estimating changes in density and entropy, and observing structural changes at the atomic level, the transition between one liquid state and the other was found to coincide with the atomic packing of its components. This approach can be applied to the search for phase transitions in systems ranging from semiconductors to folding proteins.

Titania's Face in Profile

The surface of titanium oxide, unlike the bulk material, can undergo substantial reconstruction. In many of its uses, titania is slightly reduced, and the cations must accommodate this change. Using high-resolution transmission electron microscopy images taken from different planes, **Shibata *et al.*** (p. 570) showed that shifts in the relative positions of interstitial titanium atoms and their surrounding oxygen atoms offer a structural explanation for the complexity of the oxide surface. This approach can be applied to the investigation of many complex surface structures.

CREDITS: (TOP TO BOTTOM) TOM BEECKMAN; SHIBATA ET AL.

Modeling the Midbody

During cytokinesis, the midbody forms the final tether between two daughter cells before cleavage of the plasma membrane. To initiate cleavage, the midbody protein, CEP55, recruits the ESCRT-1 complex and an associated protein, ALIX, but **Lee *et al.*** (p. 576) have discovered that ALIX and ESCRT-1 compete for binding to the same region of CEP55. This region forms a noncanonical coiled-coil with bulky and charged residues at the interface that create a single binding site for ALIX or for ESCRT. These data, together with related crystallographic and electron microscopic analyses, complete the picture of the structure of the midbody's organization.

Tropical Forest Species Dynamics

The maintenance of the extraordinary levels of diversity seen in tropical forests has long intrigued ecologists. **Kraft *et al.*** (p. 580) combined functional traits, especially leaf structure and physiology, with census data on the spatial location of over 150,000 trees in a highly diverse 25-hectare plot in Ecuadorian Amazonia, and found that subtle but pervasive habitat specialization and functional differentiation contribute to species coexistence.

Where Fat Cells Are Born

The intertwined epidemics of obesity and diabetes have heightened interest in the developmental origin of adipocytes (fat cells). The identity and precise anatomic location of the progenitor cells that give rise to adipocytes are unknown. Using mice expressing marker genes that allow cell lineage tracing, **Tang *et al.*** (p. 583, published online 18 September; see the Perspective by **Kahn**) now characterize these long-sought progenitor cells and show, surprisingly, that they reside within the walls, or mural cell compartment, of the blood vessels that feed adipose tissue. In mice, these progenitor cells appear to commit to the adipocyte lineage either prenatally or shortly after birth. Thus the adipose vasculature functions

Continued on page 503

Continued from page 501

as a progenitor niche and may provide signals for adipocyte development, which may help to explain why drugs that inhibit blood vessel growth can cause fat loss in mice.

Blood Pressure Control: It's (Another) Gas!

The discovery in the 1980s that the gaseous signaling molecule nitric oxide regulates blood vessel dilation and blood flow revolutionized biomedical research, leading most famously to new drugs for erectile dysfunction such as Viagra. **Yang *et al.*** (p. 587) provide evidence that vascular function is also controlled by hydrogen sulfide (H_2S), the same gas that is responsible for the smell of rotten eggs and that recently has been shown to induce a hibernation-like state in animals. Mice genetically deficient in cystathionine γ-lyase, an enzyme that produces H_2S, developed age-related hypertension and their blood vessels showed an impaired response to treatments that promote vasorelaxation. Thus, like nitric oxide, H_2S regulates blood pressure—a finding that could pave the way toward new treatments for vascular disorders.

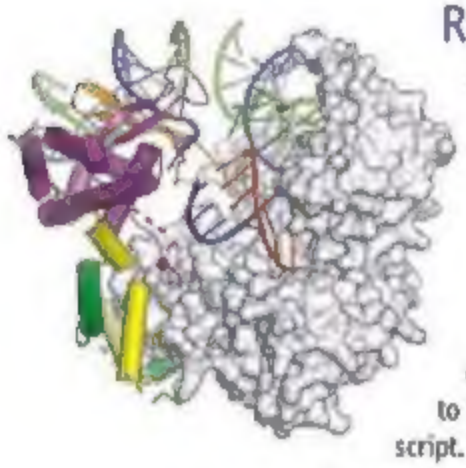

RNA Polymerase Caught in the Act

After binding to the promoter to form an initiation complex, RNA polymerase (RNAP) synthesizes short transcripts in a process known as abortive synthesis before forming the elongation complex that produces a full-length RNA transcript. In the bacteriophage T7 RNAP system, large conformational differences occur when the promoter is released and initiation shifts into elongation, but how these changes happen is unclear. **Durniak *et al.*** (p. 553) describe structures of an intermediate state: T7 RNAP bound to promoter DNA with a seven- or eight-nucleotide RNA transcript. The structures reveal the rotation that allows the polymerase to accommodate the growing transcript during abortive synthesis while still remaining bound to the promoter. Similar rearrangements are likely to occur during transcription initiation in multisubunit RNA polymerases found in bacteria and eukaryotes.

Chloride Channel Clinched

The origin of calcium-dependent chloride currents, required for cell excitability and fluid secretion, has been confusing. Taking an unusual approach, **Caputo *et al.*** (p. 590, published online 4 September; see the Perspective by **Hartzell**) identified the transmembrane protein TMEM16A as a key component. This chloride current is up-regulated when bronchial epithelial cells are treated with interleukin-4 (IL-4). By inhibiting each messenger RNA up-regulated by IL-4 using specific small interfering RNAs in bronchial epithelial cells, the authors were able to identify the gene responsible for the chloride current. Because defects in chloride transport underlie the pathology of cystic fibrosis, this discovery may offer leads into new treatments.

DNA Repair at the Edge

The nucleus of a cell can be divided into functional compartments, based on transcriptional activity and DNA replication. **Nagai *et al.*** (p. 597) reveal a physical connection between the nuclear periphery and processes of DNA damage and repair in budding yeast. Damaged DNA, specifically collapsed replication forks and persistent double-stranded breaks, are transferred to the nuclear pores, where nuclear pore components and other proteins facilitate recombinational repair.

Warm Drink—Warm Thoughts

The priming of attitudes, beliefs, or behaviors has become an active area of research, both for the remarkable range of situations under which it can be demonstrated and for the insights into unconscious cognitive processes. In many cases, the unconscious cognitive system is activated via semantic, stem-word completion tasks, with a subliminally introduced belief (for example, feeling old) buried among a variety of other, unrelated characteristics. **Williams and Bargh** (p. 606) describe a situation in which a physical stimulus influenced people's judgments about interpersonal warmth, to the extent that subjects holding a warm cup of coffee would unwittingly make more prosocial (as opposed to selfish) choices.

CREDIT: DURNIAK ET AL.

Mohamed H. A. Hassan is executive director of TWAS, Trieste, Italy.

Making One World of Science

TWAS, THE ACADEMY OF SCIENCES FOR THE DEVELOPING WORLD, CELEBRATES ITS 25TH anniversary in Mexico City next month. When the academy was first established, a great divide existed between the science-rich North and the science-poor South. A quarter-century later, advances in biology, materials science, and information and communications technologies, among other fields, have further split the global scientific community into three worlds: the North, the surging South, and the stagnant South. The global community now faces the critical challenge of preventing lagging countries from falling even farther behind.

The United States continues to dominate global science. In 2007, U.S. scientists published nearly 30% of the articles appearing in international peer-reviewed scientific journals, which is comparable to the percentage a quarter-century ago. But China, responsible for less than 1% of publications in 1983, has recently surpassed the United Kingdom and Japan to become the world's second leading nation in scientific publications. China now accounts for more than 8% of the world's total, whereas India and Brazil produce about 2.5 and 2%, respectively, of the world's scientific articles. All told, scientists in developing countries generate about 20% of the articles published in peer-reviewed international journals.

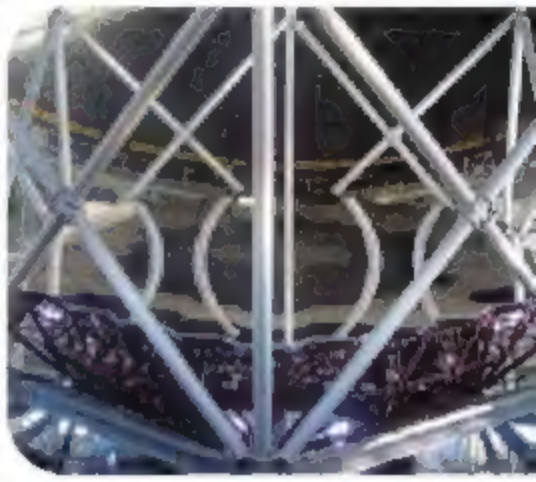

It is gratifying to see such progress made by the surging South. But we cannot ignore the fact that these advances have been largely limited to just a few countries. The top five performers (China, India, Brazil, Turkey, and Mexico) contribute well over half of the scientific publications from the South. By contrast, sub-Saharan Africa, a region of 48 countries, produces just 1% of the world's scientific publications.

The building of scientific capacity is a main reason for the South's economic progress. Several developing countries—for example, Brazil, India, China, and even Rwanda—now spend 1% or more of their gross domestic product on science and technology. Indeed, over the past 5 years, the economies of the developing world have grown at a faster pace than those in the developed world, and investment in science and technology has a lot to do with it. We see this impact in the emergence of Brazil as a leader in the development of biofuels. We see it in India's increased capacity in information and communications technologies. And we see it in the growing prowess of China in nanoscience and nanotechnology.

Increased scientific capacity is not just good for the developing world; it benefits the entire world. For example, the Chinese SARS Molecular Epidemiology Consortium cooperated with international groups to trace the evolution of the SARS virus from an animal to a human pathogen after the outbreak of 2003. The Southern African Large Telescope (SALT) near Cape Town, South Africa, the largest single telescope in the Southern Hemisphere, has boosted research in astronomy and astrophysics internationally since it became operational in 2005. And innovative efforts to devise sustainable uses for biodiversity by the National Institute of Biodiversity (INBio) in Costa Rica have served as models for institutions in both the South and North for the past two decades.

The point is, in our global world, improved scientific capacity anywhere has the potential to help everyone everywhere. The global scientific community should care about countries that remain scientifically deficient. The progress that has been achieved represents only partial success. Resting on our laurels now will only increase the risk that inequities within the developing world will grow, further marginalizing scientifically lagging countries.

The 25th anniversary of TWAS is an opportunity to applaud the success of those developing countries that are building their scientific capacity. But we must not allow the scientific success of some developing countries to overshadow the troubling scientific stagnation in others. Enabling global science to truly flourish will require making one world of science. TWAS's ultimate vision—a world in which humanity is dedicated to solving common global problems together—can only be realized when all countries have attained scientific proficiency.

– Mohamed H. A. Hassan

10.1126/science.1166199

CREDITS: (TOP) TWAS; (RIGHT) COURTESY OF THE SALT FOUNDATION

BIOMEDICINE

Solid Tumors in Living Color

The behavior of tumors is profoundly influenced by the microenvironment in which they grow. In addition to diffusible extracellular factors, this environment harbors a complex and dynamic population of stromal cells, including fibroblasts and a variety of immune cells. Because different types of stromal cells can have opposing effects on tumor progression and responses to therapy, it is important to understand how each cell type behaves in actively growing tumors.

Egeblad *et al.* have combined confocal microscopy with multicolor imaging techniques to record in living mice the movement and localization patterns of tumor-infiltrating stromal cells during a 12-hour period. One feature shared by several stromal cell types was greater motility at the tumor periphery than within the tumor mass. Regulatory T cells were found to migrate near blood vessels, and their movement was sensitive to tumor oxygen levels; in contrast, the movement of myeloid cells (the most heterogeneous group of stromal cells) was insensitive to oxygen, and their localization patterns and migration rates varied according to cell-surface marker expression, probably reflecting important functional differences. By helping to define the contributions of specific stromal cells to tumor growth, this imaging technology may lead to more effective therapies. — PAK

Disease Models Mech. **1**, 155 (2008).

BIOCHEMISTRY

A Pinch of Sugar

In metazoans, many cellular proteins are regulated by posttranslational modification of serine and threonine residues with *N*-acetylglucosamine to create an *O*-GlcNAc appendage. Acylation may compete for the same residues as phosphorylation, but in contrast to the hundreds of kinases and phosphatases that regulate phosphorylation status, there is but a single *O*-GlcNAc transferase (OGT) and a single *O*-GlcNAc hydrolase. Because no acylation sequence motif has been identified as yet, how OGT recognizes its protein substrates remains unclear.

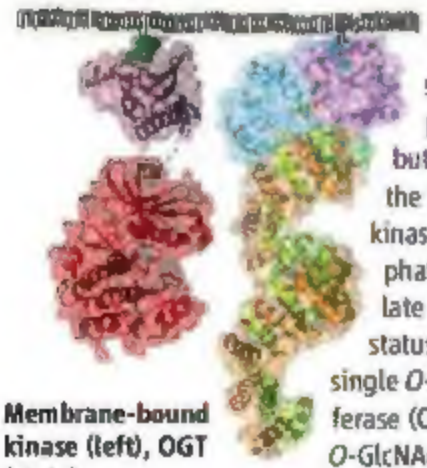

Membrane-bound kinase (left), OGT (right).

Clarke *et al.* report the structure of OGT both in the apo state and in complex with a phosphonate analog of the sugar donor UDP-GlcNAc. The N-terminal domain comprises repeats of the tetratricopeptide (TPR) protein interaction module and the catalytic C-terminal domain has two subdomains that together form the metal-independent glycosyltransferase fold GT-B. The UDP-GlcNAc analog is pinched between the subdomains at the bottom of a conserved groove that is suitably shaped to bind substrate peptides; the TPRs interact with the catalytic domain so that the putative substrate binding groove extends into the TPR domain. The authors present mutagenesis data consistent with the proposal that peptides bind in the active-site groove, with proteins binding to the extended surface formed by the TPRs. A phosphoinositide binding site is located on the surface of the catalytic domain and may recruit OGT to membrane-bound targets. — VV

EMBO J. **27**, 10.1038/emboj.2008.186 (2008).

PHYSIOLOGY

Not Fat, Just Well Covered

Adélie penguins breed on the Antarctic ice, and the chicks, to survive, must rapidly establish a layer of fat to protect themselves against the subzero temperatures and to enable them to enter the water a mere 2 months after hatching. Raccurt *et al.* investigated the transcriptional program responsible for this speedy production of adipose tissue by taking autopsy samples from the chicks of 16 out of the 34,000 penguin pairs that breed on the Pointe Geologie archipelago. They then measured the expression levels of transcription factors, hormone receptors, and other genes known from in vitro studies of mouse and chicken cells to be involved in the growth and differentiation of adipocytes. In the first 2 weeks, while a chick was at least partially protected by sheltering in a parent's brood pouch, growth hormone and 3,5,3'-triiodo-thyronine (T_3) receptors along with the transcription factor GATA3 marked a period of intensive adipocyte differentiation and development. After day 15, when chicks had outgrown their brood pouches, lipoprotein lipase, PPARγ, and other factors associated with adipocyte maturation and lipid storage took over to produce large fat-filled cells that formed a thermally insulating layer. This is similar to the changes seen in chicken cells, but subtle differences demonstrate how in penguins that pattern is tailored to their particular habitat. — CS*

Am. J. Physiol. Regul. Integr. Comp. Physiol. **295**, 10.1152/ajpregu.90371.2008 (2008).

CHEMISTRY

A Jolt from Ethanol

One advantage enzymes tend to have over synthetic catalysts is their capacity as very large molecules to create an environment that fully surrounds a substrate and thereby mediates

CREDITS (TOP TO BOTTOM): MIREILLE RACCURT; CLARKE ET AL., EMBO J. 27, 10.1038/EMBOJ.2008.186 (2008)

efficient reactivity through delocalized polarity effects. A simplified means of probing these reaction medium influences is to vary the solvent in which small-molecule catalysts operate. Liu *et al.* have explored the medium effects in a phosphate diester hydrolysis reaction catalyzed by a di-zinc complex that models enzymes that cleave nucleic acids at backbone sites. They find that although the catalyst is not highly active in aqueous solution, a shift into ethanol solvent results in marked acceleration. Moreover, the catalyst is remarkably selective for hydrolysis over ethanolysis, yielding a nearly 1:1 mixture of the competing products at an ethanol:water ratio exceeding 600:1. Based on comparison with the rate of the uncatalyzed background hydrolysis in ethanol, the authors posit a 10^{17}-fold accelerating effect of the catalyst in this conducive medium. — JSY

J. Am. Chem. Soc. **130**, 13870 (2008).

HYDROLOGY

How Wet Crops Get

One of the major challenges posed by both increasing global population and climate change is the wise use of water. An enormous quantity of fresh water is used in agriculture, and planning in the face of dwindling resources requires an understanding of current and past consumption. With the aid of a global vegetation and water balance model, Rost *et al.* provide a global assessment of agricultural water use and evaluate how changes in land use affected water consumption during the 20th century. Their analysis shows that although globally agriculture is mostly based on the use of precipitation directly, major agriculture in India, China, Pakistan, and the United States depends heavily on diversions from rivers or groundwater; about half is from nonrenewable sources. Historically, their analysis implies that the global expansion of agriculture since 1900 probably increased discharge by nearly 5% (despite an increase in withdrawals for irrigation over time), an amount about comparable in some cases to effects from climate change alone. Thus, land-use changes need to be considered in adapting water use to climate change. — BH

CREDIT: JUPITER IMAGES

Water Resour. Res. **44**, 10.1029/2007WR006331 (2008).

DEVELOPMENT

Flower Power

Some plants, such as the poppy, form a single flower at the tip of the plant; others, such as the petunia or tomato, also flower at the tip but then generate a new lateral meristem that becomes the new tip, and then makes a new flower and a new meristem, yielding a zig-zag pattern of flowers. Rebocho *et al.* have identified a gene in petunia called *EVERGREEN* (*EVG*), which is required for formation of the new lateral meristem. Mutants deficient in *EVG* grow normally, but don't zig-zag or flower. *EVG* is expressed in the apical meristem after the plant matures to the point of flowering, where it promotes the expression of *DOUBLETOP* (*DOT*), a transcriptional activator that determines flower formation. The function of *EVG* seems to be to support the separation of the new meristem as the previous meristem becomes a flower. Analysis of related genes in *Arabidopsis* suggests that *EVG* may function to control cell proliferation. — PJH

Dev. Cell **15**, 437 (2008).

SIGNAL TRANSDUCTION

Screening for Kinases

Hedgehog (Hh) ligands are regulators of developmental patterning, and overactivity of the Hh signaling pathway is associated with some human cancers. Genetic approaches in *Drosophila* have identified many components of the signaling pathway, but Hh signaling is still incompletely understood, particularly in vertebrates, in which the components of the pathway differ substantially from their counterparts in flies. Evangelista *et al.* searched for protein kinases that influenced Hh signaling by monitoring the effects of a library of siRNA molecules on the expression of a reporter gene in mammalian cells. One kinase identified in the screen was a member of the cyclin-dependent kinase family, Cdc2l1, which regulates mitosis and apoptosis; Cdc2l1 directly interacts with Suppressor of Fused (an inhibitor that keeps the Gli transcription factor from moving to the nucleus and activating Hh-dependent gene transcription). Overexpression of Cdc2l1 in cultured cells or in zebrafish embryos enhanced Hh signaling. Thus, the authors propose that Cdc2l1 is a component of the Hh pathway that may have been missed in genetic screens because of the harmful effects of the loss of a multifunctional protein. — LBR

Sci. Signal. **1**, ra7 (2008).

*Chris Surridge is a locum editor in *Science*'s editorial department.

www.sciencemag.org

Science

1200 New York Avenue, NW
Washington, DC 20005
Editorial: 202 326-6550 FAX 202 289-7562
News: 202 326-6581, FAX 202 371-9227
Bateman House, 82-88 Hills Road
Cambridge, UK CB2 1LQ
+44 (0) 1223 326500, FAX +44 (0) 1223 326501

Subscription Services For change of address, missing issues, new orders and renewals, and payment questions: 866-434 AAAS (2227) or 202-326-6417, FAX 202-842-1065. Mailing addresses: AAAS, P.O. Box 96178, Washington, DC 20090-6178 or AAAS Member Services, 1200 New York Avenue, NW, Washington, DC 20005

Institutional Site Licenses please call 202 326-6755 for any questions or information

Reprints: Author Inquiries 800-635-7181
Commercial Inquiries 803-359-4578

Permissions 202-326-7074, FAX 202-682-0816

Member Benefits AAAS/Barnes&Noble.com bookstore www.aaas.org/bn; AAAS Online Store www.aaasonlinestore.com/aaas; code MKB6. AAAS Travels: Betchart Expeditions 800 252 4910. Apple Store www.apple/eppstore/aaas; Bank of America MasterCard 1-800-833-6262 priority code FAA3YU; Cold Spring Harbor Laboratory Press Publications www.cshlpress.com/affiliates/aaas.htm; GEICO Auto Insurance www.geico.com/landingpage/go51.html?logo=17624. Hertz 800-654 2200 CDP#343457; Office Depot https://bsd.officedepot.com/portal.login.do; Seabury & Smith Life Insurance 800-424-9883, Subaru VIP Program 202-326-6417; VIP Moving Services www.vipmayflower.com/domestic/index.html; Other Benefits: AAAS Member Services 202-326-6417 or www.aaasmember.org.

science_editors@aaas.org	(for general editorial queries)
science_letters@aaas.org	(for queries about letters)
science_reviews@aaas.org	(for returning manuscript reviews)
science_bookrevs@aaas.org	(for book review queries)

Published by the American Association for the Advancement of Science (AAAS), *Science* serves its readers as a forum for the presentation and discussion of important issues related to the advancement of science, including the presentation of minority or conflicting points of view, rather than by publishing only material on which a consensus has been reached. Accordingly, all articles published in *Science*—including editorials, news and comment, and book reviews—are signed and reflect the individual views of the authors and not official points of view adopted by AAAS or the institutions with which the authors are affiliated.

AAAS was founded in 1848 and incorporated in 1874. Its mission is to advance science, engineering, and innovation throughout the world for the benefit of all people. The goals of the association are to: enhance communication among scientists, engineers, and the public; promote and defend the integrity of science and its use; strengthen support for the science and technology enterprise; provide a voice for science on societal issues; promote the responsible use of science in public policy; strengthen and diversify the science and technology workforce; foster education in science and technology for everyone; increase public engagement with science and technology; and advance international cooperation in science.

Information for Authors
See pages 634 and 635 of the 1 February 2008 issue or access www.sciencemag.org/about/authors

Bring Out Your Dead!

Life in merrie olde England was hazardous to health, especially for men, researchers have concluded after reviewing coroner records from Sussex county for the years 1485 to 1688. Of the 1169 adult deaths investigated by a coroner, 35% were accidental, the researchers report this week in the *Journal of Epidemiology and Community Health*. Men accounted for fully 86% of the victims. Drowning, either at sea or in ponds or wells, caused more than one-third of the deaths. Travel was particularly dangerous. About 30% of deaths were triggered by mishaps such as being thrown from horses or battered by an errant wagon part.

Lead author Elizabeth Towner, an injury-prevention researcher at the University of the West of England in the United Kingdom, says the statistics are more than just historical curiosity. Lack of proper safety precautions and poor health care seen in the past are still mirrored in the developing world, where activities such as travel in antiquated buses and overcrowded ferries remains dangerous. The field of accident research has much to learn from such retrospective studies, says Andrea Gielen, director of the Center for Injury Research and Policy at Johns Hopkins University in Baltimore, Maryland, who notes that accidents, most of them in poorer countries, cause 5 million deaths a year.

From A to Y

The results are in: Australia is the most prosperous country in the world; Yemen drags at the bottom of the list. But it's not just wealth that makes a country prosperous, according to the 2008 prosperity index, also known as the "happiness index," published last week by the Legatum Institute (LI) in Dubai (see www.prosperity.com). The institute based its rankings on surveys of economic competitiveness and comparative livability from 140 countries, including factors such as capital investment and the degree of social equality.

This year, for the first time, countries' environmental efforts counted toward their scores, says LI Senior Vice President William Inboden. The institute selected an objective measurement—the ratio of developed land to land remaining in its natural state in each country—and added questions about how respondents felt about their country's environmental policies. Depending on a country's wealth, the environmental measures could count for as much as 4% of a country's prosperity score. Although Australia was the most prosperous country overall, New Zealand topped the environmental measures. The most environmentally unhappy people were Ukrainians, who particularly dislike their air quality.

CREDITS (TOP TO BOTTOM): BETTMANN/CORBIS; GARY SMALL/UNIVERSITY OF CALIFORNIA, LOS ANGELES; REUTERS/JONATHAN EVANS

Genomes for the World

George Dyson learned that his sister Esther (left) planned to publish her sequenced genome after reading about it in *The New York Times*. His immediate reaction? "Gee, she didn't ask any of us," he says. But George Dyson, a historian of science in Bellingham, Washington, has no qualms about seeing personal DNA (much of which he shares) in the public domain. Admittedly, the Dysons are better versed than most in genetics: Esther Dyson, an investor in and board member of the genetics company 23andMe, had already supplied family members with the company's DNA test kits.

Dyson's is one of the first 10 genomes made publicly available in the Personal Genome Project, brainchild of Harvard Medical School geneticist George Church. Church is raising money to sequence key portions of the genomes of 100,000 people, to be released along with their health records.

"I'm certainly not presenting this as offering new science," says Church, who notes that many more genomes matched with health records will be needed first. Already, 5000 more people have expressed interest. Participants have the option of withholding some data. "I exercised a line-item veto on the hemorrhoids and erectile dysfunction," joked Harvard psychologist Steven Pinker, one of the 10. More seriously, he says, he may keep the status of his *APOE* gene—related to risk of Alzheimer's disease—under wraps, as DNA discoverer James Watson did when he had his genome sequenced last year.

Internet and the Aging Brain

Web searching activated more neurons (bottom fMRI scan) than just reading text.

Google users gasped when presidential candidate John McCain joked that he relies on his wife, Cindy, to help him navigate the Internet. But new research shows that for McCain and others like him, surfing the Net can give their brains a good workout.

Researchers recruited two groups of 12 seniors of comparable education levels and health, equally divided by gender. One group had little or no Web experience; the other used the Internet at least once a day.

Each underwent brain scans while reading text on a computer screen and searching for information on the Internet. The reading task activated areas of the brain responsible for vision and language processing. The Internet search got more neurons popping, in areas involved in reasoning and memory, such as the frontal lobes and hippocampus, the researchers report in the upcoming issue of the *American Journal of Geriatric Psychiatry*.

The Net-savvy elders showed twice as much brain activity during the search task as the Net-naïve group did, says lead researcher Gary Small, a psychiatrist at the University of California, Los Angeles. "Once we understand the task, then the circuits become more engaged," he says. So McCain would have to practice doing "a Google" or two to reap neural benefits from Internet searches.

Denise Park, a neuroscientist at the University of Texas, Dallas, calls the study "provocative and interesting." It's a "nice first step" in understanding how Web searches engage our brains, she says.

EDITED BY YUDHIJIT BHATTACHARJEE

SPREADING THE WORD

Linguistics students at the University of California, Berkeley, are getting a chance to document a rare African language—without leaving campus. The opportunity comes via Simon Nsielanga Tukumu (left), a Berkeley resident and native speaker of Nzadi, a language spoken by a few thousand people living in fishing villages in the Democratic Republic of the Congo.

Berkeley linguist Larry Hyman is an expert on the Bantu languages of Africa, but until a mutual acquaintance introduced him to Nsielanga last year, he had never heard of Nzadi. The language isn't listed in the major database of human languages. Seeing a unique opportunity, Hyman recruited Nsielanga as a teaching assistant for his undergraduate class Introduction to Field Methods. By querying Nsielanga, students are piecing together the vocabulary and grammar of Nzadi.

Nsielanga, who is working on a master's degree in ethics at the Graduate Theological Union in Berkeley, relishes the chance to share his culture. "I'm so happy to help them learn my language," he says. Happy is *yang* in Nzadi.

THEY SAID IT

"If Marty and Roger want to show me some gratitude, they can always send some cash. I'm accepting gifts and donations."

Douglas Prasher, the biochemist who isolated the jellyfish gene behind green fluorescent protein (GFP). Work on GFP earned Martin Chalfie, Roger Tsien, and Osamu Shimomura the 2008 chemistry Nobel, but Prasher—who gave Chalfie and Tsien the gene in the early 90s—now drives a courtesy shuttle for a car dealership in Huntsville, Alabama.

MOVERS

BREADTH. William Brody, the departing president of Johns Hopkins University (JHU) in Baltimore, Maryland, has been named head of the Salk Institute for Biological Studies in San Diego, California.

A radiologist, electrical engineer, and successful biotech entrepreneur, Brody helped triple JHU's endowment, now $2.5 billion, during his 12-year term. He hopes to put those fundraising skills to work at Salk, a nonprofit with 870 scientific staff and a $114 million budget. He also intends to help the institute, founded in 1960 by Jonas Salk, forge new partnerships with biotech companies and local universities.

Marsha Chandler, Salk's executive vice president, says the 64-year-old Brody "is a perfect fit" because of his "broad appreciation of science" and his interest in "innovation and tech transfer." As such, she says, Brody will advance Salk's mission of "doing curiosity-driven basic science" as well as "transferring the fruits of that research to society."

Brody leaves JHU at the end of the year and will start in the new position on 1 March 2009.

DEATHS

MR. HEALTH. Paul Rogers, a former Democratic representative from Florida who helped enact the National Cancer Act of 1971 and the Clean Air Act and increased funding for medical and scientific research, died of lung cancer on 13 October. He was 87.

Rogers, a lawyer, served in the U.S. House of Representatives from 1955 to 1979 and chaired a panel on health and the environment that oversaw, among other agencies, the National Institutes of Health (NIH) and the Environmental Protection Agency. He continued his advocacy as chair of ResearchAmerica from 1996 to 2005. "He absolutely understood the strategic importance of making NIH research available to the public," says NIH Director Elias Zerhouni, who remembers Rogers as being empathic, charismatic, and thorough.

Rogers was passionate about improving quality of life, adds Mary Woolley, president and CEO of ResearchAmerica. "It really was his hope, his optimistic vision, that people of good spirit will work together in assuring that research for health makes our country a better place."

Three Q's >>

This month, the arXiv preprint server (http://arxiv.org/) posted its 500,000th preprint. Created in 1991 by particle physicist **Paul Ginsparg** of Cornell University, the site is now the primary venue for results in many subfields of physics and also serves the mathematics, computer science, statistic, and quantitative biology communities.

Q: Did you ever envision that the arXiv would rack up hundreds of thousands of papers?

No. It was originally intended for a tiny subfield of theoretical particle physics, encompassing about 100 articles per year. And the plan was to hold them only for 3 months, by which time they would be disseminated by conventional means. Happily, I never got around to deleting anything.

Q: The arXiv hasn't put journals out of business, even though many of the papers they publish appear there first. Why not?

The journals provide both a measure of quality control and a feeling of security, like an insurance policy funded by one's institution. A decade and a half ago, I certainly would not have expected the current state in which preprint servers coexist with conventional online publications.

Q: Can researchers gain an unfair advantage by posting a slapdash manuscript and then revising the paper later?

We've long kept a full, date-stamped revision history of every article publicly available so that disputes can be adjudicated by looking at the precise contents of a particular version from a particular date. The knowledge that every version will be archivally available also helps ensure that authors are cautious about what they submit.

Got a tip for this page? E-mail people@aaas.org

CREDITS (TOP TO BOTTOM): MIKE KEPKA/SAN FRANCISCO CHRONICLE/POLARIS; SOURCE: PAUL GINSPARG, SALK INSTITUTE FOR BIOLOGICAL STUDIES

Clinical trial ethics 516

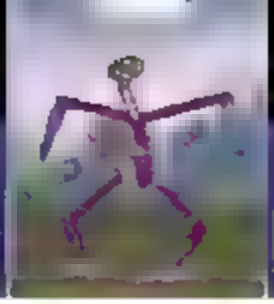

Spore video draws complaints 517

OCEAN DRILLING

Deep-Sea Scientific Drilling Hit By a Cost Double Whammy

As the oil industry gears up for the ongoing offshore-oil boom, scientists who study the sea floor say competition for scarce drilling resources is leaving them high and dry. "Funding goes down, oil goes up," laments paleoceanographer Henk Brinkhuis of Utrecht University in the Netherlands. Facing soaring costs and lengthening delays, the United States component of the Integrated Ocean Drilling Program (IODP)—the current phase of the cooperative international investigation beneath the sea floor—has been literally stuck in dry dock, leading to an unprecedented 3-year hiatus in U.S. drilling. Japanese and European components of IODP are not faring much better. "I am very concerned about the long-term future of IODP," says marine geologist Craig Fulthorpe of the University of Texas, Austin.

Perhaps the worst blow came when the United States set out several years ago to refurbish and modernize its drilling platform, the *JOIDES Resolution*, or more familiarly, the *JR*. The $130 million renovation job had a fixed cost in a Singapore shipyard, but as the rising cost of oil spurred a surge of offshore drilling, the yard shunted the scientific ship to the side to focus on building and refurbishing drilling platforms for well-heeled oil companies.

Under the resulting schedule pressure, the *JR*—originally programmed to resume drilling in October 2007—will be leaving the yard in early March 2009. This delay pushed two 8-week drilling cruises led by Fulthorpe and by Brinkhuis back a full year on less than 2 months' notice. "It is a disruption," says Fulthorpe. Meanwhile, the competition with the oil industry hit the Europeans even harder. They had signed a short-term contract for one-time use of a special-purpose drill ship, but the owner of the vessel broke the contract to lease it to a higher paying oil company, Brinkhuis says. The European component of IODP has not drilled in 2 years.

With work on the *JR* nearing completion, researchers now fear that budget cuts may curtail scientific drilling for years to come. U.S. operations are being funded well below expectations of a few years ago, says James Allan of the U.S. National Science Foundation (NSF), which funds the U.S. component of IODP. NSF funding amounts to almost a 20% cut in inflation-adjusted dollars, he says. Scientists also

Tarrying too long. Competition from the oil industry for shipyard resources has delayed the return of the drill ship *JOIDES Resolution*.

U.S. SCIENCE AGENCIES

Media Policies Don't Always Square With Reality

Most U.S. government agencies don't allow their scientists to talk freely with the media, according to a survey by an advocacy organization that has been highly critical of the Bush Administration's track record on scientific integrity. A new report (ucsusa.org) from the Union of Concerned Scientists (UCS) gives some agencies relatively high marks for adopting policies that allow considerable openness but notes that those policies are not always followed. The culture in the majority of the 15 agencies UCS examined "has become [such that] talking with the press has become fraught with risks," says UCS's Francesca Grifo.

The Bush Administration has been involved in several high-profile incidents regarding the accessibility of government researchers, including the ability of climate scientists at NASA and the National Oceanic and Atmospheric Administration (NOAA) to speak openly about their research. So UCS decided to examine the written media policies at federal agencies and ask how well they are working in practice.

Pressing issue. Survey finds most science agencies need to improve how they handle media requests.

Based on material from printed documents and agency Web sites, UCS gave grades of "excellent" or "good" to six of 15 agencies. (To keep the effort manageable, it omitted the Energy, Agriculture, and Defense departments.) The group also sent questionnaires to 6000 government scientists asking how those policies were implemented at their respective agencies. Based on a 12% response rate, UCS concluded that a minority of agencies were doing a good job (see pie chart).

The two lists don't necessarily match up. For example, UCS gave the Centers for Disease Control and Prevention an "A" for its policies and an "unsatisfactory" for its implementation of them, whereas the U.S. National Science Foundation earned an "outstanding" for allowing its science

CREDITS (TOP TO BOTTOM): CONSORTIUM FOR OCEAN LEADERSHIP; SOURCE: UCS

face three- to fourfold increases in the cost of drilling consumables such as steel liners for drill holes and a recently estimated $1-million-per-month rise in the cost of fueling the *JR*.

As a result of the soaring costs, NSF now plans for the *JR* to devote only 70% of its time to IODP drilling. The Japanese behemoth ship *Chikyu* is likewise drilling for IODP only 60% to 70% of the time. Yet, there's plenty of science to be done. "There are now 30 drilling proposals [in the pipeline] that have been highly ranked," says Brinkhuis. With the reschedulings plus the cutbacks in operating time, much of that science will be delayed and some never tackled at all, scientists worry.

The *JR*'s non-IODP time, everyone hopes, will be leased to a consortium of oil companies to drill holes of interest to both industry and scientists. But falling back on industry "is very discouraging for scientists," says longtime ocean-drilling participant Theodore Moore Jr. of the University of Michigan, Ann Arbor. Industry and academia attempted a marriage of convenience 25 years ago (*Science*, 8 February 1980, p. 627) to no avail. "It's always been a difficult task linking industry and scientists' interests," says Moore. Still, unless ship-fuel costs continue to ease, there is no other relief on the horizon. **–RICHARD A. KERR**

administrators free rein and an "incomplete" for not spelling out its policies. A 2007 law requires the White House to make sure all agencies have done so.

UCS found that calls for openness from the boss don't always translate into more transparent operations. The director of the National Institutes of Health, Elias Zerhouni, emphasized "open scientific exchange" in a 2007 agencywide memo, but the UCS survey found NIH practices "not satisfactory" because scientists still need permission before speaking to reporters. ("It's primarily an FYI rather than an approval process," says an NIH spokesperson.) In contrast, following incidents at their agencies, the directors of NOAA and NASA told their managers to give agency scientists more leeway. As a result, says Timothy Donaghy of UCS, the situation is "a lot better now."

–ELI KINTISCH

CREDITS: PATRICK D. MCDERMOTT/AP/PHOTOLIBRARY.COM

CONFLICTS OF INTEREST

Cardiologists Come Under the Glare of a Senate Inquiry

Research universities are nervously viewing an expanding Senate inquiry into alleged financial conflicts of interest among faculty members. Last week, Columbia University came under the spotlight. Senator Chuck Grassley (R–IA) publicly challenged the university to explain the industry ties of a group of Columbia cardiologists who work with a nonprofit that receives funding from medical device makers. This money may be biasing some faculty members' views on stents and other heart devices, Grassley suggests.

Widening net. Senator Grassley probes a nonprofit linked to Columbia University

Grassley zeroed in on the Cardiovascular Research Foundation (CRF), which conducts clinical trials on devices and drugs, according to its Web site. It also holds an annual educational conference. Three Columbia cardiologists sit on CRF's board; others are listed as "leadership" or "affiliated" physicians. In a 16 October letter to Columbia president Lee Bollinger, Grassley and Senator Herb Kohl (D–WI) request details on outside income for about 20 of these faculty members. In a similar letter to CRF they write: "We are ... concerned that funding from the medical device industry may influence the practices of non-profit organizations that purport to be independent in their viewpoints and actions."

Columbia and CRF say they will respond to the questions. Although none of the Columbia faculty members appears to have grants from the U.S. National Institutes of Health, and therefore may not come under NIH's rules, the university has its own conflict-of-interest policies and "expect[s] that they are followed by all ... faculty," Columbia says.

Although it may not be unusual for industry-funded charities to have ties to academic medical centers, some observers see a potential problem. "I suspect that individuals set these [charities] up to bypass university oversight procedures," suggests health policy expert Eric Campbell of Harvard Medical School in Boston.

But Susan Ehringhaus of the Association of American Medical Colleges in Washington, D.C., cautions against generalizing. The important first step, she says, is that industry funds be fully disclosed. CRF's Web site states that it has corporate funding, and two of its Columbia directors acknowledged in an article in *The Lancet* last year that the foundation has ties to four companies.

The Columbia inquiry came as a related probe of financial conflicts among NIH-funded researchers was heating up. Last week, news emerged that NIH recently responded to concerns about an Emory University psychiatrist by taking a rare step: It suspended a grant to the university after Grassley alleged that principal investigator Charles Nemeroff had failed to report at least $1.2 million in outside consulting income (*Science*NOW, 14 October: http://sciencenow.sciencemag.org/cgi/content/full/2008/1014/1). The $9.3 million, 5-year study comparing depression treatments was transferred to another faculty member in July, but NIH halted funding in mid-August, Emory says. The frozen grant has put universities on high alert to get their conflict-of-interest policies in order, says one biomedical research lobbyist.

–JOCELYN KAISER

OCEANOGRAPHY

Global Warming Throws Some Curves in the Atlantic Ocean

It was an ominous if subtle shift in the far North Atlantic. For 30 years, waters off southern Greenland and Iceland had been growing less and less salty, oceanographers reported in late 2003. It looked as if global warming could be freshening high-latitude Atlantic waters (*Science*, 2 January 2004, p. 35). If the trend continued, they worried, it could throw a monkey wrench into the "conveyor belt" of currents that warms the far North Atlantic, as is wildly overdone in the movie *The Day After Tomorrow*. New analyses have now shown that global warming is indeed messing with the Atlantic's salinity, although not as dramatically as Hollywood envisioned.

The first explicit link between global warming and ocean salinity changes comes in a study in press in *Geophysical Research Letters*. Modeler Peter Stott of the Met Office Hadley Centre in Exeter, U. K., and his colleagues simulated changing ocean salinity in the center's HadCM3 climate model with and without increasing greenhouse gases. Under past global warming conditions, the model produced salinity changes around the world much like those seen. But only in the subtropics and mid-latitudes of the North Atlantic—between 20°N and 50°N—did salinity change significantly more than the natural jigglings of the climate system would have changed it.

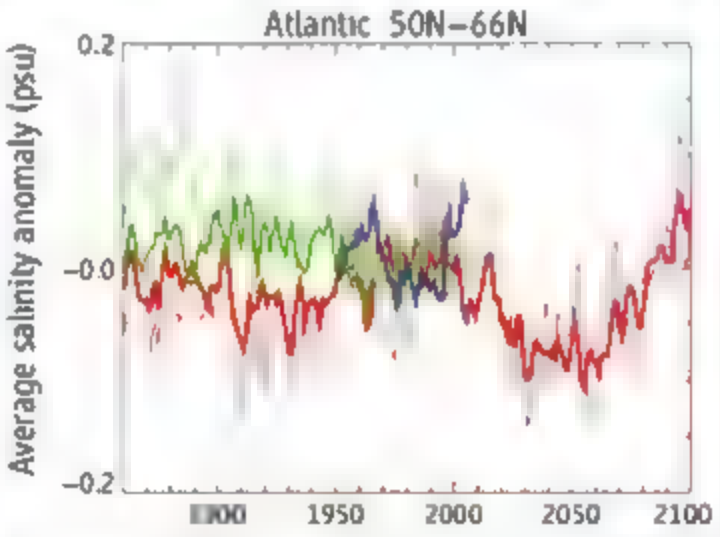

No biggie, yet. With (red) or without (green) greenhouse conditions, a model produced much the same variations in ocean salinity as observed (blue), but the variability could increase.

CREDIT: ADAPTED FROM P. A. STOTT ET AL., GEOPHYSICAL RESEARCH LETTERS, IN PRESS

The increase in salinity in North Atlantic mid-latitudes thus carries the "fingerprint" of human influence left by the effects of human-generated greenhouse gases, the group concludes. Greenhouse warming there apparently removed more water by evaporation while precipitation decreased, concentrating seawater's salts. "It looks convincing to me," says climate modeler Gabriele Hegerl of the University of Edinburgh, U. K. The signal is only now emerging, she adds, but "it looks very consistent with what is expected." She and others would like to see additional models replicate the fingerprinting, just to be sure.

Although global warming seems able to alter even the saltiness of the sea, it hasn't noticeably freshened the high latitudes of the North Atlantic, as some researchers thought it might be doing back in 2003. When run without rising greenhouse gases, the Hadley model produces so many salinity swings up and down through natural processes built into the climate system that any greenhouse fingerprint would have been smudged beyond recognition, the group found.

But global warming isn't finished with the far North Atlantic, at least according to the Hadley model. Run out to the end of the century under a strengthening greenhouse, it simulates a precipitous dip in northern salinity from a recent upturn and then a rapid recovery by 2100 (see figure). That roller-coaster ride "rings true," says physical oceanographer Ruth Curry of Woods Hole Oceanographic Institution in Massachusetts. Since publishing the observed freshening trend in 2003, she has come to understand that natural swings in atmospheric circulation over the North Atlantic—the so-called North Atlantic Oscillation (NAO)—have alternately driven fresher water from the Arctic and then saltier water from low latitudes into the far North Atlantic. Those shifts, rather than global warming, have dominated high-latitude salinity, with an NAO-driven switch from fresher to saltier coming in the mid-1990s.

The next decades-long swing in northern salinity will be large because global warming is increasing the stores of fresher water in the Arctic and of saltier water in the far south, Curry says. "I would expect some weakening of [conveyor belt] currents" as the next freshening sets in, she says, "but that's not the biggest worry." The biggest worry, she says, is losing all Arctic sea ice to global warming.

–RICHARD A. KERR

SCIENCESCOPE

Bug Hunters, Unite

Scientists working to map the microbes that naturally live in and on the human body have agreed to coordinate their efforts. Last week, representatives from nine countries announced the formation of the International Human Microbiome Consortium. The alliance will enable researchers who are sampling the microbial communities that inhabit the skin, gut, mouth, and reproductive tract of humans to deposit their data in a central repository, freely available online. Consortium members will conform to common data standards, avoid overlap in their efforts to sequence the genomes of different microbes, and follow common informed-consent and privacy standards. The consortium will give researchers from around the world the chance to directly and efficiently compare their data, says molecular biologist Jane Peterson of the National Human Genome Research Institute in Bethesda, Maryland, who represented the U.S. National Institutes of Health at the Heidelberg, Germany, meeting at which the agreement was worked out. That could allow researchers to compare, for example, the gut microbes of people in China who follow a traditional diet with those of people in Europe and North America.

–GRETCHEN VOGEL

Scientific Science Policy

Researchers will gather in Washington, D.C., in early December to bolster a White House–led effort across the government to improve how science agencies make policy decisions. The "Science of Science Policy" effort, begun in 2006 and funded mostly by the U.S. National Science Foundation, is subsidizing more than $15 million per year in work that analyzes research trends, gauges scientific progress, and develops modeling and forecasting techniques. The government's goal is to "make more informed, defensible policy decisions," says the U.S. Department of Energy's Bill Valdez.

–ELI KINTISCH

SLAC Plays a Name Game

After a spat with its owner, the U.S. Department of Energy (DOE), the Stanford Linear Accelerator Center has tweaked its name. The new appellation, SLAC National Accelerator Laboratory, resolves a disagreement between DOE, which wanted to trademark the name of its Menlo Park, California, lab, and Stanford University in Palo Alto, California, which sought to protect its own moniker. Officials say the new name also reflects a shift from just particle physics to work in an array of disciplines, including astrophysics and x-ray studies.

–ADRIAN CHO

ETHICS

Clinical Trials Guidelines at Odds With U.S. Policy

Aiming for consensus on some long-debated issues in clinical research, the World Medical Association (WMA) adopted a revised ethics manifesto at its meeting last week in Seoul, South Korea. WMA's guidelines, known as the Declaration of Helsinki, have long been used by regulatory agencies around the world as the basis of rules governing the conduct of clinical trials, although the U.S. Food and Drug Administration (FDA) is in the process of moving to a different—some say less demanding—set of ethical standards.

The revisions approved last week include sharper limits on the use of placebos and stronger language requesting that trial sponsors care for all participants after a trial is finished. In a new provision that's likely to prove controversial, WMA asks sponsors to register clinical trials in publicly available databases before recruiting the first subject. Even WMA's leaders concede that these changes in the declaration may not be the last word.

Since its adoption in 1964, the Declaration of Helsinki has been amended five times, most recently in 2000. Debate continued as footnotes were added. "It was obvious that the notes of clarification actually did not clarify something that was really confusing," says Eva Bågenholm, who chairs the WMA committee on ethics and is president of the Swedish Medical Association in Stockholm.

The new language on the use of placebos in clinical trials is likely to attract the most attention. For decades, the gold standard in new-drug development has been a randomly assigned trial that compares the effects of a new intervention with those of a placebo. But many worry that such trials in effect deny care to those who draw the placebo, often at great cost to their health.

The Helsinki Declaration's original 46-word paragraph on the use of placebos said that new interventions should be tested against the best, proven existing interventions; placebos could be used when no proven interventions existed. A 136-word note of clarification, adopted in 2002, said "a placebo-controlled trial may be ethically acceptable, even if proven therapy is available" when compelling scientific and methodological reasons made its use necessary to determine the efficacy or safety of a new intervention. The new amendment leaves little room for maneuver. It states that "a new intervention must be tested against ... the best current proven intervention." A placebo is acceptable "where no current proven intervention exists" or where its use is necessary to determine an intervention's efficacy or safety, and patients who receive placebos will not be subject to any risk of harm. The relevant paragraph concludes, "Extreme care must be taken to avoid abuse of [the placebo] option." Even so, Bågenholm recognizes that this language did not resolve all the underlying controversies. "There are still some people who are not happy with the paragraph [on using placebos]," she says.

Middle ground. Swedish physician Eva Bågenholm helped draft a compromise on the use of placebos.

PHOTO COURTESY OF EVA NILSSON BÅGENHOLM

On post-trial care, the ideal would be to assure participants of some level of continuing medical support, says Jeff Blackmer, executive director for ethics at the Canadian Medical Association (CMA) in Ontario. The new paragraph reads: "At the conclusion of the study, patients entered into the study are entitled to be informed about the outcome of the study and to share any benefits that result from it, for example, access to interventions identified as beneficial in the study or to other appropriate care or benefits." But Blackmer says the financial burden of providing such care could hinder the development of drugs for neglected diseases affecting the world's poor. "The CMA is supportive of the new wording of the paragraph," although it's "probably not perfect," he says.

The new proposal calling for registration of clinical trials before recruitment of the first patient is not likely to be followed by industry. In comments submitted to WMA before the Seoul meeting, the Biotechnology Industry Organization (BIO) in Washington, D.C., said it supports the goals of transparency and access to clinical trial information. But it worries that registration of all trials might jeopardize intellectual property rights and frustrate R&D efforts while providing little guidance to prescribers and patients. BIO suggested that the declaration exclude phase I trials, typically the first in-human tests, from registration.

The Pharmaceutical Research and Manufacturers of America, also in Washington, D.C., suggested dropping the requirement to register prior to the recruitment of the first patient because it "creates a major burden for trial sponsors and could significantly delay trials." Bågenholm says that although aware of industry concerns, "we think any trial that involves people should be registered to protect them" and to avoid having them go through repeated testing of the same intervention.

Coincidentally, the amendments were adopted just a week before an FDA decision takes effect that will let applicants for new drug approvals bypass the Declaration of Helsinki when conducting certain trials overseas. Instead, FDA will ask applicants to comply with the International Conference on Harmonization's Good Clinical Practice (GCP), which some view as having far less rigorous ethical standards. "The decision would seem to encourage pharmaceutical companies to cut ethical corners when working abroad," says Stuart Rennie, a bioethicist at the University of North Carolina, Chapel Hill. He says GCP is more open to the use of placebos and does not mention conflicts of interest, the need to publish results, or post-trial access to care.

Any suggestion that FDA is relaxing its policy on human subjects' protection is "absolutely not true," says FDA Associate Commissioner Rachel Behrman. She says FDA regulations have dropped references to the Declaration of Helsinki because some of WMA's policies—such as the bias against placebos—are "not consistent with U.S. law," not subject to a U.S. veto, and could create a "confusing" situation.

Edward Hill, chair of WMA and former president of the American Medical Association, notes that WMA has established a new working group to continue to study the placebo issue. **–DENNIS NORMILE**

With reporting by Eliot Marshall.

'Spore' Documentary Spawns Protest By Scientists Who Starred in It

CAMBRIDGE, MASSACHUSETTS—The National Geographic Channel is often praised for its meticulous science documentaries, but a show that aired last month focusing on the blockbuster video game Spore is coming in for harsh criticism. Surprisingly, the toughest critics are some of the scientists who appear in the film itself. They say that they were not informed before taking part that it would focus on a commercial product. "I literally never heard about Spore until I saw myself on television in this infomercial about the game," says Cliff Tabin, a geneticist at Harvard University. "It's an outrage."

The documentary, titled *How to Build a Better Being*, which aired on 9 September, puts Spore and its creator, Will Wright, front and center. Over the course of the 1-hour show, Wright visits several U.S.-based academic scientists to discuss their research. Between these scientific interludes, the documentary returns to Wright and Spore. "Journey into the billion-year history of the human body, led by computer game visionary Will Wright as he explores the breakthrough science that's revealing the secret genetic machinery that shapes all life in the game Spore," reads a description of the film on the National Geographic Channel's Web site.

CREDIT: ELECTRONIC ARTS

Designer creature. Biologists complain that they appear to be endorsing the video game Spore in a National Geographic film.

Tabin, along with Neil Shubin, a paleontologist at the University of Chicago in Illinois, and Michael Levine, a geneticist at the University of California, Berkeley, sent *Science* identical e-mails from the film's producers inviting them to take part. The e-mail describes the documentary as an investigation of "recent discoveries in evolutionary science" with no mention of Spore or Wright. "I thought I was being interviewed for a documentary about evolutionary biology," says Shubin, who appears to be playing the game in the film. "They didn't mention Spore until we were in the middle of [the interview]. ... I sat there with Will Wright as he fiddled with it," he says. "I don't endorse video games, particularly one that claims to be about evolution."

Ellen Stanley, National Geographic's communications vice president, says there was no intent to mislead the participants. "Our producers were transparent with all of the scientists," she says. The production of such a documentary takes "several months" she adds, and "the idea for the film evolves during that process."

Spore is described in the film as "one of the most ambitious games ever, simulating the process of evolution," and a DVD of the film is included in the $80 "Galactic Edition" of the game. "There's no question that the impression one gets from watching [the film] is that Spore is scientifically based and that scientists endorse this as not only a valid representation of how life on earth arose but moreover a really cool way that kids can learn about it," says Tabin. But "the science is told in the most superficial way and not really explained or clarified," he says. "And then it becomes more about this computer game designer than it is about the science." (A panel of scientists asked to review the game's scientific content for an online *Science* feature, www.gonzoscientist.org, gave its treatment of evolutionary biology low marks.)

Stanley declined to comment about the relationship between National Geographic and Spore's manufacturer, Electronic Arts. "We had a great time partnering with the folks over at National Geographic," wrote a spokesperson for Electronic Arts in an e-mail to *Science*. "However, we don't typically discuss business terms of our partnerships."

–JOHN BOHANNON

SCIENCESCOPE

Google Grants Fight Disease

Google.org, the philanthropic arm of the Internet search giant, has given more than $14 million to six programs aimed at identifying new infectious disease threats that could become worldwide disasters.

Among the winners are ProMED, a respected and well-utilized but perennially cash-strapped e-mail list that compiles reports about emerging diseases, and HealthMap, a Web site that takes outbreak reports from ProMED and other sources and logs them on world maps. The projects will use their combined $3 million share to expand their coverage of neglected countries. HealthMap, which relies on Google News, Google Maps, and Google Trends, will also receive support from Google technicians—"something that doesn't come with most grants," says its co-founder John Brownstein.

The rest of the funding, awarded for 3 to 4 years, will support efforts to monitor deforestation by satellite, use climate and weather data to predict epidemic hot spots, and improve the identification of pathogens in the lab. The Global Viral Forecasting Initiative plans to use $5.5 million from Google and another grant of the same size from the Skoll Foundation to hunt for new viruses in humans and animals in Africa and Asia.

–MARTIN ENSERINK

Cold Cash for Science

PARIS—The French government will spend more than €250 million over the next 3 years to make careers in science and higher education more appealing and reward its academic stars. The measures, including increased financial bonuses, are part of a "radical offensive" to make France's research system "among the most attractive in the world," science and higher education minister Valérie Pécresse said at a press conference this week.

Among the plans: A new contract with a minimal starting salary for Ph.D. students; a 12% to 25% pay hike for assistant professors; and bonuses of up to €15,000 for excellence in research or teaching and up to €25,000 bonuses for those who win scientific prizes. The plan is in line with recommendations from the French Academy of Sciences, which is "happy" with the plan, says academy president Jules Hoffman. But Sauvons la Recherche (SLR), a researchers' movement, opposes the bonuses. Eligibility criteria are vague and there's the risk of arbitrary decisions, says SLR president Bertrand Monthubert. –MARTIN ENSERINK

In Brief: Where They Stand on Science Policy

At the risk of oversimplifying these complex topics, the news staff of *Science* has boiled down what Senators John McCain and Barack Obama have said during the long campaign about some three dozen important issues.

Online

sciencemag.org

S[illegible] at the essential [illegible] www.sciencemag.org/cgi/content/full/sci;321/5891/1618

Education

[illegible]
●McCain [illegible] ●Obama [illegible] Bush [illegible]

[illegible]
●McCain Teacher bonuses, online courses
●Obama Revise and retest teachers; improve assessment
Bush Math Now, Al[illegible]

[illegible]
●McCain Students "taught all points of view" but probably not in science class
●Obama No
Bush Yes

National Security

[illegible]
●McCain No ●Obama Yes Bush No

[illegible]
●McCain Research on particles and detection
●Obama More agile, drug development and production
Bush Implemented Bioshield program

Health

[illegible]
●McCain Open, limited participation and screening
●Obama Open research and screening
Bush No specific plan

[illegible]
●McCain Yes
●Obama No; only comprehensive education
Bush Yes

[illegible]
●McCain Yes ●Obama Yes
Bush Never vetoed

[illegible]
●McCain Yes ●Obama Yes Bush Yes

Environment

[illegible]
●McCain Needs to be more cost-effective and efficient
●Obama No
Bush Backed incremental [illegible] attempt

[illegible]
●McCain Yes, some [illegible] that led to delays
●Obama No
Bush Has cited to limit review of major projects

[illegible]
●McCain Not necessarily; base standards on sound economics and science
●Obama Yes; let scientists, not politicians, set standards
Bush Not necessarily

[illegible]
●McCain Opposes "one-size-fits-all" approach
●Obama Yes
Bush Has cited uncertainty to urge the bill

Innovation

[illegible]
- McCain Yes–tied to wages
- Obama Yes
- Bush Yes

[illegible]
- McCain No–medical battery prize
- Obama $150 billion/yr clean-tech sections; capital fund; Build American Competitiveness Initiative
- Bush [illegible]

[illegible]
- McCain No
- Obama Yes
- Bush No

Government Reform

[illegible]
- McCain [illegible]
- Obama Appoint chief technology officer
- Bush Improve efficiency

[illegible]
- McCain Yes
- Obama No
- Bush No

[illegible]
- McCain Yes
- Obama Yes
- Bush Delete crossed

Basic Research

[illegible]
- McCain Yes
- Obama Yes
- Bush Yes

[illegible]
- McCain No limit number
- Obama Double over 10 years
- Bush Yes

[illegible]
- McCain Opposes [illegible]
- Obama Yes
- Bush No

[illegible]
- McCain No
- Obama Yes
- Bush No

Immigration

[illegible]
- McCain Yes
- Obama Yes
- Bush No

[illegible]
- McCain Adjustments tied to market conditions
- Obama Supports temporary boost
- Bush No

Energy

[illegible]
- McCain Spend $ billion a year
- Obama Taps $50 billion; green technologies chief
- Bush $189 million for demonstration projects

[illegible]
- McCain Yes
- Obama No
- Bush Yes

[illegible]
- McCain [illegible]
- Obama Yes
- Bush [illegible]

[illegible]
- McCain 60% of 1990 levels by 2050
- Obama 80% of 1990 levels by 2050
- Bush No mandatory targets

[illegible]
- McCain Expand nuclear power; tight timetable
- Obama Companies pay through auction
- Bush Opposes mandatory cap and trade

Space

[illegible]
- McCain Yes
- Obama Yes
- Bush No

[illegible]
- McCain Yes
- Obama Yes
- Bush Yes

[illegible]
- McCain No position
- Obama Yes
- Bush No plans

[illegible]
- McCain No position
- Obama Yes
- Bush No

[illegible]
- McCain No position
- Obama Yes
- Bush No plans

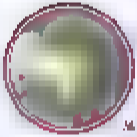

The Act of Regulating CO_2

[illegible]

Cold Cash for the Poles

[illegible]

[illegible]

Pick a Planet

[illegible]

Small Comfort

[illegible]

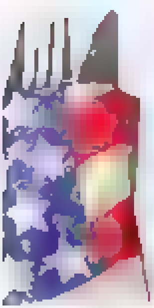

A Full Serving of Science Awaits the Next President

Many scientific issues are never discussed during the campaign. But ignoring them doesn't make them disappear. Here are 10 meaty topics that we think the 44th president will have to chew on

Being a Team Player

Combating Bioterrorism

Taking (Nuclear) Stock

the high fees charged by new corporate management. The best pro

Providing Some Assistants

to three recent reports by scientific

be enough to give science a real seat at the table of power? Sally Turner

More Intelligent Medicine

Fishing for Answers

authority to reject catch limits that

which candidates say they support sustainable fisheries, neither has

spoken out too he would make it happen.

BIOFUELS

Eyeing Oil, Synthetic Biologists Mine Microbes for Black Gold

Biotechnology researchers want to reengineer microorganisms to turn agricultural products into gasoline, diesel, and jet fuel

EMERYVILLE, CALIFORNIA—What do you do after creating a cheap antimalarial drug that could save millions of lives in the developing world? If you're Jay Keasling, you tackle two equally pressing problems: climate change and the need for abundant renewable fuels.

Keasling, a synthetic biologist at the University of California, Berkeley, made a splash a few years ago when he and his colleagues reengineered two microbes *Escherichia coli* and baker's yeast—to churn out a costly plant-derived antimalarial compound called artemisinin. Now, Keasling and dozens of colleagues working at the Joint BioEnergy Institute (JBEI) that he directs are trying to create classes of compounds, such as alkanes, that are key components of gasoline and other transportation fuels. "Artemisinin is a hydrocarbon," Keasling says. "We're just trying to engineer organisms to produce different hydrocarbons."

Keasling hopes to leapfrog over a bitter debate among agricultural economists about the value of ethanol, the first-generation biofuel. Keasling and a handful of others are starting from scratch, using synthetic biology to lend *E. coli*, yeast, and other easily grown microorganisms the ability to create mixtures of compounds that can be used to make various things, including gasoline, jet fuel, plastics, and cosmetics. "This is just at the beginning," says Keasling, sitting in his fourth-floor office with a view of the Berkeley campus and the Oakland hills. The combination of rapidly improving bioengineering technology and the massive pull for cheap, low-net carbon fuels has generated enormous excitement, he asserts. "This is just a golden period for this area."

The question is whether it will be black gold. A handful of start-up companies have leapt into the field, some even teaming up with major energy companies such as Chevron and BP. Some of these companies have already begun producing fuels, but none say they can beat the price of conventional petroleum, despite its recent spike to more than $140 a barrel. But with technology improving rapidly, "very likely it can be done," says Vinod Khosla, a venture capitalist with Khosla Ventures in Menlo Park, California, who has backed several next-generation biofuel start-ups.

Black gold. Algae (*below*) produce oils that are converted into biodiesel.

For now, most of the new biofuel producers have set their sights on displacing ethanol rather than gasoline and diesel. According to the Renewable Fuels Association, last year the world produced more than 50 billion liters of ethanol fuel. Most of it is made by fermenting food crops—corn kernels in the United States and sugar cane in Brazil.

Critics argue that this method is driving up food costs. The production of corn-based ethanol, they say, requires nearly as much energy from fossil fuels to drive the tractors, produce fertilizer, and run the ethanol plants as what comes out in the alcohol at the end. The end result, they argue, is at best a marginal reduction of carbon dioxide (CO_2). In addition, ethanol can't be shipped through existing oil pipelines because it mixes easily with water, which accumulates in the pipelines.

With so many strikes against ethanol, most synthetic biology groups are working to engineer microbes to produce fuels essentially identical to existing fossil fuels. They want bugs that can grow on the sugars from agricultural waste and other "cellulosic" materials, thereby reducing the need to use scarce agricultural land to grow fuels.

The early results are heartening. Keasling and his colleagues, for example, are having early success at reengineering *E. coli* to produce gasoline-type molecules. The work builds on Keasling's earlier triumph with artemisinin. In that case, Keasling's team focused its efforts on metabolic pathways in *E. coli* and yeast that normally produce small amounts of compounds called isoprenoids, precursors for building many pharmaceuticals such as artemisinin, among other chemicals.

Keasling's team made about 50 genetic changes—adding genes for additional enzymes, promoters, and so on—to the organisms to get them to convert these intermediate compounds to artemisinin. Keasling founded Amyris Biotechnologies, which shares space in the JBEI facility, to commercialize the work. Initially, the bugs produced only tiny amounts of artemisinin. But by outfitting *E. coli* and yeast with several new genes and turning off the expression of others, Keasling and his colleagues at Berkeley and

CREDITS (TOP TO BOTTOM): HANAUER 2008, SOLAZYME

Amyris boosted a millionfold the production of the antimalarial

That's good enough to match the average price of artemisinin, about $1 per gram. But Keasling notes that they will have to do even better to make microbial fuel cost-effective, because the production of fuel molecules at $1 per gram translates into a price of about $125 a liter for gasoline. "It has to be cheaper than water," Keasling says. To do that, the team needs to engineer the microbes to increase the flux of the starting material —sugar in this case—through the microbes' fuel-producing pathway.

At a meeting last month in Hong Kong,* Keasling reported on a novel strategy to increase the chances that the product of one reaction inside this pathway is properly handed off to the next enzyme in the chain. The team engineered *E. coli* to express a protein scaffold for a trio of enzymes that work in their isoprenoid pathway and bind them in a way that more efficiently transforms starting compounds to the final result. "This increased the flux through the pathway 77-fold," Keasling says. At Amyris, Senior Vice-President of Research Jack Newman says the company is also making significant headway on producing renewable diesel and jet fuel. Amyris has teamed up with Crystalev, one of Brazil's largest ethanol producers, to scale up the company's proprietary technology to make renewable fuels from sugar cane, beginning in 2010

Across San Francisco Bay in South San Francisco, researchers at LS9 are reengineering *E. coli* and other organisms to make what they refer to as renewable petroleum. Rather than co-opting the microbe's isoprenoid pathway, LS9 researchers are focusing on the pathway that converts sugars to fatty acids, which can then be converted to biodiesel

Gregory Pal, LS9's senior director for corporate development, notes that fatty-acid biosynthesis is the main route by which organisms convert excess energy into fats. Most organisms have evolved to do this quickly and with high efficiency, as anyone who has tried dieting knows all too well "We've made on the order of dozens of [genetic] transformations" to maximize that efficiency, Pal says. The company, he adds, has successfully produced a variety of hydrocarbons and is now focused on scaling up the technology. LS9 already has a pilot-scale fermentation facility up and running at its headquarters

*Synthetic Biology 4.0, Hong Kong University of Science and Technology, 10–12 October

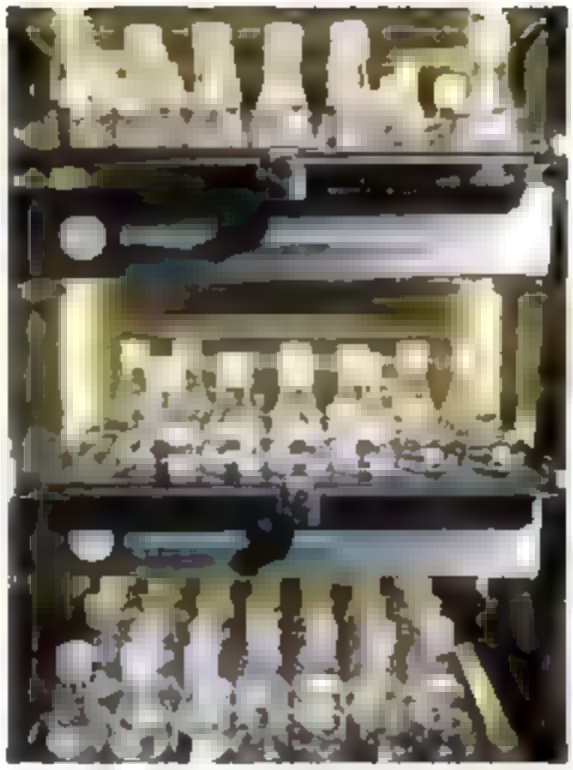

CREDIT: AMYRIS BIOTECHNOLOGIES

Variety show. Researchers are trying a host of approaches to microbial hydrocarbon fuels.

and plans to open a small-scale production facility by mid-2010.

James Liao and colleagues at the University of California, Los Angeles, are trying a third approach. In the 3 January issue of *Nature*, Liao and his co-authors described how they engineered *E. coli* to produce isobutanol, a longer chain alcohol than ethanol. That increased chain length gives isobutanol a more energetic punch per liter and enables it to be separated from water more easily, Liao says. The molecule can also easily be converted to fuels that can be blended with gasoline as well as transformed into other commodity chemicals.

Like other groups in the field, Liao has his own favored biosynthetic pathway. He and his colleagues have co-opted the metabolic pathway that bugs use to convert common starting materials, called alpha-keto acids, to amino acids. Liao focused on this pathway because it is already adapted to handle large fluxes of hydrocarbons. "Fifty-five percent of the cell's composition is protein, so it needs a lot of amino acids," Liao says of the *E. coli* microbe his team is working with. Liao has teamed up with Gevo, a bioenergy start-up in Pasadena, California, that he says is building a pilot production plant. Liao also notes that his group is making progress on getting photosynthetic bacteria to make isobutanol. The goal is for bacteria to manufacture fuel simply by absorbing sunlight and CO_2.

Getting photosynthetic organisms to produce fuel directly has long been the dream of researchers working with algae that can absorb sunlight and CO_2 to produce plant oils that, in turn, can be converted to biodiesel. But the technology has been plagued by real-world challenges such as the need to harvest algae from large, shallow ponds and separate out the oils.

Another biofuel start-up, Solazyme in South San Francisco, hopes to avoid those pitfalls. Solazyme researchers are working with natural and engineered algal strains to produce what they refer to as renewable biodiesel Instead of growing their algae outside in the sunlight, Solazyme researchers grow them inside dark stainless steel fermenters, in which the organisms convert sugars to oils. Turning off the algae's photosynthetic apparatus enables the organisms to produce oils more efficiently and makes it less costly to recover, says Harrison Dillon, Solazyme's president and chief technology officer.

The company can already produce biodiesel by the barrel and has had separate versions certified as jet fuel and biodiesel. Solazyme has managed to move quickly, Dillon says, because many of the algal strains start out as efficient oil producers. "They are naturally a long way towards where you want them to be," he says.

Are any of the next-generation biofuels likely to succeed? Khosla and others say the technology has several distinct advantages. First, synthetic biology allows researchers to test hundreds of potential improvements in a short time. "That means we can not only iterate quickly but not stop iterating," Dillon says. And Khosla adds that unlike renewable-energy technologies such as wind and hydropower, the economics of the technology improve as it is scaled up, allowing companies to take advantage of large-scale production efficiencies.

Finally, it's doubtful any biofuel start-up will be beat out by other upstarts. "The demand for fuels is so huge, there will be multiple winners out there," Dillon says "If you make it at the right price, you can sell as much as you can produce."

Still, for the near term, microbial biofuels will remain dependent on food-based agriculture to generate the sugars needed to feed the bugs. And even if cellulosic wastes can be economically converted to sugars, some wastes will likely need to be left on agricultural and forest land to return needed nutrients to the soil. Despite those drawbacks, Khosla says, next-generation biofuels won't remain a research project for long. "They're a lot closer to market than the time it takes to build a new oil refinery," he says.

–ROBERT F. SERVICE

Niche players. ASCC's David Haylock, postdoc Jochen Grassinger, and Suzie Nilsson are developing an artificial niche to get stem cells to behave better in culture.

AUSTRALIA

Last-Ditch Effort to Save Center at Vanguard of Stem Cell Research

After ousting its CEO and board, the Australian Stem Cell Centre hopes to regroup around a plan that rebalances research and commercial goals

MELBOURNE, AUSTRALIA—The moment of truth has arrived for a faltering attempt to kick-start Australia's stalled biotech industry. In July, the board of the Australian Stem Cell Centre here sacked CEO Stephen Livesey over disagreements about how quickly ASCC should seek to spin off products. A month later, the board itself stepped down. "From 1000 feet, it looks like a disaster," says ASCC founder Alan Trounson, who left in 2003. After a traumatic several weeks, a concerted effort is under way to steer ASCC back on course. An interim board is drafting a new strategic plan that was expected to be presented to the 10 ASCC consortium members and the government after *Science* went to press.

ASCC's future depends on whether the government's Department of Innovation, Industry, Science and Research, which has bankrolled the center's initial 9 years, will accept the new plan. "There's excellent research going on, but the business model just wasn't going to work," in part, because of its emphasis on rapid commercialization, argues endocrinologist and former CEO of the Australian Research Council Vicki Sara, who chaired the ASCC board that resigned en masse.

ASCC follows a hub-and-spoke model, in which a central administration based at a biotech park on the grounds of Monash University (MU) reviews and funds projects proposed by consortium members. "The center is all about building collaborations and big thematic programs that would not be possible otherwise," says director of ASCC research services and hematologist David Haylock.

According to its charter, ASCC must also commercialize its research. But from the get-go, the center's leadership has been arguing over how that should happen. The previous board asserted that ASCC should capitalize on its research through patents and licensing agreements. Livesey was keen on pushing a product through the pipeline and spinning off a company to attract outside investment. "I've always been a risk taker," Livesey says. "But clearly that degree of risk-taking wasn't for everyone."

ASCC came into being in 2002, at the height of a fervor to raise the game of Australian scientists. Two years earlier, a major review attributed the paltry payoff from biotechnology to a lack of critical mass and a poor culture of commercialization (*Science*, 13 October 2000, p. 255). To remedy the situation for biomedical researchers, the federal government invited bids for a $24 million grant to create a biotechnology center of excellence. A consortium led by Trounson, then of MU, won the competition. Australia had a leading reputation in the field largely because Trounson's group had come in a close second to James Thomson's team at the University of Wisconsin, Madison, in the race to isolate human embryonic stem cells. Given constraints on federally funded U.S. researchers, Australia had a strong chance to stake claims in a potentially rich new biomedical field.

ASCC's consortium—at the time, seven Australian universities and medical research institutes—appointed Trounson as CEO. He then recruited Livesey as chief scientific officer. An Australian who had founded the U.S. biotech company LifeCell, Livesey seemed a natural choice. He had nurtured a successful biotech venture whose lead product—AlloDerm, artificial tissue for burns and reconstructive surgery—is derived from human tissue.

But soon, Trounson and Livesey weren't seeing eye to eye.

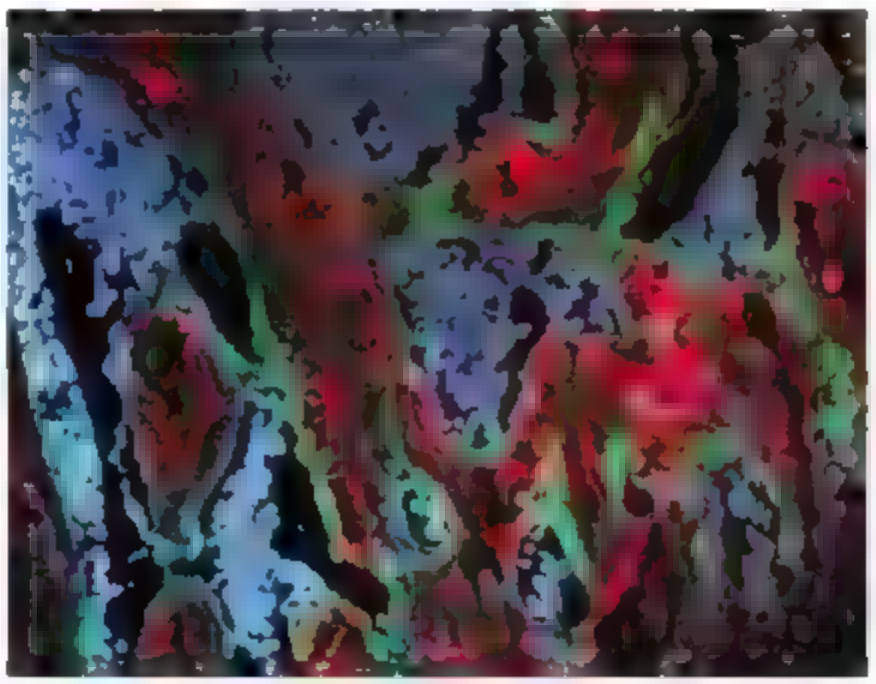

Real McCoy. This bone marrow niche regulates development of blood-forming stem cells; red stain is for osteopontin, green is for tenascin C.

CREDITS (TOP TO BOTTOM): E. PINEL/SCIENCE; SUSIE NILSSON/AUSTRALIAN STEM CELL CENTRE

A major schism opened over the center's direction, Trounson says. Livesey wanted ASCC to develop a product, and revenue stream, within 9 years. Trounson saw ASCC as fundamentally research-driven. "Stem cell science needs a really long period of research," he says. "I couldn't see how you could commercialize in that time frame."

ASCC's board, then chaired by biomedical entrepreneur Bob Moses, sided with Livesey. Trounson left to found the Monash Immunology and Stem Cell Laboratories, in 2007, he became president of the California Institute for Regenerative Medicine in San Francisco. Hugh Niall, former CEO of Biota, one of Australia's few successful biotech companies and until then a founding director of ASCC, took over as CEO.

ASCC placed its commercial bet on developing blood cell products and spinning off a start-up by 2011. First would be a novel "off the shelf" treatment for cancer patients: neutrophils derived from stem cells in cord blood or donated blood, based on research by an ASCC-funded lab led by Lars Nielsen at the University of Queensland. Other projects in the pipeline were drug candidates to replace hormones now used to stimulate blood cell regeneration in cancer patients, a stem cell bioreactor, and blood products from embryonic stem cells. Nevertheless, 90% of ASCC's R&D budget has been invested in basic research, on projects such as how to coax stem cells to form blood, lung, and kidney tissues.

In 2006, an independent review by an outside company in Spit Junction, Australia, called Growing Your Knowledge gave the center high marks and helped ASCC secure an additional $41 million in government funds. But it also warned that management, board, and consortium members lacked a common vision for ASCC's future. Later that year, Niall stepped down as CEO to rejoin ASCC's board, and Livesey took the reins. By early 2007, says Livesey, "I ran into problems. ... People weren't pulling in the same direction; there was significant dysfunction in the center."

Sara says the board was uncomfortable with Livesey's focus on commercialization, even though those efforts consumed just 10% of the R&D budget. The board instructed ASCC to modify its deed of agreement with the government, which had stipulated that the center's mission is to provide therapeutic and commercial benefits from stem cell products. The amended deed, says Livesey, stated that the center simply "should pursue excellence in stem cell research."

To bring matters to a head, Livesey wrote an aggressive 5-year business plan that would have expanded the budget devoted to commercial ventures. "I knew termination was one of the significant possibilities, but the success of the center was extremely important," he says. The board ordered Livesey to rewrite the plan with a narrower commercial focus. He did. But the innovation department rejected the revised plan, because, Livesey contends, "it did not have a fully defined commercialization strategy." Officials at the innovation department declined to comment.

"Clearly that degree of risk-taking wasn't for everyone."

—STEPHEN LIVESEY, FORMER ASCC CEO

Last July, the board asked Livesey to resign. "It was the opinion of the board that we need to build national capacity, not focus on short-term products. We needed new leadership for that," says Sara. But ASCC's consortium members had had enough of being relegated to the sidelines of ASCC's business affairs. They wanted to assume greater control of the situation, sources say. The board was purged, and an interim board was established with representatives from three consortium members—MU, the University of Queensland, and Melbourne's Howard Florey Institute—led by an independent chair, Graham Macdonald, former medical director of Merck Sharp & Dohme in Australia. With input from the consortium, Macdonald is now crafting a new plan for the remainder of the center's initial 9-year funding, which expires in June 2011, and beyond. "The board's job is to develop a model with buy-in from all the stakeholders and to present the government with plan B," Macdonald says. That could steer ASCC in one of two directions, he says: either keep the hub-and-spoke form—which earlier this year was pared down to Melbourne and Queensland, with a small contribution from New South Wales—or transform the center into a funding organization. A final plan was expected to be hammered out at a workshop on 24 October.

"I couldn't see how you could commercialize in that time frame."

—ALAN TROUNSON, ASCC FOUNDER

Most observers say that staking ASCC's success on a product was unrealistic and unnecessary. "We think there will be other ways of sustaining the center beyond 2011," such as entering into partnerships with biotech companies, providing stem cell–cultivation services, and intellectual property consulting, says acting CEO David Collins.

ASCC scientists are hoping that the management upheavals are over—and that they can get on with their work. One hot project is the development of an artificial niche to sustain stem cells by Haylock and Susie Nilsson at the center's headquarters here. Researchers have had little success at coaxing adult stem cells to remain stem cells once isolated in culture, a major limitation to producing big batches of cells. In their original source tissue, however, stem cells are renewed. Part of the explanation, researchers have long realized, is that stem cells are cocooned in a niche, where they are regulated by proteins embedded in a matrix or secreted by cells. Artificial niches should transform the culturing of adult and embryonic stem cells from a black art to a robust, scaleable technique, says Nilsson.

Haylock and Nilsson are trying to build an artificial stem cell niche using a polymer scaffolding affixed with key signaling molecules such as osteopontin and hyaluronic acid. "The center has put us in contact with surface engineers, surface chemists, polymer chemists," Nilsson says. Haylock credits Livesey for bridging biologists and engineers. "He was the sole person who understood the interactions with the engineering disciples. He should be applauded for his vision," says Haylock.

"The real issues the center faces are not about its past but about its future," says Collins. ASCC's fate should soon be clear. In the meantime, says Haylock, "We just shut the door on the politics and focus on the science. That's where the buzz is."

–ELIZABETH FINKEL

Elizabeth Finkel is a writer in Melbourne, Australia.

CREDITS (TOP TO BOTTOM): ASCC, CALIFORNIA INSTITUTE FOR REGENERATIVE MEDICINE

LETTERS

edited by Jennifer Sills

Sleepless in the Sea

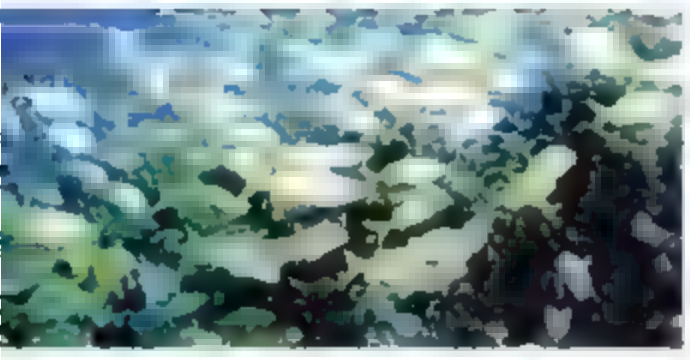

IN THEIR RESEARCH ARTICLE "IDENTIFICATION of SLEEPLESS, a sleep-promoting factor" (18 July, p. 372), K. Koh *et al.* note that "[s]leep is an essential process conserved from flies to humans." This is not quite true. Many piscine species are active continuously without sleep (*1*), including species of marine and freshwater fishes in which schooling—swimming synchronously in polarized groups (*2*)—is fully developed (*3*).

Nonsleeping fishes achieve sleep's major benefits but completely bypass a need for sleep. By schooling, they greatly reduce the average school member's reception and processing of sensory input, so that it does not interfere with ongoing memory processing. Sleep, like schooling, seems to accommodate nonurgent memory processing, leaving the activity period free for critical waking functions and enabling the brain to operate efficiently at all times (*4*).

J. LEE KAVANAU

Emeritus Professor, Department of Ecology and Evolutionary Biology, University of California, Los Angeles, CA 90095–1606, USA. E-mail: mg_kavanau@yahoo.com

References

1. J. L. Kavanau, *Brain Res. Bull.* **46**, 269 (1998).
2. D. H. Cushing, F. R. H. Jones, *Nature* **218**, 918 (1970).
3. E. Shaw, in *Development of Behavior*, L. R. Aronson, E. Tobach, D. S. Lehrman, J. S. Rosenblatt, Eds. (W. H. Freeman, San Francisco, 1970), pp. 452–480.
4. J. L. Kavanau, *Sleep Med. Rev.* **9**, 141 (2005).

A Bird's Eye View of Sleep

IN THE NEWS FOCUS STORY "SIMPLE SLEEPers" (18 July, p. 334), E. Youngsteadt highlights recent advances, derived from genetic research in fruit flies and other "simple" animal models, in our understanding of sleep. The power of this genetic approach is undeniable, but the simplicity that renders such model animals amenable to genetic manipulation necessarily limits their ability to model all aspects of sleep in mammals. Most notably, simple animal models lack the changes in brain activity that define mammalian slow-wave sleep (SWS) and rapid eye movement (REM) sleep (*1*). Until we determine the functional relevance of the changes in brain activity that define these characteristics of mammalian sleep, our understanding of human sleep may be incomplete.

We contend that birds, as the only non-mammalian taxonomic group to exhibit SWS and REM sleep, provide a largely untapped opportunity to determine the functions of these states in mammals. Reptiles and amphibians lack comparable sleep states, indicating that SWS and REM sleep evolved independently in the respective ancestors of mammals and birds (*2*). Consequently, traits shared only by mammals and birds may be the functional targets of these states. Interestingly, mammals and birds also independently evolved complex brains capable of orchestrating complex cognition, unlike that observed in reptiles and amphibians (*3*). Given that complex brains, complex cognition, and SWS and REM sleep evolved in concert, these shared traits may be functionally interrelated (*2*, *4*). Indeed, the recent discovery of mammalian-like SWS homeostasis in birds suggests that functional hypotheses that posit a role for SWS homeostasis in maintaining adaptive brain function in mammals may also apply to birds (*4*).

We believe that comparative studies of sleep in mammals and birds offer the promise of revealing overriding principles directly tied to the function(s) of SWS and REM sleep that might remain obscure through an exclusively mammal-based or simple animal model approach.

NIELS C. RATTENBORG,*
DOLORES MARTINEZ-GONZALEZ,
JOHN A. LESKU, MADELEINE SCRIBA

Sleep and Flight Group, Max Planck Institute for Ornithology, Eberhard-Gwinner Strasse, 82319 Seewiesen, Germany.

*To whom correspondence should be addressed. E-mail: rattenborg@orn.mpg.de

References

1. D. A. Nitz *et al.*, *Curr. Biol.* **12**, 1934 (2002).
2. N. C. Rattenborg, *Brain Res. Bull.* **69**, 20 (2006).
3. E. D. Jarvis et al., *Nat. Rev. Neurosci.* **6**, 151 (2005).
4. D. Martinez-Gonzalez *et al.*, *J. Sleep Res.* **17**, 140 (2008).

NSO's Environmental and Cultural Efforts

IN THE NEWS FOCUS STORY BY Y. BHATTACHARJEE "From atop a mountain, a deeper look at the Sun" (25 July, p. 478), the quote attributed to me next to my picture was used outside of the context of our discussion, leaving an unfavorable and highly inaccurate impression. Bhattacharjee and I were discussing the upcoming schedule for the construction of the Advanced Technology Solar Telescope (ATST) and the potential impact (on schedule) in the event of an impasse during mitigation negotiations. We do not expect this. It has been and remains the project's intention to support the National Science Foundation (NSF) in its plan to mitigate impacts that the ATST may have.

The impression that the National Solar Observatory (NSO), the ATST project office, or

CREDIT: JUPITER IMAGES

the NSF might be doing a perfunctory or pro forma process with regard to either cultural or environmental impact could not be further from the truth. The facts bear this out. We have conducted a very thorough environmental impact statement process and will implement the identified processes required to minimize or mitigate the impacts of the project on both environmental and cultural grounds. We have strongly supported NSF in the National Historic Preservation Act process and will support any agreements they establish. The NSO and the ATST project have been and will continue to be respectful of the Hawaiian culture and its traditions. It is my sincere belief that the proposed ATST, as the premier instrument in the world for observing phenomena on the Sun, fits well with the role that Haleakala ("House of the Sun") plays in Hawaiian culture.

STEPHEN L. KEIL

National Solar Observatory, Sunspot, NM 88349, USA. E-mail: skeil@nso.edu

A Gradual Peer-Review Process

WITH MANY THOUSANDS OF SCIENTIFIC papers published every year, peer reviewing of manuscripts is a basic and critical component of science. Many scientists—particularly those who are well established and thus in demand—are less willing to review because of the time required to evaluate the many manuscripts they receive.

In standard reviewing practice, editors send manuscripts simultaneously to several reviewers, whose comments are considered by the editor and then sent back to the author. A basic drawback to this process is that for many manuscripts, all reviewers have to spend time on a text with many problems. Moreover, making trivial corrections may distract reviewers from more substantive critiques.

As guest editor and associate editor for *Plant Signalling and Behavior*, *Communicative and Integrative Biology*, and *Israel Journal of Plant Sciences*, I have decided to change the classic review process into a gradual one. I send submitted manuscripts to a single reviewer and then ask the author to make revisions before I send the paper to the other reviewers. Later reviewers can thus focus on important aspects of the study rather than deal redundantly with trivial problems in the text. This process seems to result in better final papers, and it saves time for all reviewers except for the first. Because reviewer order varies, a broad adoption of this process would save time for many scientists in the form of easier reading and shorter evaluation letters to the editors. This tactic could save precious reviewing time and increase the general willingness to review manuscripts.

SIMCHA LEV-YADUN

Department of Science Education, Biology, Faculty of Science and Science Education, University of Haifa, Oranim, Tivon 36006, Israel. E-mail: levyadun@research.haifa.ac.il

Optimizing Ecosystem Services in China

THE POOL BEHIND THE CONTROVERSIAL Three Gorges Dam (*1*, *2*) on the Changjiang (Yangtze) River in Hubei Province, China, will top off at 175 m above sea level next winter (2008 to 2009) ("Three Gorges Dam: Into the unknown," R. Stone, News Focus, 1 August, p. 628). With this flood level, former cities, homes, and farm fields of about 1.5 million people will be seasonally under water, and a set of new unique ecosystems will develop. The extent of the impact of this unprecedented amount of wetland underwater, the potential ecological systems that will result on the borders of this reservoir, and possible approaches to minimize the impacts or enhance ecological services are mostly unknown.

Flooding in the pool behind the Three Gorges Dam will extend up to 300 km upstream, almost to the city of Chongqing. The affected area with the most impact on human settlements is on the Pengxi River; it is in this region that a city of 300,000, Kaixian, has actually been relocated to higher grounds. The Pengxi River valley includes 5500 ha of land that will now be seasonally flooded, some for 6 months. Approximately 5% of this newly flooded land is former urban area.

Opportunities exist for optimizing ecosystem services through application of ecological engineering (*3*). Algal blooms, mainly with *Peridiniopsis sp.*, were widespread in the pools during flooding in 2008, so nutrient management will need consideration. Conventional agriculture can be practiced during periods of low water level on the riparian slopes, with one major exception—no fertilizers should be used, as they will exacerbate the pool eutrophication the next spring. Nor will fertilizers be needed. Sedimentation of nutrients, especially phosphorus, will be significant during flooding, and an agriculture more harmonious with the new conditions might flourish. Cascading terraced ponds and wetlands such as those at the Honghe River (*4*) are another approach for retaining the water as it recedes, while reducing nutrient loss to the river system. Mudflats will be abundant near or at the river in summer, providing ideal habitat for shorebirds and other wading birds. Commercial enterprises for food production can be designed to utilize the pulsing water. Fish-net systems could be used to capture fish as the flood pulse recedes.

We agree with Stone that there will be a new, though perhaps uneasy, equilibrium between the Three Gorges Dam and its reservoir area in the next several decades as nature adapts with new emerging ecosystems.

WILLIAM J. MITSCH,[1]* JIANJIAN LU,[2] XINGZHONG YUAN,[3] WENSHAN HE,[2] LI ZHANG[1]

[1]Wilma Schiermeier Olentangy River Wetland Research Park, The Ohio State University, Columbus, OH 43202, USA. [2]Chongxi Wetland Research Centre, East China Normal University, Shanghai 200062, China. [3]College of Resources and Environmental Science, Chongqing University, Chongqing 400044, China.

*To whom correspondence should be addressed. E-mail: mitsch.1@osu.edu

References

1. J. Wu *et al.*, *Science* **300**, 1239 (2003).
2. G. Z. Shen, Z. Q. Xie, *Science* **304**, 681 (2004).
3. W. J. Mitsch, S. E. Jørgensen, *Ecological Engineering and Ecosystem Restoration* (Wiley & Sons, New York, 2004).
4. J. Shi, *J. Yunnan Nationalities Un.* **21**, 77 (2004) (in Chinese).

Trans-Arctic Invasion in Modern Times

IN THE PERSPECTIVE "THE COMING ARCTIC invasion" (8 August, p. 780), G. J. Vermeij and P. D. Roopnarine discuss the possibility of trans-Arctic biological invasions caused by the recent episode of climate warming. We wish to add that this interoceanic exchange may have already begun (*1*).

In 1999, the Continuous Plankton Recorder survey, a pan-oceanic long-term marine monitoring program (*2*), documented the presence of a Pacific diatom (*Neodenticula seminae*) in the Labrador/Irminger seas, between Canada and Greenland. This planktonic diatom is abundant in the cool waters of the North Pacific and the Bering Sea. The species has since spread south to Georges Bank and east to the south of Iceland. According to records from the deep-sea drilling program, *N. seminae* last lived in the North Atlantic between 1.2 million and

800,000 years ago. Its recent return to the North Atlantic could therefore be the first evidence of a trans-Arctic migration and a possible harbinger of an inundation of the North Atlantic with foreign organisms, as happened during the Pliocene trans-Arctic interchange (*3*).

This interoceanic dispersal has been attributed to the Arctic's recent diminishing ice cover and changing wind pattern (*1*). The reappearance of *N. seminae* in the North Atlantic, and its subsequent establishment over a large area of the subpolar biome, could be an indicator of the scale and speed of changes that are taking place in the Arctic and North Atlantic oceans as a response to climate warming (*4*).

PHILIP C. REID,[1,2]* MARTIN EDWARDS,[1] DAVID G. JOHNS[1]

[1]Sir Alister Hardy Foundation for Ocean Science, Plymouth PL1 2PB, UK. [2]University of Plymouth Marine Institute, University of Plymouth, Drake Circus, Plymouth PL4 8AA, UK.

*To whom correspondence should be addressed. E-mail: pcre@sahfos.ac.uk

References

1. P. C. Reid *et al.*, *Glob. Change Biol.* **13**, 1910 (2007).
2. P. C. Reid, J. M. Colebrook, J. B. L. Matthews, J. Aiken, *Prog. Oceanogr.* **58**, 117 (2003).
3. G. J. Vermeij, *Paleobiology* **17**, 281 (1991).
4. J. E. Overland, M. Wang, S. Salo, *Tellus* **60A**, 589 (2008).

Contributions to the Large Area Telescope

IN THEIR LETTER "OMISSIONS IN GLAST STORY" (4 July, p. 37), G. F. Bignami *et al.* state that "The Large Area Telescope ... was essentially made and paid for by Italy, France, and Sweden" and that "Japan supplied most of the necessary silicon."

As the Principal Investigator for the Large Area Telescope (LAT), the primary instrument on the GLAST Observatory (now renamed the Fermi Gamma-ray Space Telescope), I know first-hand the importance of contributions to the LAT from universities, laboratories, and funding agencies in France, Italy, Japan, Sweden, and the United States. In fact, the concept for LAT came from the United States, and the United States was the major contributor to its design and construction. The initial design concept for the LAT originated with William Atwood in 1992 when he was at the Stanford Linear Accelerator Center (SLAC), and about two-thirds of the total cost was funded by NASA and the U.S. Department of Energy (*1*).

As Bignami *et al.* suggest, the effort to complete a detailed design and then construct the LAT became an international collaboration of particle physicists and astrophysicists. Every nation involved—including Italy, France, Sweden, and Japan—contributed in an important way to the success of the LAT. The spirit of collective responsibility was essential during the development phase and will serve well during the operations phase of the *Fermi* mission to ensure that the full science potential of *Fermi* is realized.

PETER F. MICHELSON

Department of Physics, Stanford University, Stanford, CA 94305, USA. E-mail: peterm@stanford.edu

Reference

1. NASA, Glast Science Writer's Guide, "Exploring the Extreme Universe" (www.nasa.gov/pdf/221503main_GLAST-041508.pdf).

CORRECTIONS AND CLARIFICATIONS

Perspectives: "A natural choice for activating hydrogen" by F. A. Armstrong and J. C. Fontecilla-Camps (25 July, p. 498). The DOI was incorrect. The correct DOI is 10.1126/science.1161326.

ECONOMICS

To Incubate Progress

Stine Grodal

> The American people always do the right thing after they've tried every other alternative.
>
> *attributed to Winston Churchill*

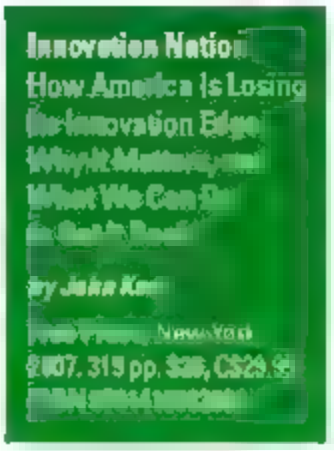

With this amusing quotation, John Kao opens *Innovation Nation*, an engaging account of the current state and possible futures of U.S. innovation policy. In it, Kao takes the reader on a fast-paced journey through both the past and prospects of innovation in America. Importantly, Kao (a consultant who formerly taught innovation and entrepreneurship at the Harvard Business School) reminds us of how government investments in education and the funding of ambitious research projects in the post–World War II era laid the foundation for our current prosperity. The results of these investments were towering accomplishments, such as Armstrong's giant leap for mankind and the ascent into the middle class for millions of Americans.

That said, Kao does not dwell on past accomplishments. Instead, he discusses two scenarios for the future. In the first, the United States mobilizes its resources in "pervasive and innovative" ways and thereby becomes an innovation nation. In the second, the country continues on its current path and abandons its innovative roots. According to Kao, this course means that future generations of Americans will face joblessness, poverty, and increasing societal instability. In other words, without an investment in innovation, the United States will become a second-tier nation in the global economy.

To ensure that the United States follows the first path, Kao offers concrete suggestions for how the country might build a national innovation toolbox. Kao does not specifically extend current wisdom among innovation scholars, but instead he provides an essential assemblage of facts that amounts to a wake-up call for the U.S. government to change course and start investing in the future as it did previously. In addition to calling for reform, Kao fills *Innovation Nation* with anecdotes from his life, friendships, and travels around the globe. These make the book enjoyable to peruse and serve to energize the reader to advocate for change.

Kao proposes that the United States focus on "wicked problems," i.e., issues so complex as to be nearly unsolvable. Only by aiming high will we further our knowledge and stretch our abilities to the utmost. To solve such problems, organizations need to collaborate across disciplines and nations, remove layers of management, and take advantage of untapped resources through open-source innovation. For Kao, the ability to foster and keep talent remains a central ability of an innovative nation. If we are to have a flexible and creative work force, capable students must receive stimulation and guidance from primary school through university. As Kao points out, too many American schools are currently underfunded, and too many students underachieve.

Not only does the United States need to cultivate its students, it should also work to attract and retain foreign talent. In the past, it was the top choice for accomplished and ambitious scientists, but today many foreign workers instead embrace opportunities in the fast-moving Asian economies. In order for the United States to secure the most talented work force, it must monitor its position against other nations. Specifically, Kao offers Singapore as a benchmark example of a premier innovative nation. Singapore has taken great strides to provide researchers with top-notch facilities, resources, and academic freedom. As a result, today it reaps the benefits of world-class scientists who previously would have made the United States their home.

But how can the United States become an innovation nation? Kao suggests that as an initial step, the country allocate the resources required to create an innovation-supporting infrastructure. In particular, he advocates spending $20 billion to invigorate 20 innovation hubs, each focused on a specific wicked problem (e.g., digital media, clean technology, agricultural biotechnology, and nanomolecular materials). While huge, that amount of money fades in comparison with the vast sums now being lost in the current financial meltdown. Kao's hubs would draw on a mix of local, state, and federal funds but be primarily shaped by local stakeholders. Furthermore, Kao suggests establishing three institutions to secure federal oversight and initiative: a national innovation adviser, a national innovation council, and an office of innovation assessment (an expanded version of the former federal Office of Technology Assessment). Although his agenda runs the risk of creating additional bureaucracy, Kao believes that having dedicated institutions will ensure that innovation becomes a top priority among government officials.

Although *Innovation Nation* focuses on the United States, nearly all of Kao's suggestions apply equally well to other nations. One of the takeaways from Kao's book is that being an innovative nation is not an end goal but a process. To stay competitive, countries need to not just constantly innovate—they must innovate their innovation process as well.

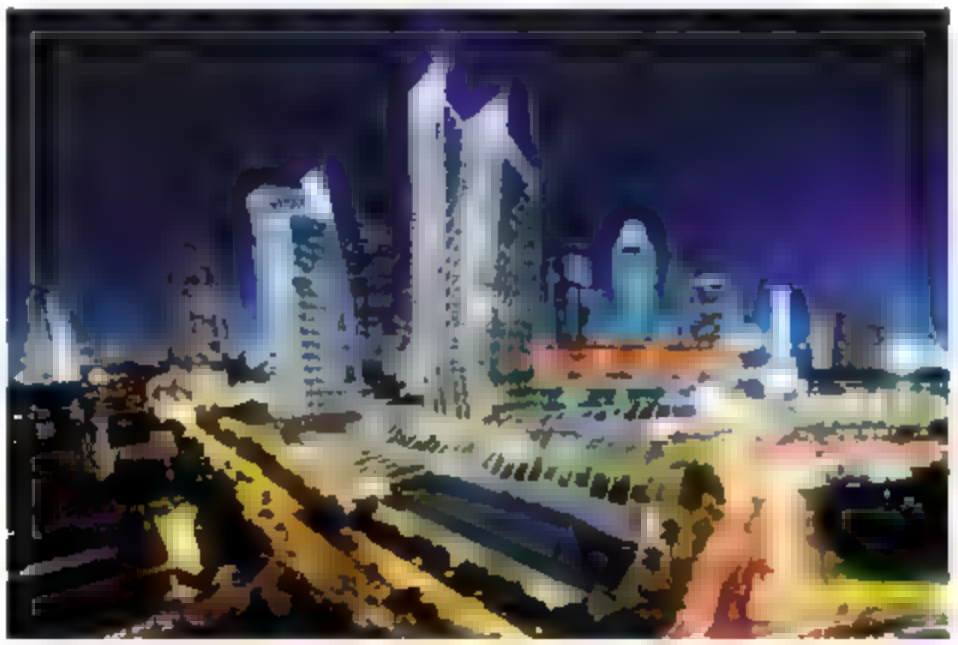

Attracting innovators. The Beach Road project will create an eco-quarter in downtown Singapore with lush planting and sky gardens.

CREDIT: COURTESY FOSTER AND PARTNERS, LONDON

The reviewer is at the Strategy and Policy Department, School of Management, Boston University, Boston, MA 02215, USA. E-mail: grodal@bu.edu

10.1126/science.1164804

OCEANS

Gigantic Losses

Michelle E. Portman

The publication in 2007 of several serious and well-researched books about whaling—including works by Eric Dolin, Peter Heller, and James Estes *et al.* (*1*–*3*)—attests to our fascination with hunting the largest animals known to have lived. This fascination is undoubtedly what drew many men to the wretched business of whaling, with its perils and inhumane conditions. What stands out about Andrew Darby's *Harpoon* is that he spares nothing in his descriptions of the butchering of whales. Whereas Dolin relates an objective history of whaling, Darby clearly stands in defense of whales and for the vilification of their hunters. He makes a good case.

The book gives readers the sense of being let in on a secret world of high-stakes conservation politics being played out through international diplomacy. Darby (an Australian environmental journalist) provokes this same sense of otherworldliness as he describes whale hunts and the means by which whalers slaughtered whales. In traditional Japanese coastal whaling, men in flimsy boats would drive their prey into nets, entangle it, and eventually clamber aboard to "cut through the dying whale's nasal septum and tail, tie it off, then finish it with long swords. Or wooden plugs were driven into blowholes so that the whale suffocated."

Darby bases his arguments for whales on their intelligence, and he describes how others have built that case. His central characters include heroic and at times outlandish figures from the hunting profession and the anti-whaling movement. For example, Jean-Paul Fortom-Goum—"the jetsetter with the hazily explained cheque book" who backed Australian protests in 1977 and "was briefly Panama's commissioner on the IWC [International Whaling Commission]"—carried a model of a sperm whale brain into meetings, "parading [it] sombrely around the room." Some of these efforts were successful: quotas increasingly gained acceptance and, more important, compliance. Nonetheless, current populations of several species contrast greatly with their former abundance.

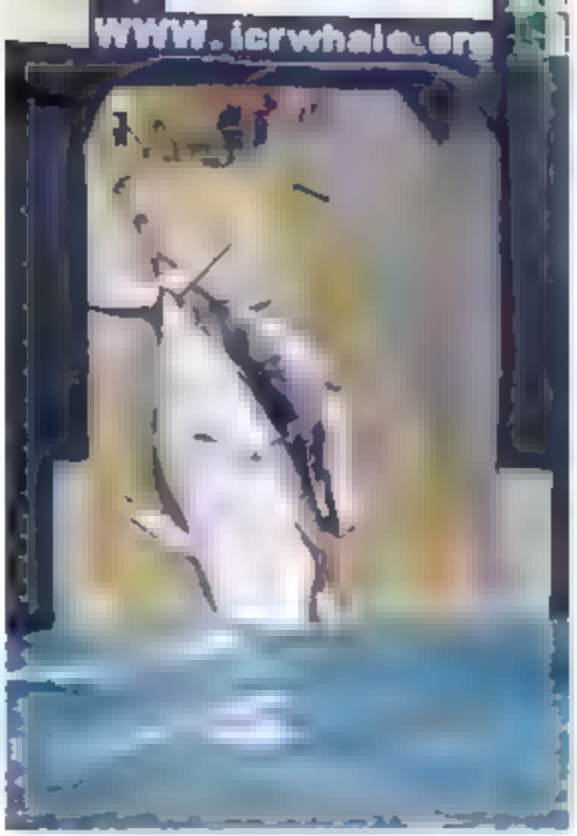

No sanctuary. Two whales killed in Antarctic waters are hauled aboard the factory ship Nisshin Maru (January 2008).

Part of the problem in understanding the effects of whaling on populations is the shoddy records from most of the industry's heyday. Darby reiterates how whaling parties—the sources of most historical survey data—had great incentives to overestimate populations and misreport takings. In the more-distant past, they wished to generate funding for continued expeditions or, as in the case of the Soviets, support raised quotas and avoid reprimand. Also, historical catch figures do not include fatally wounded whales that fled or sank at death. Coalescent models of mitochondria DNA sequence variation indicate that the current genetic diversity requires much greater pre-whaling populations than previously estimated (*4*).

More than anything, Darby's tale is one of failed regulation and management—sound familiar? The author goes back and forth on the IWC, berating it as a "circus" yet never completely giving up on its potential. Early on, the IWC agreed on measures that made a sustainable catch of whales difficult if not impossible. A fundamental mistake was setting an annual quota for Antarctic baleen whales of 16,000 Blue Whale Units (equivalents), an approach that encouraged taking the largest whales possible. The quota also set up a race among fleets to kill the most whales first, a common flaw of industrywide quotas in fisheries management (*5*). Since its early steps, the IWC has been mired in controversies over a myriad of topics related to the International Convention for the Regulation of Whaling and questions as fundamental as the role of science in stock management (*6*).

The IWC may be disappointing as a conservation institution, but it is also criticized for protecting certain stocks that can clearly support sustainable harvest. The commission has been highly polarized since the 1982 imposition of a moratorium on commercial whaling, with both sides encouraging like-minded countries to join. Japan, frequently on the verge of withdrawing, leads the pro-whaling faction. It carries out scientific whaling programs in the North Pacific and in the Southern Ocean. Darby agrees with researchers who believe that this science—largely focused on proving that whales are responsible for declining fish catches (*7*)—is questionable.

The book suffers some from its organization and lack of clarity. Each of the five sections focuses on the plundering of a different whale species. Thus, the sections are somewhat repetitive, and readers will be left confused about what, if anything, distinguishes one demise from another. In addition, the divisions among chapters within sections seem arbitrary. Nor does the flowery or overly theatrical language help. Although few things are more dramatic than the taking of one of these sea giants, in other places (such as the discussions of diplomatic maneuvering) the style complicates an already hard-to-follow situation. And Darby repeatedly fails to frame his references to whale population and kill numbers, time periods, geographic regions, and distinctions among subspecies are blurred and confusing.

Nonetheless, Darby covers a lot in *Harpoon*, including whale evolution, baseline population estimates, whale anatomy, and the political histories of whaling and anti-whaling activities. He also illuminates the larger picture of how whales became an icon of the international conservation movement. But more than anything, his vivid descriptions make palpable, even for the most dispassionate reader, the hard-heartedness of whaling.

The reviewer is at the Marine Policy Center, Woods Hole Oceanographic Institution, Mail Stop 41, Woods Hole, MA 02543, USA. E-mail: mportman@whoi.edu

References

1. E. J. Dolin, *Leviathan: The History of Whaling in America* (Norton, New York, 2007).
2. P. Heller, *The Whale Warriors. The Battle at the Bottom of the World to Save the Planet's Largest Mammals* (Free Press, New York, 2007).
3. J. A. Estes *et al.*, Eds., *Whales, Whaling, and Ocean Ecosystems* (Univ. California Press, Berkeley, 2007).
4. J. Roman, S. R. Palumbi, *Science* **301**, 508 (2003).
5. C. Costello, S. D. Gaines, J. Lynham, *Science* **321**, 1678 (2008).
6. M. Neazle, *Mar. Policy* **28**, 361 (2004).
7. M. Iliff, *Mar. Policy* **32**, 522 (2008).

10.1126/science.1166929

ECONOMICS

Risk Communication on Climate: Mental Models and Mass Balance

Public confusion about the urgency of reductions in greenhouse gas emissions results from a basic misconception.

John D. Sterman

The strong scientific consensus on the causes and risks of climate change stands in stark contrast to widespread confusion and complacency among the public (*1*, *2*). Why does this gulf exist, and why does it matter? Policies to manage complex natural and technical systems should be based on the best available scientific knowledge, and the Intergovernmental Panel on Climate Change (IPCC) provides rigorously vetted information to policy-makers. In democracies, however, the beliefs of the public, not only those of experts, affect government policy.

Effective risk communication is grounded in deep understanding of the mental models of policy-makers and citizens (*3*). What, then, are the principal mental models shaping people's beliefs about climate change? Studies show an apparent contradiction: Majorities in the United States and other nations have heard of climate change and say they support action to address it, yet climate change ranks far behind the economy, war, and terrorism among people's greatest concerns, and large majorities oppose policies that would cut greenhouse gas (GHG) emissions by raising fossil fuel prices (*1*, *2*).

More telling, a 2007 survey found a majority of U.S. respondents (54%) advocated a "wait-and-see" or "go slow" approach to emissions reductions. Larger majorities favored wait-and-see or go slow in Russia, China, and India (*1*, *2*). For most people, uncertainty about the risks of climate change means costly actions to reduce emissions should be deferred; if climate change begins to harm the economy, mitigation policies can then be implemented. However, long delays in the climate's response to anthropogenic forcing mean such reasoning is erroneous.

Wait-and-see works well in simple systems with short lags. We can wait until the teakettle whistles before removing it from the flame because there is little lag between the boil, the whistle, and our response. Similarly, wait-and-see would be a prudent response to climate change if there were short delays in the response of the climate system to intervention. However, there are substantial delays in every link of a long causal chain stretching from the implementation of emissions abatement policies to emissions reductions to changes in atmospheric GHG concentrations to surface warming to changes in ice sheets, sea level, agricultural productivity, extinction rates, and other impacts (*4*–*6*). Mitigating the risks therefore requires emissions reductions long before additional harm is evident. Wait-and-see policies implicitly presume the climate is roughly a first-order linear system with a short time constant, rather than a complex dynamical system with long delays, multiple positive feedbacks, and nonlinearities that may cause abrupt, costly, and irreversible regime changes (*7*, *8*).

Obviously, few people are trained in climatology or nonlinear dynamics, and public understanding of these topics is poor (*9*–*11*). But there is a deeper problem: poor understanding of stocks and flows—the concept of accumulation. Accumulation is pervasive in everyday experience: Our bathtubs accumulate the inflow of water through the faucet less the outflow through the drain, our bank accounts accumulate deposits less withdrawals, and we all struggle to control our weight by managing the inflows and outflows of calories through diet and exercise. Yet, despite their ubiquity, research shows that people have difficulty relating the flows into and out of a stock to the level of the stock, even in simple, familiar contexts such as bank accounts and bathtubs. Instead, people often assess system dynamics using a pattern-matching heuristic, assuming that the output of a system should "look like"—be positively correlated with—its inputs (*12*, *13*).

Although sometimes useful, correlational reasoning fails in systems with important accumulations. Since 1950, the U.S. federal budget deficit and national debt have risen dramatically and are highly correlated (r = 0.84, $P < 0.0001$). Correlational reasoning predicts that cutting the deficit would also cut the debt. However, because the national debt is a stock that accumulates the deficit, it keeps rising even if the deficit falls; debt falls only if the government runs a surplus.

Poor understanding of accumulation leads to serious errors in reasoning about climate change (see charts, left, and on page 533). Sterman and Booth Sweeney (*14*) gave 212 graduate students at the Massachusetts Institute of Technology (MIT) a description of the relationships among GHG emissions, atmospheric concentrations, and global mean temperature. The description was excerpted from the IPCC's "Summary for Policymakers" (SPM), a document intended for nonspecialists (*4*). Participants were then asked to sketch the emissions trajectory required to stabilize atmospheric CO_2. To highlight the stock-flow structure, participants were first directed to estimate future net removal of CO_2 from the atmosphere (net CO_2 taken up by the oceans and biomass), then draw the emissions path needed to stabilize atmospheric CO_2 [the SOM (*2*) provides details].

Knowledge of climatology or calculus is not needed to respond correctly. The dynamics are easily understood using a bathtub analogy in

Consider a scenario in which the concentration of CO_2 in the atmosphere gradually rises to 400 ppm, about 8% higher than the level in 2000, then stabilizes by the year 2100, as shown here:

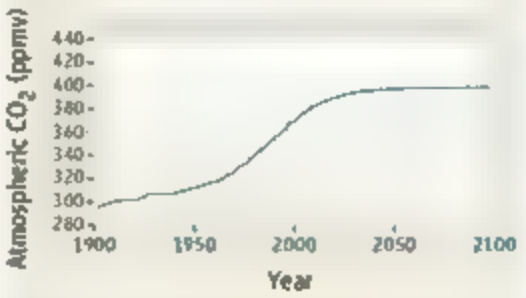

The graph below shows anthropogenic CO_2 emissions from 1900–2000, and current net removal of CO_2 from the atmosphere by natural processes. Sketch:

a. Your estimate of likely future net CO_2 removal, given the scenario above

b. Your estimate of likely future anthropogenic CO_2 emissions, given the scenario above.

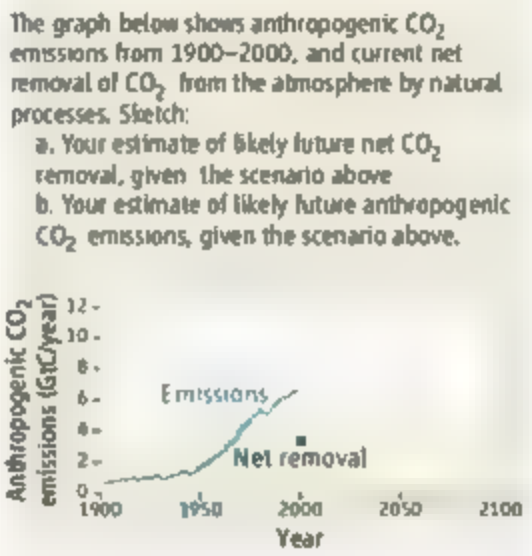

The climate stabilization task. Subjects were first given an excerpt from the IPCC SPM explicitly describing the accumulation of CO_2 in the atmosphere [see (*2*)]

MIT Sloan School of Management, 30 Wadsworth Street, Cambridge, MA 02142, USA. E-mail: jsterman@mit.edu

which the water level represents the stock of atmospheric CO_2. Like any stock, atmospheric CO_2 rises when the inflow to the tub (emissions) exceeds the outflow (net removal), is unchanging when inflow equals outflow, and falls when outflow exceeds inflow. Participants were informed that anthropogenic CO_2 emissions are now roughly double net removal, so the tub is filling.

Yet, 84% drew patterns that violated the principles of accumulation. If emissions followed the path in the typical example shown, atmospheric CO_2 would continue to rise. Nearly two-thirds of the participants asserted that atmospheric GHGs can stabilize even though emissions continuously exceed removal—analogous to arguing a bathtub continuously filled faster than it drains will never overflow. Most believe that stopping the growth of emissions stops the growth of GHG concentrations. The erroneous belief that stabilizing emissions would quickly stabilize the climate supports wait-and-see policies but violates basic laws of physics.

Training in science does not prevent these errors. Three-fifths of the participants have degrees in science, technology, engineering, or mathematics (STEM); most others were trained in economics. Over 30% hold a prior graduate degree, 70% of these in STEM. These individuals are demographically similar to influential leaders in business, government, and the media, though with more STEM training than most.

It is tempting to respond to these discouraging results by arguing that poor public understanding of climate change is unimportant because policy should be informed by scientific expertise. Many call for a new Manhattan Project to address the challenge (*15*, *16*). The desire for such technical solutions is understandable. In 1939, scientists directly alerted the nation's leaders to developments in atomic physics, then, by focusing enough money and genius in the deserts of New Mexico, created nuclear weapons in just 6 years. Science has arguably never affected geopolitical outcomes more decisively.

But a Manhattan Project cannot solve the climate problem (*17*). The bomb was developed in secret, with no role for the public. In contrast, reducing GHG emissions requires billions of individuals to cut their carbon footprints by, e.g., buying efficient vehicles, insulating their homes, using public transit, and, crucially, supporting legislation implementing emissions abatement policies. Changes in people's views and votes create the political support elected leaders require to act on the science. Changes in buying behavior create incentives for businesses to transform their products and operations. The public cannot be ignored.

The civil rights movement provides a better analogy for the climate challenge. Then, as now, entrenched interests vigorously opposed change. Political leadership and legislation often lagged public opinion and grass-roots action. Success required dramatic changes in people's beliefs and behavior, changes both causing and caused by the courageous actions of those who spoke out, registered voters, and marched in Washington and Selma (*18*).

Building public support for action on climate change is in many ways more challenging than the struggle for civil rights. Science is not needed to recognize the immorality of racism but is critical in understanding how GHG emissions can harm future generations. The damage caused by segregation was apparent to anyone who looked, but the damage caused by GHG emissions manifests only after long delays.

The scientific community has a vital role to play in building public understanding. First, the SPM is far too technical to change people's mental models. The IPCC should issue its findings in plain language. Second, clarity, while necessary, is not sufficient. When "common sense" and science conflict, people often reject the science (*3*). Even if people sincerely wish to mitigate the risks of climate change, wait-and-see will seem prudent if they misunderstand basic concepts of accumulation and erroneously believe that stopping the growth of emissions will quickly stabilize the climate. The implications go beyond the failure to understand accumulation. People's intuitive understanding of dynamics, including stocks and flows, time delays, and feedbacks, is poor (*11*). Analogous to common biases and errors in probabilistic reasoning (*19*), these errors are unlikely to be corrected merely by providing more information (*13*). We need new methods for people to develop their intuitive systems thinking capabilities. Bathtub analogies and interactive "management flight simulators" through which people can discover, for themselves, the dynamics of accumulation and impact of policies have proven effective in other settings (*20*) and may help here (*21*). Third, climate scientists should partner with psychologists, sociologists, and other social scientists to communicate the science in ways that foster hope and action rather than denial and despair. Doing so does not require scientists to abandon rigor or objectivity. People of good faith can debate the costs and benefits of policies to mitigate the risks of climate change, but policy should not be based on mental models that violate fundamental physical principles.

Of course, we need more research and technical innovation—money and genius are always in short supply. But there is no purely technical solution for climate change. For public policy to be grounded in the hard-won results of climate science, we must now turn our attention to the dynamics of social and political change.

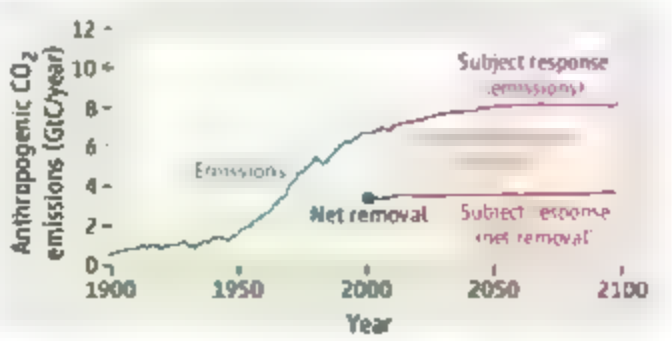

A typical response to the climate stabilization task. Future emissions are erroneously correlated with atmospheric CO_2. Gold dashed line indicates the correct emissions path to stabilize CO_2 given the subject's estimate of net removal.

References and Notes

1. A. Leiserowitz, *Public Perception, Opinion and Understanding of Climate Change—Current Patterns, Trends and Limitations* (United Nations Development Programme, New York, 2007); http://hdr.undp.org/en/reports/global/hdr2007-2008/papers/leiserowitz_anthony.pdf.
2. Materials and methods are available as supporting material on *Science* Online.
3. M. G. Morgan, B. Fischhoff, A. Bostrom, C. J. Atman, *Risk Communication: A Mental Models Approach* (Cambridge Univ. Press, New York, 2002).
4. IPCC, *Climate Change 2007: The Physical Science Basis. Contribution of Working Group I to the Fourth Assessment Report of the Intergovernmental Panel on Climate Change*, S. Solomon *et al.*, Eds. (Cambridge Univ. Press, Cambridge, 2007).
5. T. M. Wigley, *Science* **307**, 1766 (2005).
6. G. A. Meehl *et al.*, *Science* **307**, 1769 (2005).
7. R. B. Alley *et al.*, *Science* **299**, 2005 (2003).
8. M. Scheffer *et al.*, *Nature* **413**, 591 (2001).
9. B. Kasemir *et al.*, *Glob. Environ. Change* **10**, 169 (2000).
10. W. Kempton, *Environment* **39**, 12 (1997).
11. J. D. Sterman, *Syst. Dyn. Rev.* **10**, 291 (1994).
12. L. Booth Sweeney, J. D. Sterman, *Syst. Dyn. Rev.* **16**, 249 (2000).
13. M. A. Cronin *et al.*, *Org. Behav. Hum. Decis. Process.* 21 May 2008, 10.1016/j.obhdp.2008.03.003.
14. J. D. Sterman, L. Booth Sweeney, *Clim. Change* **80**, 213 (2007).
15. G. Prins, S. Rayner, *Nature* **449**, 973 (2007).
16. Searching Google for "Manhattan Project" AND "climate change" yields 164,000 hits (accessed 23 June 2008).
17. C.-J. Yang, M. Oppenheimer, *Clim. Change* **80**, 199 (2007).
18. J. Williams, *Eyes on the Prize: America's Civil Rights Years, 1954–1965* (Viking, New York, 1987).
19. A. Tversky, D. Kahneman, *Science* **185**, 1124 (1974).
20. J. D. Sterman, *Business Dynamics* (Irwin/McGraw-Hill, New York, 2000).
21. Management Flight Simulators, http://scripts.mit.edu/~jsterman/Management_Flight_Simulators_(MFS).html.

22. Financial support from the Project on Innovation in Markets and Organizations at the MIT Sloan School.

Supporting Online Material
www.sciencemag.org/cgi/content/full/322/5901/532/DC1

10.1126/science.1162574

PHYSIOLOGY

CaCl-ing Channels Get the Last Laugh

A long-sought ion-channel gene with intriguing links to cancer and development has been identified.

H. Criss Hartzell

Typically, ion-channel biophysicists and developmental and cancer biologists rarely attend the same journal clubs. But two studies might change this, one by Caputo *et al.* on page 590 in this issue (*1*) and the other by Yang *et al.* (*2*). Both studies show that a transmembrane protein, TMEM16A [also called anoctamin-1 (ANO1)], whose expression increases in many tumors, is a calcium (Ca^{2+})-activated, chloride (Cl^-) channel.

The Ca^{2+}-activated Cl^- channels were first described in the 1980s as mediating the fast block to polyspermy in amphibian oocytes (*3*). These channels, activated by increases in the concentration of intracellular Ca^{2+} ions that occur upon fertilization, conduct Cl^- ions across the plasma membrane, causing the cell to depolarize and prevent additional sperm entry. Similar channels in many cell types, including mammalian, play roles as diverse as epithelial fluid secretion, amplification of the olfactory receptor potential, and regulation of vascular tone (*3*). Yet, Ca^{2+}-activated Cl^- channels have been "a function in search of a molecule" for more than a decade. Previous claims that other molecules (CLCAs, ClC-3, and tweety) function as Ca^{2+}-activated Cl^- channels have been contentious because the ionic currents (electric currents carried by ions) conducted by these proteins do not exhibit the appropriate pharmacology, kinetics, voltage dependence, or Ca^{2+} sensitivity (*3*). Bestrophins, which can function as Cl^- channels and as regulators of voltage-gated Ca^{2+} channels, fit the bill more closely, but not exactly (*4*).

Why has the Ca^{2+}-activated Cl^- channel been so hard to find? One reason is that every cell expresses Cl^- channels, and the pharmacological tools needed to identify Cl^- channels are not very selective. Furthermore, because overexpressing some membrane proteins paradoxically increases the expression of endogenous Cl^- channels, heterologous expression of putative Cl^- channels can produce false-positives. These obstacles have made it hard to identify candidate Ca^{2+}-activated Cl^- channels.

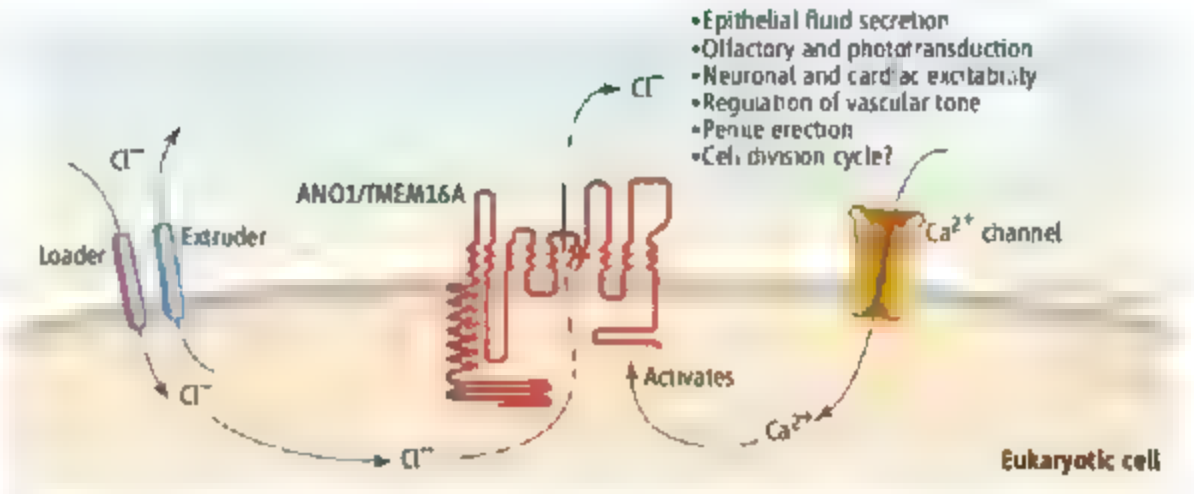

Channel identity ANO1, an eight–transmembrane domain–containing protein, mediates Ca^{2+}-activated Cl^- ionic currents involved in many physiological processes, possibly including cell proliferation.

Caputo *et al.* used microarray gene analysis to identify ANO1 as the channel responsible for increasing the Ca^{2+}-activated Cl^- current in human bronchial epithelial cells exposed to the cytokine interleukin-4. Yang *et al.* selected ANO1 from a bioinformatic search of potential Cl^- channel genes. Each group then used RNA interference (RNAi) to reduce the expression of ANO1 in various mammalian cells and tissues. In each case, the processes disrupted by RNAi treatment—secretion, ion fluxes across the plasma membrane, or whole-cell ionic currents—were exactly what one would expect following reduced expression of Ca^{2+}-activated Cl^- channels. Furthermore, in cell types that do not normally express this type of channel, overexpression of ANO1 induced an ionic current with the properties expected of a Ca^{2+}-activated Cl^- channel. Finally, mutations at critical sites in the protein altered channel function. Yang *et al.* provide the most convincing demonstration: A ~30-fold increase in relative cation permeability caused by substituting a negative charge (glutamic acid) for a positive charge (arginine) at position 621, which lies within a segment that probably inserts into the membrane from the extracellular side but does not cross it (the so-called reentrant loop) (see the figure) (*5*). This structure appears in the pore of a number of ion channels. Also, Yang *et al.* show that ANO1 is the first candidate Ca^{2+}-activated Cl^- channel that can be activated in cells by receptors at the cell surface that, when activated themselves, cause an increase in the concentration of intracellular Ca^{2+}.

Members of the ANO channel family are found in all eukaryotic kingdoms. With 10 mammalian members and multiple splice variants, ANO is the second largest of the five known Cl^- channel families (GABA, glycine receptors, ANOs, ClCs, bestrophins, and the cystic fibrosis transmembrane conductance regulator) (*4*, *6*). Interestingly, ANO8 and ANO10, the most divergent subfamilies, lack part of the reentrant loop that includes arginine 621. Moreover, one of the ANO7 RNA transcripts encodes a 179–amino acid cytosolic protein (*5*), suggesting that ANO channels could have additional nonchannel functions.

ANO channels have attracted the interest of cancer biologists as targets for therapeutic antibodies and as biomarkers because they are highly expressed in tumors and are accessible cell-surface proteins (*5*, *7*). The idea that ion channels play a role in cancer is not new (*8*, *9*), but the addition of this well-studied channel family to the list of proteins associated with cancer heralds new mechanistic insights. Although it does not appear that mutations in ANO1 are linked to carcinogenesis (*10*), ANO channels may participate in cell proliferation. The activities of several anion channels correlate with the cell division cycle (*11*, *12*). And, intriguingly, a mutant of an ANO channel [called Axs (aberrant x-segregation)] in the fly *Drosophila melanogaster* is linked to aberrant chromosomal segregation (nondisjunction) and progression of meiosis (*13*). Axs is ~35% identical to ANO8 and ANO10, and like them, it lacks the reentrant loop. Whether this means

The Department of Cell Biology, Emory University School of Medicine, Atlanta, GA 30322, USA. E-mail: criss.hartzell@emory.edu

CREDIT: P. HUEY/SCIENCE

that Axs is not a Cl^- channel or that this part of the protein is not essential for Cl^- channel function remains to be seen.

Although the exact functions of ANO channels in cancer are speculative, ANO1 and ANO5 have clear roles in development. Mutations in a conserved amino acid (cysteine 356) in the first extracellular loop of ANO5 produce gnathodiaphyseal dysplasia, a bone fragility syndrome that is caused by chondrocyte and osteoblast dysfunction. Similarly, ANO1 dysfunction causes an endoskeletal defect in mice, but by a different mechanism. Mice engineered to lack ANO1 die after birth, apparently because of tracheal cartilage malformation (*14*). ANO1 is expressed in the mouse tracheal epithelium and, intriguingly, the authors speculate that ANO1 may play a role in asymmetric cell divisions that are necessary for tracheal epithelial stratification.

An immediate question is whether all ANO proteins are Cl^- channels. It is also unclear how ANO channels are regulated by Ca^{2+} given that they do not have obvious Ca^{2+}-binding sites. Perhaps there are other regulators. Now that one of the last holdouts of a major channel family has been identified, we can begin exploring the links between its function and cancer and development.

References

1. A. Caputo *et al.*, *Science* **322**, 590 (2008); published online 4 September 2008 (10.1126/science.1163518).
2. Y. D. Yang *et al.*, *Nature* 10.1038/nature07313 (2008).
3. C. Hartzell, I. Putzier, J. Arreola, *Annu. Rev. Physiol.* **67**, 719 (2005).
4. H. C. Hartzell, Z. Qu, K. Yu, Q. Xiao, L. T. Chien, *Physiol. Rev.* **88**, 639 (2008).
5. S. Das *et al.*, *Cancer Res.* **68**, 6306 (2008).
6. T. J. Jentsch, V. Stein, F. Weinreich, A. A. Zdebik, *Physiol. Rev.* **82**, 503 (2002).
7. I. Espinosa *et al.*, *Am. J Surg. Pathol.* **32**, 210 (2008).
8. H. Sontheimer, *Exp. Biol. Med.* **233**, 779 (2008).
9. T. Shimizu, E. L. Lee, T. Ise, Y. Okada, *Anticancer Res.* **28**, 75 (2008).
10. S. Miwa, T. Nakajima, Y. Murai, Y. Takano, T. Sugiyama, *J. Gastroenterol.* **43**, 531 (2008).
11. T. K. Klausen *et al.*, *J. Cell Physiol.* **210**, 831 (2007).
12. M. Villar, J. C. Cinniger, W. J. Moody, *J. Physiol.* **488**, 689 (1995).
13. J. Kramer, R. S. Hawley, *Cell Cycle* **2**, 174 (2003).
14. J. R. Rock, C. R. Futtner, B. D. Harfe, *Dev. Biol.* **321**, 141 (2008).

10.1126/science.1165668

ASTRONOMY

Aspects of Our Sun

Accurate determination of the shape of the Sun sheds light on its inner workings.

Gary A. Chapman

The shape of the Sun touches on several issues in cosmology and solar physics, including whether Einstein's General Theory of Relativity is the correct theory of gravity, and to what extent the solar interior rotates. On page 560 of this issue, Fivian *et al.* (*1*) present compelling satellite-based observations showing that the Sun's shape is in agreement with what is expected from the rotation of its visible surface. These latest observations eliminate the possibility of a rapidly rotating core and remove one of the last remaining challenges to the validity of General Relativity from solar system studies.

Gravity is still a bit mysterious. Of the four fundamental forces, it defies unification with the other three (electromagnetism, weak nuclear, and strong nuclear). Einstein's General Theory of Relativity, the currently accepted theory of gravity, has passed all tests that have been devised for it with flying colors. Early on, the only tests involved the solar system and the Sun's gravity (*2*, *3*). The two most famous tests were the deflection of starlight and the precession of Mercury's orbit (the motion of its perihelion). Both of these effects are caused by the warping of spacetime in the vicinity of the Sun. General Relativity was able to explain the precession of 43 arc sec per century that was not accounted for by the Newtonian gravitational effects of the other planets. However, another theory of gravity, the scalar-tensor theory of Brans and Dicke (*4*), suggested a different value of the precession that depended on a proposed "coupling" of a mass with the mass of the universe. For a modestly small value of this coupling constant, the scalar-tensor theory predicted a smaller value of the precession than was observed. Then, in order for the scalar-tensor theory to agree with the observed precession of Mercury's orbit, the Sun needed to have an excess oblateness (i.e., the equatorial radius minus the polar radius) over and above what is expected from its observed surface rotation (with a rotation period of about 28 days). This proposed excess oblateness supplied the small additional precession needed to bring the sum of the two into agreement with observations.

Measuring up. A suite of sensitive aspect sensors onboard the spacecraft RHESSI is used to determine the oblateness of the Sun.

IMAGE CREDIT: BOHONA ET AND ESA

Observations with a specialized telescope at Princeton (*5*) showed that the Sun had an oblateness of 50 parts per million of the mean radius and that it was most likely caused by a rapidly rotating core (with a rotation period of 1 to 2 days). Helioseismologists have looked for this rapidly rotating core; the results have been inconclusive but have tended toward the negative. The oblateness due to the known surface rotation is about 8 ppm, or about one-sixth of that measured in (*5*). The finding of an excess solar oblateness led to years of controversy (*6*–*10*). An improved telescope derived from the earlier Princeton one found that facular contrast (the intensity of a facular feature divided by the quiet Sun intensity at the same disk position minus 1) rose toward the solar limb, the apparent edge of the solar disk (*11*), contradicting earlier results (*12*). The increase in facular contrast toward the limb of the Sun means that faculae most likely play a dominant role in the Sun's oblateness, which is the main point made by Fivian *et al.*

The spacecraft RHESSI (Reuven Ramaty High Energy Solar Spectroscopic Imager) is designed to image solar sources of high-energy radiation. Fivian *et al.* used the set of sensitive aspect sensors onboard the spacecraft to obtain a highly accurate measurement of the solar oblateness. They did find an excess oblateness but were able to show that it is due to magnetic features.

Department of Physics and Astronomy, California State University, Northridge, CA 91330, USA. E-mail: gary.chapman@csun.edu

Magnetic features on the Sun can be either dark (sunspots) or bright (faculae and a more scattered network). Faculae are more important for the excess oblateness because of their much greater area. This implies that the solar core is not rapidly rotating, although the boundary between the core and the convection zone is still a poorly understood region. Without a geometrical oblateness from a rapidly rotating core, the scalar-tensor theory fails this observational test. It has already failed tests of the so-called Shapiro time delay (*13*) and the deflection of starlight (*14*) (applied to radio sources). Part of the mission of the European spacecraft PICARD (*15*), due to be launched in 2009, is to measure the shape of the Sun at different wavelengths. It will be good to have an independent space-based determination of the Sun's shape as a comparison.

A major solar physics question has to do with the internal rotation of the Sun. Does the core rotate slightly faster than the surface? (This would have a negligible effect on the solar oblateness.) If the core rotates faster than the outer parts of the Sun, does this affect the operation of the solar dynamo? The Sun is currently in its magnetic activity minimum. This quiet period should improve the search for solar shapes more complex than a simple oblateness. There are still more things to learn in the solar interior.

References

1. M. D. Fivian, H. S. Hudson, R. P. Lin, H. J. Zahid, *Science* **322**, 560 (2008), published online 2 October 2008 (10.1126/science.1160863).
2. C. M. Will, *Science* **250**, 770 (1990).
3. C. W. Misner, K. S. Thorne, J. A. Wheeler, *Gravitation* (Freeman, San Francisco, 1973).
4. C. Brans, R. H. Dicke, *Phys. Rev.* **124**, 925 (1961).
5. R. H. Dicke, H. M. Goldenberg, *Phys. Rev. Lett.* **18**, 313 (1967).
6. G. A. Chapman, A. P. Ingersoll, *Astrophys. J.* **175**, 819 (1972).
7. R. H. Dicke, *Astrophys. J.* **175**, 831 (1972).
8. G. A. Chapman, A. P. Ingersoll, *Astrophys. J.* **183**, 1005 (1973).
9. R. H. Dicke, *Astrophys. J.* **190**, 187 (1974).
10. H. A. Hill, R. T. Stebbins, *Astrophys. J.* **200**, 471 (1975).
11. M. F. Woodard, K. G. Libbrecht, *Solar Phys.* **212**, 51 (2003).
12. K. G. Libbrecht, J. R. Kuhn, *Astrophys. J.* **299**, 1047 (1985).
13. J. D. Anderson, P. B. Esposito, W. Martin, C. L. Thornton, D. O. Muhleman, *Astrophys. J.* **200**, 221 (1975).
14. S. S. Shapiro *et al.*, *Phys. Rev. Lett.* **92**, 121101 (2004).
15. G. Thuillier *et al.*, *Adv. Space Res.* **38**, 1792 (2006).

10.1126/science.1163101

ASTRONOMY

The Pulse of Distant Stars

Space-based observations can now be used to "see" the pulsations and surface granulations of distant stars similar to those of the Sun

M. H. Montgomery

Far from being a constant light source, the Sun oscillates at thousands of different frequencies simultaneously and has granulations at its surface associated with rising and falling fluid elements. Despite the amplitudes of the induced light variations being at a level of about one part per million, the Sun's brightness has allowed its "pulse," in terms of luminosity variations, to be measured using Earth-based telescopes. On page 558 of this issue, Michel *et al.* (*1*) present data from the space satellite CoRoT (Convection Rotation and Planetary Transits), demonstrating the ability to characterize the oscillation amplitudes and the signature of stellar granulation in three other stars. In addition to the technical success that this represents, the measurements show that solar-like oscillations do occur in these stars, although with somewhat smaller amplitudes than predicted. This bodes well for the future of space-based seismology programs while simultaneously challenging us to refine our models of these stars.

Star oscillation modes. Ray paths of low- (blue), medium- (yellow, green), and high-degree (pink) modes. Each mode samples the star's interior in a different way.

Stellar pulsations allow us to probe a star's structure beneath its surface. This is analogous to seismology on Earth, in which earthquakes produce waves that travel through Earth's interior. By measuring the properties of these waves as they return to the surface, geologists have been able to constrain models of Earth's interior structure. The pulsations of a star can be thought of as a superposition of traveling waves that propagate through its interior, return to the surface, and are reflected back into the interior (see the figure). The study of a star's interior through its pulsation modes is called asteroseismology and, when applied to the Sun, helioseismology.

Because each pulsation mode samples a star's interior differently, the more pulsation modes that are present in a star, the tighter the constraints on its internal structure. Some stars, such as the well known Cepheids, pulsate in only one mode, so we learn little about their internal structure. On the other hand, these stars have proven to be extremely useful as distance indicators because their period-luminosity relationship allows the observed period to be converted into an absolute luminosity, and hence a distance, for the star (*2*). Other stars pulsate in many modes simultaneously, such as the white dwarf variables, which have amplitude variations on the order of a few percent and can have from a dozen to more than 100 observed modes. This larger number of modes allows deductions to be made concerning their inner chemical profiles and composition and their mass, temperature, and rotation rate (*3*, *4*).

In the case of the Sun, millions of pulsation modes are observed, which is the reason helioseismology has proved to be so successful over the past 30 years (*5*). We have learned that the Sun's convection zone extends over

Department of Astronomy, University of Texas, Austin, TX, USA; Delaware Asteroseismic Research Center, Mt. Cuba Observatory, Greenville, DE, USA. E-mail: mikemon@astro.as.utexas.edu

the outer 29% of its radius. Inside this point, it rotates like a solid body, whereas throughout the convection zone it shows appreciable differential rotation. In addition, helioseismology has allowed us to make a very accurate model of the Sun, and this showed that the solar neutrino problem, the deficit of detected versus predicted neutrinos from the Sun, could not be explained by an incomplete understanding of the Sun's interior. As we now know, the resolution of this problem came from new particle physics in the form of neutrino oscillations (*6*). Helioseismology has also allowed us to measure the evolutionary state of the Sun, including constraints on its age and chemical composition.

If the Sun were as distant as other stars, we would no longer be able to see the millions of pulsation modes; we would be limited to around 100 or less. Having refined our techniques and experience based on the Sun, however, this number of pulsation modes is more than sufficient for providing accurate constraints on the parameters and structure of other stars (*7*). This is fortunate, because stellar models that are calibrated to the Sun are unlikely to be as accurate for stars of different mass and temperature. The work of Michel *et al.* represents a substantial first step in understanding stars somewhat more massive than the Sun (the masses of their targets were between 1.17 and 1.4 solar masses). Their data show that the oscillation amplitudes are 1.5 times as large as those of the Sun, which is still about 25% lower than theoretical estimates. This is noteworthy because these amplitudes depend on the nature of convection in the outer layers of these stars. In addition, they were able to measure properties of the granules seen at the surface of these stars, a further manifestation of convection within them. This provides us with the opportunity to test and refine our theories of convection, which is one of the largest sources of uncertainty in the modeling of stars. And, perhaps most important, their results showed that the expected oscillations were present with measurable amplitudes, thereby demonstrating the viability of space-based investigations.

Further observations by CoRoT and the upcoming NASA mission Kepler should yield a wealth of information on other solar-like stars. It will then be possible to place tighter constraints on quantities such as the total mass, luminosity, radius, age, and rotation rate of a very large number of stars. These space-based observations will test our understanding of physical processes, such as convection in the envelopes and cores of stars, but will also enhance our understanding of the ages and evolutionary states of objects throughout our Galaxy and the local universe.

References

1. F. Michel *et al.*, *Science* **322**, 558 (2008).
2. A. Sandage, G. A. Tammann, *Astrophys. J.* **151**, 531 (1968).
3. D. E. Winget *et al.*, *Astrophys. J.* **430**, 839 (1994).
4. D. E. Winget *et al.*, *Astrophys. J.* **378**, 326 (1991).
5. D. O. Gough *et al.*, *Science* **272**, 1281 (1996).
6. Q. R. Ahmad *et al.*, *Phys. Rev. Lett.* **89**, 011301 (2002).
7. T. S. Metcalfe, http://arXiv.org/abs/0808.3136 (2008).

10.1126/science.1164633

GENETICS

GenBank—Natural History in the 21st Century?

Since its foundation, the nucleic acid sequence database GenBank has merged the values of natural history with those of the experimental sciences.

Bruno J. Strasser

The American nucleic acid sequence database GenBank, as well as its European (European Molecular Biology Laboratory, EMBL) and Japanese (DNA Databank of Japan, DDBJ) mirror organizations, each contain far more nucleotides than "the number of stars in the Milky Way," as the U.S. National Institutes of Health (NIH) once put it in a press release (*1*). The early history of this database illustrates the transformation of biology into a new science that links the methods of natural history with those of experimentation.

GenBank represents the cutting edge of biology, but it also belongs to the centuries-old tradition of natural history—a tradition best characterized as the practice of collecting, describing, naming, comparing, and organizing natural objects. The method applies equally to plants, bones, or molecular sequences. This view challenges the received historical picture, in which the experimental sciences overtook natural history in the late 19th century and triumphed in the mid-20th century with the rise of molecular biology. As GenBank and other databases attest, the practices of natural history have been imported into the experimental sciences.

In March 1979, 30 molecular biologists and computer scientists meeting at the Rockefeller University in New York agreed on the necessity to create a national, computerized database (*2*). The impetus was the same as that behind most natural history collections, which were often created in reaction to a perceived overabundance of information—for example, when the expansion of European travel to the New World led to the accumulation of previously unknown specimens. This time, it was the explosive growth in the number of known DNA sequences and the promise of producing biological knowledge by analyzing and comparing them that made a database seem indispensable. Several scientists were maintaining individual sequences collections, but none was comprehensive.

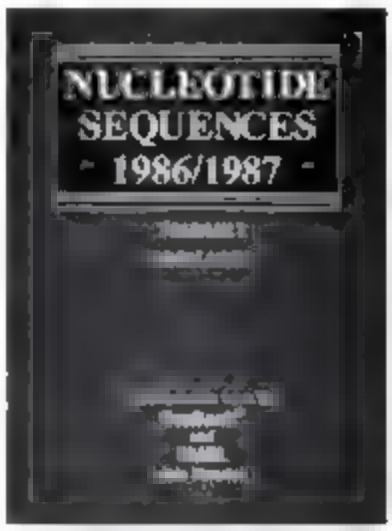

It took almost 3 years for the NIH to come up with a funding scheme, and by that time, the EMBL had already made its own sequence database publicly available. This delay—somewhat embarrassing for the NIH—resulted not only from bureaucratic inertia, as some have argued, but also from uncertain scientific prospects for a natural history collection at a time when experimentation triumphed in revealing the secrets of nature. Frederick Sanger would later put it bluntly: "'Doing' for a scientist implies doing experiments" (*3*). Pressed by a few vocal experimental scientists the NIH eventually issued a Request for Proposals. Two

Section of the History of Medicine, Yale University, New Haven, CT 06520, USA. E-mail: bruno.strasser@yale.edu

applications competed for the contract: one by a team headed by Margaret O. Dayhoff (1925 to 1983) at the National Biomedical Research Foundation (NBRF) and one by a group of researchers around Walter Goad (1925 to 2000) at Los Alamos National Laboratory, collaborating with the private company Bolt Beranek and Newman (BBN).

Dayhoff had pioneered sequence databases by gathering an extensive collection of protein sequences since the early 1960s. She believed that a "tremendous amount of information regarding evolutionary history and biochemical function [is] implicit in each sequence" and that it was essential to "collect this significant information, correlate it into a unified whole and interpret it" (*4*). In a series of volumes entitled *The Atlas of Protein Sequence and Structure*, published beginning in 1965, she presented the world's largest collection of protein and nucleic acid sequences, innovative methods to analyze them, and evolutionary inferences drawn from them.

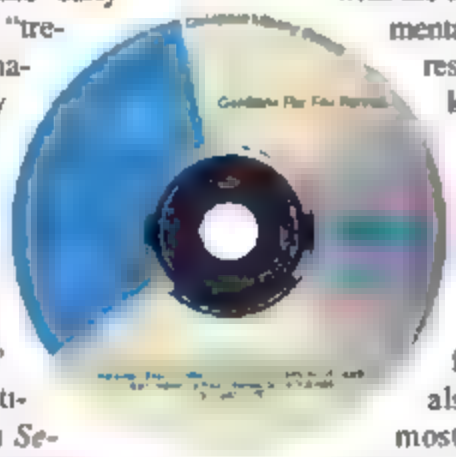

The *Atlas* became immensely popular as a reference tool among molecular and evolutionary biologists. Dayhoff had hoped that researchers would share protein sequences directly with her before they were published. This model of data collection was typical of natural history, but proved unsuccessful with experimentalists, because inclusion in the *Atlas* established neither authorship nor priority. Dayhoff and her team were left with the painstaking task of surveying manually the published literature.

The competing project for the NIH contract came from Los Alamos, where modest biomedical research had been carried out since the Manhattan Project. When he heard about the conclusions of the Rockefeller meeting, Walter Goad became convinced that Los Alamos was "the natural place to locate a center for sequence analysis of DNA," mainly because of the national laboratory's "unique computer facility" (*5*). Goad, too, began to gather nucleic acid sequences, mostly from other collections such as those of Richard Grantham in France, Kurt Stüber in Germany, and Douglas L. Brutlag and Elvin A. Kabat in the United States.

The NBRF (Dayhoff) and Los Alamos-BBN (Goad) proposals to the NIH for a centralized database were very similar, yet they contained key differences concerning property, privacy, and priority in science. The NBRF proposed to collect sequences by exploring the published literature and inviting experimentalists to submit their data. It considered sequences much as naturalists considered specimens—as unencumbered natural objects free to be collected and appropriated. The Los Alamos–BBN proposal, by contrast, suggested that journal editors would be asked to make the submission of sequences to the database a condition for the publication of an article. This system was aligned with the reward system of the experimental sciences, in which research results were considered private knowledge until they were published and authorship was attributed. Publication was the main incentive and reward for making knowledge public.

The most essential difference between the proposals, however, was also the most subtle. In 1980, the U.S. Supreme Court had declared that "anything under the sun that is made by man," including genetically modified organisms, could be patented (*6*). The NIH grew deeply concerned about who would own the data in the future database. Goad stressed that he "did not intend to assert any proprietary interest whatsoever in any data," and pointed out that Dayhoff and her team had "sought revenues from sales of their database and prevented redistribution" (*4*), without mentioning that the revenues were only meant to cover expenses, not make a profit.

Los Alamos and BBN were further able to boost the openness of their database by offering to distribute it through the Department of Defense–operated computer network ARPANET, whereas the NBRF could offer only limited online access through telephone modems. On 30 June 1982, the NIH signed a contract with Los Alamos and BBN for the establishment of a public and free nucleic acid sequence databank, which would soon be called GenBank.

Yet, the success of GenBank in collecting all published sequences was only made possible by two crucial developments. First, it instituted a tight collaboration with the EMBL database, established a few months earlier at Heidelberg, and, after 1986, with the DDBJ. Each database assumed responsibility for a subset of journals—a division that mirrored the tendency of early natural history collections to focus on specimens of a certain region and relying on exchanges with other collections for the rest. The collaborations among GenBank, EMBL, and DDBJ required delicate negotiations to establish common entry standards; database managers could not rely on an equivalent of Linnaeus's binomial system, which allowed easy exchanges between natural history collectors.

Second, as the DNA databases increasingly lagged behind the exploding number of DNA sequences, they succeeded in convincing journal editors to make electronic submission a condition for publication, solving the problem of data collection. The substantial resistance to the Human Genome Project in the late 1980s, just like that to GenBank a few years earlier, was in part due to its association with the natural history enterprise. To some, a large-scale collection of gene sequences did not sound any more exciting than a large-scale collection of butterflies (*7*).

Since then, the convergence between natural history and the experimental sciences has grown ever closer, for example, with the rise of DNA barcoding in taxonomy or the cross-linking of museum specimens and DNA sequence entries in GenBank, as is done with specimens at the Museum of Vertebrate Zoology at Berkeley. Taking into account GenBank's place in the natural history tradition can help solve some of its most vexing problems, such as obsolete or inaccurate annotations. For example, cumulative annotations have been used for centuries to accommodate the changing knowledge about specimens in natural history collections, and have now been proposed for GenBank (*8*).

Another challenge facing the DNA databases is the development of sequence and other biological databases based on the principles of open-content resources such as Wikipedia (*9*, *10*). These databases could make, critics argue, GenBank/EMBL/DDBJ obsolete, much as the *Encyclopedia Britannica* seems doomed to become. If it is any indication of the future, natural history has thrived by relying on the input of a broad community, including amateurs—not by relying solely on the expertise of its curators.

References

1. NIH, "Public collections of DNA and RNA sequence reach 100 gigabases" (22 August 2005).
2. T. F. Smith, *Genomics* **6**, 701 (1990).
3. Margaret O. Dayhoff Papers, Archives of the National Biomedical Research Foundation, Washington, DC.
4. F. Sanger, *Annu. Rev. Biochem.* **57**, 1 (1988).
5. Walter B. Goad Papers, Archives of the American Philosophical Society, Philadelphia.
6. *Diamond v. Chakrabarty*, 447 U.S. 303 (1980).
7. R. Cook-Deegan, *The Gene Wars. Science, Politics, and the Human Genome* (Norton, New York, 1994), chap. 8.
8. M. I. Bidartondo *et al.*, *Science* **319**, 1616 (2008).
9. E. Pennisi, *Science* **319**, 1598 (2008).
10. J. Giles, *Nature* **445**, 691 (2007).

10.1126/science.1163399

CHEMISTRY

Putting Electrowetting to Work

Voltage pulses that cause changes in fluid shape or movement can be used to drive optical components and miniaturized assays.

Aaron R. Wheeler

Scientists have long been fascinated by the "self-cleaning" lotus leaf and the "fog-collecting" *Stenocara* beetle. In these cases, nature has engineered materials with heterogeneous texture or chemistry to control the tendency of fluids to wet the surface. There has been great interest in developing artificial mimics with similar properties for applications such as antifouling paints and self-cleaning automobile windshields (*1*). An alternative strategy for surface-mediated fluid control is to tune a surface's wettability by applying pulses of electrical energy. This phenomenon, known as electrowetting (*2*, *3*), has the advantage of being dynamic, a property which has made it useful for applications in areas as diverse as optics and laboratory miniaturization.

In electrowetting, a fluid is positioned adjacent to an electrode that is coated with a hydrophobic insulator. When a potential, V, is applied across the insulator, it becomes charged, making it attractive for the fluid to wet the surface. For droplets of conductive liquids with relatively large liquid-vapor surface tensions, γ_{lv}, this wetting behavior is approximated by the well-known Young-Lippmann equation: $\cos\theta_w = \cos\theta + \varepsilon_i \varepsilon_o V^2/(2\gamma_{lv} t)$ where θ_w and θ are the wetted and static contact angles, respectively, ε_i and ε_o are the dielectric permittivities of the insulator and vacuum, and t is the thickness of the insulator. In a typical electrowetting device, ~50 to 100 V is applied across a 1-μm thick insulator, causing the contact angle to decrease from $\theta = 115°$ to $\theta_w = 75°$. This behavior is reversible and has attracted interest as a means to exercise dynamic control over fluids on surfaces.

In the past decade, two principal applications have emerged for electrowetting. In the first, electrically driven modulation of fluid shape has been used for optical applications. For example, when a droplet wets a surface, its radius of curvature changes, and the droplet can serve as a lens with a changeable focal length (*4*). Likewise, when a droplet is asymmetrically wetted, its angle of reflection is modulated, allowing it to serve as an active, beam-steering mirror (*5*). Devices powered by these phenomena are now being used in a variety of consumer electronics products [e.g., (*6*, *7*)]. In the second principal application, electrically driven surface energy changes have been used to modulate fluid position in place of (or in addition to) fluid shape (*2*, *3*). It is this application that is the focus here.

To modulate fluid position, droplets are placed on an array of electrodes coated with a hydrophobic insulator. When electrical potentials are applied sequentially to adjacent electrodes, the droplets, which may contain reagents and samples, can be made to move, merge, and dispense from reservoirs (see the figure, left panel). In describing the control of droplet position, the term digital microfluidics is more suitable than electrowetting because there are low-surface tension fluids that can be controlled on such devices but exhibit modest or negligible wetting (that is, $\theta \approx \theta_w$) (*8*). In fact, the motion of fluids as diverse as organic solvents, physiological buffers, ionic liquids, and concentrated surfactants can all be controlled, which allows this technique to serve as a platform for miniaturizing laboratory processes (*9*, *10*).

Digital microfluidics is similar to the more established technology of microfluidic channels in that both can perform lab analyses with much smaller samples than in bench-scale methods. Both methods can manipulate droplets [e.g., (*11*)], which can act as nanoliter vessels for carrying out reactions without cross-talk between samples or reagents. The principal difference is that in digital microfluidics, droplets are addressed individually, whereas in channels, they are controlled in series. Because digital microfluidics is inherently an array-based technique, it is a good match for array-based biochemical applications. In addition, in digital microfluidics, droplets are manipulated on relatively generic platforms (such as an array of M by N electrodes), which are reconfigurable for any desired combination of operations.

An advantage for digital microfluidics is its compatibility with conventional detection instruments. For example, a digital microfluidic array can be interfaced with a fluorescence microplate reader (*12*) by laying out the electrodes to match the pitch and geometry of microtiter plates. Microdroplets with volumes of ~100 nl serve as vehicles for stopped-flow reactions that have much lower fluorescent background and greater sensitivity compared with multiwell plates in many common assays (for example, the detection limit for an alkaline phosphatase assay is 7.0×10^{-20} moles of substrate in a digital microfluidic device versus a detection limit of 5.0×10^{-18} moles in a microtiter plate).

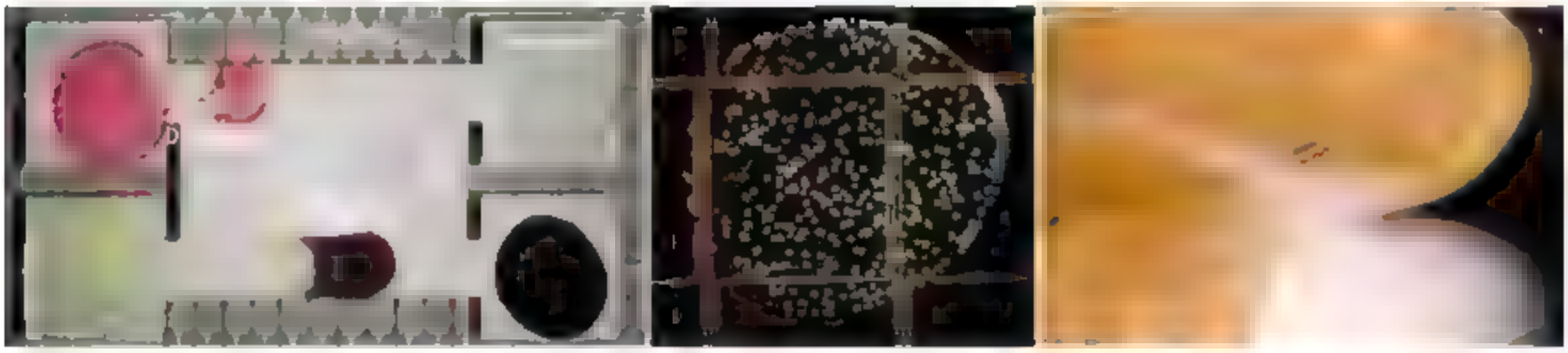

Digital microfluidics for laboratory miniaturization. (Left) By applying a sequence of electrical pulses, droplets can be made to move, merge, and dispense on an array of electrodes (these aqueous droplets contain colored dyes and have volumes of 70 nl). **(Middle)** A very low fluorescence background is useful in the analysis of cells in suspension (this 150-nl droplet contains ~250 calcein-labeled Jurkat T cells). **(Right)** Nonplanar substrates greatly enhance the capacity to integrate multiple environments on a single platform. Here, a 1-μl droplet moving upside down is shown.

PHOTO CREDIT (MIDDLE AND RIGHT PANELS): ROYAL SOCIETY OF CHEMISTRY (12, 28)

Department of Chemistry, University of Toronto, 80 St. George Street, Toronto, ON, M5S 3H6 Canada. E-mail: awheeler@chem.utoronto.ca

Digital microfluidics can also be used in analyses involving biological cells. In a cell-based screen, droplets containing cells, viability reporters, and toxic substrates at different concentrations can be dispensed, mixed, and evaluated with a fluorescence assay (see the figure, middle panel) (*13*). The dose-response curves generated by such devices are more sensitive than equivalent studies on microtiter plates, and cell vitality appears to be unaffected by droplet actuation. Another advantage of digital microfluidics for cell-based assays is the capacity to split and recombine droplets to isolate subpopulations for further analysis (*14*).

Another advantage for the digital microfluidic format is the ease with which electrical components can be integrated into the fluidic circuit. For example, when fabricating an array of droplet-driving electrodes, it is straightforward to also form integrated microheaters for applications that use the polymerase chain reaction. Amplification in such devices can be implemented in half the time and with one-third of the reagent use relative to conventional techniques (*15*).

As the technology has evolved, the pace of the development of new applications for digital microfluidics has increased. For example, in the past year, Liu *et al.* developed a system for ultra-low–volume DNA ligation (*16*), Luk *et al.* implemented a droplet-based system for proteolytic digestion (*17*), and Fouillet *et al.* reported a technique for carrying out magnetic-bead–based sample processing (*18*). In addition to new applications, there is a regular stream of innovations in digital microfluidic device infrastructure. For example, Chiou *et al.* recently reported the capacity to optically actuate "virtual electrodes," which allows for much greater flexibility in device geometry and design (*19*). Likewise, Abdelgawad *et al.* recently demonstrated digital microfluidic processes on open, nonplanar substrates, which facilitates integration of different physicochemical environments on a common platform (see the figure, right panel) (*20*).

The capacity to use electricity to control the shape and position of droplets on surfaces has led to a dynamic new field of research. Taking a cue from the lotus leaf and the *Stenocara* beetle, we are learning to put surface energies to work, in applications ranging from optics to laboratory miniaturization. Given the trajectory of innovation in this field, it is likely that this work has only just begun.

References

1. X. M. Li *et al.*, *Chem. Soc. Rev.* **36**, 1350 (2007).
2. M. G. Pollack *et al.*, *Appl. Phys. Lett.* **77**, 1725 (2000).
3. J. Lee *et al.*, *Sens. Actuators* **A 95**, 259 (2002).
4. B. Berge, J. Peseux, *Eur. Phys. J.* **E 3**, 159 (2000).
5. L. Hou *et al.*, *Appl. Phys. Lett.* **90** (2007).
6. Varioptic, www.varioptic.com.
7. Philips, www.research.philips.com/technologies/light_dev_microsys/fluidlocus.
8. D. Chatterjee *et al.*, *Lab Chip* **6**, 199 (2006).
9. M. Abdelgawad, A. R. Wheeler, *Adv. Mater.*, 10.1002/adma.200802244, in press.
10. E. M. Miller, A. R. Wheeler, *Anal. Bioanal. Chem.*, 10.1007/s00216-008-2397-x, in press.
11. A. Huebner *et al.*, *Lab Chip*, **8**, 1244 (2008).
12. E. M. Miller, A. R. Wheeler, *Anal. Chem.* **80**, 1614 (2008).
13. I. Barbulovic-Nad *et al.*, *Lab Chip* **8**, 519 (2008).
14. S. K. Fan *et al.*, *Lab Chip* **8**, 1325 (2008).
15. Y.-H. Chang *et al.*, *Biomed. Microdevices* **8**, 215 (2006).
16. Y.-J. Liu *et al.*, *J. Micromechan. Microeng.* **18**, 045017 (2008).
17. V. N. Luk, G. C. Mo, A. R. Wheeler, *Langmuir* **24**, 6382 (2008).
18. Y. Fouillet *et al.*, *Microfluid. Nanofluid.* **4**, 159 (2008).
19. P. Y. Chiou *et al.*, *J. Microelectromechan. Syst.* **17**, 133 (2008).
20. M. Abdelgawad *et al.*, *Lab Chip* **8**, 672 (2008).

10.1126/science.1165719

GEOLOGY

The Story of O_2

How did biological, geochemical, and geophysical processes produce an atmosphere that allowed complex animal life to evolve?

Paul G. Falkowski[1] and Yukio Isozaki[2]

Two gases overwhelmingly dominate Earth's atmosphere: N_2 and O_2. The former is primordial, and its presence and abundance are not driven by biological processes. Indeed, N_2 is virtually inert and has an atmospheric lifetime on the order of 1 billion years (*1*). In contrast, O_2 is continuously produced biologically via the oxidation of water driven by energy from the Sun. The gas was almost certainly virtually nonexistent in Earth's early atmosphere, is highly reactive, and has an atmospheric lifetime of ~4 million years (*2*). Yet despite this comparatively short atmospheric lifetime, O_2 came to constitute ~10 to 30% of the atmospheric volume for the past ~500 million years (*3*, *4*).

How did O_2, a gas critical to the evolution of animal life, become the second most abundant gas on Earth? The story is not as simple as it might first appear (*5*, *6*). To understand it, we must know not only how and when O_2 was first generated, but also how it came to persist in high concentrations in the atmosphere.

Elemental oxygen (O) is produced via the so-called "main line" nuclear reaction sequence from successive ^{4}He fusion reactions in hot stars. It was delivered to the early Earth chemically bound to other elements. Through successive cycles of heating and cooling, O reacted with Si and C to form two of the major anions that, together with metal cations, constitute the fundamental minerals in mantle and crust, and with H to form water (*7*). Additional water was delivered to the planetary surface via meteorites and possibly comets; however, the relative proportions of the three sources are not well known (*8*). Regardless of the source, isotopic data suggest that Earth's surface contained liquid water within ~200 million years after the accretion of the planet (*9*). Liquid water is a necessary condition for life as we know it, but it is not a sufficient condition for the biological production of O_2.

Although water can be oxidized to its component elements by ultraviolet light, this reaction can produce only extremely small concentrations of O_2 because of strong negative feedbacks (*10*). The overwhelming source of O_2 on Earth is photobiological oxidation of water; neither the evolution nor the mechanism of this process are completely understood (*11*, *12*). Apparently it arose once in a single clade of bacteria and was then appropriated via a single event, in which one cell engulfed another (endosymbiosis) to form a new symbiotic organism. The latter became the progenitor of all photosynthetic eukaryotes, including algae and higher plants (*12*).

The core of the oxidation machinery is photosystem II, a large protein complex containing four manganese atoms that are photocatalytically oxidized to create electron holes upstream. O_2 is produced as a waste product via the reaction

$$2H_2O \rightarrow 4e + 4H^+ + O_2$$

The protons and electrons generated are used to reduce CO_2 to form organic matter via

$$CO_2 + 4e + 4H^+ \rightarrow (CH_2O) + H_2O$$

[1]Department of Earth and Planetary Sciences and Institute of Marine and Coastal Sciences, Rutgers University, 71 Dudley Road, New Brunswick, NJ 08901, USA. [2]Department of Earth Science and Astronomy, University of Tokyo, 3-8-1 Komaba, Meguro, Tokyo 153-8902, Japan. E-mail: falko@imcs.rutgers.edu; isozaki@ea.c.u-tokyo.ac.jp

On time scales of years to millennia, these reactions are closely coupled to the reverse process of respiration, such that net production of O_2 is virtually nil. That is, without burial of organic matter in rocks, there would be very little free O_2 in the atmosphere. Hence, the evolution of oxygenic photosynthesis was a necessary but not a sufficient condition to oxidize Earth's atmosphere.

Net oxidation of the atmosphere requires long-term storage of the reductants, primarily as organic carbon. The largest reservoir, by far, is Earth's crust. The major mechanism for burial of organic matter is sedimentation and accretion onto cratons (stabilized continents) and, to a lesser extent, subduction deep into the mantle (see the figure). These processes are driven by plate tectonics, in which radiogenic heat in Earth's interior drives mantle convection, allowing continents to collide and separate to form new ocean basins. During these cyclical collisions and separations, oceanic plates are eventually subducted under continents, and a fraction of the organic matter buried in the sediments is tectonically added to the continent, forming coastal mountain belts and thus increasing continental mass. Indeed, unless a large fraction of the organic matter stored in marine sediments is stabilized in cratons, it will be subducted, heated, and in part recharged to the atmosphere via volcanism, where it would become reoxidized (*13*, *14*).

Thus, burial of organic matter, which contains reducing equivalents derived from the biological oxidation of water, implies a net oxidation of the atmosphere. The presence of O_2 in the atmosphere requires an imbalance between oxygenic photosynthesis and aerobic respiration on time scales of millions of years, hence, to generate an oxidized atmosphere, more organic matter must be buried than respired.

How well do we know the concentration of O_2 in Earth's atmosphere over geological time? Perhaps surprisingly, not very well. The major tool for quantitative reconstruction of the oxidation state of the planet is based on isotopic analysis of carbon in carbonates, and to a lesser extent, sulfur in various mineral phases (*3*). Photosynthetic carbon fixation strongly discriminates against $^{13}CO_2$, such that the resulting organic matter is enriched in $^{12}CO_2$ relative to the source (mantle) carbon. In contrast, carbonates, formed by the precipitation of HCO_3^- in seawater with Ca^{2+} and Mg^{2+}, retain the isotopic signal of the source carbon. If photosynthesis exceeds respiration (implying burial of organic carbon), ^{12}C is removed from the mobile pool of carbon in the atmosphere and oceans, leaving a ^{13}C-enriched carbon source for biological and geochemical processes. Thus, the isotopic composition of carbon in carbonates can be used to track the extent to which organic matter was buried and was returned to the mobile pools over geological time (*3*, *15*).

Although the initial oxidation of the atmosphere appears to have occurred about 2.2 billion years ago, atmospheric O_2 concentrations were probably ~1% of the present atmospheric level or less, and the deep ocean was likely still anoxic (*16*, *17*). Large increases in atmospheric O_2 appear to have occurred much later in Earth history, in the late Neoproterozoic (~750 to 550 million years ago) and the Carboniferous (360 to 300 million years ago).

The boost in O_2 inferred in the Neoproterozoic, inferred from carbon isotopic data, corresponds biologically to a rise in ecological prominence of large, single-celled eukaryotic algae (*12*)—that is, phytoplankton—which would have greatly accelerated the burial of organic matter in marine sediments, as well as geophysical controls resulting from mantle cooling and enhanced subduction. Metamorphic rock records through history suggest that heat flow from Earth's interior decreased steadily as the planet gradually cooled, and the geothermal gradient reached a threshold where hydrous (OH-containing) minerals were subducted deeper into the mantle (*18*). This process would have led to a massive transfer of surface water into mantle, potentially accelerating the extensive emergence of continents. This hypothesis is further supported by the historical record of oxygen isotopes (*19*).

The burial of large amounts of organic carbon over the past 750 million years is mirrored in a substantial rise in atmospheric O_2, which may have triggered the Cambrian explosion of animal life (*18*, *20*). Further increases in burial efficiency were accelerated in the Carboniferous (350 to 300 million years ago), as land plants, especially trees, came to double the primary productivity of the planet (*3*). Indeed, models based on the isotopic record of carbon and sulfur suggest that this period of Earth's history witnessed O_2 concentrations as high as ~30% (*3*). A very small fraction of the buried marine and terrestrial carbon was preserved as natural gas, petroleum, and coal. Currently, humans extract these resources at a rate about 1 million times the rate at which they were deposited in the lithosphere.

By the end of the Triassic extinction, O_2 concentrations appear to have been much lower (*21*), perhaps even as low as 10 to 12% (*3*, *4*).

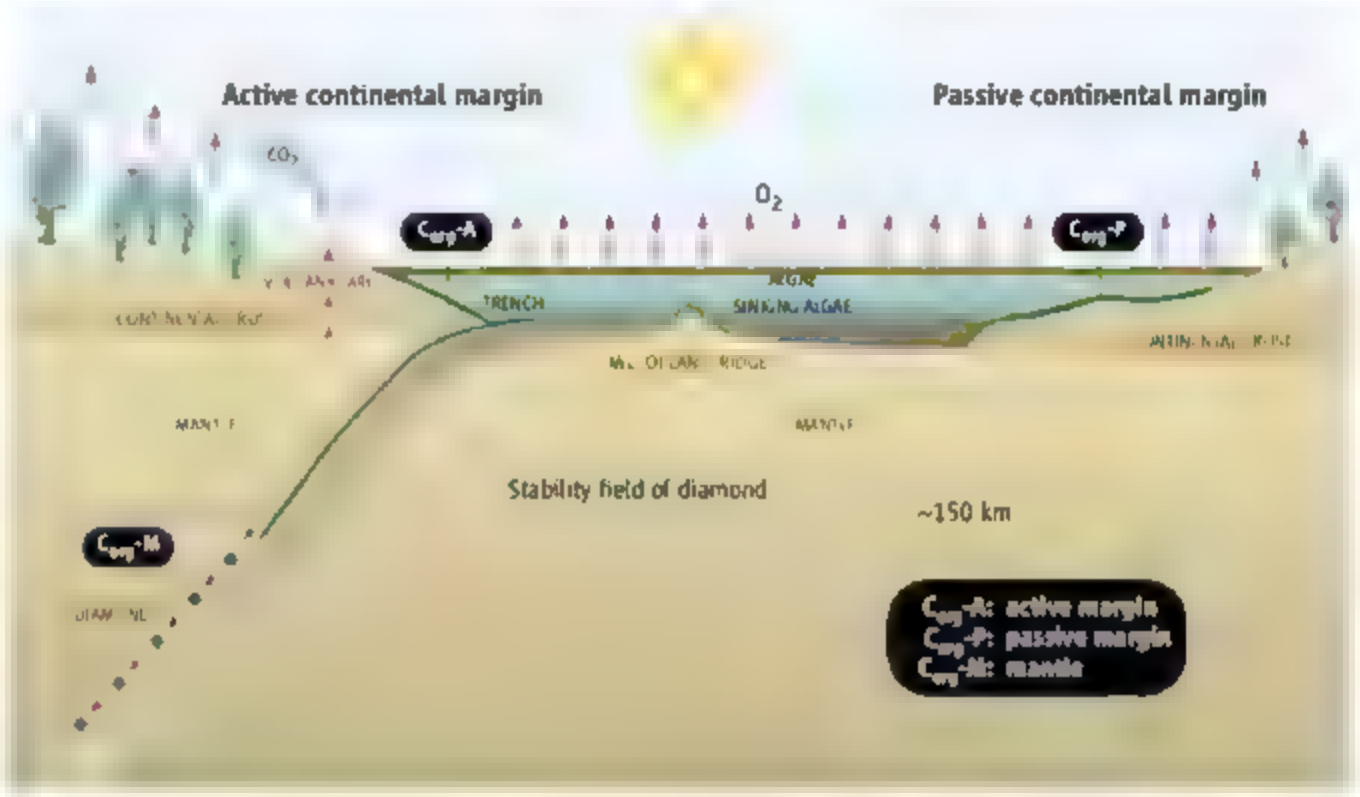

Processes controlling the flux and accumulation of O_2 on Earth. Water is photobiologically split with solar energy by algae in the ocean and plants on land. A very small fraction of the organic matter produced by these organisms is buried in sediments, and ultimately tectonically added to continents and subducted deep into Earth's mantle, thereby permitting O_2 levels to accumulate in the atmosphere. The balance between burial of organic matter and its oxidation appears to have been tightly controlled over the past 500 million years.

CREDIT: ADAPTED BY P. HUEY/SCIENCE

Over the past 200 million years, O_2 concentrations have varied from ~10% at the low end to as much as 23% at the high end (*4*). The relatively narrow range of variability suggests tight controls on the rate of burial and oxidation of organic matter on Earth's surface. Indeed, existing data do not show a long-term nonperiodic increase in ^{13}C in carbonates over the past 2 billion years, implying that the reservoir of inorganic carbon in Earth's mantle is extremely large relative to the fraction of organic carbon buried, and that the burial of organic carbon is roughly balanced by oxidation and weathering.

This brief exploration shows that we understand in broad terms how O_2 came to form a substantial part of Earth's atmosphere, but many details remain sketchy. We still do not understand the mechanism responsible for water splitting in oxygenic photosynthesis, nor do we know what controls the concentration of the gas in our planetary atmosphere (*6*, *13*). The former issue should be resolved within a decade with the aid of high-resolution structures of the photosystems and sophisticated biophysical approaches to measuring electron transfer reactions (*22*). The latter issue will be more difficult to constrain, but a better understanding will emerge from more complete models coupled with better-integrated biogeochemical measurements (*15*).

Each mole of oxygen in Earth's atmosphere required ~450 kJ equivalents of photon energy to produce. Given a concentration of ~4×10^{19} moles of O_2 in the contemporary atmosphere, the reservoir of the gas represents a staggering 2×10^{10} TJ hydrogen bomb equivalents of energy that is replaced every ~4 million years. Nature certainly has provided an incredible source of potential energy for the evolution of life on Earth.

1. R. A. Berner, *Geology* **34**, 413 (2006).
2. R. F. Keeling *et al.*, *Global Biogeochem. Cycles* **7**, 37 (1993).
3. R. A. Berner, *The Phanerozoic Carbon Cycle: CO_2 and O_2* (Oxford Univ. Press, New York, 2004).
4. P. G. Falkowski *et al.*, *Science* **309**, 2202 (2005).
5. D. C. Catling, M. W. Claire, *Earth Planet. Sci. Lett.* **237**, 1 (2005).
6. L. R. Kump, *Nature* **451**, 277 (2008).
7. H. D. Holland, *The Chemical Evolution of the Atmosphere and Oceans* (Princeton Univ. Press, Princeton, NJ, 1984).
8. F. Robert, *Science* **293**, 1056 (2001).
9. S. Mojzsis *et al.*, *Nature* **409**, 178 (2001).
10. J. Kasting, J. Walker, *J. Geophys. Res.* **86**, 1147 (1981).
11. R. E. Blankenship, *Photosyn. Res.* **33**, 91 (1992).
12. P. G. Falkowski, A. H. Knoll, Eds., *Evolution of Primary Producers in the Sea* (Academic Press, San Diego, CA, 2007).
13. P. G. Falkowski, L. Godfrey, *Philos. Trans. R. Soc. London Ser. B* **363**, 2705 (2008).
14. R. Tappert *et al.*, *Geology* **33**, 565 (2005).
15. J. M. Hayes, J. R. Waldbauer, *Philos. Trans. R. Soc. London Ser. B* **361**, 931 (2006).
16. D. E. Canfield, *Nature* **396**, 450 (1998).
17. D. E. Canfield, *Annu. Rev. Earth Planet. Sci.* **33**, 1 (2005).
18. S. Maruyama, J. Liou, *Int. Geol. Rev.* **47**, 775 (2005).
19. J. Jaffres *et al.*, *Earth Sci. Rev.* **83**, 83 (2007).
20. A. H. Knoll, S. B. Carroll, *Science* **284**, 2129 (1999).
21. Y. Isozaki, *Science* **276**, 235 (1997).
22. J. Barber, A. Rutherford, Eds., *Philos. Trans. R. Soc. London Ser. B* **363**, 1125 (2008).

10.1126/science.1162641

MEDICINE

Can We Nip Obesity in Its Vascular Bud?

The origin of fat tissues and identity of factors that direct fat development in animals are becoming more clear.

C. Ronald Kahn

Almost all animal species store energy in the form of fat. The worm *Caenorhabditis elegans* stores fat in intestinal epithelium, and sharks store fat in the liver, but most animal species store fat in white adipose tissue (*1*). In normal-weight adult humans, white adipose tissue represents 10 to 29% of body weight, making fat the largest organ in the body. Moreover, fat mass increases in obesity, and we are in the midst of a worldwide epidemic of obesity. Indeed, two-thirds of the U.S. population and more than 1 billion people worldwide are either overweight or obese. As a result, obesity-related pathologies, such as diabetes, cardiovascular disease, imbalances in lipid metabolism (dyslipidemias), and fatty liver (hepatic steatosis) have surpassed tobacco use as a cause of death. Although we have a detailed understanding of how preadipocytes differentiate into adipocytes (fat cells), very little is known about the origin of preadipocytes. On page 583 in this issue, Tang *et al.* (*2*) show that the precursor cells that give rise to white adipocytes reside within the walls of the blood vessels that supply adipose tissue.

Joslin Diabetes Center, One Joslin Place, Boston, MA 02215, USA. E-mail: c.ronald.kahn@joslin.harvard.edu

Adipose tissue is generally thought to originate from the mesoderm (*1*). In this model, embryonic mesoderm gives rise to mesenchymal stem cells, which in turn give rise to common early precursors or adipoblasts. Under appropriate conditions, adipoblasts develop into committed white and brown preadipocytes and ultimately mature adipocytes (see the figure). However, there are no unique molecular markers expressed by preadipocytes, and thus the exact nature of these precursors, the specific steps in lineage commitment and differentiation, and the factors controlling these pathways are not clear. Tang *et al.* used lineage tracing in mice to show that the precursor cells that give rise to white adipocytes are pericytes, smooth muscle–like cells that cover the endothelial cells of blood vessels. These specialized cells express the proteins peroxisome proliferator-activated receptor γ (PPARγ), stem cell antigen 1 (sca1), and CD34. This cell population also expresses smooth muscle actin (SMA), platelet-derived growth factor receptor–β (PDGFR-β), and neural glial cell 2 (NG2), which are all markers of pericytes, but not perilipin, a marker of mature adipocytes. Previously, the only known marker of preadipocytes was Pref-1 (also known as DLK-1), a cell surface protein in the epidermal growth factor family (*3*). However, Pref-1 is not unique to the preadipocyte and is unsuitable for isolation or tracking of these cells.

The findings of Tang *et al.* support previous work in mice showing that when the stromovascular fraction of adipose is analyzed by flow cytometry (a technique that examines individual cells for physical and molecular characteristics), preadipocytes are enriched in the fraction of cells that express the cell surface protein CD34 but not CD31 (*4*, *5*), and that the vascular supply to fat can be rate limiting in the accumulation of adipose (*6*). Although Tang *et al.* find the PPARγ-expressing cells only in blood vessels that supply adipose tissue, pericytes isolated from other locations have adipogenic, myogenic, osteogenic, and chondrogenic potential (*7*), with the switch between fates controlled in part by developmental signals (such as Wnt) and growth factor signaling.

Multipotent stem cells can also be isolated from adipose stromovascular fraction and

may reside in a perivascular location and express CD34 and smooth muscle actin (*5*). These adipose-derived stem cells can renew themselves for many passages in culture (*8*) and be induced to differentiate into adipose, muscle, bone, cartilage, endothelium, and even neuronal cells, similar to bone marrow–derived mesenchymal stem cells (*9*). Some studies have suggested that the adipocyte precursor is a circulating cell derived from bone marrow, although this is controversial. Both stromovascular fraction–derived stem cells and bone marrow–derived mesenchymal stem cells share some cell surface markers, such as CD105 (*7*), which is not present in the pericytes identified by Tang *et al.* Parenthetically, although most pericytes, adipocytes, myoblasts, and osteoblasts have been suggested to be of mesodermal origin, in all four cases, similar cell types in the head and neck appear to derive from neural crest (which derives from embryonic neuroectoderm) (*10*, *11*).

Despite this major step toward understanding the origins of fat, much remains to be learned. For example, recent studies indicate that the adipocyte population is more dynamic than previously believed. In humans, adipocyte number increases dramatically throughout the first two decades of life and continues to turn over at the rate of about 10% per year throughout adulthood (*12*). Individuals with early-onset obesity develop increased numbers of adipocytes and have increased adipocyte production rates as adults. How this relates to the origin of adipocytes in the vascular wall is unclear. In rodents, obesity can be limited by treatment with agents that block the growth of new blood vessels. However, this is thought to be due to effects on the vascular endothelium and blood supply rather than on pericytes (*6*).

Adipose tissue is also heterogeneous, and how this relates to precursor lineage remains to be defined. White adipose tissue depots in different parts of the body have different developmental timing and different physiological effects. The most striking is the association of visceral adiposity, but not subcutaneous adiposity, with diabetes and other metabolic diseases (*1*). Recent data suggest that this may relate to intrinsic differences in white adipose tissue in different depots. Adipocytes (*13*, *14*) and preadipocytes (*15*) from different white adipose tissue depots express different patterns of developmental genes (such as *Hox*, *Shox*, *Engrailed*, and *Tbx*), which are maintained through multiple generations in culture (*16*). The expression levels of some of these developmental genes are strongly correlated with fat mass and fat distribution (*14*).

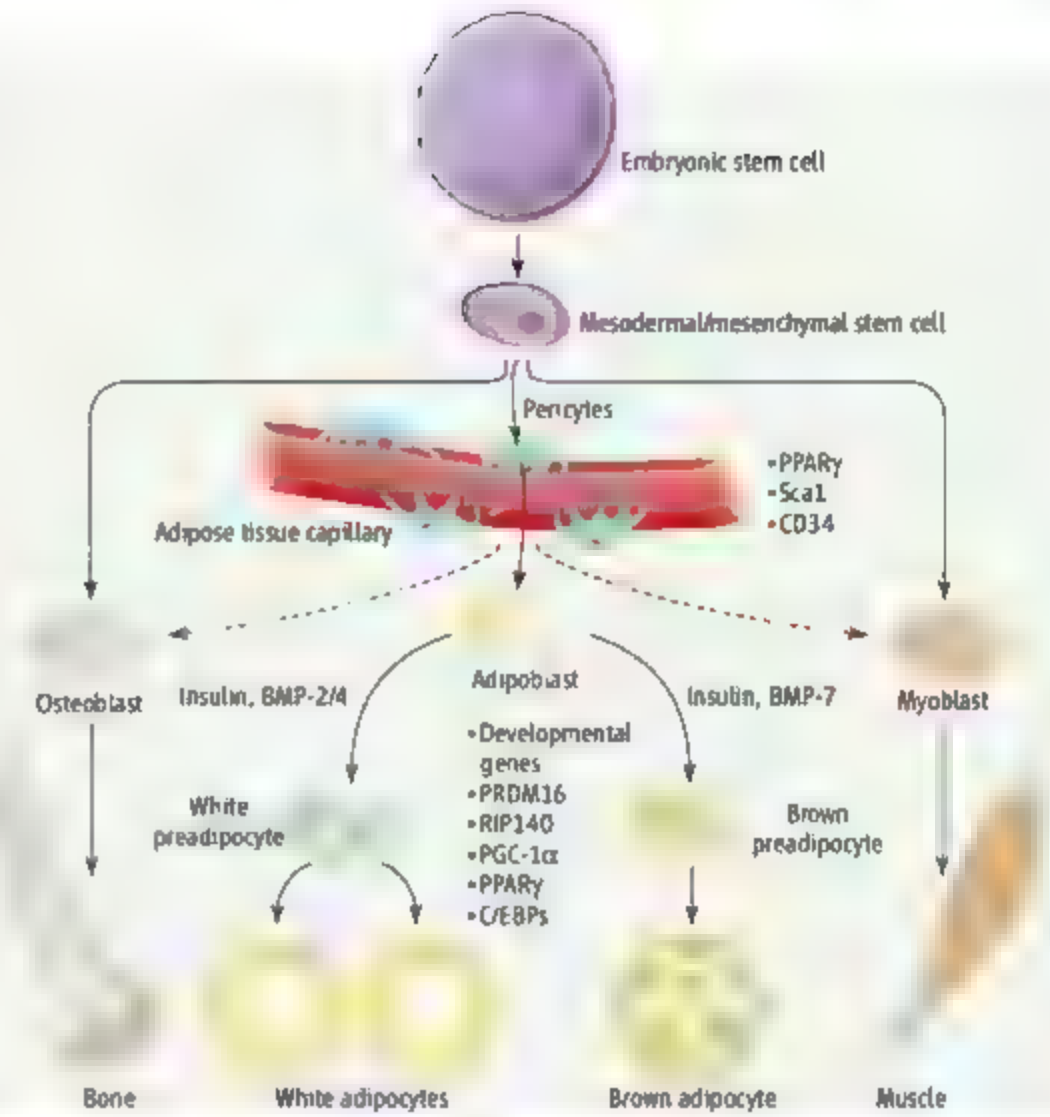

The origins of fat. A hypothetical scheme of adipocyte development is shown. C/EBPs, enhancer binding proteins.

In addition to white fat, mammals possess brown adipose tissue, which is important for basal and inducible energy expenditure in the form of thermogenesis through the unique expression of mitochondrial uncoupling protein–1 (UCP-1) (*17*). Brown adipose tissue also appears to be of mesodermal origin, but the developmental patterns of brown versus white adipose tissue are quite distinct. Thus, cells in the stromovascular fraction isolated from brown adipose tissue differentiate into UCP-1–expressing brown adipocytes, whereas cells in the stromovascular fraction from white adipose tissue do not (*18*). This result is supported by lineage-tracing studies in the mouse with the UCP-1 promoter (*19*). Indeed, brown preadipocytes possess a more "myogenic" gene expression signature (*20*), and recent lineage-tracing studies with Myf5 have suggested a myogenic origin for brown adipose tissue (*21*). Other factors involved in brown versus white adipogenesis include different members of the bone morphogenetic protein (BMP) family of morphogens, the transcriptional repressor receptor interacting protein 140 (RIP140), the transcriptional regulator PPARγ coactivator 1α (PGC-1α), and the zinc finger–containing protein PR domain containing 16 (PRDM16) (*18*, *21*).

We are beginning to define the precursors of adipocytes and understand how adipose tissue can be so varied in its physiological and pathological roles. These insights should provide new approaches to prevention and treatment of obesity and its associated pathologies.

References

1. S. Gesta, Y. H. Tseng, C. R. Kahn, *Cell* **131**, 242 (2007).
2. W. Tang *et al.*, *Science* **322**, 583 (2008).
3. C. M. Smas, H. S. Sul, *Cell* **73**, 725 (1993).
4. C. Sengenes *et al.*, *J. Cell. Physiol.* **205**, 114 (2005).
5. G. Lin *et al.*, *Stem Cells Dev.* 10.1089/scd.2008.0117 (2008).
6. M. A. Rupnick *et al.*, *Proc. Natl. Acad. Sci. U.S.A.* **99**, 10730 (2002).
7. M. Crisan *et al.*, *Cell Stem Cell* **3**, 301 (2008).
8. P. A. Zuk *et al.*, *Mol. Biol. Cell* **13**, 4279 (2002).
9. Y. Jiang *et al.*, *Nature* **418**, 41 (2002).
10. N. Billon *et al.*, *Development* **134**, 2283 (2007).
11. S. M. Müller *et al.*, *J. Immunol.* **180**, 5344 (2008).
12. K. L. Spalding *et al.*, *Nature*, **453**, 783 (2008).
13. M. Cantile, A. Procino, M. D'Armiento, L. Cindolo, C. Cillo, *J. Cell. Physiol.* **194**, 225 (2003).
14. S. Gesta *et al.*, *Proc. Natl. Acad. Sci. U.S.A.* **103**, 6676 (2006).
15. T. Tchkonia *et al.*, *Diabetes* **55**, 2571 (2006).
16. T. Tchkonia *et al.*, *Am. J. Physiol. Endocrinol. Metab.* **292**, E298 (2007).
17. B. Cannon, J. Nedergaard, *Physiol. Rev.* **84**, 277 (2004).
18. Y. H. Tseng *et al.*, *Nature*, **454**, 1000 (2008).
19. K. Moulin *et al.*, *Biochem. J.* **356**, 659 (2001).
20. J. A. Timmons *et al.*, *Proc. Natl. Acad. Sci. U.S.A.* **104**, 4401 (2007).
21. P. Seale *et al.*, *Nature* **454**, 961 (2008).

10.1126/science.1165667

PRESIDENTIAL ADDRESS

A Global Perspective on Science and Technology

David Baltimore

THE UNITED STATES IS A HUGE OCEAN-FLANKED country that, since World War II, has led the world in the development of science and technology. But other countries are now catching up. The American Association for the Advancement of Science (AAAS) has been a support for the development of American science since the 19th century, but as the rest of the world becomes increasingly relevant, it has chosen to expand its purview to become more of an international friend of science. At the 174th annual meeting of the AAAS, we chose to reflect this new perspective.

As president of the AAAS, I was excited to make a global perspective on science and technology the focus of the meeting. I was inspired by Thomas Friedman's powerful book *The World Is Flat* (*1*), in which he suggests there is an increasingly level field for global commerce and competition. The increasingly global reach of *Science* was another impetus for the global theme. But most importantly, the key issues of science and technology today are not limited to the space encompassed by particular political borders. Provision of clean energy in the world is our most pressing problem and one we can only tackle together. Issues of health are international ones, especially in this era of jet travel. Poverty is a problem of some countries, but its effects spread throughout the world. Lack of sufficient clean water has become an international concern, affecting both rural populations and urban ones. And economics, the dismal but all-powerful driver of global wealth creation, highlights the interrelationship of all the world's people.

Science and the Coming Election

Before getting to our theme, I want to make a political aside focused on the United States. We have an imminent presidential election. Science and technology have played at best minor roles in the campaigns. A debate on science was proposed, and some 38,000 people, including scientists, engineers, business leaders, and concerned citizens, signed on to the proposal. The AAAS was a co-sponsor. The candidates' views of science, whether they want to hear its conclusions or want to hide from them, whether they want to have the thinking of our community represented in the White House or relegated to a distant office, whether they will support intensive investigation of alternative energy sources, whether they will liberate the biomedical community to fully investigate the power of stem cell technology, whether they will face the reality that abstinence is not the only way to protect people against HIV transmission, whether they will provide leadership or bury their heads in the sand when tough choices must be made, whether they will leave a better country than the one they inherit; all of these are critical questions with which they should be faced. They have commented on many of these issues in response to questions from the organization Science Debates 2008 (*2*) but refused to debate them.

A key question they should have been asked, which is of particular interest to me, is whether they support an increase in funding for the National Institutes of Health. Barack Obama has indicated that he does, while John McCain has been less specific. It is criminal that at a time when the opportunities in biomedical research outstrip those at any other moment in history, there has been a 13% real decrease in the buying power of the health research budget between 2004 and the 2009 proposal. The current president has presided over this decimation of one of the jewels of American science, a jewel that has spawned the biotechnology industry, the one industry in which America is the unquestioned leader. How can we cede that lead to others by reducing support for the research that made it possible?

A Personal Perspective

Let me first share a bit about my history. As a Jewish boy growing up around New York in the post–World War II era, I lived with the parental expectation that I would become a doctor. In fact, I have always been interested in mammalian biology but, much to the chagrin of my father, although not my mother who was a scientist, I opted not to get an M.D. and have made my career as a Ph.D. Luckily, I received the Nobel Prize when I was still young, so both of my parents were alive to come to Stockholm and witness the event. And they forgave me for not getting an M.D.

My choice to go into research was not only an intellectual one; it was also a matter of having fun. For me, discovery was and remains, fun. As a high-school student, I spent a summer at the Jackson Laboratory in Maine, where senior investigators oversaw us in doing little experiments on the genetics of mice. I worked on three such experiments and although none was particularly important, I learned the pleasure of discovery and never forgot the lesson. In college, I spent a summer at Cold Spring Harbor and again had the thrill of being the first person to see a new piece of data from an experiment I had designed and performed. The joy of a new scientific result returns at each encounter, and it has been over 50 years since my first. That joy can come from someone else's result too, which is why I stopped doing experiments myself some 30

A flatter world. Globalization of resources and technology is leveling the competitive playing fields between industrial and emerging-market countries.

David Baltimore is the Robert Andrews Millikan Professor of Biology at the California Institute of Technology. He served as president of the AAAS from February 2007 to February 2008. This essay is adapted from the Presidential Address he delivered at the AAAS Annual Meeting in Boston on 14 February 2008.

years ago and have been directing others since then. The joy of discovery doesn't even have to come from work in my laboratory; reading a great paper in the literature is a thrill of which I never tire. So, I come to global science topics as a working scientist but a rank amateur when it comes to internationalism. However, I feel deeply that a scientist must go beyond his pleasure in his personal science and take some responsibility for the larger issues of the field.

And so I did a little globetrotting last year. Most memorably, I went to Rwanda and India. The contrast between these countries is striking. One is a tiny country, with 8 million closely packed people; the other is a sprawling nation with a billion people. One is still deeply underdeveloped but emerging sprightly from the unimaginable hell of genocide; the other is an established and vibrant democracy on an economic takeoff platform. What I saw in these two countries led me to believe that liberating the spirit of entrepreneurship is a key to economic development. People are the same around the world; free them and they start expressing their individual creativity. I saw the beginnings of that liberation in Rwanda (see sidebar). There is no doubt that in India, as in China, the liberation is in full swing.

Strengthening Science at Home and Abroad

In beginning a more general consideration of science in the world, I must admit to an apparent contradiction. We as scientists, engineers, and technologists generally believe that our professions know no borders. We read the literature to gain knowledge, independent of where the experiments were done. We travel to meetings all over the world, sharing our knowledge with anyone who wishes to listen. During the Cold War, we met with our Russian colleagues when we could, ignoring the headlines that made them out to be our enemies. The Pugwash movement, honored with the 1995 Nobel Peace Prize, was an embodiment of that world view (*3*). A good idea is a treasure, no matter what mind conceives it. The stronger world science is, the more ideas will bubble up, and the richer will be the brew of ideas and experiments that each of us can draw upon.

That is one side of the picture; the other is that we want our own countries to be strong. As an American, I will present this argument from our point of view, but it is equally applicable to any nationality. Our economic health, our security, our ability to live fulfilling and peaceful lives depend on America maintaining a strong base in science and technology. And America remains strong today. But we see that strength slipping and it worries us. The U.S. National Academy of Sciences embodied these worries in its report *Rising Above the Gathering Storm* (*4*). It is a highly nationalistic document, one that resonated with the science and education communities. It calls for programs to strengthen U.S. science so that we can compete in the newly global economy. By implication, strengthening foreign science would appear

CREDITS: (TOP) TIMOTHY A. CLARY/GETTY IMAGES; (BOTTOM) MICHAEL GOLDWATER/GETTY IMAGES

Cultivating science. For countries such as Rwanda, training in science and technology can help build economies and lift people out of poverty

Challenges and Prospects of Advancing Science and Technology in Africa: The Case of Rwanda

Paul Kagame, President of the Republic of Rwanda

I was delighted to participate in the 2008 Annual Meeting of the American Association for the Advancement of Science and have the opportunity to highlight Africa's and Rwanda's challenges in using the power of science and technology to transform our societies. I believe that all nations must relentlessly build world-class knowledge institutions that create a robust stock of scientists and researchers, foster a dynamic private sector in which industries nurture innovative talents for prosperity creation, and establish professional public services managed by insightful policy-makers who actively promote science and education.

There can be no better inspiration than the United States. What we seek to achieve in Africa and in Rwanda is what is taken for granted in the U.S.: the continuous expansion of knowledge and innovation that lead to even greater prosperity through a triangular relationship between government, business, and academia. This multifaceted relationship is evident in the entire value chain of education from elementary school to tertiary level, and subsequently to the transfer of skills and knowledge in industry and workforce.

How, then, are we in Africa to create an environment that encourages the harnessing of science and education, which in turn permits a more rapid socioeconomic transformation? More specifically, what socioeconomic development choices have we made in Rwanda, and how are we progressing in utilizing education and science to achieve them?

The challenge on our continent is that each of the three players—government, business, and the university—has yet to consolidate their roles into an interdependent relationship that links demand and supply of scientific and technological innovations on a scale needed to transform our societies. This partly explains why Africa remains impoverished and trapped in the trading of raw

Continued on page 547

to be against our interests. Therein lies the apparent contradiction.

Having wrestled with this contradiction in my own mind, I feel that I can resolve it. We need to look at the question from two points of view, each of which is equally valid but which give different perspectives. On the one hand, we want a peaceful world. The tension of economic competition helps to produce that because each country is concerned with its own development in a global context Development promotes stability, optimism, independence, competitiveness, and a belief in the further value of progress. It counters the envy, pessimism, and hopelessness that generate terrorism. If science and technology are wellsprings of economic growth, the stronger the science internationally, the more peaceful will be the world. The other side of the coin is that we as Americans want our country to be particularly strong. We should, as we do, encourage that. We must recognize that we will not have a monopoly on innovation, but we will be able to keep our fair share. So the resolution of the contradiction is that we need to do both keep ourselves strong and encourage others to develop. That will create a world where the tension of competition enriches us all

The Institutional Perspective

Many American scientists are asked to advise countries abroad about how they can build great research institutions. This has been true for years; many of the Indian Institutes of Technology (IITs), which were started back in 1951, benefited from the advice of foreign scientists. IIT Kanpur was advised in the 1960s by faculty from nine U.S. universities: I am proud to say that the California Institute of Technology (Caltech) and Massachusetts Institute of Technology (MIT) were among them. Remember that when you hear about the successes in India today and the many Indian scientists who populate U.S. academic institutions. For instance, InfoSys, the company that convinced Thomas Friedman that the world is flattening, was started by IIT Bombay graduates. Today, getting into an IIT is the dream of well-prepared Indian students, and the world competes for their graduates. When I visited InfoSys recently, I heard that they hire every IIT graduate they can convince to join them, no matter what their major. Then InfoSys trains them for its computer science–based needs. InfoSys competes with IBM and many other national and international companies for a too-small pool of talent. They keep setting up branches within India and now in the rest of the world to satisfy their voracious appetite for people. This success rests on the aid that India received from the world scientific community years ago.

So India, and China, and Saudi Arabia, and many other countries are now in the institution-building mode, and foreign scientists are again in demand as advisors. A former head of the National Academy of Sciences, for instance, is now a key advisor to Saudi Arabia in the building of the King Abdullah University of Science and Technology on the Red Sea—a bold attempt to build a modern institution with significant freedoms in a very repressive society. I too have been called upon for advice and have recently worked with the Indian government on their ambitious program to greatly extend their involvement in the life sciences. The American experience in building its institutions has been a remarkably effective process, and the American community of scientists is the embodiment of that experience—sharing it is both personally satisfying and an important contribution to world stability.

Five Rules for International Science Development

Every developing country has gotten the word that education is key to progress, and as they amass the resources to build, they are building. What I've seen in India and in China is a desire to build rapidly. These countries have the resources and now seem to want instant excellence. I find that very worrisome because building excellence takes time. So I have evolved a set of rules about development that I would like to share.

These rules have been inspired by my own personal history. I built one research institute, the Whitehead, and headed one specialized research university, Rockefeller, and one small comprehensive research university, Caltech. They have in common a characteristic that is central to my thinking: They are small and grow at most marginally. They run counter to the trend in academia to measure success by growth and to solve problems by growing away from them But they have another common characteristic; they are, by anyone's measure, homes for excellence. And they have maintained excellence over decades, in one case for more than a century. Not all institutions in a society need aspire to this level of excellence, but the best ones are the bellwethers of academic life and thus key. The rules I have taken from these experiences are five:

1) In choosing people, demand excellence. Because excellent people are hard to find, this means hiring slowly and deliberately, never letting the desire to fill slots force poor decisions. Another corollary is that in a developing country, with a small base of developed talent, starting many institutions at once could be counterproductive.

2) Concentrate resources. This means favoring one great small enterprise, perhaps at the expense of larger institutions. It is especially relevant today when the cost of doing pioneering research is so large.

3) Create small environments. One might counter my focus on smallness with the reasonable point that today research is increasingly interdisciplinary, giving an advantage to large, comprehensive institutions. However, by creating within large universities smaller, well-resourced centers, it is possible to get the values of both smallness and comprehensiveness. The Whitehead Institute, in its affiliation with MIT, is a good example. Caltech, amazingly, is both small and comprehensive, a notably hard mix to maintain.

4) Build institutions that unify teaching and research. In the United States, we know well that integrating teaching with research benefits both and ensures that there is always a pool of people trained to work at the forefront of their fields. But abroad, this unity is often lacking, imperiling continuity and short-changing students.

5) Ensure academic freedom. In the United States, this means maintaining tenure, a value that I rate more highly than do many others. Without academic freedom, there is a risk of

FIVE RULES FOR INTERNATIONAL SCIENCE DEVELOPMENT

1. Demand excellence
2. Concentrate resources
3. Create small environments
4. Maintain unity of teaching and research
5. Ensure academic freedom

PHOTO CREDIT: SIMON JARRATT/CORBIS

government dictation of the directions of science. Recently, the United States has seen how a government can attempt to suppress uncomfortable scientific knowledge when it dislikes the policy implications. Remember, in most countries of the world, governments control academic and research institutions. I will come back to this point.

Science Around the World

Science fits into different countries in different ways. In the United States and Europe, it is an established part of the culture and a generator of economic progress. In the United States especially, we have built commercial engines of innovation around our science and have a highly developed process for funding that innovation. In China, science is venerated and a rapidly growing enterprise, but it is still immature. In India, it is venerated and has an impressive history that is undergoing a renewal. In Africa, practicing science at almost any level is mainly a dream, but in certain countries, the dream is part of the plans for the future. Small countries aspire to having great science but are unable to produce a critical mass unless they import a significant fraction of their scientists. Israel, strikingly, shows that it is possible to keep the flow of scientists and engineers coming in spite of a small population.

> **"American science, although largely government-funded, is actually a bottom-up entrepreneurial activity."**
>
> —DAVID BALTIMORE, CALIFORNIA INSTITUTE OF TECHNOLOGY

For all the differences of how science is practiced in different places and how it affects different countries, there is one constant. It is that basic science is funded by governments. It may be done in research institutes or in universities, it may be funded through institutions or directly to scientists, but it is a governmental activity because only governments have both the funds to afford it and the desire to support it. Poor countries therefore do little; rich countries can choose. In developing countries, there are limited funds and their investment becomes a matter of values. Private enterprise does a lot of applied science, and its research is often the proximate work that spurs innovation, but I believe that it is basic science that makes the leaps that produce the breakthrough concepts. The funding of basic science through investigator-initiated grants is America's secret weapon.

American science, although largely government-funded, is actually a bottom-up entrepreneurial activity. The institutions of science are largely not governmental—even the state universities are no longer mainly funded by the states. The practitioners are employees of the institutions but they get their funds through individual initiative. Tenure is a wonderful guarantee because it enables each scientist to run an individual program, to decide who to involve, who to collaborate with, how big an operation to run.

In the last few years, I have had occasion to visit many places around the world and have had at least a cursory look at their biological sciences activities. I'll begin with China and India. Together they represent almost 50% of the world's population, so what they do is of overriding importance. They are very different places.

China is a totalitarian country, which we should not forget. They may have a free market of commerce, but science is funded by the government, and the government, including the country's communist party, makes decisions. They decide where to build new universities, how much funding to distribute, where to send funds, and the priority that individual programs should have. The notion of a free market for doing science has not penetrated. There is a place for personal initiative, but the heavy hand of government dominates. They are involved in a huge expansion, but they score poorly on Baltimore's rules of scientific development.

India is a most interesting place. It has a great tradition of science, which was seeded under British rule and was carried forward by Nehru. However, it has fallen into mediocrity, and bright Indians have been traveling abroad, where opportunity is greater. The country is now committing itself to building strength in basic science. It is growing at an apparently sustainable 9% per year, spinning off huge resources for institutional development. India has a few pillars upon which to build: some fine existing institutions; a remarkable knowledge-based industry, mostly in the information technology area, an impressive generic pharmaceutical business; and a government commitment to building strength in education and research through new institutions. They understand quality and want it; whether they can stick to Baltimore's rules will be interesting to watch.

materials and natural resources, thereby transferring the more wealth-creating aspects of a value addition to developed countries. Innovative companies fail to emerge due to the low level of domestic processing. The government's role in promoting education and science both in industry and knowledge institutions remains feeble. Meanwhile, African universities have become almost irrelevant to our socioeconomic development, resulting in perpetual decline and brain drain as capable scientists and professionals leave the continent for better opportunities. The point here, however, is not to lament this condition, but rather to share with you what we are doing about it in Rwanda.

Let me first acknowledge that, in our country, we have neither a dynamic private sector that constitutes a strong demand factor for science and technology, nor strong knowledge institutions to meet such a demand. We do have, however, a developmental vision and a commitment to achieving it. Over the past 7 years, we have been laying the foundation for education and science to play their rightful roles in realizing our goals. As the strongest of the actors in development, Rwanda's public sector will continue to play a leading role for some time, while other pillars gain strength. Our modest progress in building this foundation may be summarized as follows:

First, we believe that "business as usual" in terms of depending on an economy based on raw material exports will merely entrap us into poverty. We must transcend this mindset and practice. With our objective of becoming a middle-income country by the year 2020, we reasoned that not only would we have to modernize our agriculture for value-added exports, but also to enter "nontraditional" economic niches, such as finance, high-end tourism, and the information and communication technologies (ICT) sectors.

Second, we concluded that Rwandans themselves constitute our principal national asset. We therefore had to refocus our education so that it can provide the people with the requisite skills and knowledge to become a viable multifaceted human capital. That is why we have consistently increased our education budget; about 25% of our national budget now goes to formal and nonformal education, constituting the largest single component of Rwanda's annual expenditure.

Continued on page 549

At the same time, we shouldn't underestimate the challenge facing India. Today, only 57% of the 411 million school-age children in India ever enter school. They are experiencing a huge shortfall in trained engineers. For instance, although they graduate many computer scientists, they will need many times that over the next 3 years to fuel projected growth in their information technology–based industry. So they are outsourcing to Mexico, the Philippines, Thailand, and even Europe and the United States. Meanwhile, the rest of the world is still hungrily scanning India's talent pool for those we can entice to move West and feed our own appetite for effective workers in science and technology. What can be flatter than a world where a European company outsources a problem to India, which works it out in Asia, and then sees it applied in the United States?

To add a little color here, I want to tell you about an industry I found in India that I had no idea about. I was recently the guest of an Indian company called TnQ, which is partly housed in a modern building in Chennai. Inside this and their other buildings were 1000 people, mainly Ph.D.'s, sitting in front of computers, editing and preparing for both Web and print publication many of the journals that are "published" in the developed world. In particular, they publish many Elsevier journals, notably those of the Cell Press subsidiary. They printed out for me an article of mine that they had dealt with. I had no idea they were involved, because it can be difficult to know where in cyberspace your e-mails originate. With huge data pipes open to India, and English as their national language, Indians can play some surprising roles in the knowledge industry.

So, India and China are working hard to become competitive, but they both have a long way to go. Developing excellence is a slow, painstaking process. The developed world has a big head start and our job is an easier one, to maintain our established strength rather than building anew. Yes, the world is flatter, but it is still tipped in a Western and Northerly direction, with people sliding down the incline in our direction. Whether it is Indian computer scientists or Chinese biologists or Nigerian nurses, we offer better salaries, better opportunities, better educational environments for their children, and so we are still a huge draw. It will not last forever and we desperately need to provide the education for our citizens that will allow us to staff our own high-tech activities, but right now, as long as we don't scare people off, we are a great draw.

Gaining ground. India is working to build strength in education and basic research, yet struggles to retain its trained scientists and engineers.

CREDIT: BRIAN LEE/CORBIS

Interestingly, while China and India are developing and are often cited as America's most serious competitors, our proximal competition actually comes from Europe. As an example, London is supplanting New York as the world's economic center. All you need do, as I did, is to spend some time in what Londoners call the City, their financial district. It is huge, full of glassy new buildings, and the plaques on the buildings tell the story: The world's commerce is represented here, even such quintessentially U.S. firms as Fidelity and T. Rowe Price. Parag Khanna of the *New York Times* recently analyzed the growth of Europe (*5*). He pointed out how effectively Europe is incorporating the vibrant border countries previously in the Soviet domain. Russia itself, as it shrinks in population and develops economic strength, could end up in the European sphere of influence, although its recent activities indicate that it may attempt to regain its own sphere of influence. Europe is even making inroads in South America. As the United States has allowed itself to become mesmerized by the terrorist threat from the Middle East, and allowed its relations to its historic neighbors and friends to diminish, it has left Europe to unite and become again a world power. Similarly, China is developing influence elsewhere in Asia and in Africa. We run a danger of returning to isolation. One might think of us as muscle-bound, but even our military is looking a bit tattered.

Yes, the world is flattening in the sense that you can do today in Bangalore what you could only do in the developed world 10 years ago. But there are huge differences between India and China and the United States in terms of infrastructure, education, culture, and capital, and these will not go away soon. We in the United States have a platform on which to build our future and secure a strong position in the global world coming in the next decades. We must be conscious of the long-term threat of competition that we face and prepare ourselves to compete. Our military will not be our ticket, and one could argue that it has seduced us into a misapplication of our remarkable resources. When America gained the mantle of being a world superpower, it took on responsibility for the world. We need to spend more time thinking about our responsibility to ourselves, about the need to rebuild our internal infrastructure, our educational system, our scientific prowess. Those will be the elements of the future. The AAAS can play a role, helping to guide the country back on a path that can at once provide internal strength, interna-

Controlled growth. Science is a growing enterprise in China, but government funds and decisions rather than personal initiatives dominate its practice

CREDIT: JUPITER IMAGES

tional morality, and a concern for worldwide development. It will be the tension of economic competition, not the threat of a military strike, that will keep the world stable and peaceful in the future, and we need to focus on the leadership role we can play.

Science in Less Developed Countries

Thus far, our major focus in discussing science has been its role in driving economic development in the developed and developing world. But how about the truly needy countries, the ones where development has yet to make much of a dent? Nongovernmental organizations (NGOs) have generally felt that the needs in these countries are so pressing and so basic that aid should concentrate on their immediate needs, not on high-tech science. But a number of thinkers disagree. At the 2007 AAAS annual meeting, Mohamed Hassan, executive director of the Academy of Sciences for the Developing World, spoke of the role that science, technology, and innovation can play in the development of Africa. I agree with him that the innovation enabled by strong science and technology can catalyze development and that investments there will pay off in the future. He also pointed out that countries that are now more developed and growing (like Brazil, China, India, Malaysia, South Africa, Turkey, and others) are investing in science and technology, creating a multipolar world of science. These are countries with a strong base, positive growth rates, and increasingly replete government coffers. They can afford to build research facilities. But they all had traditions of research and education as well as institutions to build upon. Sometimes these date from their colonial period. The African countries have much less, and even when their colonial masters built universities, periods of ruinous dictatorship and wars left the institutions in a shambles. Many are now trying to rebuild.

There needs to be an emphasis on institution-strengthening in Africa. Africa needs research, but perhaps a greater need is more trained people. People trained in science and technology can contribute in many ways to economic development. And Baltimore's rules apply. Thus, the institutions that are built should combine teaching and research. It is important to start small, concentrating available resources and talent until such time as there are sufficient trained personnel for further expansion. International institutions within Africa would be best, but it may be too much to wish that African countries

Third, we made primary-school education free of tuition fees in 2004, and this policy was extended to the first 3 years of secondary education as of last year. The goal is to enable all Rwandan youth to access basic education. Ninety-six percent of primary-school–age children in Rwanda now have free access to education, a statistic that we are determined to improve, in addition to working harder to improve the quality of our education. It is in this context that the teaching of mathematics and sciences at all levels of our educational system now constitutes a national priority.

Fourth, we have concurrently established and strengthened tertiary education to provide knowledge and skills in areas critical for realizing our socioeconomic development objectives. Institutions for this sector include the Kigali Health Institute, the Kigali Institute of Education, and the Institute of Agriculture and Animal Husbandry, among others. The National University of Rwanda also continues to undergo capacity development, especially in the teaching of science subjects.

Lastly and more directly related to the promotion of science, we have increased our expenditure for this field. Today, 1.6% of our gross domestic product supports this effort. Our target is to increase this to 5% by the year 2012. We have also established a ministry in charge of science and technology, which, in turn, has elaborated a strategy to ensure the achievement of the above efforts.

What are the results so far?

More and more Rwandans are literate, and these trained citizens are contributing to the rise of a more dynamic and nontraditional private sector that is increasingly playing a more substantive role in our economy. For example, tourism has already surpassed tea as one of Rwanda's leading economic subsectors. With more focus on strengthening the different clusters of tourism, we believe this sector will soon become a vital export niche.

But it is the ICT sector, led by mobile telephone technologies, that confirms our belief in pursuing nontraditional economic development pathways. Consider, for instance, the fact that the subscribers of the leading mobile phone company numbered about 320,000 in 2006. This number almost doubled last year to about 613,000, and the number of subscribers is projected to increase to one million by the end of 2008. This company, which is a joint venture

Continued on page 551

share resources to build the best possible universities. It will take significant and sustained foreign aid and assistance from universities of the developed world to build such institutions, but the payoff could be immense

Building science and technology capability is a long-term effort Only in the context of political stability will it work. The NGOs of the world have learned this lesson and are putting an increasing fraction of their aid into countries that are stable, reasonably honest, and intelligently led. This is also where the long-term bets should be made, with the understanding that present stability may not be a guarantee of future stability

Africa is a patchwork of countries in very different circumstances. Some very small countries provide great opportunity, like Paul Kagame's Rwanda. When I visited there earlier this year, I was impressed by the commitment to science and technology as a generator of economic growth even in this very poor country, so recently caught up in its horrific spasm of genocide. They are now building institutions able to train nurses and other medical personnel so that they have the people to deal with AIDS and other medical needs. They are also increasing their university education to train doctors, engineers, and scientists. Although it may take some years for this country to achieve political maturity amidst lingering ethnic tensions, the honest and meritocratic government of President Kagame, supported by investments from abroad, is encouraging. Theirs is a leading-edge experiment, testing the role that science and technology can play in African development.

But huge challenges remain in Africa, where legacies of tribal conflict often undermine attempts to develop institutions. Congo is an example. It is one of the largest countries of Africa but perennially dealing with internal strife South Africa is by far the leading country of Africa and has some impressive universities and even does world-class science But there, the leadership has believed in myths about AIDS, not realities, sadly leaving the country to fight this scourge without high-level support. And the toll has been terrible.

A grand challenge. Combating AIDS and other diseases that disproportionately affect the world's poor demands the best scientific resources available.

The AIDS Vaccine Grand Challenge

Addressing the most pressing scientific and medical challenges facing less developed countries is not something that these nations can do alone. Halting the scourge of AIDS in Africa is a prime example. There is still no AIDS vaccine and no hopeful candidate vaccine. HIV, the cause of AIDS, has evolved to be virtually impossible to attack by antibody, and without antibody sensitivity it is pretty well uncontrollable by the immune system This means that to control HIV immunologically, the scientific community has to beat out nature—to do something that nature, with its advantage of 4 billion years of evolution, has not been able do.

The vaccine community has tried its best. It initially made an attempt to control the virus through antibodies but found that the virus was quite solidly protected against that mode of attack. It then switched to trying the other arm of immune protection, the cellular immune system That has never been mobilized to protect against a virus because it was not thought to be powerful enough. Sure enough, in a full-scale clinical trial the first such candidate vaccine gave no protection. The community is still trying this route of attack because it is one of the few natural hopes we have.

None of this work could have been done anywhere but in the most technologically advanced countries It involves the most sophisticated concepts and techniques of modern science. But even so, it has not worked. Although our lack of success of may be understandable, it is not acceptable. Our only hope may lie in inventing new ways of providing antiviral protection. Four years ago, I proposed such an endeavor to the Grand Challenges in Global Health Initiative (6) of the Bill and Melinda Gates Foundation. Without getting too technical, the strategy was to combine gene therapy, immunologic therapy, and stem cell therapy to stimulate an immunological attack on HIV Now in our third year of this challenge, I can report that it is as difficult as we imagined. We are still in the stage of developing the tools, the systems, and the materials we need to even attempt a serious test of the idea. But one thing is for sure: Only in the most highly developed laboratories with the best-trained people would this endeavor even be conceivable

An AIDS vaccine, a tuberculosis vaccine, and a malaria vaccine are all grand challenges. We need the very best laboratories to undertake them And we need visionary funders like the Gates family to make these efforts possible. Then, of course, if there is even a glimmer of hope, the materials need to be tested in a partnership between the counties that suffer from the diseases and those that have developed candidate vaccines. And we must be certain that the developed materials are affordable by those who most need them

An Admission and a Wish

In concluding this essay, I want to say something very difficult. I don't know if I speak for just myself or for many readers. Since 2001, I have lived a life of denial. I have denied responsibility for the actions of America. I have denied that President Bush speaks for and represents my country. I have held my breath, awaiting new inhabitants of Washington who will again be the moral, thoughtful, balanced people who are the true Americans.

But do I have that right of denial, the right to pretend that American actions are not about me? Mustn't I take some responsibility because our government is a creature of the democracy we cherish? Forced by the president, the Congress this year accepted a budget that does not meet the needs of America but there was no uprising by the people. We accepted the right of the president to starve our scientific enterprise: We can only complain, not change the result. Denial is wonderful. We tell ourselves that we travel as people, not as representatives of our country, when in fact we should travel with our head held low, doing penance for the horrors inflicted by our country at Abu Ghraib, at Guantanamo Bay, and in secret jails in eastern Europe. I am old enough to remember going to Europe in 1960 when we were so proud to be Americans, when we could still bask in the reflected glory of the gift of victory we gave the world in World War II. What a long time it has been.

But I have a hope for the future. I hope that when Jim McCarthy takes the reins as the next AAAS president, he will be able to bring a message of optimism. Optimism that our country is prepared to once again act morally, no matter what the provocation; optimism that we will face up to our responsibility to posterity to seriously deal with global warming; optimism that we will reinvigorate our investment in our future, rising to meet the gathering storm; optimism that the tide of religion-based anti-intellectualism that has gripped our nation is being turned.

Then we can reassert our belief in America once again. We can move from denial to pride. We can hold our heads up high as we travel the world, knowing that our fine democracy has once again produced leadership worthy of our great country.

Is this too much to ask, I wonder.

References and Notes

1. T. L. Friedman, *The World Is Flat* (Farrar, Straus & Giroux, New York, 2005).
2. Science Debate 2008 worked with Scientists and Engineers for America, the AAAS, the National Academies, the Council on Competitiveness, and other organizations to craft the top 14 questions the candidates should answer. Their answers can be found at www.sciencedebate2008.com/index.php?id=42.
3. The 1995 Nobel Peace Prize was jointly awarded to Joseph Rotblat and to the Pugwash Conferences on Science and World Affairs, for their efforts to diminish the part played by nuclear arms in international politics and, in the longer run, to eliminate such arms. Today, the Pugwash mission is to bring scientific insight and reason to bear on threats to human security arising from science and technology, and particularly the threats to humanity posed by nuclear and other weapons of mass destruction (www.pugwash.org/).
4. *Rising Above the Gathering Storm: Energizing and Employing America for a Brighter Economic Future* (National Academy Press, Washington, DC, 2007).
5. P. Khanna, "Waving goodbye to hegemony," *New York Times Magazine* (27 January 2008).
6. The Grand Challenges in Global Health Initiative aims to address the health problems that disproportionately affect the world's poorest people and was built on the assumption that with greater encouragement and funding, contemporary science and technology can remove some of the obstacles to more rapid progress (www.gcgh.org/Pages/default.aspx).

10.1126/science.1166647

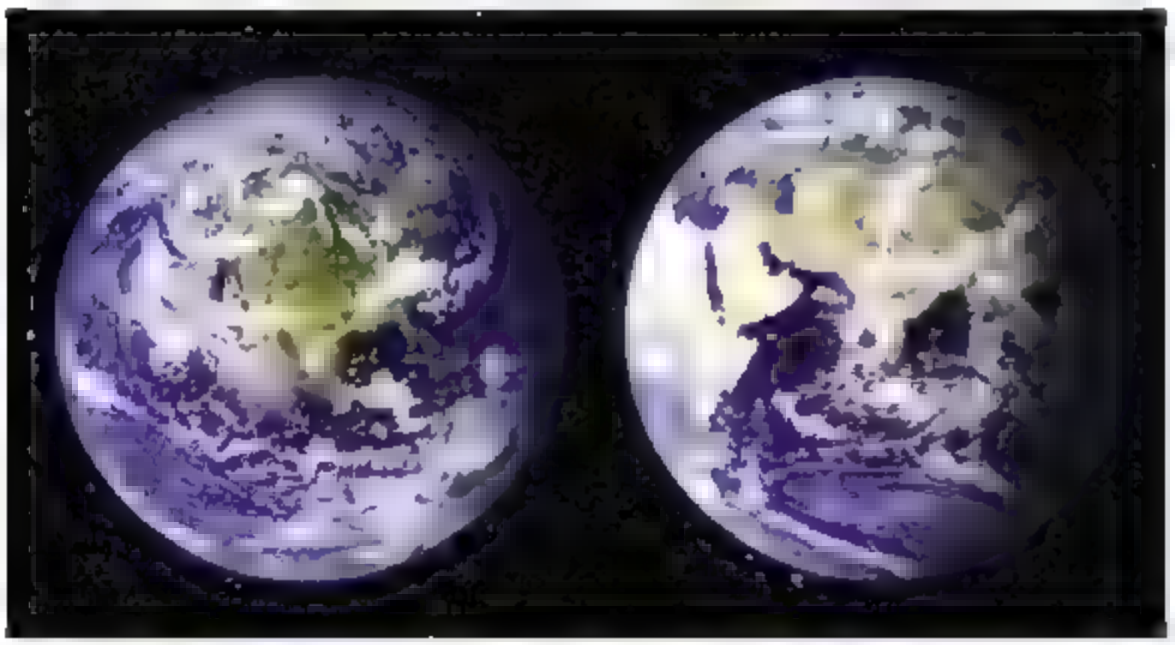

A global perspective. Innovation fueled by a strong science and technology base is as crucial for developing countries as it is for the rest of the world.

between Rwandans and a South African firm, has become the largest taxpayer in our country. And the ICT sector in general has surpassed all other fields to become the leading wealth creator in our country.

The multiplier effects on the rest of Rwanda's private sector have been significant, especially in service industries including advertising agencies, printing companies, public relations, radio stations, and newspaper businesses. We have also recently privatized the national telephone company with the goal of transferring business operations from government to the private sector and to promote innovative foreign investments. In terms of ICT infrastructure expansion, I should note that our global system for mobile communications (GSM) network now covers 82% of Rwanda, while a fiber optic backbone rings our capital city, Kigali. The overall objective is to link all Rwandan towns and districts by the year 2009, which will greatly improve service delivery to rural areas, especially in health and education.

I would like to conclude on the following note. Advancing science in the developing world is vital for creating an engaged, prosperous, healthier, and peaceful world. Africa is no exception, and we Africans must lead the way promoting education, science, and technology to urgently enhance our prospects for improving lives. It is evident that social, economic, and political development processes in Africa remain uneven with occasional setbacks, but we must keep the steady course of using the powerful tools of science and technology.

We have made a good start in Rwanda, but challenges clearly remain. Among them is the human factor. Because we have started from a particularly low base, enabling our universities and tertiary sector to provide capable professionals to power our development process is no easy task. I am certain that AAAS has a role to play in this effort. I have requested the Rwandan minister in charge of science and technology to work with AAAS closely and tap into the American network of scientists and educators to improve our science and teaching institutions. We should strive to make this relationship a two-way endeavor. For example, Rwanda's rich biodiversity could provide American scientists with considerable research opportunities. I look forward to our continued partnership.

Comments delivered at the 2008 AAAS Annual Meeting.

Genetic Compatibility Affects Queen and Worker Caste Determination

Tanja Schwander*† and Laurent Keller

The mechanisms through which a single genotype can give rise to multiple phenotypes are still unknown (*1*). Ants provide an example of phenotypic plasticity, in which females develop into two highly differentiated castes: reproductive queens and functionally sterile workers (*1*). Kin selection theory predicts that the differences between castes stem from environmental effects influencing developmental processes (*2*). We tested whether phenotypic plasticity could also be affected by interactions between parental genomes. We hypothesized that some genetic combinations are more likely to develop into queens, whereas others are more likely to produce workers. If this is true, genetic effects may be maintained over evolutionary time because the fitness of an allele and whether it is associated with the queen or worker phenotype would depend on its genetic background. Although never investigated, genetic compatibility effects may also greatly constrain the evolution and maintenance of plasticity in other polyphenic species. Accordingly, the ability of a given queen to produce workers and new queens should depend on her own genotype and the genotype of the males with which she mates. We examined caste development in the harvester ant *Pogonomyrmex rugosus*, which is characterized by colonies comprising a single, multiply mated queen with discrete periods of queen and worker production.

In colonies with a multiply mated queen, genetic compatibility effects on caste determination should translate into a shift in patriline (i.e., offspring fathered by the different mates of the queen) frequencies over the development from eggs to workers versus eggs to queens. Genetic markers were used to infer egg, worker, and queen paternity in each of five colonies founded by naturally mated queens. As predicted, patriline frequencies were similar for eggs laid during the period of queen production and eggs laid during the period of worker production (five independent G tests: G = 0.15 to 0.89; df = 4 to 7; P = 0.89 to 0.99) but often differed significantly between eggs and workers, eggs and queens, and queens and workers. In each case, significant differences were found in three out of the five colonies (significant differences between new queens and workers found in colonies B20, B22, and B24; G tests G = 12.3 to 14.3, df = 4 to 7, and all $P < 0.05$; between eggs and workers in colonies B20, B75, and B381, G tests G = 9.5 to 14.2, df = 5 to 7, and all $P < 0.05$; and between eggs and queens in colonies B75, B22, and B24; G tests G = 11.9 to 16.3, df = 4 to 6, and all $P < 0.05$).

To directly test for genetic interaction effects on female caste, we conducted controlled crosses in the field (*3*). Because reproduction is monopolized by the mother queen, new queen and male offspring from the same colony are genetically more similar than offspring from different colonies. Hence, genetic compatibility effects would result in an interaction between male and female colony of origin on the caste proportion produced by queens from the controlled crosses, whereas genetic predispositions of certain lineages to forming queens would result in a significant main effect of male and/or female colony of origin. As predicted if there are genetic interaction effects on caste, a two-way analysis of variance revealed no main effect of either the colony of origin of males ($F_{5,19}$ = 0.78, P = 0.58) or females ($F_{5,19}$ = 0.69, P = 0.63) but a significant interaction effect ($F_{19,135}$ = 9.5, $P < 0.001$) between the parental colonies on the proportion of new queens and workers produced (Fig. 1).

Because genetic compatibility effects strongly interfere with phenotypic plasticity, our results support the view that they may select for polyandry (*4*). Compatibility effects could evolve as a consequence of intergenomic conflicts that may generate antagonistic coevolution and genotype-by-genotype interactions (*5*). They are likely to be particularly important in species where selection varies between alternate phenotypes because such variation can further generate ontogenetic conflicts (*6*). Lastly, genetic compatibility effects on caste are likely to be common in social insects and may provide an important step toward the evolution of strong genetic effects on caste and the specialization in the production of specific castes among queens in multiple queen colonies [e.g., (*7*)].

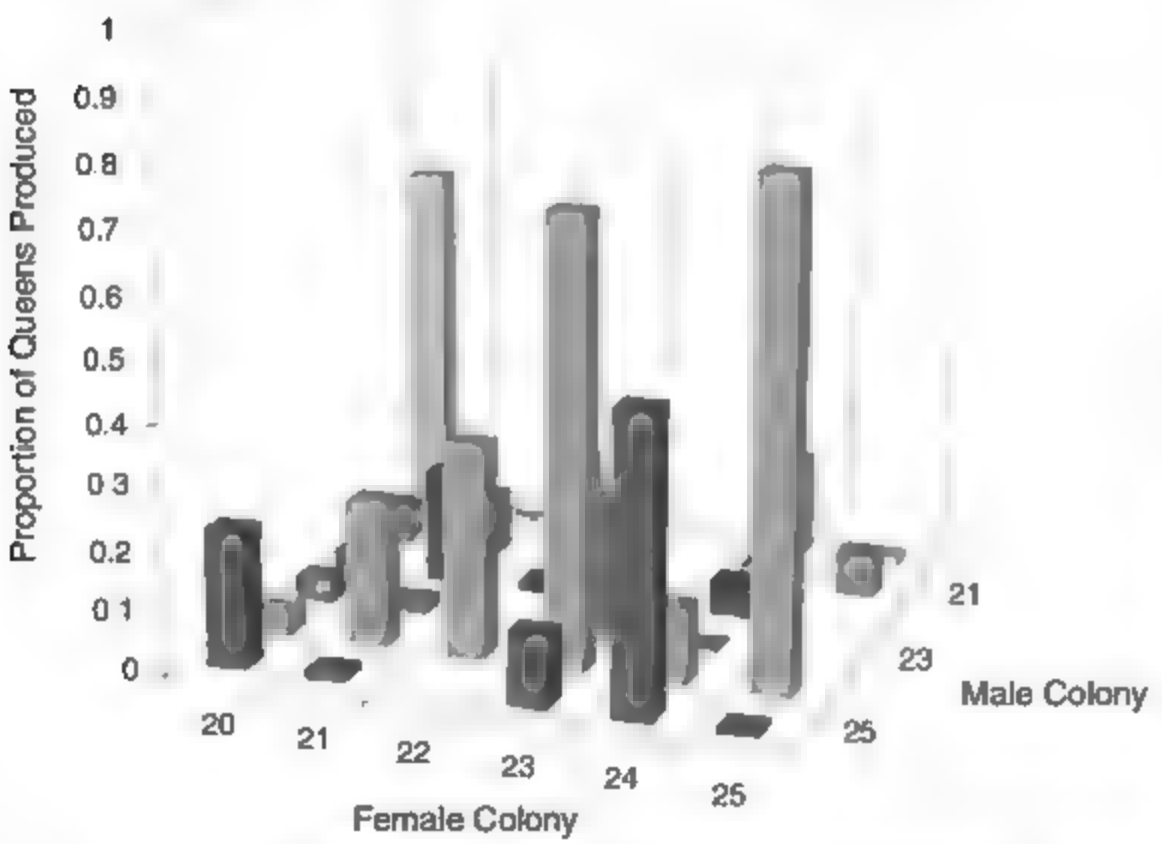

Fig. 1. The proportion of new queens produced by singly mated queens in 30 crosses between pairs of parental colonies is shown to be significantly affected by an interaction of male and female colony of origin (each bar depicts the average for all queens per cross; mean number of queens per cross is 6.2, with a range from 1 to 11).

References and Notes

1. H. F. Nijhout, *Bioscience* **49**, 181 (1999).
2. R. H. Crozier, P. Pamilo, *Evolution of Social Insect Colonies: Sex Allocation and Kin Selection* (Oxford Univ. Press, Oxford, 1996).
3. Materials and methods are available as supporting material on *Science* Online.
4. M. D. Jennions, M. Petrie, *Biol. Rev. Camb. Philos. Soc.* **75**, 21 (2000).
5. W. R. Rice, in *Endless Forms: Species and Speciation*, D. J. Howard, S. H. Berlocher, Eds. (Oxford Univ. Press, Oxford, 1998), pp. 261–270.
6. A. K. Chippindale, J. R. Gibson, W. R. Rice, *Proc. Natl. Acad. Sci. U.S.A.* **98**, 1671 (2001).
7. R. Kümmerli, L. Keller, *Behav. Ecol.* **18**, 375 (2007).
8. We thank C. Campbell for help in the field; F. Dessimoz and C. Ohayon for ant care and laboratory work; B. J. Crespi, P. Christe, M. Chapuisat, and D. Queller for comments; and K. Parker and D. Arbuthnott for help with English. Supported by the Swiss National Science Foundation.

Supporting Online Material

www.sciencemag.org/cgi/content/full/322/5901/552/DC1
Materials and Methods
Table S1
References

1 July 2008; accepted 27 August 2008
10.1126/science.1162590

Department of Ecology and Evolution, University of Lausanne, CH-1015 Lausanne, Switzerland.

*Present address: Department of Biological Sciences, Simon Fraser University, 8888 University Drive, Burnaby, BC V5A 1S6, Canada.

†To whom correspondence should be addressed. E-mail: tanja.schwander@gmail.com

The Structure of a Transcribing T7 RNA Polymerase in Transition from Initiation to Elongation

Kimberly J. Durniak,[1] Scott Bailey,[1,2*] Thomas A. Steitz[1,2,3†]

Structural studies of the T7 bacteriophage DNA-dependent RNA polymerase (T7 RNAP) have shown that the conformation of the amino-terminal domain changes substantially between the initiation and elongation phases of transcription, but how this transition is achieved remains unclear. We report crystal structures of T7 RNAP bound to promoter DNA containing either a 7- or an 8-nucleotide (nt) RNA transcript that illuminate intermediate states along the transition pathway. The amino-terminal domain comprises the C-helix subdomain and the promoter binding domain (PBD), which consists of two segments separated by subdomain H. The structures of the intermediate complex reveal that the PBD and the bound promoter rotate by ~45° upon synthesis of an 8-nt RNA transcript. This allows the promoter contacts to be maintained while the active site is expanded to accommodate a growing heteroduplex. The C-helix subdomain moves modestly toward its elongation conformation, whereas subdomain H remains in its initiation- rather than its elongation-phase location, more than 70 angstroms away.

RNA polymerases (RNAPs) exhibit three phases of transcription—initiation, elongation, and termination. The initiation and elongation phases have been studied extensively in the T7 RNAP system by biochemical and structural approaches [reviewed in (*1*, *2*)]. During the initiation phase, the RNAP binds to a specific promoter DNA sequence, opens the DNA duplex, and feeds the template strand into the active site (*3*, *4*). The structure of a T7 RNAP initiation complex identified a six-helix-bundle subdomain (residues 72 to 150, and 191 to 267)—the promoter binding domain (PBD)—that is responsible for many of the interactions with the 17–base pair (bp) promoter and, in part, for melting the DNA duplex (*3*, *4*) (Fig. 1A). While remaining bound to the promoter, the polymerase undergoes abortive synthesis, producing many short transcripts from 2 to 12 nucleotides (nt) in length (*5*, *6*). After the transition to the elongation phase and release of the promoter, the polymerase proceeds processively down the DNA template, producing a full-length RNA transcript. Comparison of the structures of the T7 RNAP initiation and elongation complexes revealed extensive conformational changes within the N-terminal 267 residues (N-terminal domain) and little change in the rest of the RNAP (Fig. 1B) (*7*, *8*). A rigid body rotation of the PBD as well as the refolding of the C helix (residues 28 to 71) and H (residues 151 to 190) subdomains abolishes the promoter binding site, enlarges the active site, and creates an exit tunnel for the RNA transcript.

The structural changes within the N-terminal domain account for the increased stability and the processivity of the elongation complex, yet provide little insight into how the polymerase accommodates a growing transcript while maintaining its promoter contacts during abortive synthesis. Covalent cross-linking of the template strand to the RNA transcript established that the heteroduplex can be as long as 8 bp (*9*, *10*). Yet, modeling the elongation of the 3-nt RNA transcript observed in the structure of the initiation complex to a 4-nt transcript produced a steric clash with the PBD, and incorporation of an additional nucleoside triphosphate (NTP) destroyed the crystal (*4*). Whereas the enlarged active site observed in the structure of the elongation complex (Fig. 1B) can accommodate a 7- to 8-bp heteroduplex, the new orientation of the PBD abolishes the promoter binding site.

Cross-linking, mutagenesis, and proteolytic digestion experiments suggest the existence of at least one intermediate structure and a transition mechanism that consists of two stages. The first stage allows synthesis of up to 8 nt of RNA with minimal changes to the N-terminal subdomains (*11*–*15*), whereas the second stage is presumed to include the major refolding events that occur during the synthesis of 9 to 14 nt and allow the stable elongation complex to form (*16*). A transition mechanism consisting of two stages has also been proposed for the larger, multisubunit eukaryotic RNAPs (*17*).

Models of the transition from initiation to elongation proposed previously have suggested that the N-terminal domain undergoes a gradual structural rearrangement to accommodate an 8-bp heteroduplex (*7*, *8*). One model proposes a 10 Å translation of the PBD and subdomain H away from the active site (*18*), while another suggests that the PBD can maintain its promoter contacts after rotating into the position observed in the elongation complex (*7*). None of these models are entirely consistent with the biochemical data (*14*, *19*). However, Tang *et al.* recently posited that a rotation of the N-terminal domain could accommodate their fluorescence resonance energy transfer (FRET) data, as well as previous biochemical data (*2*). Although these FRET data predict a 20° rotation, they do not provide the direction of the rotation or which components are rotating.

Here, we have determined the structures of T7 RNAP bound to promoter DNA containing either a 7- or an 8-nt RNA transcript representing complexes that are between the early initiation and the elongation phases.

Structures of intermediate transcription complexes. The structure of a mutant T7 RNAP with promoter DNA and a 7-nt RNA transcript was solved at 3.0 Å resolution (Fig. 1C). Our initial attempts to capture this structure by using wild-type T7 RNAP resulted in structures of complexes with DNA that lacked the added RNA transcript, presumably due to the instability of an intermediate complex relative to an aborted complex. To address this problem, we used a mutant T7 RNAP that produces fewer abortive products and dissociates more slowly than the wild type when stalled at 6 nt of RNA (*13*). The polymerase with a proline-to-leucine point mutation at residue 266 (P266L) was cocrystallized with a 33-bp duplex DNA containing a 17-bp conserved promoter region, a transcription bubble of six noncomplementary bases followed by a 10-bp downstream complementary region, and a 7-nt-long synthetic RNA that was complementary to the template in the bubble region (Fig. 2B). Complexes with smaller RNA transcripts either failed to crystallize or resulted in aborted complexes. The substrate template DNA, nontemplate DNA, and nascent RNA were annealed and then mixed with the P266L mutant polymerase to form the intermediate complex (*20*). The structure was solved by molecular replacement with the protein component of the initiation complex (PDB accession no. 1QLN) as the search model (*4*). An electron density map calculated with $2Fo - Fc$ as coefficients and phases derived from coordinates that did not ever include the nucleic acid is shown in Fig. 2A. The refined model has an R_{factor} of 25.0% (R_{free} of 29.2%). Data collection and refinement statistics are shown in Table 1. We also determined the structure of an initiation complex bound to promoter DNA and an 8-nt RNA transcript at 6.7 Å resolution (supporting online material).

The structure of the polymerase containing the 7-nt RNA exhibits interactions with both the upstream and downstream DNA and has an 11-nt transcription bubble (Fig. 2, A and B). The single-stranded nontemplate strand in the transcription

[1]Department of Molecular Biophysics and Biochemistry, Yale University, 266 Whitney Avenue, New Haven, CT 06520–8114, USA. [2]Howard Hughes Medical Institute, Yale University, 266 Whitney Avenue, New Haven, CT 06520–8114, USA. [3]Department of Chemistry, Yale University, 266 Whitney Avenue, New Haven, CT 06520–8114, USA.

*Present address. Department of Biochemistry and Molecular Biology, Bloomberg School of Public Health, Johns Hopkins University, 615 North Wolfe Street, Baltimore, MD 21205, USA.

†To whom correspondence should be addressed. E-mail: thomas.steitz@yale.edu

bubble makes interactions with the finger and thumb domains similar to those seen in the elongation complex (fig S2, A and B). The RNA backbone of nucleotides 4 and 5 contacts the thumb domain. The 5′ end of the RNA is located toward the specificity loop, and its 3′ end is situated in the active site in a pretranslocated position with the closed fingers domain conformation. The Cα backbones of the palm domains (residues 411 to 552) of the initiation and the intermediate complexes superimpose with a root mean square deviation (RMSD) of 0.40 Å.

Movements of the N-terminal subdomains, specificity loop, and the promoter DNA. The structure of the 7-nt intermediate complex reveals a left-handed 40° rotation of the PBD, the specificity loop, and the bound promoter about an axis passing through residues 198 to 204, consistent with biochemical data indicating that T7 RNAP maintains promoter contacts during abortive synthesis (Fig. 3, A and B). The specificity loop (residues 739 to 769), which is an insertion into the fingers domain, is responsible for making sequence-specific contacts with base pairs in the promoter region (*4*, *9*, *21*). Superimposing the Cα backbone of the PBD and the specificity loop of the initiation complex on that of the intermediate complex gives an RMSD of 2.0 Å, in agreement with a largely rigid body motion of the PBD and the specificity loop. The contacts between the PBD, the specificity loop, and the promoter DNA in the structure of the intermediate complex remain the same as those in the initiation complex, but their rotational movement enlarges the active site to accommodate the 7 nt of elongated RNA. Previous footprinting analyses of the promoter DNA show protection by T7 RNAP during synthesis of up to 9 nt of RNA (*22*). Experiments using ultraviolet-laser cross-linking, mutagenesis of the promoter sequence, or transcription assays in conjunction with a promoter sink challenge indicate that the specificity loop loses its promoter contacts after the synthesis of 8 to 9 nt (*16*, *23*). Furthermore, the PBD rotates by 45° during the transcription of 8 nt of RNA (movie S1), which is consistent with these biochemical data. In the initiation-to-elongation structural change, a loop between the C1 helix (residues 28 to 41) and the C2 helix (residues 46 to 55) refolds to create an elongated C-helix subdomain that is important for elongation complex stability (*14*). Superposition of the polymerase palm domains of the initiation and elongation complexes reveals that the C1 helix does not change its position; rather, the C2 helix stacks onto the C1 helix, thereby lengthening it from 20 to 50 Å (*8*) (Fig. 4A). The C2 helix in the intermediate complex has a structure in between the conformations observed in the initiation and elongation complexes. As the PBD rotates away from the active site during the transition, the loop between the C1 and C2 helices starts to refold as the C2 helix rotates by 40° toward the C1 helix. The C2 helix must rotate by an additional 50° to form the continuous elongated C-helix subdomain observed in the elongation complex. A comparison of all three structures reveals that the refolding of this loop is important for formation of the C-helix subdomain (Fig. 4A). This is consistent with the mutagenesis of residues within this loop to proline, which disrupts the refolding event, increases the accumulation of transcripts 6 to 7 nt long, and prevents the formation of stable elongation complexes (*14*).

Subdomain H is an insertion into the six-helix bundle of the PBD, and the flexible loop connecting these two domains allows the PBD to rotate with minimal changes in the conformation and location of subdomain H. During the initiation phase, subdomain H consists of a loop (residues 165 to 190) and a helix of 14 residues (151 to 164). Although 10 residues within this loop (residues 167 to 177) are disordered in the structure of the intermediate complex, superposition of the initiation and intermediate complexes along the palm domain reveals little movement in the helix of subdomain H during the first part of the transition from initiation to elongation (fig. S3). This is consistent with experiments that show that subdomain H remains sensitive to proteolytic cleavage until a 12-nt transcript is formed and subdomain H takes on the conformation of antiparallel helices in the elongation complex (*8*, *16*).

Role of the P266L mutation. Comparison of the conformations of residue 266 in the structures of the initiation, the intermediate, and the

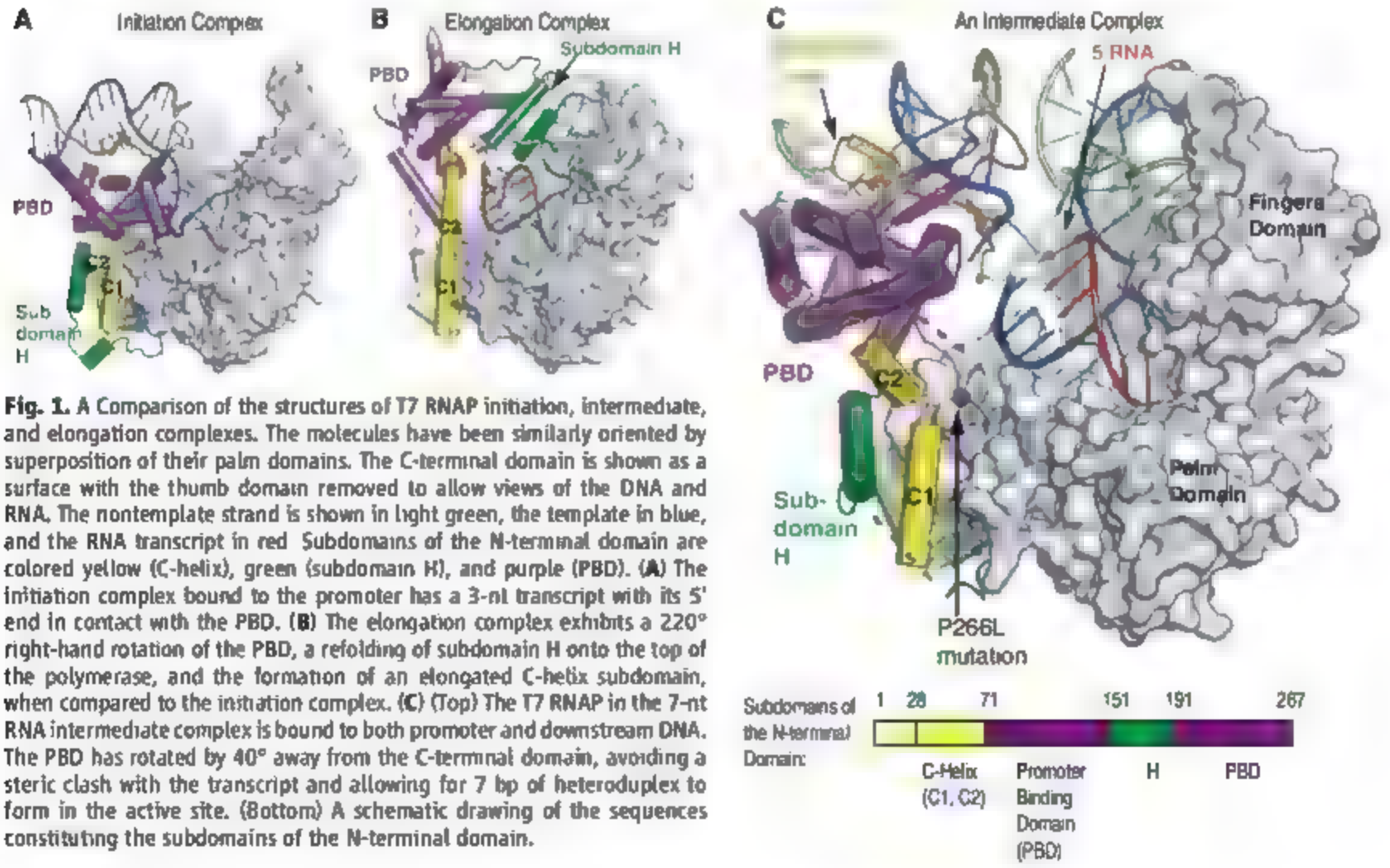

Fig. 1. A Comparison of the structures of T7 RNAP initiation, intermediate, and elongation complexes. The molecules have been similarly oriented by superposition of their palm domains. The C-terminal domain is shown as a surface with the thumb domain removed to allow views of the DNA and RNA. The nontemplate strand is shown in light green, the template in blue, and the RNA transcript in red. Subdomains of the N-terminal domain are colored yellow (C-helix), green (subdomain H), and purple (PBD). (**A**) The initiation complex bound to the promoter has a 3-nt transcript with its 5′ end in contact with the PBD. (**B**) The elongation complex exhibits a 220° right-hand rotation of the PBD, a refolding of subdomain H onto the top of the polymerase, and the formation of an elongated C-helix subdomain, when compared to the initiation complex. (**C**) (Top) The T7 RNAP in the 7-nt RNA intermediate complex is bound to both promoter and downstream DNA. The PBD has rotated by 40° away from the C-terminal domain, avoiding a steric clash with the transcript and allowing for 7 bp of heteroduplex to form in the active site. (Bottom) A schematic drawing of the sequences constituting the subdomains of the N-terminal domain.

elongation complexes reveals that this residue plays a key role during the transition. The P266L mutation is located at the C terminus of the PBD in a loop connecting the N-terminal domain with the C-terminal thumb, palm, and fingers domains (Fig. 1C). A rotation of 180° around the peptide bond between residues 267 and 268 allows the conformational changes in the N-terminal domain to occur without any change in the C-terminal domain (Fig. 4, B and C). A proline at residue 266, though not at the center of rotation, presumably limits the flexibility of the protein near this point because the covalent bond between the Cδ and the backbone nitrogen restricts the peptide backbone ϕ angle of proline to about −70°. However, the weak electron density in this region (residues 258 to 264) precludes a more detailed analysis of the backbone angles of the P266L mutant. Perhaps the mutation allows formation of an intermediate structure that is more energetically favorable relative to the initiation structure than is allowed by the proline. Consistent with this hypothesis, we were unable to produce crystals of this intermediate complex with wild-type T7 RNAP.

Movements within the thumb domain and the downstream DNA. The position of the thumb domain in the intermediate complex is between its position in the initiation complex and in the elongation complexes (Fig. 4D), as is observed with the C2 helix. In the structure of the elongation complex, the thumb domain has moved by 8 Å from its position in the initiation complex, creating a binding cleft for the upstream DNA (*8*). Although the binding cleft has not yet formed in the structure of the intermediate complex, the thumb domain has moved by 4 Å from its position in the initiation complex and makes interactions with the backbone of the nontemplate strand as well as with the RNA chain at residues 4 and 5. These interactions are similar to those seen in the structure of the elongation complex. Thus structure is consistent with mutagenesis experiments indicating the role that the thumb domain plays in stabilizing the transcription complex (*24*, *25*).

The structure of the T7 RNAP intermediate complex shows the polymerase bound to the promoter as well as to downstream DNA. Comparison of the downstream DNA in the structures of the intermediate complex with those of the elongation complexes reveals that the downstream DNA is rotated by 30° toward the N-terminal domain in the intermediate complex (Fig. 5A). The angle between the promoter and the downstream DNA is about 40°, bringing the upstream and downstream duplex DNAs to within 6 Å of each other (Fig. 5B). The differences in the positions of the downstream DNA may be correlated to the positions of subdomain H. A superposition of the Cα backbone of the palm domains of the intermediate and the elongation complexes (PDB accession no. 1MSW) (*8*) reveals that the position of subdomain H in the elongation complex would clash with the position of the downstream DNA in the intermediate complex (Fig. 5C). Perhaps upon refolding into its position on top of the polymerase in the elongation complex, subdomain H is responsible for not only interacting with the nascent RNA chain and the specificity loop (*8*, *26*), but also for moving the downstream DNA into the position observed in the structure of the elongation complex. In our low-resolution structure of the 8-nt intermediate complex, the position of the downstream DNA is different in each of the two copies in the asymmetric unit. The unbiased electron density for the downstream DNA agrees with the position of the downstream DNA seen in the 7-nt intermediate complex in one copy, while in the other copy, the density agrees better with the position seen in the elongation complex. This is consistent with movement of the downstream DNA during the transition from initiation to elongation. The results of FRET (*27*) and chemically tethered nuclease (*28*) experiments that were conducted to determine the relation of the downstream DNA to the fingers domain are consistent with either of the positions observed in the crystal structures.

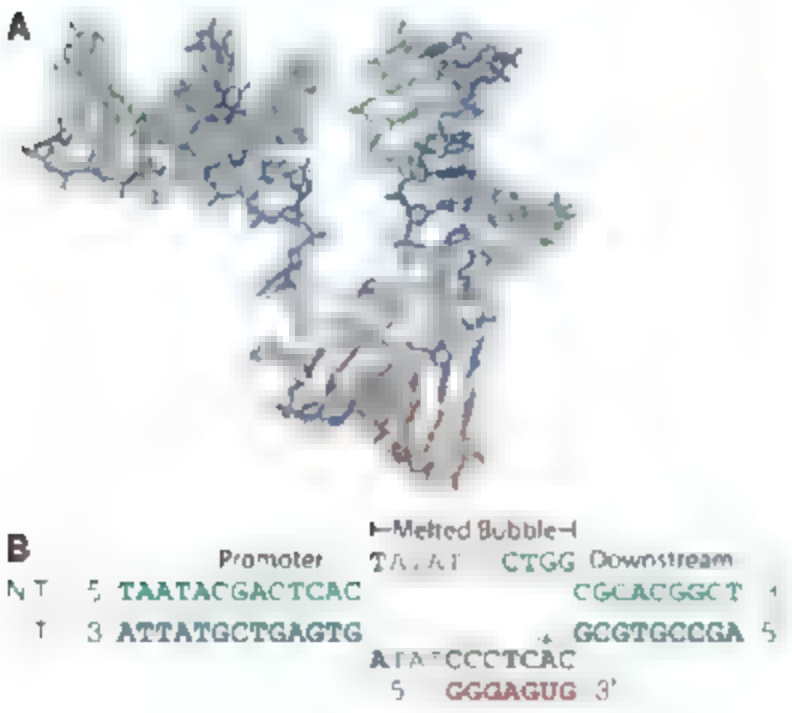

Fig. 2. Nucleic acid substrate. **(A)** A 3 Å resolution electron density omit map of the nucleic acid component of the active site calculated with $2Fo - Fc$ as coefficients and contoured at 1.0σ. A model of the template (blue) and the RNA (red) is superimposed. **(B)** The sequence of the substrate observed in the 7-nt intermediate complex structure. The polymerase has opened an 11-nt transcription bubble, and "+1" marks the transcription start site. Shaded nucleotides are not seen in the electron density map.

Table 1. Crystallographic data and refinement statistics.

Space group	$P6_1$ (7-nt RNA)	$P2_12_12_1$ (8-nt RNA)
Unit cell dimensions (Å)	81.0 by 81.0 by 358.8	99.2 by 180.6 by 198.6
Resolution (Å)	50–2.9	50–6.7
R_{merge}*	8.1 (62.0)	15.2 (60.1)
I/σ*	17.7 (1.6)	7.1 (1.1)
Completeness (%)	93.6 (49.4) (3.0 Å, 88.9)	87.8 (39.7)
Unique reflections	27,490	6,016
Redundancy	6.4 (2.5)	3.5 (1.7)
Copies in AU	1	2
Phasing resolution (Å)	50–3.0	50–6.7
RMSD bond length (Å)	0.006	
RMSD bond angle (°)	1.205	
R_{cryst} (%)	25.0	39.22
R_{free} (%)	29.2	45.42
PDB ID	3E2E	3E3J

*Numbers in parentheses correspond to the highest-resolution shell. †R_{merge} is $\Sigma_i |I_i - \langle I \rangle|$, where I_i is the intensity of an individual reflection and $\langle I \rangle$ is the mean intensity for multiple observations of symmetry-related reflections. ‡I/σ is the mean intensity divided by the SD.

A model for the transition from initiation to elongation. These structures of intermediate complexes resolve the ambiguity in the current models of the transition mechanism (*7*, *8*, *18*). The model proposed by Theis *et al.*, and later supported by FRET data, suggested that the initial step of the transition from initiation to elongation involves a 10 Å translation of the PBD and subdomain H away from the C-terminal active site (*18*, *19*). However, the FRET data also correlate well with these crystal structures of the intermediate complex. The left-handed rotation of the PBD moves the FRET probe on the nontemplate strand ~10 Å from its original position, in agreement with the 10 Å change observed from the FRET data, but achieved through a different mechanism. Our structures also reveal

minimal changes in subdomain H during the initial stage of the transition. The rotation of the C2 helix toward the C1 helix observed in the structure of the 7-nt RNA intermediate complex indicates that formation of the C-helix subdomain is underway before the loss of promoter contacts and is consistent with mutagenesis experiments that disrupt the formation of the C-helix subdomain and result in the accumulation of RNA transcripts of 6 to 7nt in length (*14*). Experimental FRET data have disproved another model that proposed that the PBD would be able to maintain its contacts with the promoter DNA after the conformational changes and refolding of the N-terminal subdomains that occur during the transition from initiation to elongation (*7*, *19*).

Recently, Tang *et al.* (*2*) proposed on the basis of FRET data that the promoter and the N-terminal domain rotate by 20° about an axis passing through the −4 position on the nontemplate strand, during the synthesis of a 3- to 7-nt RNA transcript. However, the direction of the rotation, as well as the specific changes of the individual subdomains of the N-terminal domain during the rotation, was not determined. Our structures show that the synthesis of an 8-nt RNA transcript results in a left-handed rotation of 45° about an axis that passes through the end of a central helix within the middle of the PBD (movie S1) rather than at one end of the PBD (−4NT strand) as proposed from the FRET measurements (Fig. 3).

It is possible that during the initial stages of the transition, additional stable intermediate conformations occur. For example, as the RNA elongates, the PBD may undergo a stepwise rotation to reach the position observed in the structure of the 7-nt intermediate complex (movie S1). Attempts to capture additional intermediates by using shorter RNAs have thus far failed to yield crystals or have resulted in structures without an RNA transcript in the active site. The difference between the 7-nt RNA and a shorter 6-nt RNA could be the lower stability of the shorter heteroduplex, which may shift the equilibrium toward the more stable T7 RNAP initiation state conformation. In addition, the buried surface area (~100 Å^2) between part of the PBD (residues 246 to 266) and part of the C-terminal thumb domain (residues 398 to 403) in the initiation complex (*18*) becomes partially solvent accessible. The energy cost of exposing the hydrophobic surfaces may also contribute to the instability of the intermediate states. The PBD rotates by an additional 5° in the 8-nt intermediate complex compared to the 7-nt intermediate complex, consistent with multiple rotation states and the recent FRET data (*2*) that show an increase in probe distances as the transcript increases in length.

The second stage of the transition, after the RNA is extended beyond 8 nt, involves the loss of promoter contacts and larger structural changes in the specificity loop, the PBD, and subdomain H (*12*, *14*, *15*, *29*). Modeling the longer RNA transcript observed in the structure of the elongation complex onto the intermediate structure shows that an RNA chain extended beyond 8 nt will clash with the specificity loop (Fig. 5D). This is consistent both with mutagenesis (*16*) and cross-linking studies (*9*) that indicate that the specificity loop loses its contacts with the promoter and

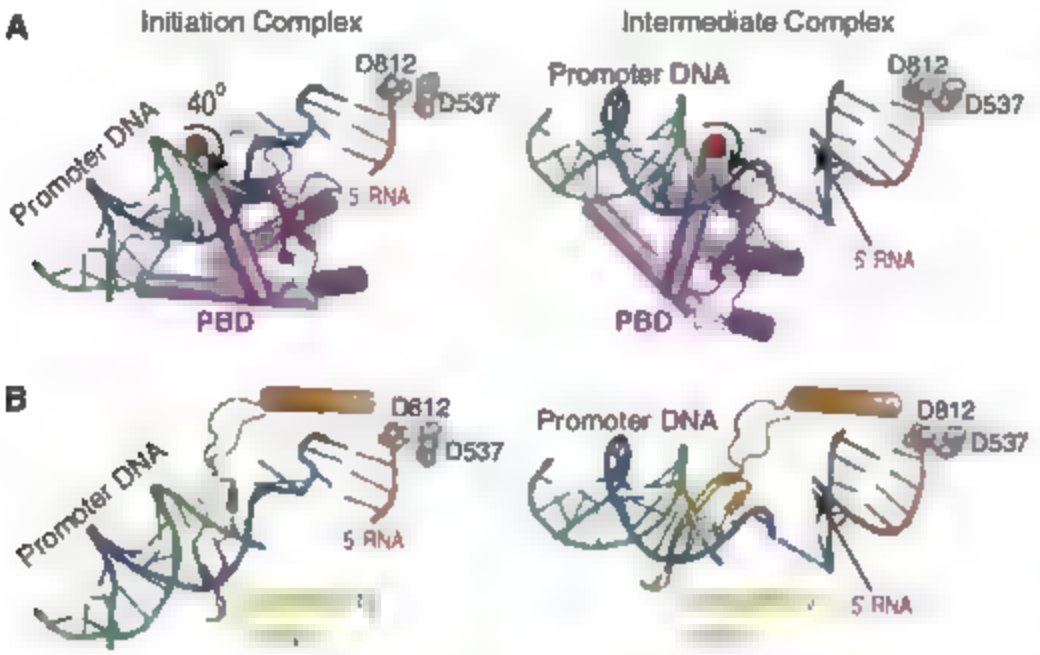

Fig. 3. Promoter and PBD movements during the transition. (**A**) A view looking down onto the promoter bound to the PBD. A 40° rotation of the PBD away from the active site occurs around an axis that passes through a flexible loop of residues 198 to 204. The catalytic aspartic acid residues (D812 and D537) represent the active site. (**B**) The same view as in (A), without the PBD but showing the specificity loop, which also rotates.

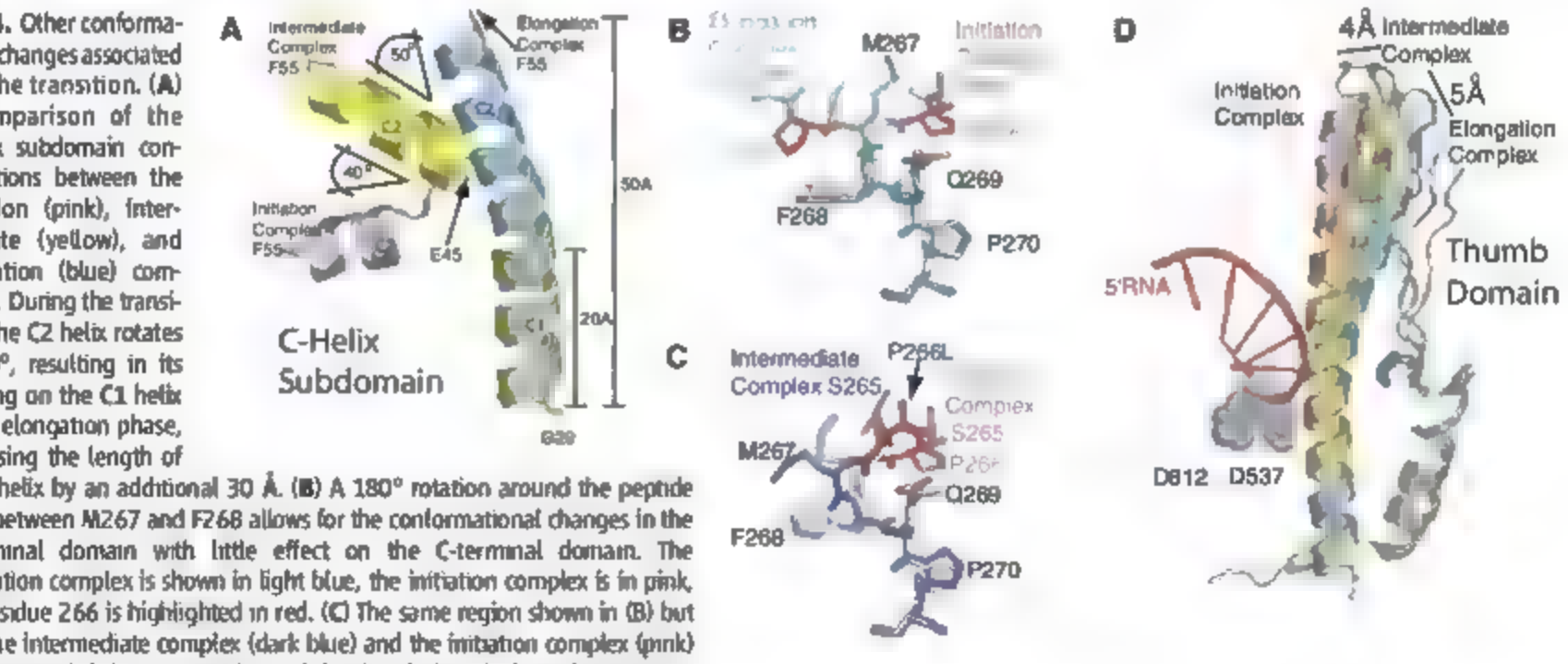

Fig. 4. Other conformational changes associated with the transition. (**A**) A comparison of the C-helix subdomain conformations between the initiation (pink), intermediate (yellow), and elongation (blue) complexes. During the transition, the C2 helix rotates by 90°, resulting in its stacking on the C1 helix in the elongation phase, increasing the length of the C-helix by an additional 30 Å. (**B**) A 180° rotation around the peptide bond between M267 and F268 allows for the conformational changes in the N-terminal domain with little effect on the C-terminal domain. The elongation complex is shown in light blue, the initiation complex is in pink, and residue 266 is highlighted in red. (**C**) The same region shown in (B) but with the intermediate complex (dark blue) and the initiation complex (pink) superimposed. (**D**) A superposition of the thumb domain from the initiation complex (pink), the intermediate complex (pale orange), and elongation complex (blue). The thumb backs away from the active site by 4 Å during the transition and by another 5 Å in the elongation complex, creating a binding cleft for the upstream DNA in the elongation complex. Abbreviations for the amino acid residues are as follows: D, Asp; E, Glu; F, Phe; M, Met; P, Pro; Q, Gln; and S, Ser.

begins to interact with the growing RNA chain upon synthesis of 8 to 9 nt. The PBD must also be released from its contacts with the promoter and rotate into the position it occupies in the elongation phase. During the first stage of the transition that we observe here, the PBD undergoes a left-handed 45° rotation. However, further examination suggests that the PBD can only achieve its final position in the elongation complex through a 260° right-handed rotation, as proposed by Theis *et al.* (*18*). This larger rotation of the PBD is likely to be associated with changes in subdomain H, consistent with mutant T7 RNAPs that suggest that the hinge region between subdomain H and the PBD is important for the transition to the elongation phase (*26*).

Relation to the multisubunit RNA polymerases. The abortive synthesis phase of transcription initiation raises a common problem among the structurally unrelated RNAPs of bacteriophage T7, bacteria, and eukaryotes. How does the polymerase maintain contact with the promoter while accommodating an increase in the size of the elongating heteroduplex and progress down the template DNA? The sequence-specific recognition of the promoter DNA is carried out by the σ factor in *Escherichia coli* RNA polymerase and transcription factor IIB (TFIIB) (with other cofactors) in the eukaryotic RNA polymerase II (*30*–*32*). Structural studies of the three RNAP families have revealed that extension of the RNA transcript requires displacement of a steric block during the transition from initiation to elongation (*4*, *33*–*35*). The steric block is caused by a region of the polymerase or associated protein that is important for promoter recognition—the PBD in T7 RNAP, the σ factor in bacterial RNAP, or TFIIB in eukaryotic RNAP. The intermediate structure of T7 RNAP reveals that as the RNA chain lengthens during abortive synthesis, the obstacle is rotated out of the way, which allows the polymerase to maintain promoter contacts while enlarging the product site. Likewise, the extension of the transcript is proposed to push a domain of the σ protein from the exit tunnel of bacterial RNAP (*35*, *36*), leading to promoter release, and the extension of the heteroduplex by yeast polymerase II must displace TFIIB from the product binding site (*34*).

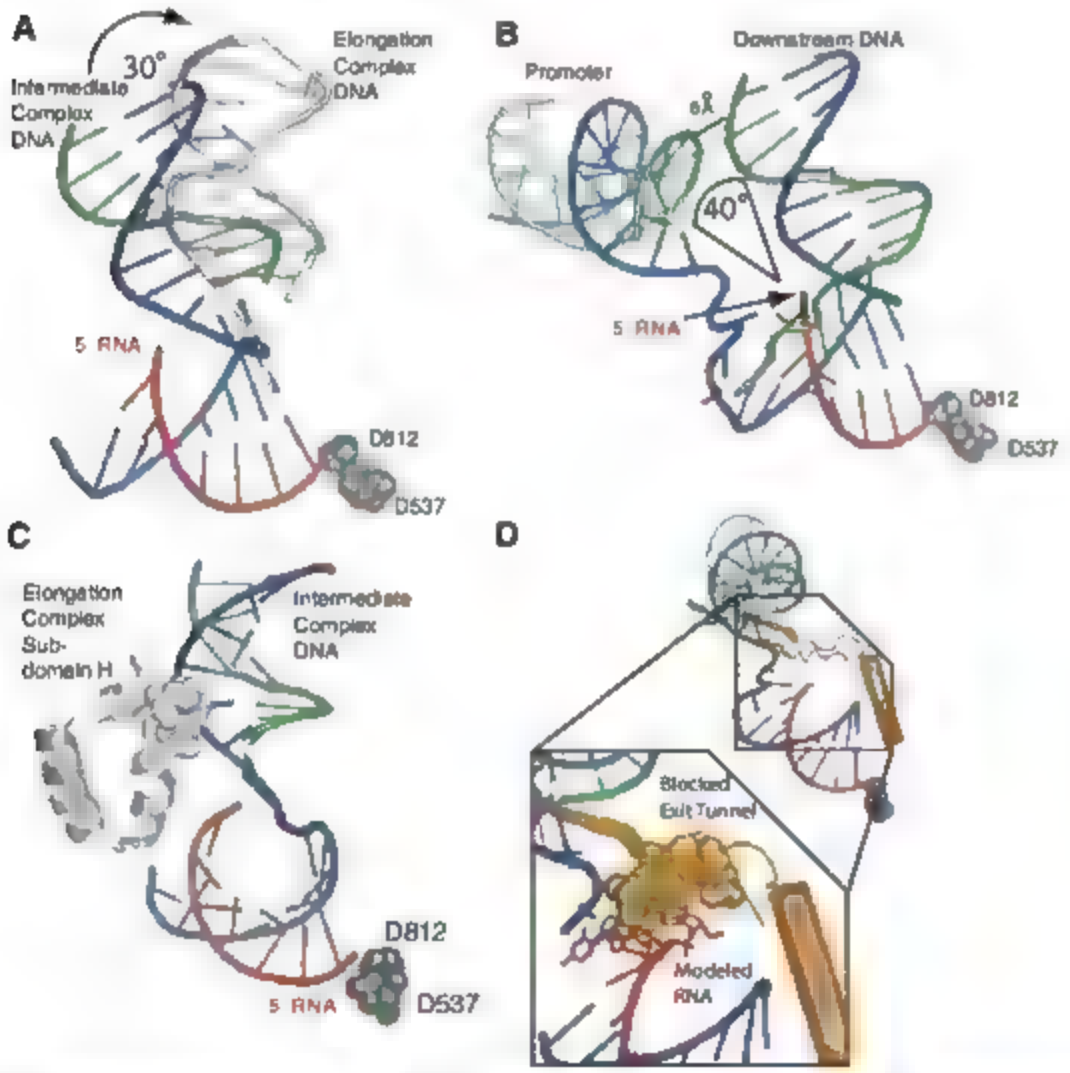

Fig. 5. Arrangement of the downstream DNA. (**A**) The downstream duplex is rotated by 30° toward the N-terminal domain compared to its position in the elongation complex (shown in gray). (**B**) The angle between the upstream and downstream duplex DNA is about 40°, bringing the phosphate backbones within 6 Å of each other. (**C**) The refolded subdomain H from the structure of the elongation complex (gray) creates a clash with the position of the downstream DNA as observed in the intermediate complex. Residues involved in the clash are shown as spheres. (**D**) A close-up view of the 5′ end of the 7-nt RNA reveals that a modeled extension of the RNA by three additional nucleotides would clash with the specificity loop in the position observed in the intermediate complex.

References and Notes

1. T. A. Steitz, *Curr. Opin. Struct. Biol.* **14**, 4 (2004).
2. G. Q. Tang, R. Roy, T. Ha, S. S. Patel, *Mol. Cell* **30**, 567 (2008).
3. R. A. Ikeda, C. C. Richardson, *J. Biol. Chem.* **262**, 3790 (1987).
4. G. M. T. Cheetham, T. A. Steitz, *Science* **286**, 2305 (1999).
5. C. T. Martin, D. K. Muller, J. E. Coleman, *Biochemistry* **27**, 3966 (1988).
6. L. G. Brieba, R. Sousa, *EMBO J.* **20**, 6826 (2001).
7. T. H. Tahirov *et al.*, *Nature* **420**, 43 (2002).
8. Y. W. Yin, T. A. Steitz, *Science* **298**, 1387 (2002).
9. D. Temiakov *et al.*, *Proc. Natl. Acad. Sci. U.S.A.* **97**, 14109 (2000).
10. J. Huang, R. Sousa, *J. Mol. Biol.* **303**, 347 (2000).
11. K. Ma, D. Temiakov, M. Anikin, W. T. McAllister, *Proc Natl. Acad. Sci. U.S.A.* **102**, 17612 (2005).
12. Q. Guo, D. Nayak, L. G. Brieba, R. Sousa, *J. Mol. Biol.* **353**, 256 (2005).
13. J. Guillerez, P. J. Lopez, F. Proux, H. Launay, M. Dreyfus, *Proc. Natl. Acad. Sci. U.S.A.* **102**, 5958 (2005).
14. R. P. Bandwar *et al.*, *J. Biol. Chem.* **282**, 22879 (2007).
15. S. Mukherjee, L. G. Brieba, R. Sousa, *Cell* **110**, 81 (2002).
16. R. P. Bandwar, G. Q. Tang, S. S. Patel, *J. Mol. Biol.* **360**, 466 (2006).
17. M. Pal, D. S. Luse, *Proc. Natl. Acad. Sci. U.S.A.* **100**, 5700 (2003).
18. K. Theis, P. Gong, C. T. Martin, *Biochemistry* **43**, 12709 (2004).
19. R. S. Turingan, K. Theis, C. T. Martin, *Biochemistry* **46**, 6165 (2007).
20. Materials and methods are available as supporting material on *Science* Online.
21. G. M. T. Cheetham, D. Jeruzalmi, T. A. Steitz, *Nature* **399** 80 (1999).
22. R. A. Ikeda, C. C. Richardson, *Proc. Natl. Acad. Sci. U.S.A.* **83**, 3614 (1986).
23. C. Place, J. Oddos, H. Buc, W. T. McAllister, M. Buckle, *Biochemistry* **38**, 4948 (1999).
24. L. G. Brieba, V. Gopal, R. Sousa, *J. Biol. Chem.* **276**, 10306 (2001).
25. P. E. Mentesana, S. T. Chin-Bow, R. Sousa, W. T. McAllister, *J. Mol. Biol.* **302**, 1049 (2000).
26. B. He, M. Rong, R. K. Durbin, W. T. McAllister, *J. Mol. Biol.* **265**, 275 (1997).
27. R. S. Turingan, C. Liu, M. E. Hawkins, C. T. Martin, *Biochemistry* **46**, 1714 (2007).
28. D. Nayak, Q. Guo, R. Sousa, *J. Mol. Biol.* **372**, 490 (2007).
29. K. Ma, D. Temiakov, M. Jiann, M. Anikin, W. T. McAllister *J. Biol. Chem.* **277**, 43206 (2002).
30. D. K. Muller, C. T. Martin, J. E. Coleman, *Biochemistry* **28**, 3306 (1989).
31. K. S. Murakami, S. A. Darst, *Curr. Opin. Struct. Biol.* **13**, 31 (2003).
32. S. Hahn, *Nat. Struct. Mol. Biol.* **11**, 394 (2004).
33. H. T. Chen, S. Hahn, *Cell* **119**, 169 (2004).
34. D. A. Bushnell, K. D. Westover, R. E. Davis, R. D. Kornberg, *Science* **303**, 983 (2004).
35. K. S. Murakami, S. Masuda, S. A. Darst, *Science* **296**, 1280 (2002).
36. D. G. Vassylyev *et al.*, *Nature* **417**, 712 (2002).

37. We thank the staff at the Advanced Photon Source beamline 24-ID and at the National Synchrotron Light Source beamline X25. We also thank T. Jorgensen for help with the supplemental movie and the staff of the Center for Structural Biology core facility at Yale University. This work was supported by NIH grant GM57510 (to T.A.S.). The coordinates have been deposited in the Research Collaboratory for Structural Bioinformatics Protein Data Bank with accession numbers 3E2E and 3E3J for the 7- and 8-nt RNA intermediate complex structures, respectively.

Supporting Online Material

www.sciencemag.org/cgi/content/full/322/5901/553/DC1
Materials and Methods
Figs. S1 to S3
Movie S1

18 July 2008; accepted 19 September 2008
10.1126/science.1163433

CoRoT Measures Solar-Like Oscillations and Granulation in Stars Hotter Than the Sun

Eric Michel,[1]* Annie Baglin,[1] Michel Auvergne,[1] Claude Catala,[1] Reza Samadi,[1] Frédéric Baudin,[2] Thierry Appourchaux,[2] Caroline Barban,[1] Werner W. Weiss,[3] Gabrielle Berthomieu,[4] Patrick Boumier,[2] Marc-Antoine Dupret,[1] Rafael A. Garcia,[5] Malcolm Fridlund,[6] Rafael Garrido,[7] Marie-Jo Goupil,[1] Hans Kjeldsen,[8] Yveline Lebreton,[9] Benoît Mosser,[1] Arlette Grotsch-Noels,[10] Eduardo Janot-Pacheco,[11] Janine Provost,[4] Ian W. Roxburgh,[12,1] Anne Thoul,[10] Thierry Toutain,[13] Didier Tiphène,[1] Sylvaine Turck-Chieze,[5] Sylvie D. Vauclair,[14] Gérard P. Vauclair,[14] Conny Aerts,[15] Georges Alecian,[16] Jérôme Ballot,[17] Stéphane Charpinet,[14] Anne-Marie Hubert,[9] François Lignières,[14] Philippe Mathias,[18] Mario J. P. F. G. Monteiro,[19] Coralie Neiner,[9] Ennio Poretti,[20] José Renan de Medeiros,[21] Ignasi Ribas,[22] Michel L. Rieutord,[14] Teodoro Roca Cortés,[23] Konstanze Zwintz[3]

Oscillations of the Sun have been used to understand its interior structure. The extension of similar studies to more distant stars has raised many difficulties despite the strong efforts of the international community over the past decades. The CoRoT (Convection Rotation and Planetary Transits) satellite, launched in December 2006, has now measured oscillations and the stellar granulation signature in three main sequence stars that are noticeably hotter than the sun. The oscillation amplitudes are about 1.5 times as large as those in the Sun; the stellar granulation is up to three times as high. The stellar amplitudes are about 25% below the theoretic values, providing a measurement of the nonadiabaticity of the process ruling the oscillations in the outer layers of the stars.

The discovery of global oscillations in the Sun (*1*, *2*) opened the way to solar seismology, that is, to sounding the Sun's interior, measuring, for instance, the depth of its convection zone and its rotation at different depths and latitudes (*3*). High-precision photometry from space has long been considered the best way to extend these techniques to other main sequence stars of moderate mass where such oscillations are expected. However, the first attempts were ambiguous (*4*, *5*), casting some doubt on the theoretical estimates of intrinsic amplitudes and questioning to what extent the oscillations might be hidden by stellar granulation. We present here the detection of solar-like oscillations in three stars observed by the CoRoT (Convection Rotation and Planetary Transits) (*6*) space mission, and we characterize their amplitudes and the granulation signature.

Detecting and measuring solar-like oscillations in main sequence stars other than the Sun is challenging. Tracking the variations in the light from a star to one part per million (ppm) requires high accuracy on individual measurements. It also requires long uninterrupted sequences of observations to enhance the statistics of the measurements without being polluted by the spurious frequency components induced by data gaps. Solar-like oscillations have been detected from the ground in radial velocity in several stars (Fig. 1). However, ground-based observations are hampered by diurnal interruptions, weather instabilities, and the annual motion of the Earth. As a result, all existing data sets suffer more or less severely from a limited time base and large gaps in the data, which hamper the measurement of mode characteristics. In addition, radial velocity observations are strongly biased toward low-effective temperature stars (and slow rotators), for they require many narrow spectral lines, and toward subgiant and giant stars, which show oscillations of the same nature as the Sun and other main sequence stars but with larger intrinsic amplitudes. On the other hand, photometric detection of solar-like oscillations has not been possible from the ground because of the higher sensitivity to atmospheric scintillation, and the previous space projects detected only power excess so far [for Procyon and beta Hydri with WIRE (Wide-Field Infrared Explorer) (*7*, *8*) and eta Boo with MOST (Microvariabilité et Oscillations

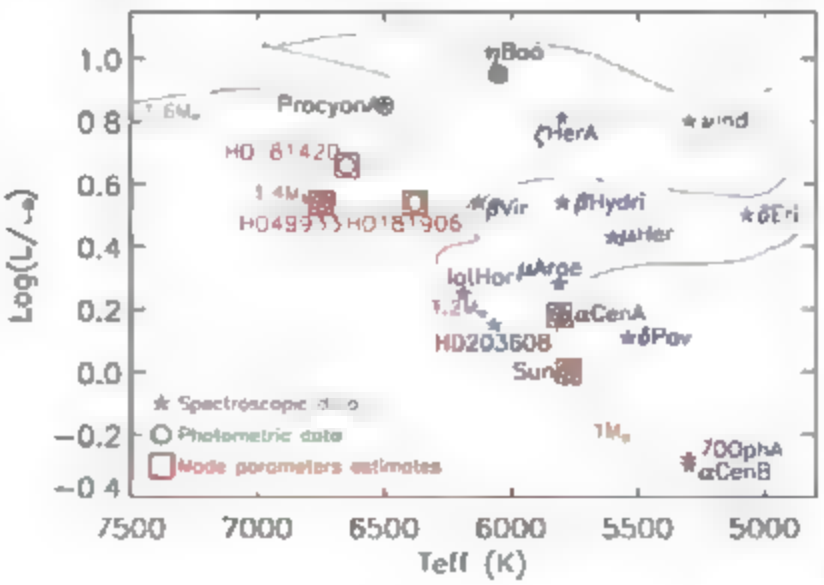

Fig. 1. HR diagram featuring stars for which mode structure has been observed in photometry (red squares), a power excess has been detected in photometry (green circles), and a detection has been performed in radial velocity (blue stars). Stellar evolutionary tracks are taken from (*20*), for solar chemical composition. Red giant pulsators (~6 objects) are out of the upper right corner of the figure.

[1]Laboratoire d'Etudes Spatiales et d'Instrumentation Astrophysique (LESIA), Observatoire de Paris, CNRS (UMR 8109)-Université Paris 6 Pierre et Marie Curie-Université Paris 7 Denis Diderot, Place Jules Janssen, F- 92195 Meudon, France. [2]Institut d'Astrophysique Spatiale (IAS), Université Paris-Sud 11, CNRS (UMR 8617), Bâtiment 121, F-91405 Orsay, France. [3]Institute for Astronomy, University of Vienna, Tuerkenschanzstrasse 17, A-1180 Vienna, Austria. [4]Laboratoire Cassiopée, Observatoire de la Côte d'Azur, CNRS (UMR 6202), BP 4229, F-06304 Nice Cedex 04, France. [5]Laboratoire Astrophysique Interactions Multi-échelles (AIM), Commisariat à l'Energie Atomique/DSM (Direction des Sciences de la Matière)-CNRS Université Paris 7 Denis Diderot, CEA, IRFU (Institut de Recherche sur les Lois Fondamentales de l'Univers), SAp (Service d'Astrophysique), F-91191 Gif-sur-Yvette Cedex, France. [6]Astrophysics Mission Division, Research and Scientific Support Department, European Space Agency (ESA), European Space Research and Technology Center, SCI-SA, Post Office Box 299, Keplerlaan 1 NL-2200AG, Noordwijk, Netherlands. [7]Instituto de Astrofísica de Andalucía (CSIC) C/ Camino Bajo de Huétor, 50 E-18008 Granada, Spain. [8]Danish AsteroSeismology Centre (DASC) Institut for Fysik og Astronomi Aarhus Universitet Bygning 1520, My Munkegade DK-8000 Aarhus C, Denmark. [9]Laboratoire Galaxies, Etoiles, Physique et Instrumentation (GEPI), Observatoire de Paris, CNRS (UMR 8111), Place Jules Janssen, F-92195 Meudon, France. [10]Institut d'Astrophysique et de Géophysique Université de Liège, Allée du 6 Août 17, B-4000 Liège, Belgique. [11]Instituto de Astronomia, Geofísica e Ciencias Atmosfericas, Rua do Matao, 1226/05508-090 Sao Paulo, Brazil. [12]Queen Mary University of London, Mile End Road, London E1 4NS, UK. [13]School of Physics and Astronomy, University of Birmingham, Edgbaston B15 2TT, UK. [14]Laboratoire d'Astrophysique de Toulouse-Tarbes, Université de Toulouse, CNRS (UMR 5572), 14 Avenue Edouard Belin, F-31400 Toulouse, France. [15]Instituut voor Sterrenkunde, Departement Natuurkunde en Sterrenkunde, Katholieke Universiteit Leuven, Celestijnenlaan 200 D, B -3001 Leuven, Belgium. [16]Laboratoire Univers et Theories (LUTH), Observatoire de Paris, CNRS (UMR 8102), Université Paris 7 Denis Diderot, 5 Place Jules Janssen, F-92190 Meudon, France. [17]Max Planck Institut für Astrophysik, Karl-Schwarzschild-Strasse 1, Postfach 1317, D-85741 Garching, Germany. [18]Laboratoire Hippolyte Fizeau, Observatoire de la Côte d'Azur, CNRS (UMR 6525), Université Nice Sophia-Antipolis, Campus Valrose, F-06108 Nice Cedex 2, France. [19]Centro de Astrofisica da Universidade do Porto, Rua das Estrelas, 4150-762 Porto, Portugal. [20]Istituto Nazionale di Astrofisica-Osservatorio Astronomico di Brera Via Emilio Bianchi 46, 23807 Merate (LC), Italy. [21]Departamento de Física, Universidade Federal do Rio Grande do Norte, 59072-970, Natal RN, Brasil. [22]Institut de Ciencies de l'Espai (CSIC-IEEC) Campus UAB Facultat de Ciéncies, Torre C5-parell, 2a pl. 08193 Bellaterra, Spain. [23]Instituto de Astrofísica de Canarias, and Departamento de Astrofísica, Universidad de La Laguna, 38207 La Laguna, Tenerife, Spain.

*To whom correspondence should be addressed. E-mail: Eric.Michel@obspm.fr

Table 1. Parameters obtained in the present analysis, with standard deviation estimates.

Star	A_{bol} (l = 0)(ppm)	B_{bol} (ppm^2/μHz)	C (s)	Δ (μHz)
HD 49933	4.02 ± 0.57	1.97 ± 0.53	1967 ± 431	86 ± 2
HD 181420	3.82 ± 0.40	2.41 ± 0.31	1936 ± 206	77 ± 2
HD 181906	3.26 ± 0.42	1.12 ± 0.20	1650 ± 0276	88 ± 2
Sun PMO6	2.39 ± 0.17	0.85 ± 0.06	1440 ± 86	135 ± 2

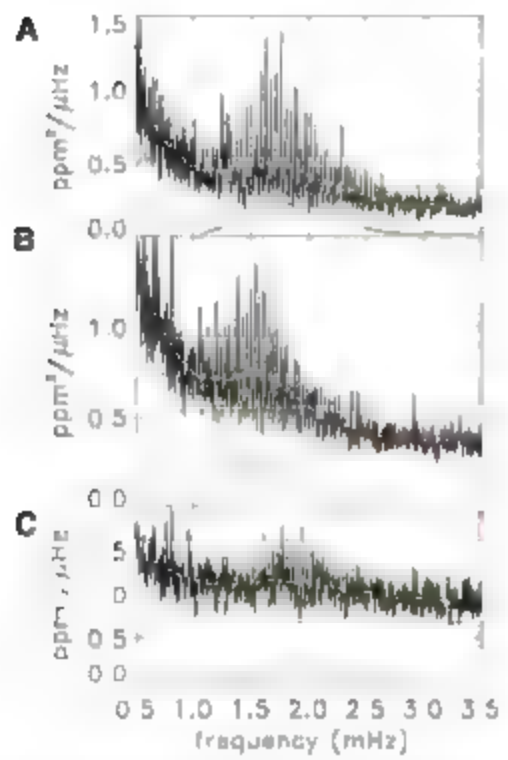

Fig. 2. Instrumental power spectral density. (**A**) For HD49933; a moving mean is applied with a 4-μHz boxcar (black); yellow curve: same spectrum highly smoothed (4 times Δ boxcar); green curve: mean level of the granulation + white noise components; red curve: mean white noise component level alone; blue curve: oscillation mean power density contribution alone. (**B**) Same for HD181420. (**C**) Same for HD181906.

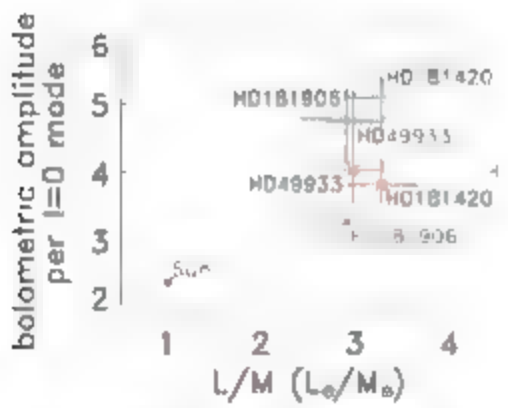

Fig. 3. Maximum bolometric amplitudes per radial mode measured (red) for HD49933, HD181420, HD181906, and for the Sun. Theoretical values are also given (blue). Error bars on amplitudes are standard deviation estimates associated with the accuracy of the measurements (red), and with the error estimate on T_{eff} (blue).

Stellaires) (*9*)]. For alpha Cen A, WIRE (*10*) detected the characteristic comblike pattern of the oscillations, which could be analyzed with the help of complementary velocity data (*11*). However, alpha Cen A is very close to the Sun in terms of its global characteristics. The results here are based on light curves obtained with CoRoT over 60 days for HD49933 and 156 days for HD181420 and HD181906, three main sequence F stars noticeably hotter than the Sun (Fig. 1 and table S1).

The CoRoT satellite was launched on December 2006 in an inertial polar orbit at an altitude of 897 km. The instrument is fed by a 27-cm diameter telescope. During each run, it simultaneously provides light curves (variations in stellar flux with time) from 10 bright stars ($5.5 < m_v < 9.5$) dedicated to seismic studies, while 12,000 fainter stars ($11.5 < m_v < 15.5$) are monitored to search for transits due to planets (*6*). The sampling rate is 1 s for an integration time of 0.794 s. Pointing stability reaches a precision of 0.15" root mean square. The duty cycle was higher than 93%; the missing data correspond essentially to the time spent in the South Atlantic magnetic anomaly where the perturbations due to energetic particles have not, as yet, been effectively corrected. These gaps, about eight per day, from 5 to 15 mn each, have been linearly interpolated (with a 2000-s boxcar on each side of the gap to prevent the introduction of any spurious high frequencies) before we computed the Fourier power spectra, to minimize the aliases of the low-frequency components due to the window. We used synthetic spectra to check that this procedure has no noticeable influence on the measured mean values.

For each of the three stars, the Fourier power density spectra (Fig. 2) show three components that can be understood as (i) a flat white-noise component essentially due to photon counting noise, (ii) a stellar background component (essentially granulation in this frequency domain) following a Lorentzian profile $B/[1+(C\nu)^2]$ as suggested in (*12*), and (iii) the stellar oscillation spectrum with its comblike pattern characterized by the large separation Δ (*13*).

Although dedicated analyses are under way to extract individual mode frequencies and profiles for each star, we measure here the contributions of these three components. We follow the method proposed in (*14*) and illustrated in Fig. 2, and we convert these instrumental values into intrinsic bolometric maximum amplitude per radial mode [$A_{bol}(l = 0)$] and bolometric maximum power spectral density B_{bol} (*15*). We apply the same analysis to the solar SOHO/VIRGO/PMO6 (Solar and Heliospheric Observatory/Variability of Solar Irradiance and Gravity Oscillations) data (*16*). The amplitudes of the three stars are larger than in the Sun by a factor of ~1.5 (Fig. 3).

Theoretical predictions suggest that velocity amplitudes follow a scaling law in $(L/M)^{\alpha}$ with $\alpha \sim 0.7$ (L and M standing for luminosity and mass), in broad agreement with the existing velocity measurements (*17*). In the adiabatic approximation (*18*), this would give photometric amplitudes scaling as $(L/M)^{\alpha}\,(T_{eff})^{1/2}$, where T_{eff} is effective temperature. As shown in Fig. 3 (see also Table 1), the measured values for the three stars are of the same order but significantly lower (by 24 ± 8% globally) than the theoretical values. The measurement of this systematic departure from the adiabatic case, which is not observed in velocity, tells us about the exchange of energy between convection and oscillations in the outer part of the convection zone. This process is responsible for the existence, and the specific amplitudes and lifetimes, of the oscillations. Both radial velocity and photometry measurements are sensitive to the oscillation momentum induced by this energy exchange; the photometric amplitudes are in addition more sensitive to the details of this process, via radiation-matter interaction. These measurements offer the possibility of testing theoretical models of the nonadiabatic effects of the processes governing the oscillations and illustrate the complementary interest of photometry and radial velocity measurements (when they are possible), which probe the oscillations differently.

The spectral signature of granulation is expected to reveal time scales and distance scales characteristic of the convection process in different stars (*12*, *19*). Our data show (fig. S1 and Table 1) that (i) the maximum bolometric power density (B_{bol}), associated with the number of eddies seen at the stellar surface and the border/center contrast of the granules, is higher for the three stars than for the Sun by a factor up to 3; and (ii) the characteristic time scale for granulation (C) associated with the eddy turnover time increases slightly with T_{eff} (up to 30% higher than the Sun).

References and Notes

1. A. Claverie, G. R. Isaak, C. P. McLeod, H. B. van der Raay, T. Roca Cortes, *Nature* **282**, 591 (1979).
2. G. Grec, E. Fossat, M. Pomerantz, *Nature* **288**, 541 (1980).
3. D. Gough, J. W. Leibacher, P. Scherrer, J. Toomre, *Science* **272**, 1281 (1996).
4. J. M. Matthews *et al.*, *Nature* **430**, 51 (2004).
5. D. G. Guenther *et al.*, *Astrophys. J.* **635**, 547 (2005).
6. A. Baglin *et al.*, in *The CoRoT Mission, Pre-Launch Status, Stellar Seismology and Planet Finding*, M. Fridlund, A. Baglin, J. Lochard, L. Conroy, Eds. (ESA SP-1306, ESA Publications Division, Noordwijk, Netherlands, 2006), pp. 33–37.
7. H. Bruntt *et al.*, *Astrophys. J.* **633**, 440 (2005).
8. C. Karoff, H. Bruntt, H. Kjeldsen, T. Bedding, D. L. Buzasi, *Commun. Asteroseismol.* **150**, 147 (2007).
9. D. B. Guenther *et al.*, *Commun. Asteroseismol.* **151**, 5 (2007).
10. J. Schou, D. L. Buzasi, in *Proceedings SOHO 10/GONG 2000 Workshop: Helio- and Asteroseismology at the Dawn of the Millennium*, P. L. Pallé, A. Wilson, Eds. (ESA SP-464, ESA Publications Division, Noordwijk, Netherlands, 2001), pp. 391–394.

11. S. T. Fletcher, W. J. Chaplin, Y. Elsworth, J. Schou, D. Buzasi, in *Proceedings SOHO 18/GONG 2006/HELAS I, Beyond the Spherical Sun*, K. Fletcher, M. Thompson, Eds. (ESA SP-624, ESA Publications Division, Noordwijk, Netherlands, 2006), published on CDROM, p. 27.1.
12. J. W. Harvey, *Proceedings Future Missions in Solar, Heliospheric and Space Plasma Physics*, E. Rolfe, B. Battrick, Eds. (ESA-SP 235, ESA Publications Division, Noordwijk, Netherlands, 1985), pp. 199–208.
13. The large separation (Δ) refers to the first order regular spacing in frequency between consecutive overtone eigenfrequencies, responsible for the characteristic comb-like pattern of the oscillation spectrum.
14. H. Kjeldsen *et al.*, *Astrophys. J.* **635**, 1281 (2005).
15. Materials and methods are available as supporting material on *Science* Online.
16. C. Fröhlich *et al.*, *Sol. Phys.* **170**, 1 (1997).
17. R. Samadi *et al.*, *Astron. Astrophys.* **463**, 297 (2007).
18. H. Kjeldsen, T. R. Bedding, *Astron. Astrophys.* **293**, 87 (1995).
19. F. Baudin, R. Samadi, T. Appourchaux, E. Michel, in *The CoRoT Mission, Pre-Launch Status, Stellar Seismology and Planet Finding*, M. Fridlund, A. Baglin, J. Lochard, L. Conroy, Eds. (ESA SP-1306, ESA Publications Division, Noordwijk, Netherlands, 2006), pp. 403–407.
20. Y. Lebreton, E. Michel, *Astrophys. Space Sci.* **316**, 167 (2008).
21. The CoRoT space mission, launched on December 2006, was developed and is operated by CNES (Centre National d'Etudes Spatiales), with participation of the Science Program of ESA, ESA's RSSD (Research and Scientific Support Department), Austria, Belgium, Brazil, Germany, and Spain. We acknowledge the access to data from the VIRGO instrument aboard SOHO, the mission of international collaboration between ESA and NASA.

Supporting Online Material

www.sciencemag.org/cgi/content/full/322/5901/558/DC1
SOM Text
Fig. S1
Table S1
References

9 July 2008; accepted 10 September 2008
10.1126/science.1163004

A Large Excess in Apparent Solar Oblateness Due to Surface Magnetism

Martin D. Fivian,[1]* Hugh S. Hudson,[1] Robert P. Lin,[1,2] H. Jabran Zahid[1,3]

The shape of the Sun subtly reflects its rotation and internal flows. The surface rotation rate, ~2 kilometers per second at the equator, predicts an oblateness (equator-pole radius difference) of 7.8 milli–arc seconds, or ~0.001%. Observations from the Reuven Ramaty High-Energy Solar Spectroscopic Imager satellite show unexpectedly large flattening, relative to the expectation from surface rotation. This excess is dominated by the quadrupole term and gives a total oblateness of 10.77 ± 0.44 milli–arc seconds. The position of the limb correlates with a sensitive extreme ultraviolet proxy, the 284 angstrom limb brightness. We relate the larger radius values to magnetic elements in the enhanced network and use the correlation to correct for it as a systematic error term in the oblateness measurement. The corrected oblateness of the nonmagnetic Sun is 8.01 ± 0.14 milli–arc seconds, which is near the value expected from rotation.

Motions within the interior of the Sun affect the location of the photosphere, so the precise measurement of the shape of the solar limb is a long-standing astrometric objective (*1*). The shape also relates to Le Verrier's 1859 observation of an anomalous perihelion precession of Mercury (only some 43″ per century), which could be precisely calculated in Einstein's theory of general relativity (*2*). A discrepancy from the predictions of this theory would point to either a need for a new theory or else to a distortion of the Sun's internal gravity not reflected in the surface rotation. The two leading possibilities for such a gravitational field would be a rapidly rotating core left over from the early stages of star formation—perhaps on an oblique axis—or a strong magnetic field (*3*).

The modern era of measurements of the solar oblateness began in the 1960s with Dicke's Princeton Solar Distortion Telescope (*4*) and other ground-based telescopes (*5*–*8*). Dicke's initial results (*4*) implied that the Sun was much more oblate than the surface rotation predicts. More recent observations have tended to show smaller values, closer to the 7.8 milli–arc sec predicted by the surface rotation (*3*), but the uncertainties in the measurements have remained relatively large. The theoretical estimate is difficult because of the differential nature of solar rotation, both in latitude and in radius. The ground-based data also hinted at time variations in the oblateness (*6*). Including the two data points (1997 and 2001) from the Michelson-Doppler Imager (*9*) on board the Solar Heliospheric Ob-

[1]Space Sciences Laboratory, University of California–Berkeley, Berkeley, CA 94720, USA. [2]Physics Department, University of California–Berkeley, Berkeley, CA 94720, USA. [3]Institute for Astronomy, University of Hawaii, Manoa, HI 96822, USA.

*To whom correspondence should be addressed. E-mail: mfivian@ssl.berkeley.edu

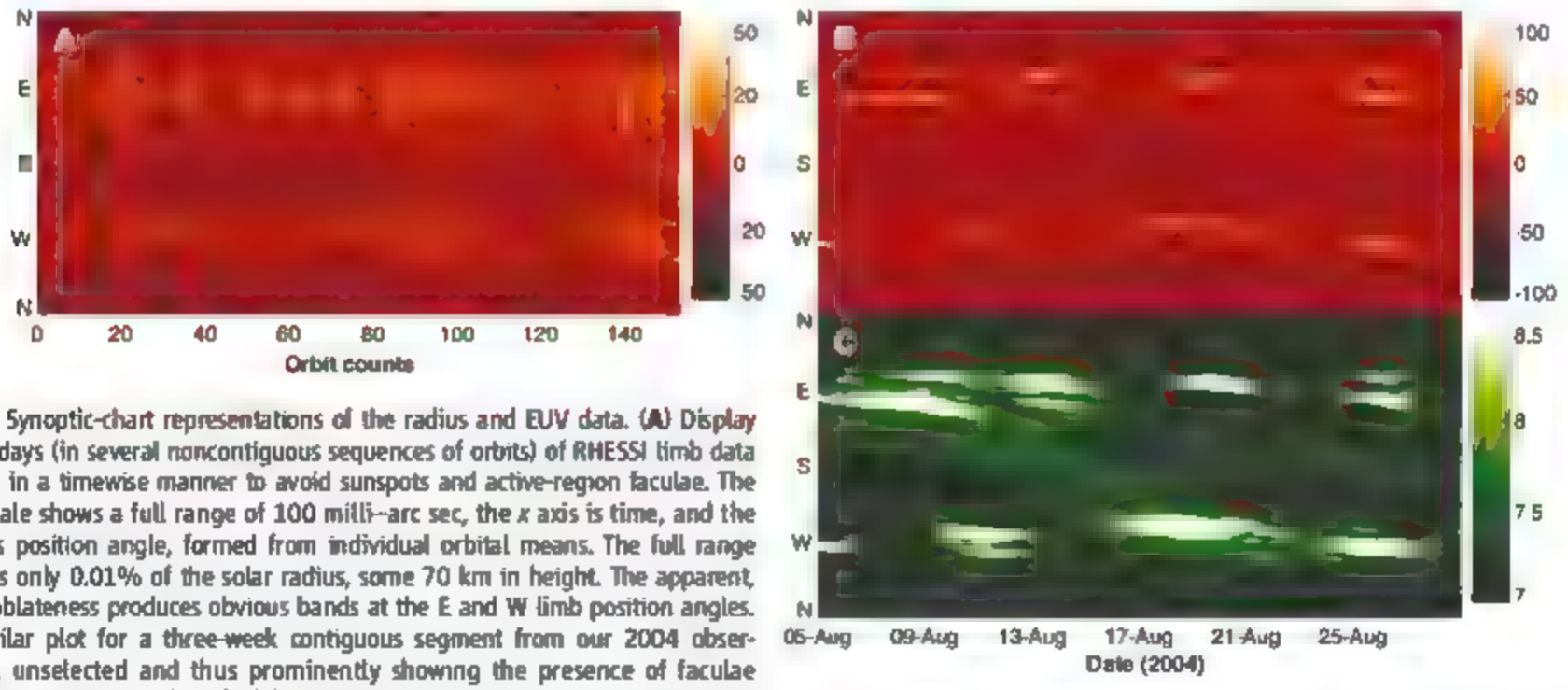

Fig. 1. Synoptic-chart representations of the radius and EUV data. (**A**) Display of ~10 days (in several noncontiguous sequences of orbits) of RHESSI limb data selected in a timewise manner to avoid sunspots and active-region faculae. The color scale shows a full range of 100 milli–arc sec, the *x* axis is time, and the *y* axis is position angle, formed from individual orbital means. The full range shown is only 0.01% of the solar radius, some 70 km in height. The apparent, excess oblateness produces obvious bands at the E and W limb position angles. (**B**) Similar plot for a three-week contiguous segment from our 2004 observations, unselected and thus prominently showing the presence of faculae (bright) and sunspots (dark). (**C**) Corresponding limb data from the SOHO observations in the EUV 284 Å band (*18*), which shows the locations of faculae and other kinds of magnetic activity. The contours of this synoptic map determine the data fraction for our masking analysis, as detailed in the SOM.

servatory (*10*) (SOHO/MDI), the first measurements from a satellite (*11*, *12*) further hunted at a solar-cycle variation. The balloon (*13*) and satellite (*12*) instruments yielded uncertainties on the order of 1 milli–arc sec in the oblateness. We report an order-of-magnitude reduction of these uncertainties from the new Reuven Ramaty High-Energy Solar Spectroscopic Imager (RHESSI) observations.

RHESSI is a solar x-ray/γ-ray observatory, and our astrometric data come serendipitously from its solar aspect sensor (SAS) (*14*, *15*), as described in the supporting online material (SOM). The RHESSI measurement essentially follows Dicke's method of using a rapidly rotating telescope to control systematic errors. The SAS consists of three independent optical systems, each with a simple lens (4-cm diameter) mounted on the front tray of the RHESSI modulation collimators and a linear charge-coupled device (CCD) sensor mounted on the rear tray at a separation of 1.55 m. The 2048-element CCD pixels are 1.73 arc sec square, and the observing wavelength is a 12-nm bandpass at 670 nm. The telemetry provides frequent samples (~16 s^{-1}) of each of the six limb intercepts in nominal pointing conditions, as well as full CCD images at a slower cadence (~1 min^{-1}). Data collection began in early February 2002 and continues to the present time.

We determine solar oblateness (equator-to-pole radius difference) from the axisymmetric quadrupole term of the Fourier components of the limb position given by the RHESSI data. The radius measurements are numerous, telemetered at ~100 samples per second, and are distributed approximately uniformly in azimuth around the limb. For this analysis, we averaged the data in 1°-bins and organized them (Fig. 1) as a function of two variables: (i) position angle (0 to 360° azimuth) and (ii) time. Each vertical line of such a synoptic plot shows the radius data from one RHESSI orbit (orbital period of 96 min). The color scale shows only a limited range of departures from the ephemeris reference value. Sunspots (negative excursions) and active-region faculae (positive excursions) produce obvious effects.

The RHESSI observations are differential measurements of the radius based on a simple fixed-brightness threshold (see SOM). This necessarily results in cross talk between limb po-

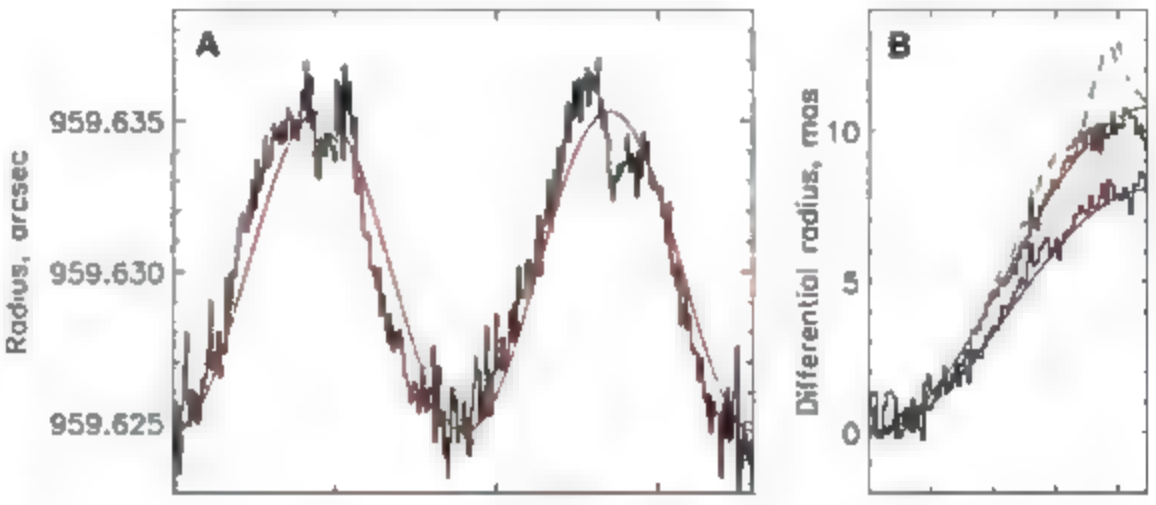

Fig. 2. Variation of apparent radius with position angle (azimuth). (**A**) Mean limb shape for the data set (Fig. 1) obtained from a timewise selection of visually clean orbits (i.e., those with minimal active-region faculae). The red line shows the fit of the axisymmetric quadrupole ($l = 2$) term showing an oblateness of 10.77 ± 0.44 milli–arc sec. Terms for the dipole and small (on the order of 1 milli–arc sec) hexadecapole have been subtracted from the data for clarity. Excesses near position angles 90 (W limb) and 270 (E limb) show the presence of some faculae, even in this "clean" data set. (**B**) Data folded onto one quadrant of position angle (colatitude). The red line shows the same fit as in (A), together with the overlaid data. The blue line shows a theoretical expectation (*3*). Masking against facular and facula-like confusion using the EIT data set (as shown in Fig. 1) results in a shape measurement with excellent agreement with this expectation (data over blue line). The dashed green line shows the whole unselected data set, including the strong facular signal but essentially having the same excess oblateness. mas, milli–arc sec.

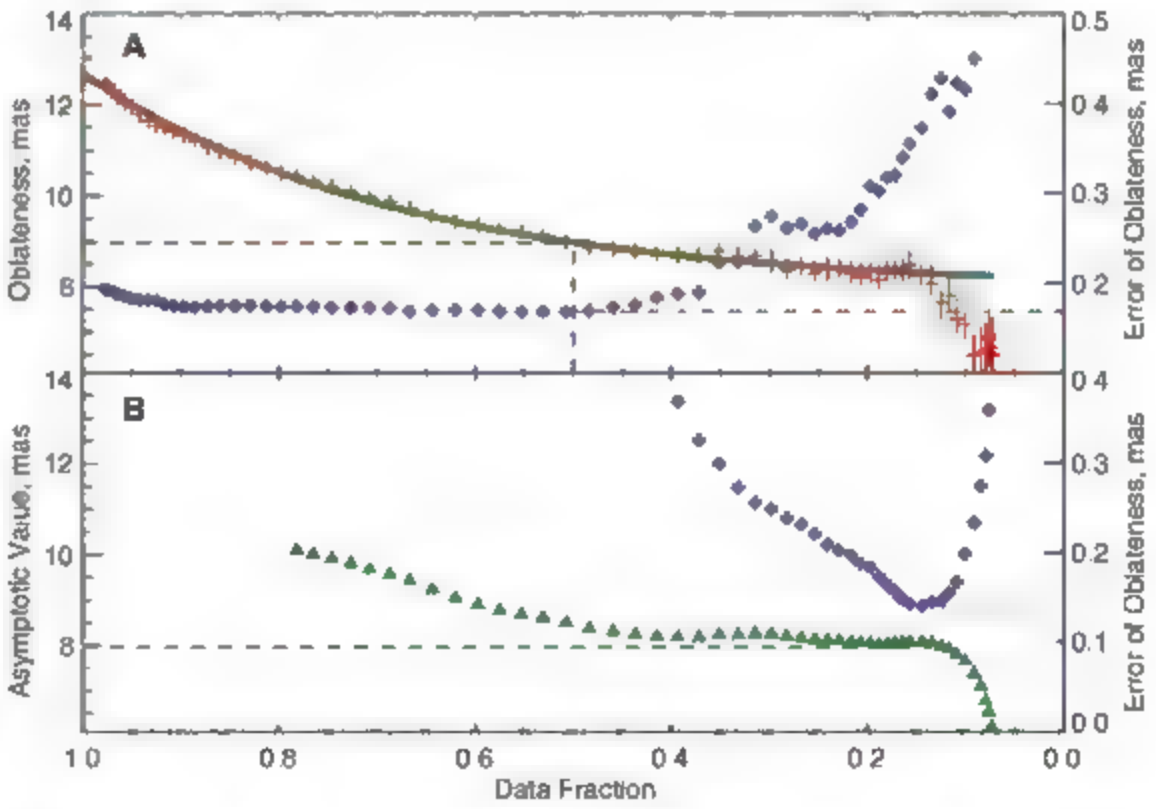

Fig. 3. Derivation of the oblateness measurement of the nonmagnetic Sun. (**A**) Oblateness fit (axisymmetric quadrupole term) as a function of the fraction of data incorporated in the analysis (red crosses), masking the RHESSI data against simultaneous EUV observations as described in the text. The blue diamonds show the orbit-to-orbit statistical errors (right *y* axis); i.e., the magnitudes of the error bars. The vertical dashed line shows the 50% point at which we are confident that the masking has removed faculae and little else. Because of the monotonic decrease of apparent oblateness versus data fraction, this point represents a conservative upper limit on the true oblateness. The horizontal dashed lines indicate its derived value and error of 8.96 ± 0.17 milli–arc sec. (**B**) Asymptotic value of oblateness (green triangles) from simple exponential model fit [green line in (A)]. The asymptotic values are derived by fitting the model up to and including the measurements of oblateness (red crosses) at the same data fraction. Including measurements of oblateness with smaller data fraction improves the determination of the asymptotic value (error from χ^2 minimization shown as blue diamonds, right *y* axis) down to a data fraction of 15%, but it is insensitive to the exact fraction beyond ~40%. The fit [green curve in (A)] and the asymptotic value of 8.01 ± 0.14 milli–arc sec for oblateness are derived by fitting measurements up to and including 15% data fraction, the minimum point of the χ^2 error fit.

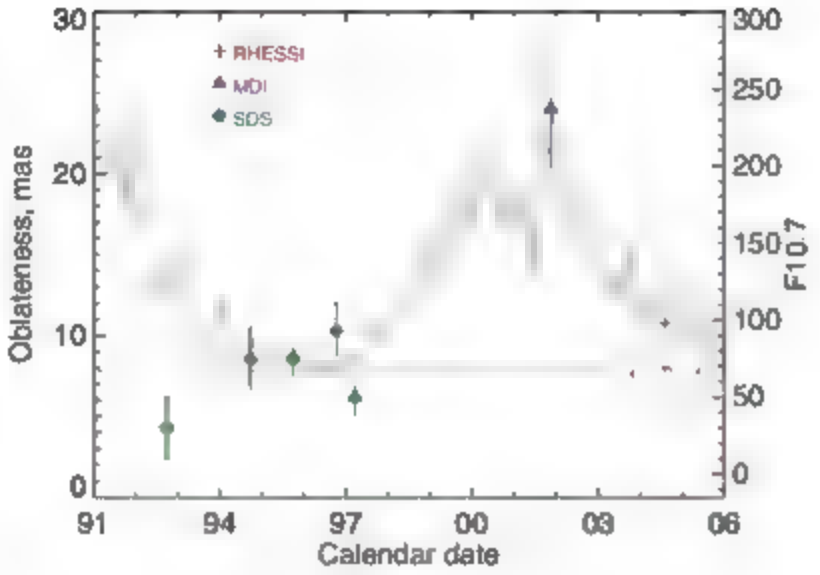

Fig. 4. Comparison of oblateness measurements from space. Here, we compare the RHESSI oblateness measurement, representing data from 29 June to 24 September 2004 (red crosses), with the best earlier values, namely the balloon-borne Solar Disk Sextant (SDS) experiment (green diamonds) (*13*) and the MDI instrument on board SOHO (blue triangles) (*12*). The surface rotation rate predicts the value shown with the dotted line. The histogram (scaled to the uniform-rotation oblateness at solar minimum and to the higher MDI data point) shows the radio flux index F10.7, a good indicator of the solar cycle. All errors are ±1σ.

sition and brightness (Fig. 1B) (*16*, *17*). Because of this cross talk, it is necessary to make a correction (prolate, 0.03 milli–arc sec) for ellipticity dimming as a result of Von Zeipel's theorem (*3*). We make the further strong assumption, discussed in detail in the SOM, that no other global brightness variation presently needs to be considered.

We averaged a synoptic map over time to produce a single shape profile (apparent radius versus position angle) for any particular set of orbits. A data set selected to avoid the obvious active-region faculae (synoptic plot shown in Fig. 1A) yields the limb profile of Fig. 2A. The oblateness (axisymmetric quadrupole) term dominates the shape and is 10.77 ± 0.44 milli–arc sec. This quantity is significantly (>6σ) larger than the prediction from surface rotation (*3*). Our 2004 result also differs significantly from either of the two SOHO/MDI results (*12*). The limb profile shows additional structure in higher-order Fourier components, but the bin-to-bin variation is relatively small.

In Fig. 2B, the red line shows the fit to a data set that does not include obvious active-region signatures. This selection still shows a large excess oblateness. Therefore, the analysis establishes that the active-region faculae do not solely produce the apparent excess oblateness. We need a new source spread around the surface of the Sun, and yet one that is concentrated into a predominantly axisymmetric quadrupole (apparent oblateness) component. Because of previous suggestions of a solar-cycle dependence, the sense of this discrepancy (an excess), and the appearance of the synoptic plots, processes related to solar magnetic activity are likely to be a direct cause.

We have made use of sensitive proxy data that show magnetic activity at the limb. The extreme ultraviolet (EUV) limb brightness (284 Å) from the EUV Imaging Telescope (*18*) on SOHO (SOHO/EIT) images correlates linearly with the RHESSI apparent radius (see SOM). We used this relation as a basis for data rejection to reduce the confusion with magnetic effects.

Corresponding to the threshold in the EUV data, the oblateness term decreases as more data are removed. Initially, there is a rapid decrease as the active regions are screened out and then a slower decrease as weaker facula-like regions are excluded. The oblateness as a function of data fraction inferred by this procedure has a plateau (Fig. 3A) and therefore gives us a robust measure of the oblateness in the absence of magnetic features. We also fit this monotonic decrease with an ad hoc exponential function (green line in Fig. 3) and take its asymptotic limit as a measure of the oblateness. We also find a stable limit for the asymptotic value as a function of data fraction and estimate its uncertainty by a weighted χ^2 minimization. The oblateness is 8.01 ± 0.14 milli–arc sec for a nonmagnetic Sun. This value is consistent within errors and model uncertainties of the prediction (*3*). The error estimate 0.14 milli–arc sec is smaller than those of previous observations. This error estimate (minimum of the diamonds in Fig. 3B) is consistent with the orbit-to-orbit scatter.

There are three distinct patterns in the limb profiles (Fig. 2B). The green dashed line shows the profile of the entire data set, and the active-region faculae appear prominently. If we reject the obvious faculae on an orbit-by-orbit basis (as shown in Fig. 1A), we obtain the data fit by the red line. This shows an excess oblateness, Δr, above that predicted by the surface rotation, Δr_{surf}, as described above. The blue line in Fig. 2B, based on our screening against EUV limb brightness, does not show the excess oblateness component and agrees with the oblateness expected from the surface rotation ($\Delta r_{surf} \approx 7.8$ milli–arc sec). We interpret the excess oblateness (red line) as the counterpart of the active network component of total irradiance variation (*19*, *20*), which is associated on a longer time scale with the redistribution of active-region magnetic flux to higher latitudes.

The oblateness measurements from space, prior to and including our RHESSI result, suggest variability (*6*, *12*), in spite of the large uncertainties (Fig. 4). Together the data also indicate an excess oblateness in the sense predicted by our identification of this phenomenon with the enhanced network. They also generally suggest a positive correlation with the solar cycle, again consistent with this notion. These appearances could also result from simple facular confusion (*16*), because the measurements from space may not have had adequate diagnostics for this systematic error. Our analysis of the EUV limb brightness points to the active network outside the faculae themselves as the source of this behavior.

The measured oblateness gives an estimate of the gravitational moment J2 via $J2 = (2/3)(\Delta r - \Delta r_{surf})/r_\odot$ (*6*), where Δr is our observed value of 8.01 ± 0.14 milli–arc sec, $\Delta r_{surf} \approx 7.8$ milli–arc sec (*3*), and $r_\odot$ denotes the mean solar radius, 95,963 arc sec. Formally, we obtain $J2 = (1.46 \pm 1.0) \times 10^{-7}$, a value consistent with other determinations (*21*, *22*). Here, the uncertainty does not include the uncertainty in the estimation of the rotational term.

References and Notes

1. A. Auwers, *Astron. Nachr.* **128**, 361 (1891).
2. C. M. Will, *Living Rev. Relativ.* **9**, 3 (2006).
3. R. H. Dicke, *Astrophys. J.* **159**, 1 (1970).
4. R. H. Dicke, H. M. Goldenberg, *Phys. Rev. Lett.* **18**, 313 (1967).
5. H. A. Hill *et al.*, *Phys. Rev. Lett.* **33**, 1497 (1974).
6. R. H. Dicke, J. R. Kuhn, K. G. Libbrecht, *Astrophys. J.* **318**, 451 (1987).
7. S. Sofia, W. Heaps, L. W. Twigg, *Astrophys. J.* **427**, 1048 (1994).
8. J. Rozelot, S. Lefebvre, V. Desnoux, *Sol. Phys.* **217**, 39 (2003).
9. P. H. Scherrer *et al.*, *Sol. Phys.* **162**, 129 (1995).
10. V. Domingo, B. Fleck, A. I. Poland, *Sol. Phys.* **162**, 1 (1995).
11. J. R. Kuhn, R. I. Bush, P. Scherrer, X. Scheick, *Nature* **392**, 155 (1998).
12. M. Emilio, R. I. Bush, J. Kuhn, P. Scherrer, *Astrophys. J.* **660**, L161 (2007).
13. A. Egidi *et al.*, *Sol. Phys.* **235**, 407 (2006).
14. M. Fivian, R. Henneck, A. Michedlishvili, A. Zehnder, *Sol. Phys.* **210**, 87 (2002).
15. M. Fivian, R. Henneck, A. Zehnder, *Innovative Telescopes and Instrumentation for Solar Astrophysics*, S. L. Keil, S. V. Avakyan, Eds. (SPIE, Waikoloa, HI, 2003), vol. 4853, pp. 60–70.
16. G. A. Chapman, B. Ziegler, *Sol. Phys.* **168**, 259 (1996).
17. J. R. Kuhn, K. G. Libbrecht, R. H. Dicke, *Science* **242**, 908 (1988).
18. J.-P. Delaboudinière *et al.*, *Sol. Phys.* **162**, 291 (1995).
19. C. Zwaan, *Annu. Rev. Astron. Astrophys.* **25**, 83 (1987).
20. R. C. Willson, H. S. Hudson, *Nature* **351**, 42 (1991).
21. J. Armstrong, J. R. Kuhn, *Astrophys. J.* **525**, 533 (1999).
22. I. W. Roxburgh, *Astron. Astrophys.* **377**, 688 (2001).
23. We thank NASA for support under grants NAGS-12878 and NNX07AI41G.

Supporting Online Material

www.sciencemag.org/cgi/content/full/1160863/DC1
SOM Text
Figs. S1 to S5
References

22 May 2008; accepted 24 September 2008
Published online 2 October 2008;
10.1126/science.1160863
Include this information when citing this paper

Complete Characterization of Quantum-Optical Processes

Mirko Lobino, Dmitry Korystov, Connor Kupchak, Eden Figueroa, Barry C. Sanders, A. I. Lvovsky*

The technologies of quantum information and quantum control are rapidly improving, but full exploitation of their capabilities requires complete characterization and assessment of processes that occur within quantum devices. We present a method for characterizing, with arbitrarily high accuracy, any quantum optical process. Our protocol recovers complete knowledge of the process by studying, via homodyne tomography, its effect on a set of coherent states, that is, classical fields produced by common laser sources. We demonstrate the capability of our protocol by evaluating and experimentally verifying the effect of a test process on squeezed vacuum.

Construction of a complex machine requires precise characterization of each component's properties. In electronics, this information is obtained from network analyzers, which measure circuit response to simple oscillatory inputs and reveal the device transfer function. Optical quantum technologies, which can be used to build quantum computers (*1*), precise metrological systems (*2*), and unconditionally secure communication (*3*), have similar characterization requirements. In this context, we are interested in the process associated with a quantum circuit component, that is, in being able to predict the transformation that an arbitrary quantum state will undergo when subjected to the action of the component.

A quantum process $\mathcal{E}$ can be represented by a completely positive, trace-preserving linear map (superoperator) on the linear space $\mathbb{L}(\mathbb{H})$ of all density matrices over Hilbert space $\mathbb{H}$. It can be expressed as a rank-4 tensor that relates the matrix elements of the output $\mathcal{E}(\hat{\rho})$ and input $\hat{\rho}$ states in some basis:

$$[\mathcal{E}(\hat{\rho})]_{ik} = \sum_{mn} \mathcal{E}_{ik}^{mn} \rho_{mn} \qquad (1)$$

where summation is from 1 to dim $\mathbb{H}$.

Characterization of a process (known as quantum process tomography or QPT) means finding all components of the superoperator tensor. It can be implemented by determining the output state for each of the $(\dim \mathbb{H})^2$ elements of a spanning set of $\mathbb{L}(\mathbb{H})$. Such a direct approach to QPT (*4*) was experimentally realized on one-qubit teleportation (*5*), the Hamiltonian evolution of vibrational states of atoms in an optical lattice (*6*), and is fine on a two-qubit controlled-NOT gate (*7*, *8*) and Bell-state filter (*9*). As an alternative, ancilla-assisted QPT exploits an isomorphism between processes and states (*10*) and has been used to characterize a controlled-NOT gate (*11*) and a general single qubit gate (*12*, *13*); see (*14*) for a comparative review of ancilla-assisted QPT.

Existing QPT suffers from serious shortcomings, including either the requirement of an unwieldy set of input states for direct QPT or a high-dimensional entangled input state for ancilla-assisted QPT; these shortcomings deleteriously affect scalability and restrict accessible systems to very low dimension. In optics, QPT has been applied to processes on one and two dual-rail qubits, with postselection based on photon coincidences projecting the input and output states onto these qubit subspaces. This approach cannot provide complete information about a state or a process because optical losses, imperfect sources, detector dark counts, and other imperfections lead to departure from the qubit subspaces. Postselected tomography can only estimate the fraction of such phenomena by comparing the coincidence rate and the photon production rate (*9*).

We introduce a scheme that enables complete characterization of a general quantum-optical process. We used optical homodyne tomography followed by maximum likelihood reconstruction to obtain full information on the process across all photon number sectors and also the coherence between sectors. The state reconstruction algorithm provides an efficient method for compensating losses in homodyne detection (*15*). As inputs, we used only coherent states that are readily available from a laser source, so our method can be easily scaled up.

We experimentally tested our approach by characterizing a quantum process that consists of a simultaneous absorption and phase shift. The reconstructed superoperator allows us to predict, with a fidelity of over 99%, the effect of the process on a squeezed vacuum.

Our method has its basis in the fact that any density matrix can be represented as a sum of coherent states' density matrices (*16*, *17*). Although such a representation (the Glauber-Sudarshan P function) may be highly singular, it can be arbitrarily closely approximated with a regular P function. By measuring the process output for many coherent states and exploiting the linearity, we can predict the process output for any arbitrary state.

The Glauber-Sudarshan decomposition of a quantum state $\hat{\rho}$ is given by

$$\hat{\rho} = 2\int P_\rho(\alpha)|\alpha\rangle\langle\alpha| d^2\alpha \qquad (2)$$

where $P_\rho(\alpha)$ is the state's P function, α is the coherent state with mean position, and momentum observables $(x, p) = (\sqrt{2}\ \mathrm{Re}\ \alpha, \sqrt{2}\ \mathrm{Im}\ \alpha)$. We used the convention $[\hat{x}, \hat{p}] = i$, and integration is performed over the entire phase space. Therefore, if we know the effect $|\alpha\rangle\langle\alpha| \mapsto \hat{\varrho}(\alpha) = \mathcal{E}(|\alpha\rangle\langle\alpha|)$ of the process on all coherent states, we can predict its effect on state $\hat{\rho}$:

$$\mathcal{E}(\hat{\rho}) = 2\int P_\rho(\alpha)\hat{\varrho}(\alpha) d^2\alpha \qquad (3)$$

An obstacle to direct application of this approach is posed by singular behavior of the function $P_\rho(\alpha)$. Indeed, the P function exists only as a generalized function, more singular than the Dirac delta function, when the corresponding quantum state has nonclassical features (*18*).

This can be overcome by applying a theorem proven by Klauder (*19*): For any bounded operator $\hat{\rho}$, there exists an operator $\hat{\rho}_L$ with continuous and rapidly decreasing P function arbitrarily close to $\hat{\rho}$ in the trace-class norm. The Klauder approximation is obtained as follows: We assume that the Wigner function of $\hat{\rho}$ belongs to the Schwartz class $\mathcal{S}^2$, that is, is infinitely smooth and rapidly decreasing (which is the case for all physically plausible density matrices). The Fourier transform of the operator's Glauber-Sudarshan function $P_\rho(\alpha)$ can be expressed as (*18*)

$$\tilde{P}_\rho(k_x, k_p) = \tilde{W}_\rho(k_x, k_p) \exp\left(\frac{k_x^2 + k_p^2}{4}\right) \qquad (4)$$

where $\tilde{W}_\rho(k_x, k_p)$ is the Fourier transform of the operator's Wigner function. The function defined by Eq. 4 always exists and is infinitely smooth (albeit not necessarily square integrable). We multiply $\tilde{P}_\rho(k_x, k_p)$ by a regularizing function

$$G_L(k_x, k_p) = e^{-[f(k_x - L) + f(-k_x - L) + f(k_p - L) + f(-k_p - L)]} \qquad (5)$$

with $f(y) = y^4 \exp(-1/y^2)$ for $y > 0$, $f(y) = 0$ for $y \leq 0$. This regularizing function is equal to 1 in a square domain of side $2L$ and rapidly drops to zero outside. The product $\tilde{P}_{L,\rho}(k_x, k_p) = \tilde{P}_\rho(k_x, k_p) G(k_x, k_p)$ now belongs to the Schwartz class. Applying the inverse Fourier transform, we obtain the new Glauber-Sudarshan function $P_{L,\rho}(\alpha)$, which defines the Klauder approximation $\hat{\rho}_L$. By choosing L sufficiently high (*20*), the operator $\hat{\rho}_L$ can be made to approximate $\hat{\rho}$ arbitrarily well (fig. S1A).

As an example, we applied the Klauder approximation to squeezed vacuum, a nonclassical state characterized by a highly singular P function whose Fourier transform grows exponentially with increasing k_x and/or k_p. We tested our protocol with a state that has a noise reduction in

Institute for Quantum Information Science, University of Calgary, Calgary, Alberta T2N 1N4, Canada.

*To whom correspondence should be addressed. E-mail: lvov@ucalgary.ca

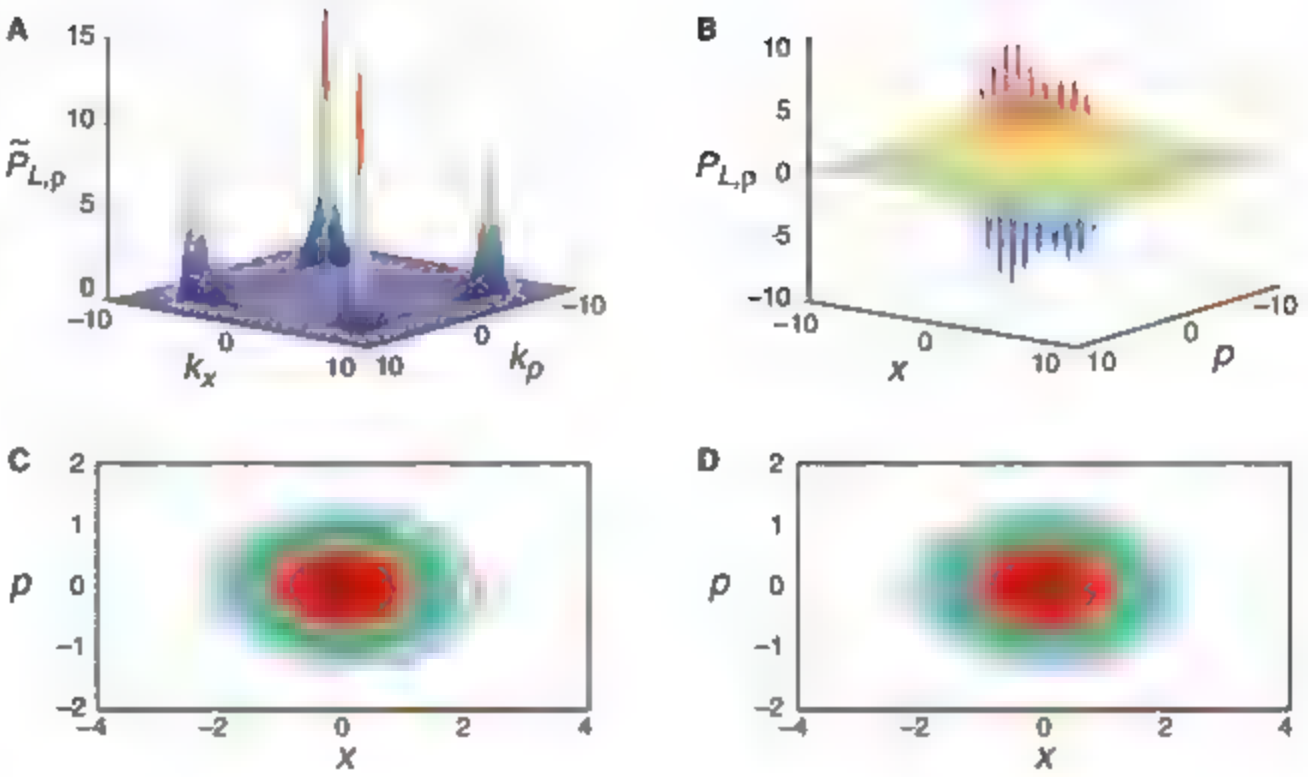

Fig. 1. Regularized Glauber-Sudarshan decomposition of the squeezed state. (**A**) Absolute value of the regularized Fourier transform of the squeezed vacuum P function. (**B**) Approximated P function calculated from the inverse Fourier transform of $\tilde{P}_{L,p}(k_x,k_p)$. (**C** and **D**) Wigner representations of, respectively, the measured and the approximated squeezed vacuum states.

the squeezed quadrature of −1.58 dB and excess noise in the orthogonal quadrature of 2.91 dB. The function $\tilde{P}(k_x,k_p)$ was calculated from the state's density matrix according to Eq. 4 and subsequently regularized as described above using $L = 5.2$. Figure 1A shows $\tilde{P}_L(k_x,k_p)$ calculated from our experimental data, and Fig. 1B displays its inverse Fourier transform $P_L(\alpha)$. In Fig. 1, C and D, we compare the Wigner functions of the original state and the one obtained from the regularized P function. The two states exhibit a quantum fidelity of more than 0.9999.

Although the above method permits finding the process output for an arbitrary input state, it requires one to first determine the input state's P function. This step can be avoided by calculating the process superoperator in the Fock basis, so the output can be found from the input density matrix according to Eq. 1. To this end, we express the Glauber-Sudarshan function as

$$P_\rho(\alpha) = \sum_{mn} \rho_{mn} P_{mn}(\alpha) \qquad (6)$$

where $P_{mn}(\alpha)$ is the P function of the operator $|n\rangle\langle m|$. We now replace these functions by their regularized versions $P_{L,mn}(\alpha)$ and rewrite Eq. 3 as

$$\mathcal{E}(\hat{\rho}) = 2\sum_{mn} \rho_{mn} \int P_{L,mn}(\alpha)\hat{Q}(\alpha)d^2\alpha \qquad (7)$$

from which we determine the process superoperator as

$$\mathcal{E}_{ik}^{mn} = 2\int P_{L,mn}(\alpha)Q_{ik}(\alpha)d^2\alpha \qquad (8)$$

Before applying the latter result to experiments, a number of practical issues have to be addressed. First, parameter L must be chosen to ensure proper approximation of input states. The second issue is that, in a realistic experiment, the measurement can be done only for coherent states whose amplitude does not exceed a certain maximum α_{max}. Lastly, the experiment can only be performed with a finite, discrete set of coherent states. Density matrix elements $Q_{ik}(\alpha)$ for an arbitrary α, required for calculating the superoperator, must then be obtained by polynomial interpolation. These matters are discussed in (*20*).

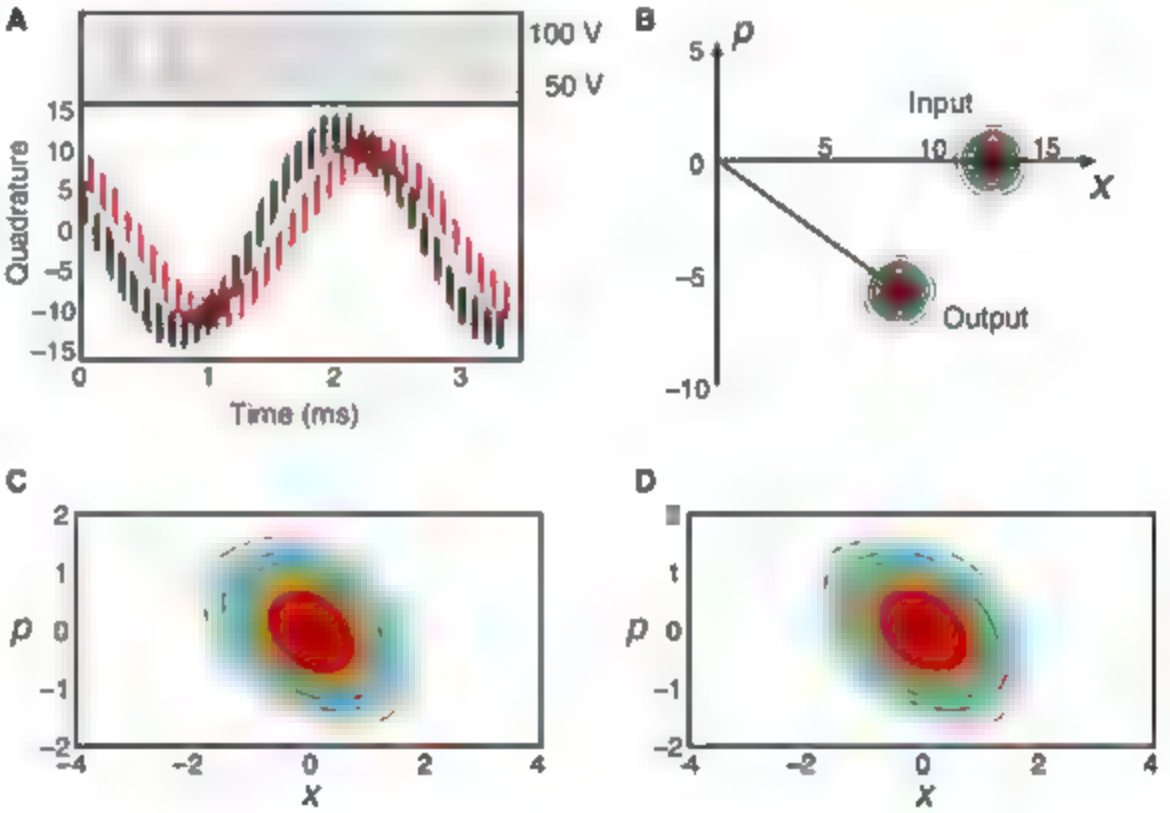

Fig. 2. (**A**) Time-dependent quadrature values acquired from homodyne detection of a coherent state with input $\alpha = 8.3$. Black dots correspond to the state before the process; red dots, after the process. The top curve shows the EOM driving voltage. (**B**) The Wigner function of the coherent state before and after the process. (**C** and **D**) Wigner representations of the measured output squeezed state compared to the one obtained from process tomography.

A simplification arises for phase-symmetric processes, in which there is no phase coherence between the "processing unit" and input states. In this case, if two inputs $\hat{\rho}$ and $\hat{\rho}_1$ are different by an optical phase shift $\hat{U}(\varphi)$, the states $\mathcal{E}(\hat{\rho})$ and $\mathcal{E}(\hat{\rho}_1)$ will differ by the same phase shift:

$$\mathcal{E}[\hat{U}(\varphi)\hat{\rho}\hat{U}^\dagger(\varphi)] = \hat{U}(\varphi)\mathcal{E}(\hat{\rho})\hat{U}^\dagger(\varphi) \qquad (9)$$

Then, if we know the effect of the process on a coherent state $|\alpha\rangle$, we also know what happens to $|\alpha e^{i\varphi}\rangle$, so it is enough to perform measure-

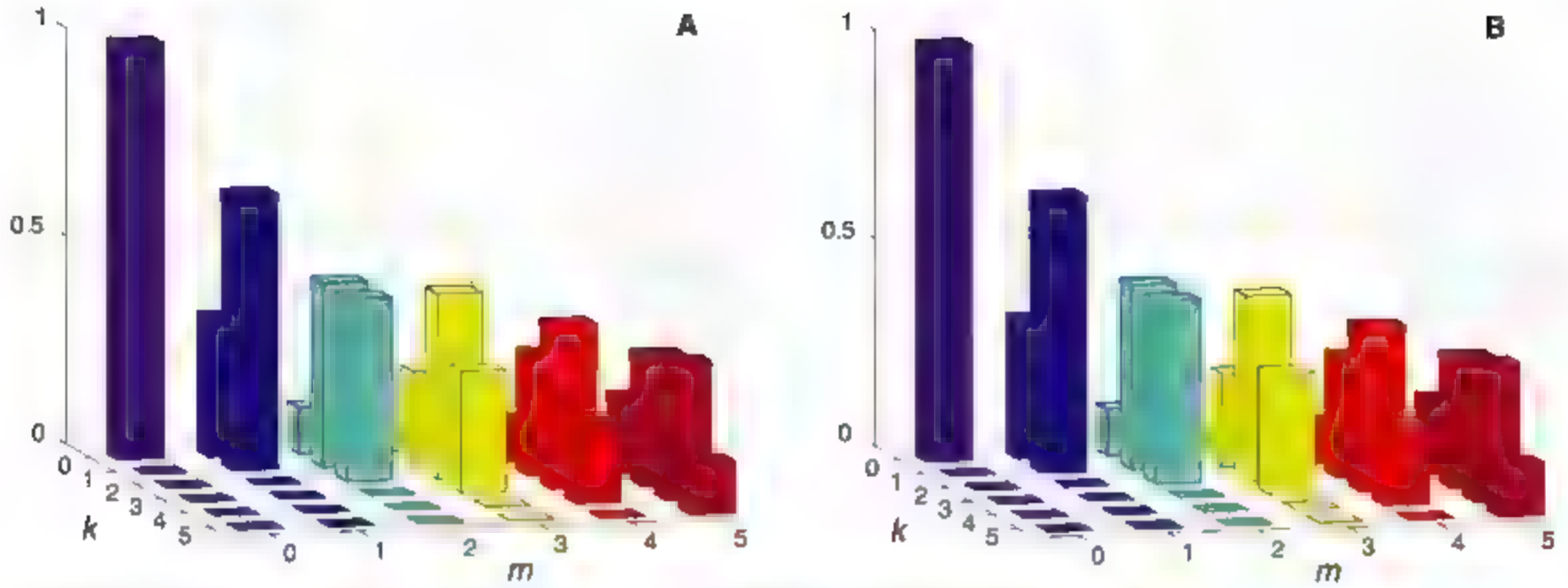

Fig. 3. The "diagonal" values of the superoperator $\mathcal{E}_{kl}^{mn}$. **(A)** As obtained in the experiment. **(B)** Theoretical model.

ments on input coherent states with real, positive amplitudes. For the process superoperator in the Fock basis, the phase symmetry implies that $\mathcal{E}_{mn}^{kl}$ vanishes unless $k - l = m - n$

The process studied in our experiment was electrooptical amplitude and phase modulation of the optical field. The process was implemented by using an electrooptical modulator (EOM) followed by a polarizer. The field experienced minimal distortion when a bias voltage $V_1 = 100$ V was applied to the EOM. Switching the voltage to $V_2 = 50$ V produced birefringence and thus losses at the polarizer, along with a phase shift.

A continuous-wave Ti:Sapphire laser at 795 nm was the coherent state source used for the device characterization. We reconstructed the input and output states at 11 different input amplitude levels between $\alpha_1 = 0$ and $\alpha_{11} = 10.9$. In order to keep track of the relative phase shift, we switched the EOM voltage between V_1 and V_2 every 100 μs (Fig. 2A, top), whereas the phase of the local oscillator was linearly scanned by a piezoelectric transducer at 100 Hz. The homodyne photocurrent was recorded with an oscilloscope. To obtain quadrature measurements, we integrated the photocurrent over time intervals of 20 ns. The bottom plot in Fig. 2A shows the recovered quadrature values after normalization to the vacuum noise. The time dependence of the local oscillator phase was recovered from the slow, sinusoidal variation of the average homodyne photocurrent as a function of time.

In this manner, for each input amplitude, we sampled 50,000 phase and quadrature values for both the input and output states and used them to calculate density matrices by likelihood maximization (*15*, *21*) (Fig. 2B). The output state reconstruction showed a phase shift of 36° and a loss of 34% with respect to the input state.

The interpolated experimental data have been used to determine the process superoperator tensor. We used the phase symmetry assumption in Eq. 9, which is justified by the fact that the EOM driver is independent from the master laser. The elements $\mathcal{E}_{kl}^{mn}$ of the tensor in the photon number basis are plotted in Fig. 3A. This plot should be interpreted as follows: For a given input Fock state $|n\rangle$, the values of $\mathcal{E}_{kl}^{mn}$ give the diagonal elements of the output density matrix. For example, the single-photon state $|1\rangle$ after passing through the EOM will be transformed into a statistical mixture of the single-photon and vacuum states. A theoretical prediction for the process tensor has been calculated by using the Bernoulli transformation to account for a lossy channel and a phase shift superoperator; the superoperator diagonal elements in the Fock basis are displayed in Fig. 3B, and these diagonal elements bear close resemblance to the experimental result. A similar agreement was also obtained for nondiagonal terms of the superoperator, but it is not shown here.

For additional verification, we applied this result to predict the effect of the device on the squeezed vacuum state described in the previous section. This state was produced by pumping an optical parametric amplifier (OPA) in bow-tie configuration with the second harmonic of the Ti:Sapphire laser and using a periodically poled $KTiOPO_4$ crystal as nonlinear medium (*22*, *23*).

The state before (Fig. 1C) and after (Fig. 2C) the process was reconstructed by using homodyne tomography as described above. By applying the process superoperator to the input squeezed state, we predict the process output (Fig. 2D). The maximum quadrature noise variance amounted to 2.19 dB for the measured state and 2.15 dB for the prediction, and the minimum quadrature noise variance was −1.07 dB for the measured state and −0.95 dB for the prediction, corresponding to a quantum fidelity of 0.9935 ± 0.0002.

Whereas here we demonstrate our tomographic method for single-mode inputs, multimode or multichannel processes can be characterized by using multimode P representation, multiple homodyne detectors, and feeding product coherent states as inputs. Our method overcomes substantial limitations of previous optical QPT schemes. Process characterization is not restricted to a Hilbert space associated with a specific qubit and thus reveals the imperfections of a quantum information processing unit. Additionally, it uses only coherent states as inputs, which are readily available from the laser and whose intensities and phases are easily manipulated. This permits characterization of complex processes used in quantum information processing and communication.

References and Notes

1. E. Knill, R. Laflamme, G. J. Milburn, *Nature* **409**, 46 [redacted].
2. J. Ye, H. J. Kimble, H. Katori, *Science* **320**, 1734 (2008).
3. N. Gisin, G. Ribordy, W. Tittel, H. Zbinden, *Rev. Mod. Phys.* **74**, 145 (2002).
4. J. F. Poyatos, J. I. Cirac, P. Zoller, *Phys. Rev. Lett.* **78**, 390 (1997).
5. M. A. Nielsen, E. Knill, R. Laflamme, *Nature* **396**, 52 (1998).
6. S. H. Myrskog, J. K. Fox, M. W. Mitchell, A. M. Steinberg, *Phys. Rev. A* **72**, 013615 (2005).
7. J. L. O'Brien *et al.*, *Phys. Rev. Lett.* **93**, 080502 (2004).
8. A. M. Childs, I. L. Chuang, D. W. Leung, *Phys. Rev. A* **64**, 012314 (2001).
9. M. W. Mitchell, C. W. Ellenor, S. Schneider, A. M. Steinberg, *Phys. Rev. Lett.* **91**, 120402 (2003).
10. G. M. D'Ariano, P. Lo Presti, *Phys. Rev. Lett.* **86**, 4195 (2001).
11. M. Riebe *et al.*, *Phys. Rev. Lett.* **97**, 220407 (2006).
12. J. B. Altepeter *et al.*, *Phys. Rev. Lett.* **90**, 193601 (2003).
13. F. De Martini, A. Mazzei, M. Ricci, G. M. D'Ariano, *Phys. Rev. A* **67**, 062307 (2003).
14. M. Mohseni, A. T. Rezakhani, D. A. Lidar, *Phys. Rev. A* **77**, 032322 (2008).
15. A. I. Lvovsky, *J. Opt. B* **6**, S556 (2004).
16. R. J. Glauber, *Phys. Rev. Lett.* **10**, 84 (1963).
17. E. C. G. Sudarshan, *Phys. Rev. Lett.* **10**, 277 (1963).
18. U. Leonhardt, *Measuring the Quantum State of Light* (Cambridge Univ. Press, Cambridge, 1997).
19. J. R. Klauder, *Phys. Rev. Lett.* **16**, 534 (1966).
20. Materials and methods are available as supporting material on *Science* Online.

21. J. Řeháček, Z. Hradil, E. Knill, A. I. Lvovsky, *Phys. Rev. A* 75, 042108 (2007)
22. J. Appel, D. Hoffman, E. Figueroa, A. I. Lvovsky, *Phys. Rev. A* 75, 035802 (2007)
23. J. Appel, E. Figueroa, D. Korystov, M. Lobino, A. I. Lvovsky, *Phys. Rev. Lett.* 100, 093602 (2008).
24. This work was supported by Natural Sciences and Engineering Research Council, Canadian Institute for Advanced Research (CIFAR), Informatics Circle of Research Excellence (iCORE), Alberta Ingenuity Fund, Canada Foundation for Innovation, and QuantumWorks. A.I.L. is a CIFAR scholar, and B.C.S. is a CIFAR associate

Supporting Online Material
www.sciencemag.org/cgi/content/full/1162086/DC1
SOM Text
Fig. S1
References

20 June 2008; accepted 17 September 2008
Published online 25 September 2008;
10.1126/science.1162086
Include this information when citing this paper

Detection of First-Order Liquid/Liquid Phase Transitions in Yttrium Oxide–Aluminum Oxide Melts

G. N. Greaves,[1]* M. C. Wilding,[1] S. Fearn,[1] D. Langstaff,[1] F. Kargl,[1] S. Cox,[1] Q. Vu Van,[1] O. Majérus,[2] C. J. Benmore,[3] R. Weber,[4] C. M. Martin,[5] L. Hennet[6]

We combine small-angle x-ray scattering (SAXS) and wide-angle x-ray scattering (WAXS) with aerodynamic levitation techniques to study in situ phase transitions in the liquid state under contactless conditions. At very high temperatures, yttria-alumina melts show a first-order transition, previously inferred from phase separation in quenched glasses. We show how the transition coincides with a narrow and reversible maximum in SAXS indicative of liquid unmixing on the nanoscale, combined with an abrupt realignment in WAXS features related to reversible shifts in polyhedral packing on the atomic scale. We also observed a rotary action in the suspended supercooled drop driven by repetitive transitions (a polyamorphic rotor) from which the reversible changes in molar volume (1.2 ± 0.2 cubic centimeters) and entropy (19 ± 4 joules mole^{-1} kelvin^{-1}) can be estimated.

Liquids represent some of the most familiar everyday materials. Recognized by their ability to flow, liquids adopt whatever shape contains them and in suspension form spherical drops. They are the intermediate state between solids and gases, and they extend over temperature and pressure up to sharp phase boundaries along which they coexist with the adjacent states. Phase transitions across these boundaries are discontinuous and of first-order, involving reversible changes in extensive thermodynamic parameters, such as molar volume ΔV and entropy ΔS. Together these parameters define the slope of the phase boundary $dT/dP = \Delta V/\Delta S$ (for instance, the melting curve that separates the liquid from the crystalline state). Phase boundaries themselves can terminate at critical points if the coexistent phases become indistinguishable, the most well-known being the formation of fluids from their liquid and vapor states.

The physics of phase transitions and critical phenomena is extensive (*1*). It also includes the wealth of crystalline phases within the solid state where periodic structures can abruptly transform under pressure and temperature into new crystalline states distinct in density and symmetry (*2*). One of the most exciting developments in liquid state science is the growing evidence for different phases of the same liquid and for phase transitions between them at characteristic temperatures and pressures (*3*–*7*). At first glance such "polyamorphism" is counterintuitive, as diffusion processes in a liquid would appear to lead to the same time-averaged aperiodic structure. However, unlike crystals, liquids are characterized by temporal and spatial fluctuations in density (*1*). These potentially could be the antecedents for different self-assembled phases distinguished by density and entropy (*7*), particularly in the metastable supercooled state where liquid flow becomes increasingly viscous with falling temperature or increasing pressure. As the concept of polyamorphism has developed, the so called "two-state model" (*8*, *9*) has proved influential in defining the phase boundary between a low-density liquid (LDL) phase and a high-density liquid (HDL) phase straddled by spinodal limits. This is illustrated in Fig. 1. In particular, there is a critical point *C* on the phase boundary below which the LDL and HDL states coexist and beyond which the liquid is single phase. If *C* lies at negative pressures, a liquid-liquid phase transition between HDL and LDL states is expected at ambient pressure and characteristic temperature T_{LL} (Fig. 1).

Speculation about the existence of liquid polyamorphs has its origins in the effort to better explain negative melting curves [i.e., $dT/dP < 0$ (*3*, *5*, *7*–*9*)] for which the fusion of ice is the most familiar (*10*). Even though transitions between polyamorphic states in water have now been well-studied (*3*, *11*–*15*), controversy still exists as to whether these are truly of first-order character (*13*, *14*), analogous to phase transitions in the crystalline solid state (*2*), or whether they occur via numerous intermediate glassy states (*12*, *15*).

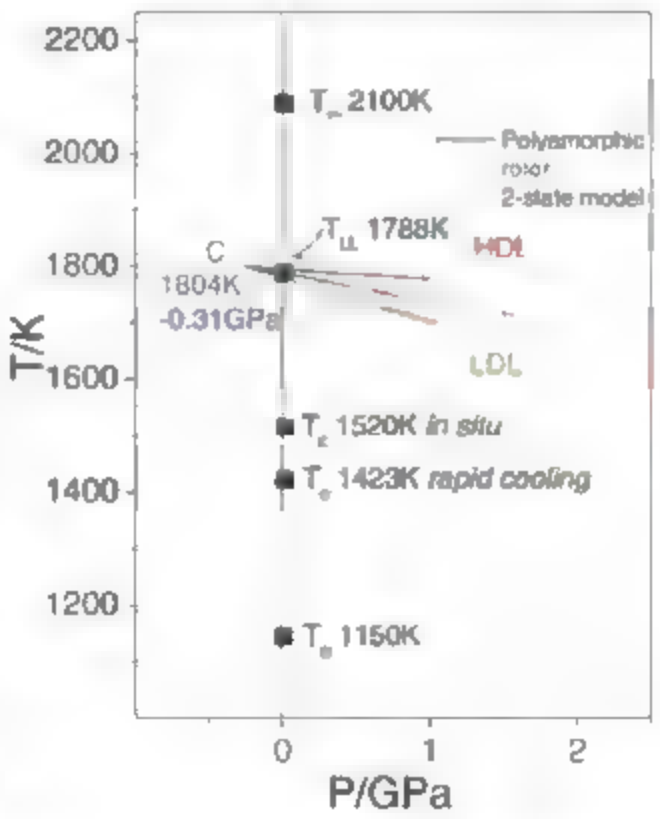

Fig. 1. *T*/*P* phase boundary separating HDL and LDL phases surrounded by spinodal limits. Dashed curves represent calculations from the two-state model (*8*, *9*). Solid curves indicate $dT/dP = \Delta V_{LL}/\Delta S_{LL}$, as determined from the changes in entropy ΔS_{LL} and molar volume ΔV_{LL} for supercooled AY20, with ±σ limits taken from Fig. 3C. This places the critical point *C* at 1804 K and −0.31 GPa. T_m and the HDA T_g for AY20 are also included (*26*, *31*), together with T_c taken from Fig. 3B and from rapid quenching (*29*).

[1]Centre for Advanced Functional Materials and Devices, Institute of Mathematics and Physics, Aberystwyth University, Aberystwyth SY23 3BZ, UK. [2]Ecole Nationale Supérieure de Chimie de Paris, 11 rue Pierre et Marie Curie, 75231, Paris, France. [3]Advanced Photon Source, Argonne National Laboratory, Argonne, IL 60439, USA. [4]Materials Development, 3090 Daniels Court, Arlington Heights, IL 60004, USA. [5]Synchrotron Radiation Source, STFC Daresbury Laboratory, Warrington, Cheshire, WA4 4AD, UK. [6]CNRS-CEMHTI, 1d Avenue de la Recherche Scientifique, 45071 Orléans Cedex 9, France

*To whom correspondence should be addressed. E-mail: gng@aber.ac.uk

Pairs of polyamorphic phases have been identified in many other amorphous and glassy systems (*7*, *16*) such as silica (*17*), Si (*18*), Ge (*19*), and microporous zeolites (*20*). With two exceptions, however, transitions have not been observed in the liquid or supercooled state, other than through computer simulation (*4*, *7*, *11*, *21*). The first of these is liquid phosphorous, which exhibits a first-order transition above its melting point T_m at positive pressure (*22*) between a low-density molecular fluid and a high-density network liquid—the fluid and liquid phases separated by a large density difference $\Delta\rho/\rho$ close to 0.4 (*23*). Second, polyamorphic macrosegregation (but at ambient pressure) has been reported in yttria-alumina melts (*24*). In this case, it occurs in the supercooled state and was explored for miniature specimens close to the glass transition temperature T_g. High- and low-density states with a density difference $\Delta\rho/\rho$ of ~0.04 smaller than in liquid phosphorous were reported, the phase separation being consistent with a first-order liquid/liquid transition process. Only ex situ studies were possible, however, rapidly quenched glasses being used to avoid crystallization. The liquid/liquid transition temperature was estimated to rise above T_g with increasing alumina content (*24*). Subsequent studies on larger specimens (*25*, *26*) have shown that liquid unmixing is sometimes overtaken by crystallization, with the formation of glass ceramics (*27*, *28*), and in other cases rapid quenching overshoots liquid coexistence, resulting in single-phase glasses (*26*, *29*) that become polyamorphic on reheating to T_g (*26*).

Recent developments in contactless aerodynamic levitation furnaces offer the opportunity to study liquids in situ in the supercooled range (*30*). Suspended on a stream of gas, heterogeneous nucleation from contact with any solid container is avoided. Yttria-alumina has been adopted as the model system to study polyamorphism in the supercooled state. Compositions [$(Al_2O_3)_{100-x}(Y_2O_3)_x$ or AYx] have been chosen to search for liquid-liquid transitions in situ at temperatures higher than have been possible in previous ex situ studies (*24*, *25*, *27*–*29*) and where full conversion to LDL might be expected (*24*). Small-angle x-ray scattering (SAXS)/wide-angle x-ray scattering (WAXS) methods enable structure to be followed at the nano and atomic levels (*31*, *32*). The geometry of the aerodynamic levitator furnace adapted for combined x-ray experiments [see supporting online material (SOM)] is shown schematically in Fig. 2A. Data were recorded at temperatures from above T_m through many hundreds of degrees into the supercooled regime, up to the point of crystallization T_c (Fig. 1). A selection of SAXS profiles at low and high T are plotted in Fig. 3A for three different supercooled liquids: (i) AY15, (ii) AY20, and (iii) AY25. Each of these liquids exhibits a maximum at a wave vector Q_{min}, separating the bottom of the interatomic structure factor $S(Q > Q_{min})$ from small-angle scatter $I_{SAXS}(Q < Q_{min})$, which is caused by nanostructural inhomogeneities. Both are underpinned by a Q-independent background related to thermal density fluctuations (*1*, *6*). The rise in I_{SAXS} as $Q \to 0$ is indicative of liquid inhomogeneities with a narrower size distribution. Where $S(Q)$ and I_{SAXS} increase modestly with temperature across the whole wave vector range for all three liquids, the behavior captured for AY20 contains a previously unseen feature: a narrow and reversible peak just below 1800 K (Fig. 3A), which is an additional transient source of inhomogeneity.

Precision liquid structure factors $S(Q)$ for the same three liquids obtained at 2500 K with high-energy x-rays (Fig. 4A) show compositional trends that can be clearly seen in the different patterns $\Delta S(Q)$ (Fig. 4A, inset): namely, the progressive rise in the principal peak close to 2.2 $Å^{-1}$ with increased yttria and the developments in the subsequent broad feature between 3 and 5 $Å^{-1}$. Temperature effects in the supercooled region were explored by combining SAXS (Fig. 3A) with WAXS (Fig. 4B). In particular, WAXS from supercooled AY20 alters abruptly and reversibly in the vicinity of 1800 K, matching the sharp feature in the SAXS (Fig. 3A).

Whereas the liquid drops levitated extremely stably to a few microns mechanically and thermally to better than 5 K over the whole supercooled range (see SOM), the temperature sometimes became variable close to where reversible nanostructural changes affect SAXS (Fig. 3A) and interatomic changes affect WAXS (Fig. 4B). De-

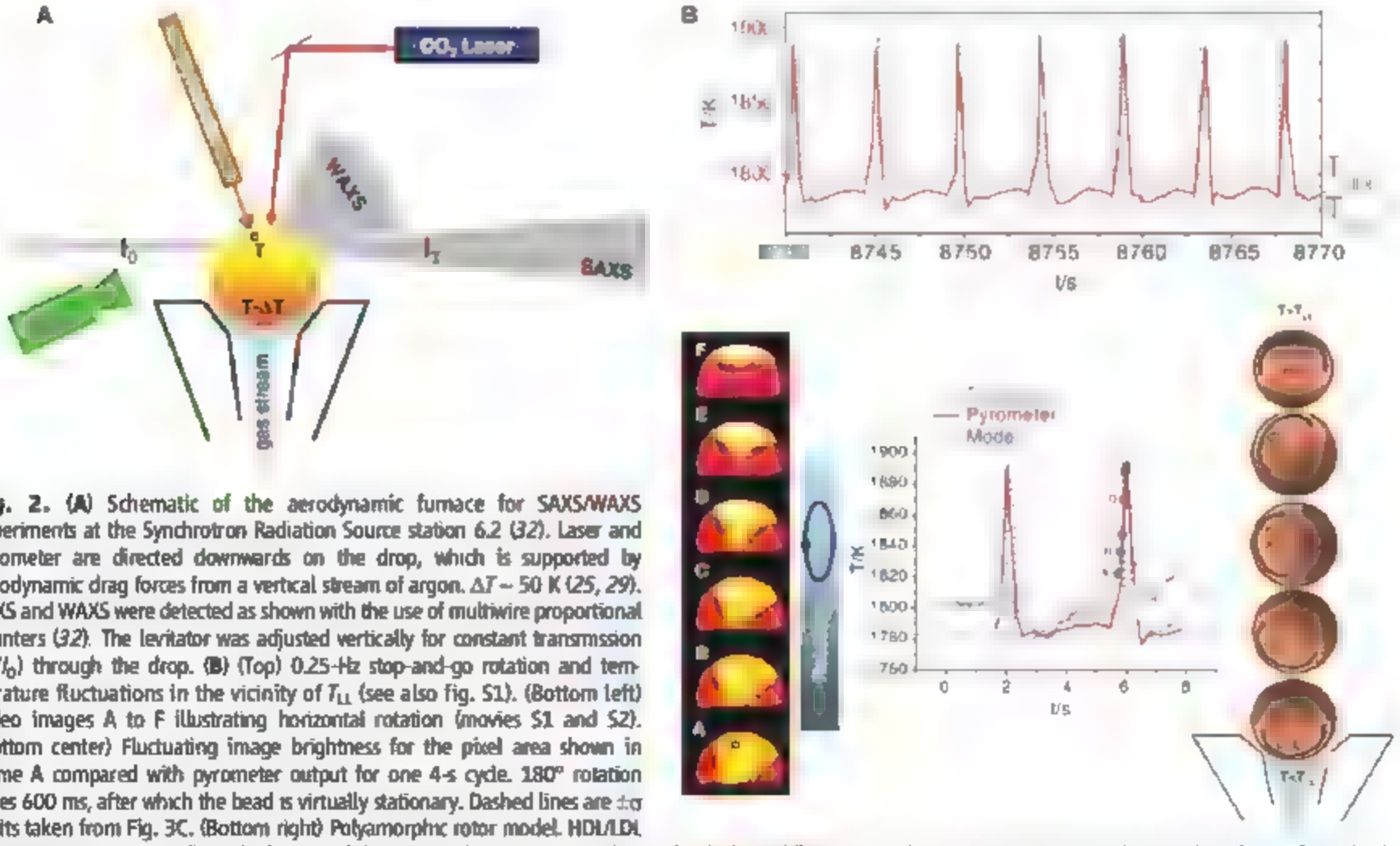

Fig. 2. (**A**) Schematic of the aerodynamic furnace for SAXS/WAXS experiments at the Synchrotron Radiation Source station 6.2 (*32*). Laser and pyrometer are directed downwards on the drop, which is supported by aerodynamic drag forces from a vertical stream of argon. $\Delta T \sim 50$ K (*25*, *29*). SAXS and WAXS were detected as shown with the use of multiwire proportional counters (*32*). The levitator was adjusted vertically for constant transmission (I_T/I_0) through the drop. (**B**) (Top) 0.25-Hz stop-and-go rotation and temperature fluctuations in the vicinity of T_{LL} (see also fig. S1). (Bottom left) Video images A to F illustrating horizontal rotation (movies S1 and S2). (Bottom center) Fluctuating image brightness for the pixel area shown in frame A compared with pyrometer output for one 4-s cycle. 180° rotation takes 600 ms, after which the bead is virtually stationary. Dashed lines are ±σ limits taken from Fig. 3C. (Bottom right) Polyamorphic rotor model. HDL/LDL transition occurs repeatedly at the bottom of the sphere whenever $T < T_{LL}$, the mechanical instability causing the LDL zone to rotate to the top where it transforms back to HDL in the laser beam. Dotted lines follow polyamorphic model (*34*), also shown above for extended sequence.

pending on the precise laser alignment (Fig. 2A) highly regular oscillations in temperature were observed in separate experiments ~1800 K, as illustrated in Fig. 2B, pointing to a repetitive pattern of convection within the drop with a fixed frequency (fig. S1). Video imaging revealed the supercooled drop revolving through 180° about a horizontal axis (movies S1 and S2) at the start of each cycle (Fig. 2B), the movement coinciding with a temperature spike. This unusual behavior was observed for periods of up to an hour and could be resumed after re-melting (fig. S1).

The changes in the nanostructural order evident from the SAXS (Fig. 3A) are distinguished in Fig. 3B, where $I_{SAXS}Q^2$ data integrated for $Q < Q_{min}$ are plotted between 1500 and 2400 K until interrupted by crystallization. The integrated SAXS is proportional to $\langle\Delta\rho^2\rangle$, the amplitude of thermal fluctuations, which rises slowly with temperature if the isothermal compressibility β_T is reasonably constant (*6*). However, this behavior is decorated with a sharp maximum for liquid AY20 that we interpret as direct evidence for the coexistence of LDL and HDL states with a density difference $\Delta\rho_{LL}$ at T_{LL}. The maximum is separated from the background in Fig. 3C and deconvoluted into two components. We attribute these to the decline of the HDL phase x_{HDL} accompanied by the rise in the LDL phase x_{LDL} as the temperature drops and vice versa. The peak in x_{HDL}:x_{LDL} is at 1788 K. This is 250 K higher than previously reported from ex situ experiments (*24*) and indicates that the rise in T_{LL} with increasing alumina is much steeper than can be estimated from the cooling rates of rapidly quenched yttria-alumina glasses (SOM). The T_{LL} maximum for AY20 (Fig. 3C) has a full width at half maximum of 22 K. Its narrowness and reversibility are the hallmarks of a first-order phase transition (*1*) in the liquid state (*8*, *9*), in contrast to the gradual transformation through incremental metastable states proposed by some groups (*12*, *15*) for high-density amorphous (HDA)/low-density amorphous (LDA) transitions in glassy water.

With the large Q range available from high-energy x-rays, detailed real-space distributions $g(r)$ for the three yttria-alumina liquids at 2500 K (Fig. 4C) provide signatures for the various nearest-neighbor (Al–O, Y–O) and interpolyhedral (Al–Y, Y–Y) partial-pair distribution functions. In the difference distributions $\Delta g(r)$s (inset in Fig. 4C), compositional trends inferred from computer modeling of yttria-alumina glasses (*7*) can be seen far more easily. In particular, an increase in yttria content naturally leads to an increase in Y–O and a decrease in Al–O correlations. However, it is also accompanied by an increase in Y–Y correlations, suggesting the microsegregation of modifying yttria polyhedra occurring within decreasing proportions of the network-like liquid alumina matrix. This clustering of yttria polyhedra is similar to the formation of channels that percolate through silicate networks (*6*).

Compositional changes affecting cation-cation correlations at high temperatures can also be seen in $\Delta S(Q)$ for the three liquids (Fig. 4A, inset). The principal peak at 2.2 Å^{-1} is mainly due to Al–Y

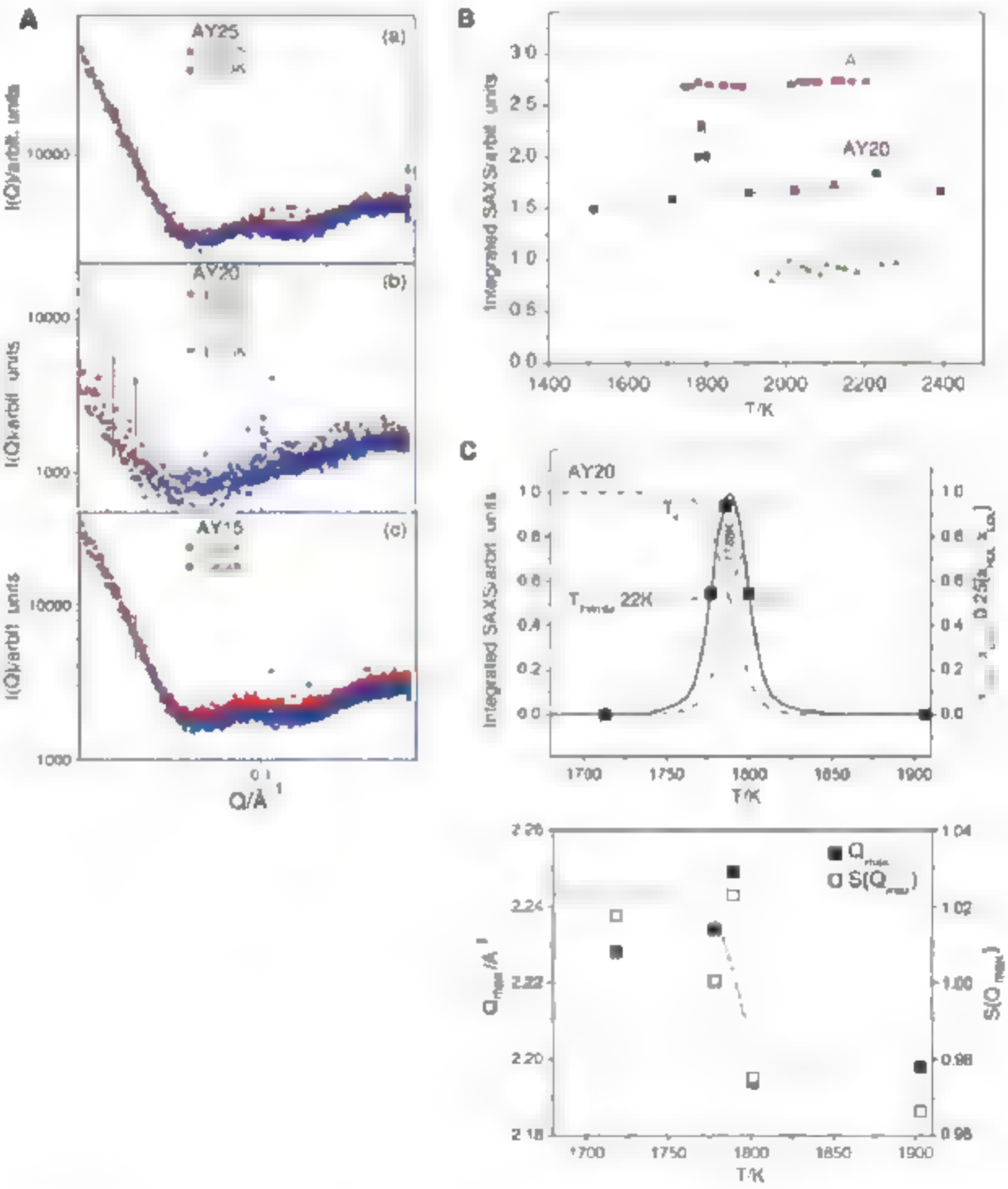

Fig. 3. SAXS data for supercooled AY15, AY20, and AY25 liquids revealing the intensity of random fluctuations measured at the Synchrotron Radiation Source station 6.2 (SOM). (**A**) LogI_{SAXS} versus Log$Q$ plots with a minimum at $Q_{min} < 0.05$ Å^{-1} between the rise for $Q < Q_{min}$ and the increase in the structure factor for $Q > Q_{min}$. Note the rise and fall in I_{SAXS} for AY20 in the vicinity of 1788 K. (**B**) SAXS integrated for $Q < Q_{min}$ $\int_{0.03}^{Q_{min}} I_{SAXS}Q^2 dQ$, showing the linear temperature rise for the three supercooled liquids. SAXS was followed as far as crystallization T_c in each case (SOM). The sharp peak for AY20 at 1788 K identifies a liquid/liquid transmission. AY20 and AY25 are offset vertically with respect to AY15 by 1 and 2, respectively. (**C**) (Top) Integrated SAXS $\int_{0.03}^{Q_{min}} I_{SAXS}Q^2 dQ$ for supercooled AY20 from Fig. 3B with the thermal background removed (black solid line) and deconvoluted into two back-to-back Avrami-like sigmoids: x_{LDL} (blue dash-dot-dashed line) and x_{HDL} (orange dashed line), where $x_{LDL} = e^{-\left(\frac{T-T_0}{1.48}\right)^{14}} = 1 - x_{HDL}$ and $T_0 = 1752$ K, from which $T_{LL} = 1788 + -9$ K. (Bottom) Discontinuities in $S(Q)$ in the position Q_{max} (black squares) and intensity $S(Q_{max})$ (open squares) of the principal peak occurring at 1788 K (inset in Fig. 4B), which follow x_{LDL}.

correlations, whereas the broad feature centered around 4 Å^{-1} is principally related to Y–Y and Al–Y correlations (*7*, *26*, *33*). On the other hand, $\Delta S(Q)$ in supercooled AY20 at high and low temperatures is different and, with the above attributions, indicates a shift to higher Q for Al–Y correlations, the opposite of what occurs for Y–Y correlations for the HDL/LDL transition. These changes point to a decrease in average Al–Y distances and an increase in Y–Y distances. The latter is illustrated by the cartoon in Fig. 4B showing a switch from edge- to corner-sharing yttria polyhedra for LDL. Molten alumina is largely tetrahedral (*6*, *30*, *33*) with most oxygens present as triclusters (OAl_3), in which case the shortening of Al–Y distances for AY20 between HDL and LDL (Fig. 4B) may be due to the break up of OAl_3 groups. Overall, the density is expected to decrease. The movement in the principal peak Q_{max} and its increase in intensity $S(Q_{max})$ through the HDL/LDL transition (Fig. 4, A and B) coincides with the growth of the LDL phase x_{LDL} analyzed from the maximum in the integrated SAXS data (Fig. 3C). The SAXS/WAXS results (Fig. 3C) therefore show how the switch in interatomic polyhedral packing at 1788 K (Fig. 4B) matches the nanostructural changes that occur in density fluctuations (Fig. 3B). The present results for AY20 contradict nanocrystalline models proposed for yttria-alumina phase transformations (*27*–*29*), where much larger increases in I_{SAXS} would be expected, accompanied by diffraction features in $S(Q)$. Both characteristics are clearly seen in SAXS/WAXS measurements when glass nanoceramics are formed close to the glass transition (*31*) but are absent in these experiments on supercooled yttria-alumina liquids at temperatures well above T_g (Figs. 2 and 3).

We turn now to the dynamic oscillations observed in molten AY20 in the vicinity of 1788 K (Fig. 2B, fig. S1, and movies S1 and S2). A model for this unique stop-and-go behavior is outlined in Fig. 2B. We propose that the rotation of the supercooled drop is driven by the HDL/LDL transition occurring within the levitation nozzle adjacent to the upward flow of gas (Fig. 2A)—a polyamorphic rotor. Whenever $T < T_{LL}$, the liquid within the nozzle [which is approximately one-third of the drop (see movies S1 and S2)] switches abruptly to LDL. As $\Delta\rho/\rho < 0$ the drop is destabilized, resulting in the low-density zone at the bottom flipping to the top, the high viscosity of the LDL phase (*26*) maintaining the rigidity of the drop. The unmixing time is at least as short as the frame exposure time (30 ms). Taking the flip time τ from the full video sequence (movies S1 and S2) gives $\Delta\rho/\rho = 0.031 \pm 0.004$ (*34*), close to the ex situ value determined from recovered, rapidly quenched material (*26*).

The HDL-LDL increase in molar volume in supercooled AY20 in the nozzle ΔV_{LL} is 1.2 ± 0.2 cm^3. This initiates the rotation (movie S1), bringing the LDL cap into the laser beam where it switches back to HDL when T exceeds T_{LL} (Fig. 2B). In the meantime, material at the bottom surrounded by the nozzle gradually cools, and when T there drops below T_{LL}, the HDL/LDL transition repeats and a new cycle commences. Because the HDL/LDL transition is ordering (*26*), this will be accompanied by an exotherm emanating within the material in the nozzle and spreading through to the rest of the drop. However, as soon as the rotor spins the LDL zone under the laser spot (Fig. 2B), the HDL/LDL exotherm should be interrupted by an LDL/HDL endotherm. This qualitatively explains the thermal spike at the start of each cycle where the initial exotherm is overtaken by a sharp dip, followed by gradual warm-

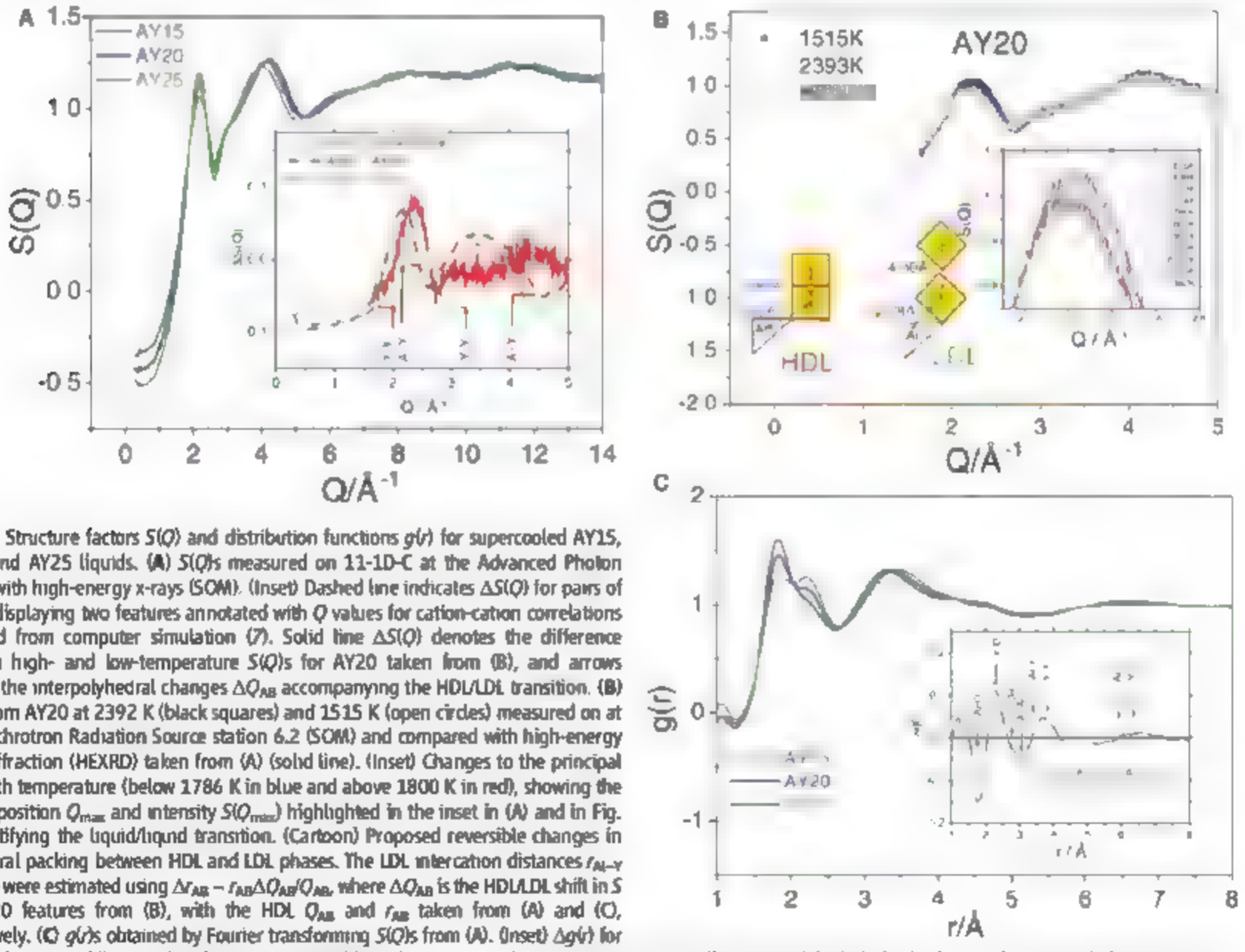

Fig. 4. Structure factors $S(Q)$ and distribution functions $g(r)$ for supercooled AY15, AY20, and AY25 liquids. (**A**) $S(Q)$s measured on 11-ID-C at the Advanced Photon Source with high-energy x-rays (SOM). (Inset) Dashed line indicates $\Delta S(Q)$ for pairs of liquids displaying two features annotated with Q values for cation-cation correlations obtained from computer simulation (*7*). Solid line $\Delta S(Q)$ denotes the difference between high- and low-temperature $S(Q)$s for AY20 taken from (B), and arrows identify the interpolyhedral changes ΔQ_{AB} accompanying the HDL/LDL transition. (**B**) $S(Q)$s from AY20 at 2392 K (black squares) and 1515 K (open circles) measured on at the Synchrotron Radiation Source station 6.2 (SOM) and compared with high-energy x-ray diffraction (HEXRD) taken from (A) (solid line). (Inset) Changes to the principal peak with temperature (below 1786 K in blue and above 1800 K in red), showing the shift in position Q_{max} and intensity $S(Q_{max})$ highlighted in the inset in (A) and in Fig. 3C identifying the liquid/liquid transition. (Cartoon) Proposed reversible changes in polyhedral packing between HDL and LDL phases. The LDL interaction distances r_{Al-Y} and r_{Y-Y} were estimated using $\Delta r_{AB} \sim r_{AB}\Delta Q_{AB}/Q_{AB}$, where ΔQ_{AB} is the HDL/LDL shift in $S(Q)$ AY20 features from (B), with the HDL Q_{AB} and r_{AB} taken from (A) and (C), respectively. (**C**) $g(r)$s obtained by Fourier transforming $S(Q)$s from (A). (Inset) $\Delta g(r)$ for each of the pairs of liquids identifying nearest-neighbor Al–O, Y–O, and O–O separations as well as interpolyhedral Al–Al, Al–Y, and Y–Y correlations. Arrows are centered on the average distances r_{AB} obtained from simulations (*7*).

ing before the next cycle starts (Fig. 2B). The pyrometer and video brightness fluctuations (SOM), however, can also be attributed in part to variations in emissivity over the surface, adding some uncertainty to the temperatures recorded by the pyrometer. Nevertheless, taking the measured temperature limits from Fig. 2B, a figure for the enthalpy change ΔH_{LL} associated with the polyamorphic transition of 34 ± 8 kJ/mol is obtained (*34*), similar to the calorimetric value reported from reheating quenched glasses (*26*).

The critical temperature for the two-state model (*8*), which is defined by $\Delta H/2R$ (where R is the gas constant), is 2030 ± 480 K. Moreover, the HDL/LDL decrease in entropy $\Delta S_{LL} = \Delta H_{LL}/T_{LL}$ is 19 ± 4 J mol^{-1} K^{-1}, approximately half the entropy of fusion (*35*), which therefore excludes alternative explanations of liquid/liquid transitions in supercooled yttria-alumina based on crystallization (*27*–*29*). ΔS_{LL} and ΔV_{LL} are the first-order thermodynamic drivers for the polyamorphic transition and determine the gradient of the HDL/LDL phase boundary in supercooled AY20; namely $dT/dP = \Delta V_{LL}/\Delta S_{LL} = -62$ K/GPa. This negative slope and the ±σ limits (Fig. 3C) closely match predictions from the two-state model (Fig. 1), from which a more precise value for the critical point C (1804 K, −0.31 GPa) is obtained using the Ponyatovsky formalism (*36*).

We believe that the contactless in situ approach described here, which has enabled us to detect the variables that define the liquid/liquid transition in supercooled yttria-alumina, can also be applied at lower temperatures to search for polyamorphic and nonequilibrium transitions more generally where ambient pressure is the norm (for instance, in other supercooled inorganic systems like liquid metals as well as in organic liquids). With levitated drops and SAXS/WAXS, it may well be possible to explore instabilities in supercooled water at temperatures that have so far proven inaccessible (*3*).

References and Notes

1. A. Onuki, *Phase Transition Dynamics* (Cambridge Univ. Press, Cambridge, 2004).
2. P. W. Bridgeman, *The Physics of High Pressure* (G. W. Bell and Sons, London, 1949).
3. P. G. Debenedetti, *Metastable Liquids* (Princeton Univ. Press, Princeton, NJ, 1997).
4. P. H. Poole, T. Grande, C. A. Angell, P. F. McMillan, *Science* **275**, 322 (1997).
5. P. F. McMillan, *J. Mater. Chem.* **14**, 1506 (2004).
6. G. N. Greaves, S. Sen, *Adv. Phys.* **56**, 1 (2007).
7. P. F. McMillan *et al.*, *J. Phys. Condens. Matter* **19**, 415101 (2007).
8. E. Rapoport, *J. Chem. Phys.* **46**, 3279 (1967).
9. E. G. Ponyatovsky, O. I. Barkalov, *Mater. Sci. Rep.* **8**, 147 (1992).
10. O. Mishima, L. D. Calvert, E. Whalley, *Nature* **310**, 393 (1984).
11. P. H. Poole, F. Sciortino, U. Essmann, H. E. Stanley, *Nature* **360**, 324 (1992).
12. J. L. Finney, A. Hallbrucker, I. Kohl, A. K. Soper, D. T. Bowron, *Phys. Rev. Lett.* **88**, 225503 (2002).
13. O. Mishima, Y. Suzuki, *Nature* **419**, 599225503 (2002).
14. R. J. Nelmes *et al.*, *Nature Phys.* **2**, 414 (2006).
15. M. M. Koza, R. P. May, H. Schober, *J. Appl. Crystallogr.* **40**, S517 (2007).
16. V. V. Brazhkin, S. V. Popova, R. N. Voloshin, *High Pressure Res.* **15**, 267 (1997).
17. M. Grimsditch, *Phys. Rev. Lett.* **52**, 2379 (1984).
18. P. F. McMillan, M. Wilson, D. Daisenberger, D. Machon, *Nat. Mater.* **4**, 680 (2005).
19. A. Di Cicco *et al.*, *High Pressure Res.* **24**, 93 (2004).
20. G. N. Greaves, F. Meneau, O. Majerus, D. G. Jones, J. Taylor, *Science* **308**, 1299 (2005).
21. S. Sastry, C. A. Angell, *Nat. Mater.* **2**, 739 (2003).
22. Y. Katayama *et al.*, *Nature* **403**, 170 (2000).
23. Y. Katayama *et al.*, *Science* **306**, 848 (2004).
24. S. Aasland, P. F. McMillan, *Nature* **369**, 633 (1994).
25. J. K. Weber *et al.*, *J. Am. Ceram. Soc.* **83**, 1868 (2000).
26. M. C. Wilding, P. F. McMillan, *J. Non-Cryst. Solids* **293–295**, 357 (2001).
27. K. Nagashio, K. Kuribayashi, *J. Am. Ceram. Soc.* **85**, 2353 (2002).
28. J. A. Tangeman, B. L. Phillips, R. Hart, *J. Am. Ceram. Soc.* **90**, 758 (2007).
29. L. B. Skinner, A. C. Barnes, P. S. Salmon, W. A. Crichton, *J. Phys. Condens. Matter* **20**, 205103 (2008).
30. C. Landron *et al.*, *Phys. Rev. Lett.* **86**, 4839 (2001).
31. W. Bras, G. N. Greaves, M. Oversluizen, S. M. Clark, G. Beckhaut, *J. Non-Cryst. Solids* **351**, 2178 (2005).
32. R. J. Cernik *et al.*, *J. Synchrotron Radiat.* **11**, 163 (2004).
33. V. Cristiglio *et al.*, *J. Phys. Condens. Matter* **19** 415105 (2007).
34. The equation of motion for an unstable spherical pendulum is $d^2\theta/dt^2 = Q\sin\theta$, where θ is the angular displacement from vertical and $Q = A(\Delta\rho/\rho)g/a$ [where a is the radius (1.15 mm) and g is the acceleration due to gravity (9.8 ms^{-2})]. For the polyamorphic rotor model, $\Delta\rho/\rho$ is the density contrast between HDL and LDL components of the sphere and A is a constant that governs the moment of inertia and is approximately equal to the fraction of the sphere converted to LDL (~1/3). The time for the sphere to flip through 180° is $\tau \approx 6Q^{-1/2}$. From the video frames, $\tau = 600 \pm 70$ ms, giving $\Delta\rho/\rho = 0.031 \pm 0.004$. If the enthalpy associated with the HDL/LDL transition is emitted radiatively, $dT/dt = \frac{\varepsilon\sigma S(T^4 - T_0^4)}{C_p}$, where ε is the emissivity, σ is Stefan's constant (5.67×10^{-8} W m^{-2} K^{-4}), S is the area of the sphere, T_0 is the equilibrium temperature, and the specific heat C_p is set equal to the Dulong and Petit value of 24.96 J/mol. The radiant exotherm is parameterized from the measured temperature limits shown in Fig. 2B, the onset of the equivalent LDL/HDL endotherm being offset by 250 ms from the rise of the initial HDL/LDL exotherm that starts the cycle. The resulting oscillating temperatures are shown by the dashed blue curve with the emitted/absorbed powers yielding a value for the enthalpy ΔH_{LL} of the polyamorphic transition of 34 ± 8 kJ/mol.
35. If alumina or yttrium-aluminum-garnet nucleated instead of LDL, as has been proposed by some researchers (*27*–*29*), the exotherm would be due to ΔS_{liquid}, which equals 48 J mol^{-1} K^{-1} and 30 J mol^{-1} K^{-1}, respectively, compared with the ΔS_{LL} value of 19 ± 4 J mol^{-1} K^{-1} measured in these in situ experiments. Also, $\Delta\rho/\rho > 0$, which would not destabilize the rotor action (Fig. 2B and movies S1 and S2).
36. The measured temperature rise at the top of the rotor, which we attribute to the LDL/HDL transition initiated in the nozzle, indicates substantial superheating. This is in excess of the upper spinodal limit shown in Fig. 2B and defined by the two-state model (*9*), in which case internal superheating might trigger the reverse endothermic LDL/HDL transition rather than external laser heating.

37. We thank W. Bras, P. McMillan, and P. Poole for very useful discussions; the Science Technology Facilities Council and staff at the Synchrotron Radiation Source for access to the SAXS/WAXS facilities on station 6.2; and the Advanced Photon Source for access to high-energy x-ray scattering facilities on 11-ID-C. We also acknowledge the support of the Higher Education Funding Council in Wales through the Centre for Advanced Functional Materials and Devices.

Supporting Online Material

www.sciencemag.org/cgi/content/full/322/5901/566/DC1
Materials and Methods
Figs. S1 and S2
References
Movies S1 and S2

21 May 2008; accepted 17 September 2008
10.1126/science.1160766

Direct Imaging of Reconstructed Atoms on TiO_2 (110) Surfaces

N. Shibata,[1,2]* A. Goto,[1] S.-Y. Choi,[1†] T. Mizoguchi,[1] S. D. Findlay,[1] T. Yamamoto,[1,3] Y. Ikuhara[1,3,4]

Determining the atomic structures of oxide surfaces is critical for understanding their physical and chemical properties but also challenging because the breaking of atomic bonds in the formation of the surface termination can involve complex reconstructions. We used advanced transmission electron microscopy to directly observe the atomic structure of reduced titania (TiO_2) (110) surfaces from directions parallel to the surface. In our direct atomic-resolution images, reconstructed titanium atoms at the top surface layer are clearly imaged and are found to occupy the interstitial sites of the TiO_2 structure. Combining observations from two orthogonal directions, the three-dimensional positioning of the Ti interstitials is identified at atomic dimensions and allows a resolution of two previous models that differ in their oxygen stoichiometries.

Determining the atomic as well as electronic structures of surfaces is critical for understanding the physical and chemical properties of oxide materials. Because of the abrupt discontinuity of atomic bonds, it is well known that oxide surfaces often undergo atomic-scale structural reconstructions. Surface-science techniques such as diffraction and scanning-probe microscopy have revealed the presence of atomic-scale structural reconstructions, and density-functional theory (DFT) calculations have provided energetic backgrounds for them (*1*–*3*). However, detailed experimental estimation of reconstructed structures in oxides is still controversial because the direct determination of complex rearrangement of metal as well as oxygen atoms in three dimensions is extremely difficult with these approaches. Direct atomic-scale observation from the direction parallel to the surface, "profile imaging" in transmission electron microscopy (TEM) (*4*–*6*), may provide crucial structural information on how atoms are actually rearranged and reconstructed on oxide surfaces.

Titania (TiO_2) is used in many technological applications, such as heterogeneous catalysts, photocatalysts, gas sensors, and coatings. These applications strongly depend on its surface properties, so an understanding of the atomic as well as the electronic structure of its surfaces has been sought for many years (*2*). However, the atomic-scale structure of TiO_2 surfaces is still controversial, even for low-index stable surfaces such as (110), which has long been studied as a model oxide surface (*1*, *2*, *7*). In particular, when the (110) surfaces are reduced by vacuum annealing, the expected [stoichiometric bulk (1×1)] termination evolves into several atomic-scale surface reconstructions (*2*, *7*), and there has been growing speculation that these surface reconstructions involve Ti atoms in the interstitial sites of rutile structure (*8*–*14*). (In a strict sense, we cannot define interstitial sites on surfaces in the same way as we do in bulk, but we follow this conventional terminology throughout this paper.)

Recently, Park *et al.* proposed a new structural candidate for the (1×2) reconstruction based on scanning tunneling microscopy observations combined with DFT calculations (*10*). In this model, Ti atoms occupy interstitial sites on the surface, similar to the commonly accepted added Ti_2O_3 row model proposed by Onishi and Iwasawa (*8*, *9*). However, the critical difference in these two models is the occupation of different Ti interstitial sites on the surface. In each (110) layer, there are two Ti interstitial sites surrounded by distorted O octahedra in rutile TiO_2. We adopted the standard notation for these two Ti interstitial sites as *ih* and *iv* sites (*11*), whose octahedra have parallel (horizontal) and perpendicular (vertical) equatorial planes to the (110) surface, respectively. In the Park *et al.* model, Ti interstitials are proposed to occupy *ih* sites, whereas in the Onishi-Iwasawa model, they occupy *iv* sites. A recent detailed low-energy electron diffraction study supported the formation of the Onishi-Iwasawa model rather than the Park *et al.* model (*15*). Thus, although Ti interstitials have been suggested as the fundamental building block of surface reconstructions in reduced TiO_2 (110) surfaces, their presence and positioning have not yet been established (*2*, *6*).

We used atomic-resolution TEM to directly observe surface structures of TiO_2 (110) from directions parallel to the surface. Combining the advanced TEM techniques of high-voltage electron microscopy (HVEM), aberration-corrected high-angle annular dark-field (HAADF), scanning TEM (STEM), and observations made using these techniques from orthogonal directions, we show definitive evidence of the presence and positioning of Ti interstitials in the reconstructed surface structure under a reducing atmosphere. We used a single-crystalline (110) substrate of rutile TiO_2 as a starting material and thinned it with mechanical polishing followed by ion bombardment in order to obtain electron-transparent TEM samples. The TEM samples were then annealed in air at 973 K for 30 min to obtain atomically flat (110) specimen edges. It has been demonstrated that annealing in air at similar temperatures promotes the formation of atomically flat unreconstructed structures on the TiO_2 (110) surface (*16*, *17*). We confirmed this result in the as-annealed TEM samples by HAADF-STEM observations, as shown in fig. S1 (*18*), and determined that the (110) flat surfaces found in our TEM samples can be regarded as a model of the extended (110) surfaces.

Figure 1 shows a HVEM image of the (110) surface observed from the [001] direction. According to systematic HVEM image simulations based on the multislice method, the sample thickness at the specimen edge is estimated to be less than 5 nm. The (110) surfaces are atomically flat over extended regions up to several tens of nanometers along the [$\bar{1}$10] direction. This result indicates that the present annealing condition enhanced the formation of stable (110) terraces at the specimen edge. However, it is also clear that structural reconstruction has occurred at the top surface layer. These reconstructions are thought to be caused by the high-voltage electron irradiation that occurs in HVEM; electron irradiation in medium-voltage TEM (300 to 400 kV) reduces TiO_2 surfaces mainly by a radiolytic process (*19*, *20*) in which O atoms are progressively lost from the irradiated volume through electron-stimulated desorption (*21*, *22*). Under the ultrahigh-voltage electron-beam irradiation, "knock-on" or sputtering may also have a substantial effect on the structure, enhancing the surface reduction by preferentially sputtering lighter elements, in this case oxygen. Whichever mechanism dominates, we have experimentally confirmed the reduction of the surface.

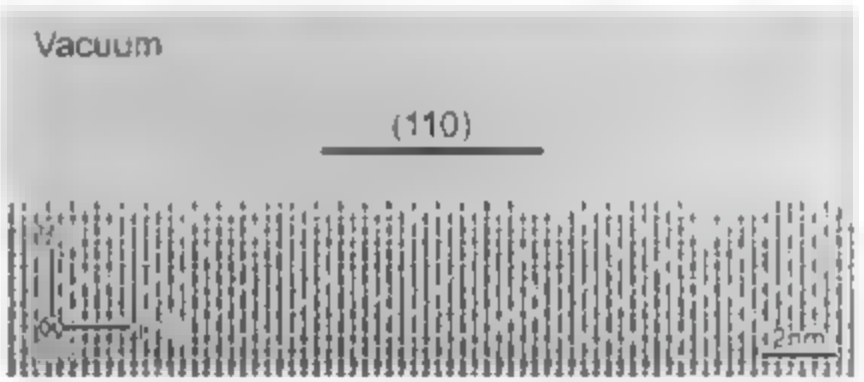

Fig. 1. High-resolution HVEM image of a TiO_2 (110) surface observed from the [001] direction. The (110) surface is atomically flat over extended regions up to several tens of nanometers in the [$\bar{1}$10] direction. According to systematic HVEM image simulations, the sample thickness at the specimen edge is estimated to be less than 5 nm. The structural reconstruction is visibly formed at the top surface in the image, and the reconstruction further progressed during extended observation. The observed reconstruction is thus considered to be introduced by the high-energy electron irradiation in HVEM.

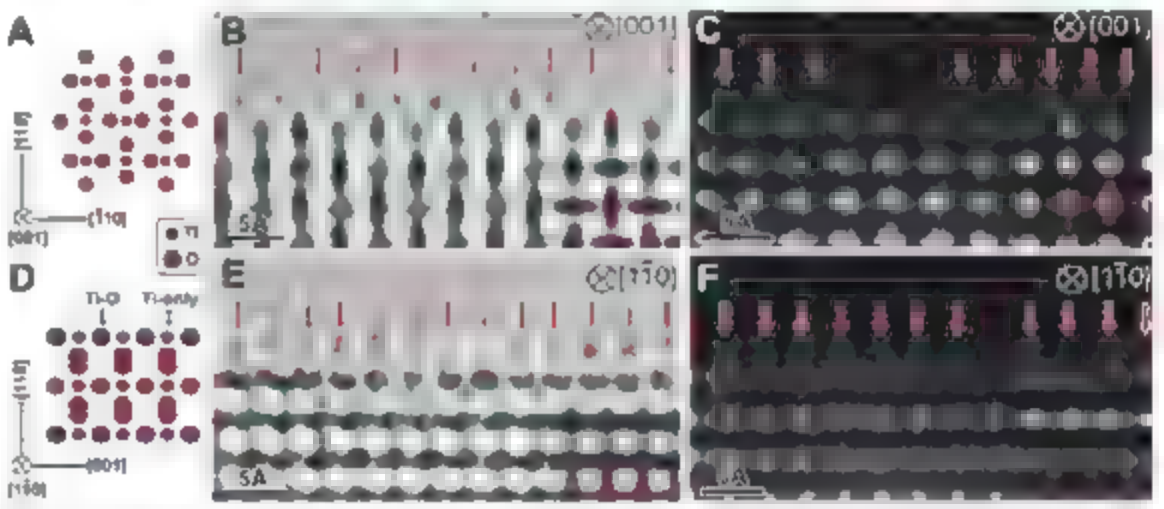

Fig. 2. Atomic-resolution cross-sectional HVEM and HAADF-STEM images of TiO_2 (110) surface observed from the [001] and [1$\bar{1}$0] directions. (**A** and **D**) Schematic illustrations of a rutile TiO_2 structure viewed along the [001] (A) and [1$\bar{1}$0] (D) directions. (**B** and **E**) The magnified HVEM images of the (110) surface viewed from the [001] (B) and [110] (E) directions. Comparing them with the simulated HVEM images in the insets, the dark image contrast corresponds to the position of atomic columns. These simulations were performed with a defocus value of −35 nm and a film thickness of 3 nm ([001] projection) and 7 nm ([1$\bar{1}$0] projection). (**C** and **F**) Atomic-resolution HAADF-STEM images of the TiO_2 (110) surfaces after HVEM observations viewed from the [001] (C) and [110] (F) directions. In these images, bright contrast corresponds to the position of Ti-containing atomic columns. The HAADF image simulations shown as insets were performed with a defocus value of 0 nm and the same film thicknesses as the HVEM simulations.

[1]Institute of Engineering Innovation, University of Tokyo, 2-11-16, Yayoi, Bunkyo, Tokyo 113-8656, Japan. [2]Precursory Research for Embryonic Science and Technology (PRESTO), Japan Science and Technology Agency, 4-1-8 Honcho Kawaguchi, Saitama 332-0012, Japan. [3]Nanostructures Research Laboratory, Japan Fine Ceramic Center, 2-4-1 Mutsuno, Atsuta-ku, Nagoya 456-8587, Japan. [4]World Premier International Research Center, Advanced Institute for Materials Research, Tohoku University, 2-1-1, Katahira, Aoba-ku, Sendai 980-8577 Japan.

*To whom correspondence should be addressed. E-mail: shibata@sigma.t.u-tokyo.ac.jp

†Present address: Korea Institute of Materials Science, Changwon, South Korea.

face after HVEM observations by STEM electron energy-loss spectroscopy analysis shown in fig. S2 (*18*). We used this in situ reduction process to induce structural reconstructions on the TiO_2 (110) surfaces. We experimentally observed several types of structural reconstructions depending on the degree of electron irradiation (fig. S3) (*18*) and therefore reduction, but we focus here on the early stage of reconstruction that occurs at the top-surface Ti atoms.

Figure 2, A and D, shows crystal structure models of rutile TiO_2 viewed from the [001] and [1$\bar{1}$0] directions, respectively. The Ti and O columns are separated as different atomic columns in the [001] projection, whereas there are two different Ti-containing atomic columns alternately aligned in the [1$\bar{1}$0] projection (which we refer to as Ti-O columns and Ti-only columns, respectively). Figure 2, B and E, shows typical magnified HVEM images of TiO_2 (110) surfaces viewed from the [001] and [1$\bar{1}$0] directions, respectively. These two incident-beam directions are both parallel to the (110) surface but are perpendicular to each other. In agreement with the simulated images in the insets, the dark image contrast corresponds to the position of atomic columns under the present imaging condition. Moreover, their intensities correspond to the atomic species of the columns in the [001] projection (there is a stronger contrast in Ti columns and weaker contrast in O columns, as shown in the inset). The [001] projected HVEM image in Fig. 2B shows the positions of Ti atoms at the top surface layer shifted from the expected positions in the rutile structure, as indicated by the arrows. These Ti sites correspond to the interstitial sites as referred to the bulk rutile structure, but we cannot determine whether these Ti interstitials occupy *iv* or *ih* sites from this projection. In the [110] projected HVEM image in Fig. 2E, top-surface Ti atoms are also clearly observed (arrows), which correspond to the Ti interstitials found in the [001] projection. Comparing them with the simulated image in the inset, these surface Ti atoms are only found on top of Ti-O columns. After the above observation by HVEM, the same samples were transferred into STEM and observed by the HAADF imaging mode, as shown in Fig. 2, C and F. We can directly determine the atomic column positions from the image contrast in the HAADF imaging mode because of its incoherent imaging characteristics and atomic number (Z)–dependent contrast (proportional to ~Z^2) (*23*). In the HAADF imaging mode, bright contrast corresponds to the Ti-containing atomic columns, as confirmed by the simulated images in the insets. In the [001] HAADF image in Fig. 2C, Ti atoms at the surface layer are shifted from the expected positions in the bulk, as indicated by the arrows. These observed sites correspond to the Ti interstitial sites, which is consistent with the HVEM observations. In the [110] HAADF image in Fig. 2F, surface Ti atoms are found only on top of the brighter Ti-containing columns, as indicated by arrows. In the bulk [1$\bar{1}$0] HAADF image, there are two atomic columns with different image contrasts along the [001] direction. The image simulation, shown in the inset, clearly shows that the brighter contrast corresponds to the Ti-O columns, whereas the weaker contrast corresponds to the Ti-only columns. The difference in contrast between the two Ti-containing columns mainly results from the difference in the atomic-column occupancy along the [1$\bar{1}$0] axis. Again, the top-surface Ti atoms are found only on top of the Ti-O columns. Thus, both HVEM and HAADF-STEM images provide consistent information on the position of the reconstructed Ti atoms on the (110) surface. From these orthogonal projected images, the three-dimensional positioning of the reconstructed Ti atoms on the TiO_2 (110) surface can be identified. The orthogonal observations were carried out on separate TEM samples. However, the heights of the Ti atoms in the reconstructed surface monolayer above the unreconstructed bulk are the same for the two different orientations for the same imaging mode, and the Ti interstitial sites are found to be reproducible. Thus, we conclude that the same surface structure is being observed in the two orthogonal atomic-resolution images. The height of the Ti interstitials from the bottom Ti layer is estimated to be about 1.6 Å by the HAADF-STEM images.

Figure 3 shows the two previously proposed double-strand models for the (1×2) surface reconstruction involving Ti interstitials by Onishi-Iwasawa (Fig. 3A) (*8*, *9*) and Park *et al.* (Fig. 3B) (*10*). That surface reconstruction was typically formed during sputter-annealing cycles in ultra-high vacuum conditions and is considered to be the representative structure formed for a relatively low level of reduction (*7*). Although apparent (1×2) periodicity is not necessarily found in our reduction process by using electron irradiation, our observations are reproducible, which indicates the stability of the reconstruction and, hence, of the positioning of the Ti interstitials. Additionally, the same Ti positioning is found in observations carried out on vacuum-annealed samples, more similar to those used by Onishi-Iwasawa and Park *et al.*, as shown in fig. S4 (*18*). Therefore, we compared these proposed surface reconstruction models with the present observations as

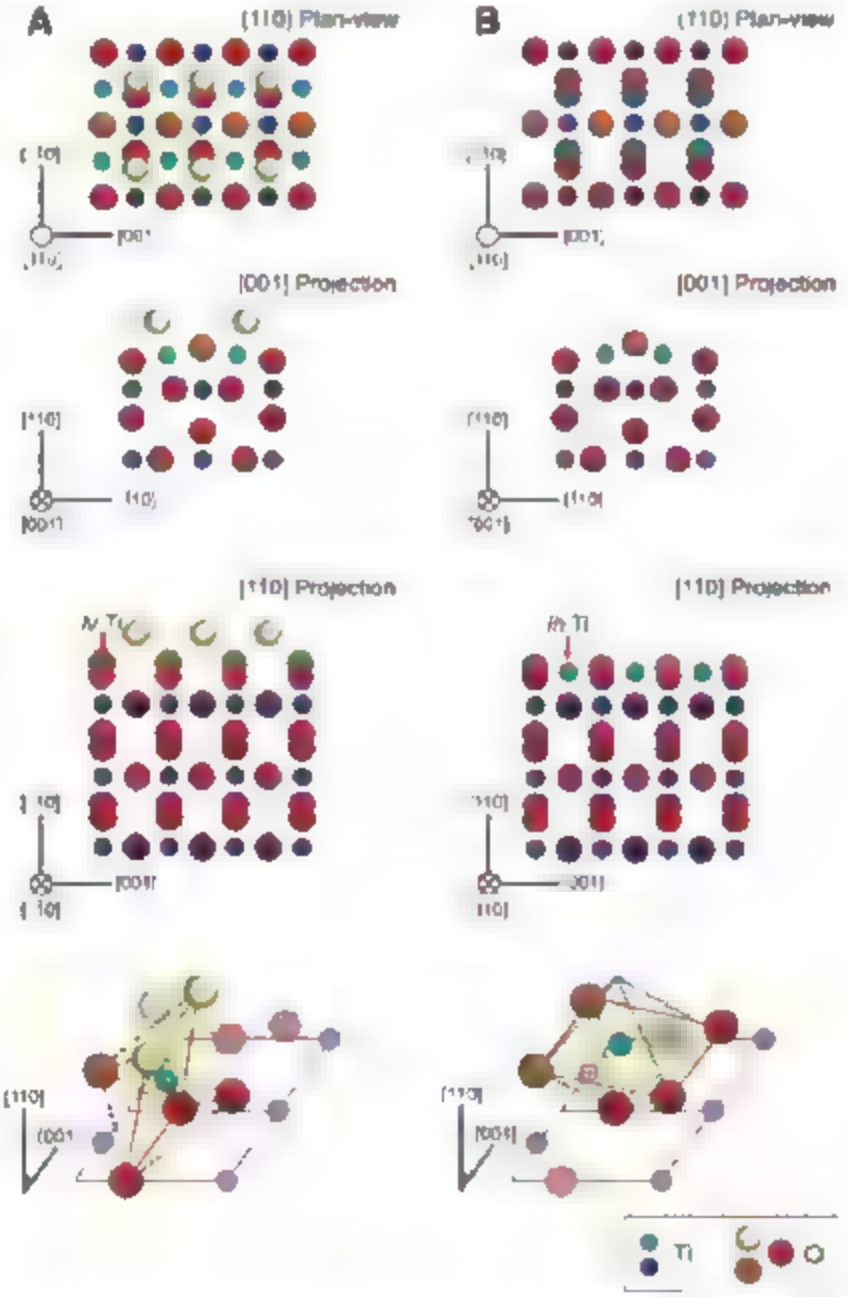

Fig. 3. Two surface reconstruction models of a reduced TiO_2 (110) surface. (**A**) The reconstruction model proposed by Onishi-Iwasawa (*8*, *9*). (**B**) The reconstruction model proposed by Park *et al.* (*10*). In the schematics, large and small circles correspond to O and Ti atoms, respectively. Slight differences in colors represent the height difference on the (110) surface. Light blue atoms are the reconstructed Ti atoms on the top surface. In each model, we provide four schematics ((110) plan-view, [001] projection, [1$\bar{1}$0] projection, and a bird's-eye view of the Ti interstitial coordination polyhedra). The equatorial planes of the Ti interstitial coordination polyhedra are surrounded by red lines and are yellow in the schematics. In both models, the reconstructed Ti atoms occupy interstitial sites of the TiO_2 rutile structure and appear to be almost identical in the [001] projection. However, these two models differ in the [1$\bar{1}$0] projection. The interstitial Ti atoms (in *iv* sites) are found on top of Ti-only columns in the Onishi-Iwasawa model, whereas the interstitial Ti atoms (in *ih* sites) are found on top of Ti-O columns in the Park *et al.* model. The present HVEM and STEM observations coincide only with the Park *et al.* model.

the representative structural candidates formed in the early stages of reduction of the TiO_2 (110) surface.

Four schematics in each structural model are shown: (110) plan-view, [001] projection, [110] projection, and a bird's-eye view of the Ti interstitial coordination polyhedra. From the [001] projection, the reconstructed Ti atoms (Fig. 3, light blue) are viewed to occupy the same interstitial sites in the two models. However, from the [110] projection, we can distinguish the two models by the positioning of the Ti interstitials along the [001] direction. In the [1$\bar{1}$0] projected models, Ti interstitials are positioned on top of Ti-only columns (*iv* sites) in the Onishi-Iwasawa model, whereas they are on top of Ti-O columns (*ih* sites) in the Park *et al.* model. The present [110] projected HVEM and HAADF-STEM images show that the Ti interstitials are found on top of Ti-O columns. In all observations, our results directly evidence the formation of Ti interstitials in the *ih* sites under the present reducing condition, which is consistent with the Park *et al.* model but not with the Onishi-Iwasawa model.

It has been theoretically predicted that the above two models are energetically favorable structures (*10*, *12*). However, the fundamental difference in the two models is the stoichiometry of the surface: O is more deficient in the Park *et al.* model than in the Onishi-Iwasawa model. As shown in the schematics, the Ti interstitials are octahedrally coordinated to O in the two models, but the O atom at one apex of the O octahedra is absent (one Ti-O dangling bond is present) in the Park *et al.* model. However, if we remove the topmost O atoms (Fig. 3, yellow) from the Onishi-Iwasawa model to equalize the surface stoichiometry, two Ti-O dangling bonds would be introduced to the Ti interstitials because these O atoms lie on the equatorial plane of the O octahedra. Thus, simple dangling bond considerations suggest that the Ti interstitials in the *ih* sites should be energetically more favorable under the progressive reduction, which is consistent with our experimental findings.

Our observations show that interstitial Ti atoms (in *ih* sites) are actually involved in the reconstruction of TiO_2 (110) surfaces. The distance between proximate *ih* and *iv* sites is less than 1.5 Å along the [001] direction, but the present direct atomic-resolution images distinguish the two interstitial sites on the surface. These results not only provide an atomic-scale cornerstone for complex surface reconstructions in TiO_2, they also open up new possibilities for characterizing the atomic-scale structure and chemistry of oxide surfaces. Recently, Ti interstitials near the TiO_2 (110) surface region have been proposed to be responsible for the defect state in the band gap (*24*), although O vacancies have been thought to be the key for many years. The ability to directly see interstitial atoms at surfaces should substantially assist our understanding of surface structures and, hence, properties of TiO_2 and other oxide materials. Direct atomic-scale imaging with recent advanced EM is a powerful method for unraveling complex atomic structures of oxide surfaces.

References and Notes

1. V. E. Henrich, P. A. Cox, *The Surface Science of Metal Oxides* (Cambridge Univ. Press, Cambridge, 1994).
2. U. Diebold, *Surf. Sci. Rep.* **48**, 53 (2003).
3. D. S. Deak, *Mater. Sci. Technol.* **23**, 127 (2007).
4. J. M. Cowley, *Prog. Surf. Sci.* **21**, 209 (1986).
5. A. N. Chiaramonti, L. D. Marks, *J. Mater. Res.* **20**, 1619 (2005).
6. S. Li *et al.*, *Appl. Surf. Sci.* **241**, 68 (2005).
7. M. Bowker, *Curr. Opin. Solid State Mater. Sci.* **10**, 153 [redacted]
8. H. Onishi, Y. Iwasawa, *Surf. Sci.* **313**, L783 (1994).
9. H. Onishi, Y. Iwasawa, *Phys. Rev. Lett.* **76**, 791 (1996).
10. K. T. Park, M. H. Pan, V. Meunier, E. W. Plummer, *Phys. Rev. Lett.* **96**, 226105 (2006).
11. S. D. Elliott, S. P. Bates, *Phys. Chem. Chem. Phys.* **3**, 1954 (2001).
12. S. D. Elliott, S. P. Bates, *Phys. Rev. B* **65**, 245415 (2002).
13. M. Blanco-Rey *et al.*, *Phys. Rev. Lett.* **96**, 055502 (2006).
14. K. T. Park, M. Pan, V. Meunier, E. W. Plummer, *Phys. Rev. B* **75**, 245415 (2007).
15. M. Blanco-Rey *et al.*, *Phys. Rev. B* **75**, 081402 (2007).
16. Y. Lu, B. Jaeckel, B. A. Parkinson, *Langmuir* **22**, 4472 [redacted]
17. R. Nakamura *et al.*, *J. Phys. Chem. B* **109**, 1648 (2005).
18. Materials and methods are available as supporting material on *Science* Online.
19. D. J. Smith, M. R. McCartney, L. A. Bursill, *Ultramicroscopy* **23**, 299 (1987).
20. M. R. McCartney, D. J. Smith, *Surf. Sci.* **250**, 169 (1991).
21. M. L. Knotek, P. J. Feibelman, *Phys. Rev. Lett.* **40**, 964 (1978).
22. R. D. Ramsier, J. T. Yates Jr., *Surf. Sci. Rep.* **12**, 243 (1991).
23. S. J. Pennycook, D. E. Jesson, *Ultramicroscopy* **37**, 14 (1991).
24. S. Wendt *et al.*, *Science* **320**, 1755 (2008).

25. We thank H. Tsunakawa for assistance with HVEM observations. This work was supported in part by the Grant-in-Aid for Scientific Research on Priority Areas Nano Materials Science for Atomic-scale Modification 474 from the Ministry of Education, Culture, Sports and Technology. N.S. acknowledges support from PRESTO, the Japan Science and Technology Agency, and the Industrial Technology Research Grant Program in 2007 from the New Energy and Industrial Technology Development Organization. S.D.F. is supported as a Japanese Society for the Promotion of Science Fellow.

Supporting Online Material

www.sciencemag.org/cgi/content/full/322/5901/570/DC1
Materials and Methods
Figs. S1 to S4
References

25 August 2008; accepted 12 September 2008
10.1126/science.1165044

The Extent of Non–Born-Oppenheimer Coupling in the Reaction of Cl(^2P) with *para*-H_2

Xingan Wang,[1] Wenrui Dong,[1] Chunlei Xiao,[1] Li Che,[1] Zefeng Ren,[1] Dongxu Dai,[1] Xiuyan Wang,[1] Piergiorgio Casavecchia,[1*] Xueming Yang,[1]† Bin Jiang,[2] Daiqian Xie,[2,3]† Zhigang Sun,[2,4] Soo-Y. Lee,[4] Dong H. Zhang,[1]† Hans-Joachim Werner,[5] Millard H. Alexander[6]†

Elementary triatomic reactions offer a compelling test of our understanding of the extent of electron-nuclear coupling in chemical reactions, which is neglected in the widely applied Born-Oppenheimer (BO) approximation. The BO approximation predicts that in reactions between chlorine (Cl) atoms and molecular hydrogen, the excited spin-orbit state (Cl*) should not participate to a notable extent. We report molecular beam experiments, based on hydrogen-atom Rydberg tagging detection, that reveal only a minor role of Cl*. These results are in excellent agreement with fully quantum-reactive scattering calculations based on two sets of ab initio potential energy surfaces. This study resolves a previous disagreement between theory and experiment and confirms our ability to simulate accurately chemical reactions on multiple potential energy surfaces.

For more than 150 years, the reaction of chlorine atoms with molecular hydrogen, $Cl(^2P) + H_2 \rightarrow HCl + H$, has been one of the most widely studied elementary chemical reactions (*1*–*3*). In particular, investigations of this reaction laid the framework for the development of transition-state theory (*4*). Recently, this reaction (*2*, *5*–*8*), as well as the reaction of F with H_2 (*9*–*11*), have become testing grounds for improving the depth and accuracy of our understanding of how quantum mechanics is manifested in chemical reactivity.

The Cl atom is a free radical, with an unfilled p shell, which imparts an electronic directionality to the atom. Only one of the three possible orientations leads, over a substantial barrier, to products (*5*, *12*). The other two orientations are nonreactive at low to moderate energies (Fig. 1). The interaction between the orbital and spin angular momenta of the atom results in two possible spin-orbit states, separated energetically by ~2.5 kcal/mol of energy (880 cm^{-1}). The dependence of the reactive potential energy surfaces (PESs) on the orientation of the p shell then manifests itself in a differing reactivity for the two spin-orbit states of the atom.

The understanding of collisions between atoms and molecules is vastly simplified by the Born-Oppenheimer (BO) approximation, which states that nuclear motion will occur on PESs that correspond to the energies of the rapidly rearranging electrons as a function of the positions of the more slowly moving nuclei. Thus, a particular electronic energy state of the reactants will evolve along a

single PES. In the case of the Cl + H_2 reaction, the excited spin-orbit state will react only if the BO approximation is broken during the reaction, which then allows the excited spin-orbit reactants to transfer from a nonreactive PES to the reactive PES, by means of what is called a "nonadiabatic transition" (*13*). This process is illustrated schematically in Fig. 1.

The overall applicability of the BO approximation to chemical reactions has been established by a large number of experimental studies (*3*, *14*). More specifically, in the case of the analogous reaction of F with D_2, Yang, Alexander, Werner, and their co-workers have shown (*11*) that the reactivity of the excited spin-orbit state of the F atom, compared to that of the ground spin-orbit state, is small except at very low collision energies, where the barrier limits reaction of the ground spin-orbit state. Here, molecular-beam experimental measurements agreed quantitatively with predictions of fully quantum calculations based on the accurate ab initio PESs for the FD_2 system determined by Li, Werner, and co-workers (*15*).

A natural extension would be to the Cl + H_2 reaction. Because of the significant increase in the reaction barrier [8.45 kcal/mol for Cl + H_2 (*16*) as compared to 1.63 kcal/mol for F + H_2 (*17*), without including the atomic spin-orbit splitting], the reaction cross section will be much smaller, so that experimental investigation of Cl + H_2 is a greater challenge. Quantum-scattering studies, similar to those done for F + H_2/D_2, predicted that the excited spin-orbit state of Cl will be even more unreactive than that of F, because of the larger spin-orbit splitting in the heavier Cl atom (*5*, *12*). However, contrary to the predictions of theory, an experimental molecular-beam study of the Cl + H_2 reaction by means of Doppler-selected time-of-flight (TOF) detection of the H-atom product suggested that reactivity of the excited spin-orbit state becomes increasingly dominant as the collision energy increases (*18*, *19*).

Other experiments have been designed to resolve this disagreement (*8*, *7*, *20*). Crossed–molecular beam measurements of differential cross sections for the Cl + H_2 reaction by Casavecchia and co-workers by means of mass-spectrometric detection of the HCl product suggested that the excited spin-orbit state played only a minor role (*7*). However, the experimental resolution was insufficient to separate unambiguously products formed by reaction of Cl* from those formed by Cl. Recently, Neumark and co-workers (*8*) used photodetachment spectroscopy of the ClH_2^- anion to probe the extent of non-BO coupling in the region of the ClH_2 PES where this coupling is most likely to occur. Neumark's experiments, and the analysis of the accompanying theoretical calculations (*21*), indicate that the breakdown in the BO approximation is small.

Having achieved high precision in the comparison of theory and experiment for the F + D_2 reaction (*11*), we applied the same strategy to the Cl + H_2 reaction. As discussed above, a particular challenge is the much smaller cross section for the latter reaction, due to the higher reaction barrier. We report here a high-resolution, crossed–molecular beam study of the Cl + H_2 reaction in which we make use of the H-atom Rydberg tagging method (*22*). We concentrated on low collision energies (E_c = 4 to 6 kcal/mol), where nonadiabatic effects are expected to be most pronounced (*5*, *12*). Because the barrier to the Cl + H_2 reaction, corrected for zero-point energy, is ~5.5 kcal/mol (*23*), quantum-mechanical tunneling will contribute appreciably to the reaction at the collision energies considered here.

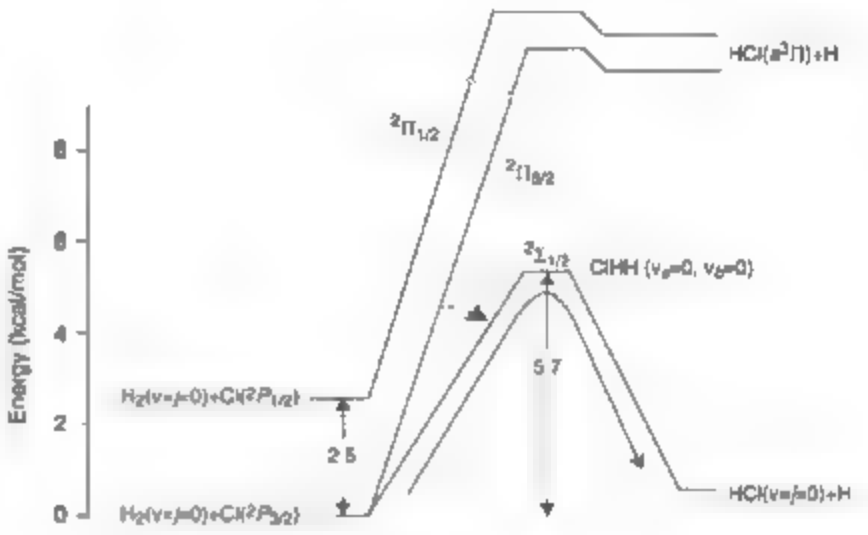

Fig. 1. Relative energies (to scale) for the Cl/Cl* + H_2 reaction, after inclusion of the spin-orbit splitting, with a schematic representation of the three ClH_2 electronically adiabatic PESs, labeled for collinear geometry. The vibrational zero-point energy (for reactants, products, and at the barrier) has been included. The PESs for the two Π states correlate, in the product arrangement, with HCl($a^3\Pi$) + H, which lies at least 150 kcal/mol above the Cl($^2P_{3/2}$) + H_2 asymptote. Consequently, the position of this asymptote is not drawn to scale. Reaction of Cl($^2P_{3/2}$) is BO-allowed and can proceed along the lowest PES (shown schematically by the solid arrow). However, for the excited spin-orbit state to react, a nonadiabatic "hop" (shown schematically by the dashed arrow) must occur from an excited PES to the lowest PES.

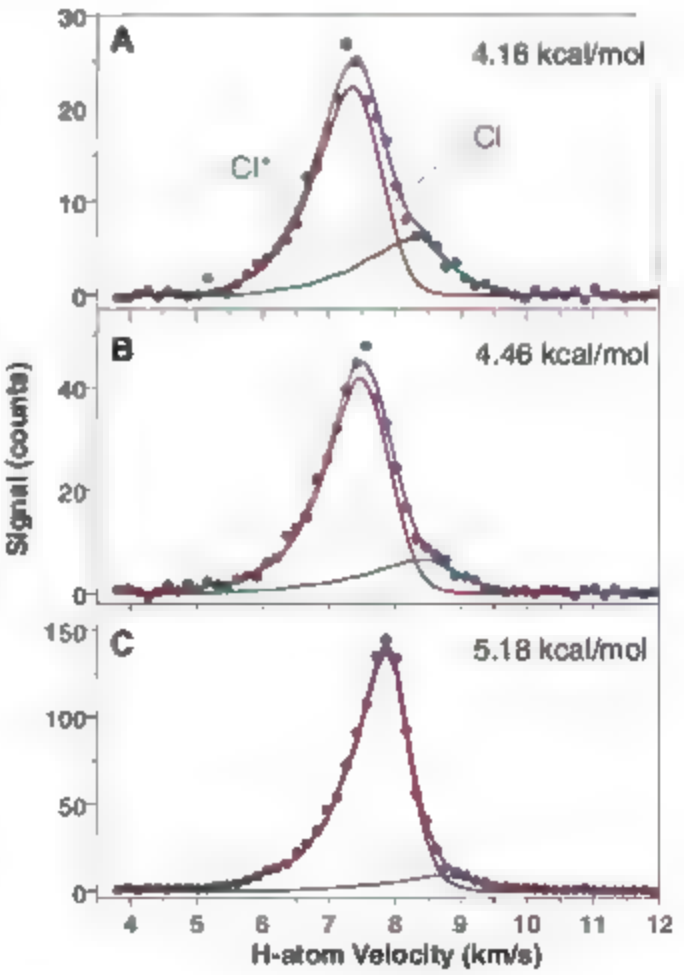

Fig. 2. Velocity spectra of the H-atom product from the Cl($^2P_{3/2}$)/Cl*($^2P_{1/2}$) + H_2 reaction in the backward direction at collision energies of (**A**) 4.16 kcal/mol, (**B**) 4.46 kcal/mol, and (**C**) 5.18 kcal/mol. In these spectra, the solid blue circles are the experimental results. To fit the experimental spectra, we used two components, corresponding to reaction of Cl and Cl*. As described in more detail in the SOM (*25*), we used the fitting procedure described in our F/F* + D_2 work (*11*). The blue curve shows the overall fit to the experimental velocity spectra and is the sum of the Cl component (red curve) and the Cl* component (green curve). From the simulations, it is apparent that the faster component, which corresponds to reaction of Cl*, makes a smaller contribution as the collision energy increases.

[1]State Key Laboratory of Molecular Reaction Dynamics, Dalian Institute of Chemical Physics, Chinese Academy of Sciences, Dalian, Liaoning 116023, People's Republic of China. [2]Institute of Theoretical and Computational Chemistry, Key Laboratory of Mesoscopic Chemistry of Ministry of Education, School of Chemistry and Chemical Engineering, Nanjing University, Nanjing 210093, People's Republic of China. [3]Division of Chemistry and Biological Chemistry, School of Physical and Mathematical Sciences, Nanyang Technological University, Singapore 637371, Singapore. [4]School of Physical and Mathematical Sciences, Nanyang Technological University, Singapore 637371, Singapore. [5]Institute für Theoretische Chemie, Universität Stuttgart, Pfaffenwaldring 55, D-70569 Stuttgart, Germany. [6]Department of Chemistry and Biochemistry and Institute for Physical Sciences and Technology, University of Maryland, College Park, MD 20742–2021, USA.

*Present address: Dipartimento di Chimica, Università di Perugia, 06123 Perugia, Italy.

†To whom correspondence should be addressed. E-mail: xmyang@dicp.ac.cn (X.Y.), dqxie@mail.nju.edu.cn (D.X.), zhangdh@dicp.ac.cn (D.H.Z.), and mha@umd.edu (M.H.A.)

Our experimental apparatus has been described previously (*10*, *24*, *25*). Briefly, we generated a doubly skimmed Cl-atom beam by expanding a mixture of 5% Cl_2/95% He through a two-stage discharge. We determined the Cl:Cl* ratio in the beam to be 3.3, by using 2+1 resonance-enhanced multiphoton ionization (REMPI). This ratio is similar to the ratio in the earlier experimental scheme of Liu and co-workers (*18*, *19*). Measurement of this ratio made it possible for us to extract the relative reactive cross sections of Cl* compared to Cl.

The *p*-H_2 was made by passing *n*-H_2 gas through a column filled with an *o*-*p* conversion catalyst cooled to about 20 K. The pure *p*-H_2 was expanded through a pulsed nozzle at room temperature. We estimate the rotational temperature of the emergent H_2 beam to be 140 K, at which point 89% is cooled to the lowest ($j = 0$) rotational state. The H-atom product from the Cl reaction with *p*-H_2 was detected with the H-atom Rydberg tagging technique (*25*).

TOF spectra of the H-atom products from the Cl/Cl* + *p*-H_2 reaction (with an initial Cl:Cl* ratio of 3.3) were measured at a range of laboratory angles varied in ~10° intervals. These TOF spectra were then converted to velocity spectra of the H-atom product. For scattering in the backward direction (H products rebounding opposite to the direction of the initial H_2 beam), Fig. 2 shows three typical H-atom velocity spectra at E_c = 4.16, 4.46, and 5.18 kcal/mol. The velocity spectra, which are proportional to the HCl product intensity at various laboratory scattering angles, were then simulated, as described in the Supporting Online Material (SOM) (*25*), to obtain the relative differential cross sections (DCSs) in the center-of-mass (CM) frame for the Cl and Cl* reactions. With this, and the experimentally determined Cl:Cl* population ratio in the beam, we can determine the relative reactivity of Cl and Cl* with H_2.

The accompanying theoretical simulations entailed time-independent, fully quantum-reactive scattering calculations, based on the time-independent formalism of Alexander, Manolopoulos, Werner and colleagues (*26*, *27*). This treatment of the dynamics includes explicitly four diabatic PESs; three of these correspond to the three possible orientations of the singly filled Cl 3p orbital with respect to the H_2, whereas the fourth diabatic PES represents the coupling between the two PESs of A' reflection symmetry (*23*, *26*). In addition, we include two coordinate-dependent spin-orbit constants, as well as Coriolis coupling between the four internal angular momenta (electronic spin, electronic orbital, diatomic rotational, and overall tumbling).

To determine differential reactive cross sections, we extended standard expressions to treat a system with multiple internal angular momenta (*27*). Our calculations were based on the Capecchi-Werner (CW) set of PESs (*23*) that were used in our previous work (*5*, *8*, *7*, *12*, *21*). In addition, to rule out any inaccuracies introduced by the method used to fit the CW ab initio points, we used a second set of diabatic PESs, which are a fit to additional multireference, configuration-interaction calculations by Jiang and Xie (JX). The methodology (in particular, the determination of the diabatic PESs) and computer codes used by JX were identical to those used by CW (*23*, *26*, *28*), but with some differences in the technicalities of the calculations, the number of points determined, and the way in which the ab initio points were fit (*25*).

Figure S3 displays the calculated DCSs for a collision energy of 4.75 kcal/mol, predicted by simulations on both sets of PESs. For reaction of both Cl and Cl*, the DCSs are smooth and peaked in the backward direction, identical in qualitative appearance to figures 2 to 4 of (*27*). The calculated DCSs for the BO-allowed reaction of Cl are nearly identical to those determined in earlier reactive scattering calculations in which the spin-orbit Hamiltonian and the electronic anisotropy of the Cl atom were ignored (*2*, *29*). The DCSs for reaction of the excited SO state are less backward peaked, which is consistent with the 2.5-kcal/mol increase in the total available energy due to the spin-orbit energy of Cl*. Figure 3 compares the CW DCSs at 4.75 kcal/mol, summed over accessible HCl rotational levels, with the experimentally determined CM angular distributions. The agreement between experiment and theory is excellent, although theory predicts a slightly broader distribution for the Cl* channel.

To assess the relative reactivity of the Cl and Cl* reactants, we examined the dependence on collision energy of the DCSs in the backward direction in the center-of-mass frame, where they are the largest. Figure 4 compares the experimentally determined, and theoretically predicted, DCSs in the backward direction ($\theta_{CM} = 180°$) for the Cl and Cl* reactions for collision energies ranging between 4 and 6 kcal/mol. For all colli-

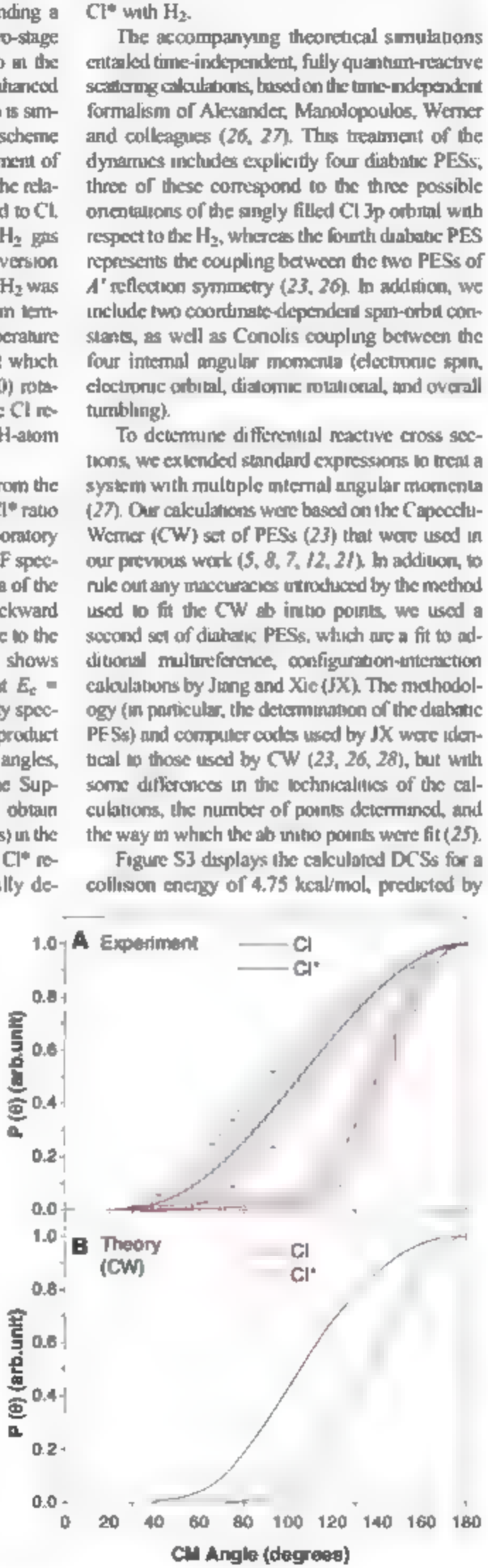

Fig. 3. Angular distributions in the CM system at a collision energy of 4.75 kcal/mol for reaction of Cl($^2P_{3/2}$) (red curve) and Cl*($^2P_{1/2}$) (blue curve) + *p*-H_2, as determined by our crossed–molecular beam experiments (**A**) and by fully quantum simulations on the CW set of PESs (**B**). In both cases, angular distributions were determined for the $j = 0$ and 2 rotational levels of H_2 with fractional populations corresponding to a Boltzmann distribution at $T = 140$ K. The error bars in (A) indicate the range of error in the experimentally derived CM angular distribution $P(\theta)$. The evaluation of the error bars of the experimental data is discussed in the SOM (*25*).

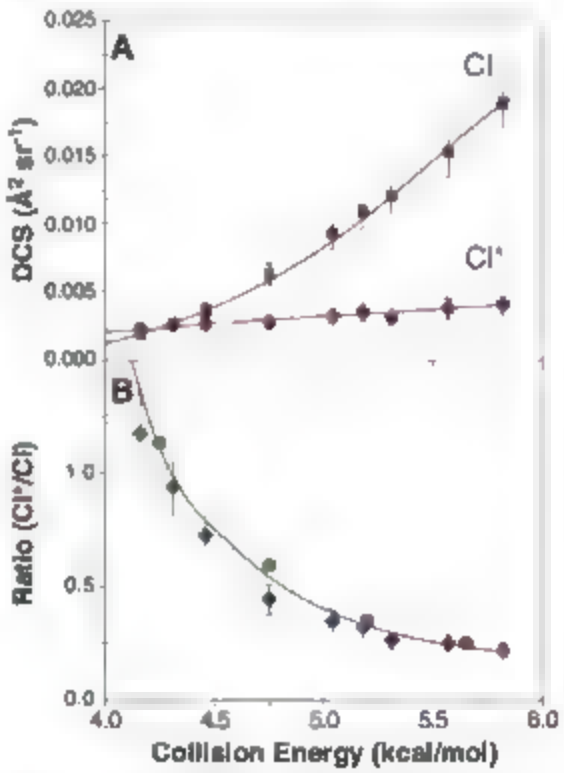

Fig. 4. (**A**) Collision-energy dependence of the differential reactive scattering cross sections, in the backward direction, summed over product vibrational and rotational levels, for the Cl/Cl* + *p*-H_2 reactions for $4 \le E_c \le 6$ kcal/mol. The squares and circles are the experimental data, and the lines display the theoretical results from calculations on the CW set of PESs. (**B**) The ratio of the cross sections shown in (A). The red curve and the green circles indicate, respectively, the results of our theoretical calculations on the CW and XJ PESs, whereas the diamonds indicate the experimental results. The evaluation of the error bars of the experimental data in this figure is discussed in the SOM (*25*).

sion energies at which experiments were done, the experimental Cl/Cl* + H_2 DCSs were scaled to the theoretical CW values by means of a single multiplicative factor.

The reactive backward DCS for the BO-allowed Cl-atom reaction increases much more rapidly with increasing collision energy than that for the BO-forbidden reaction of Cl*. This was the prediction of our earlier scattering calculations (*5*). The energy dependence of the ratio of the backward DCSs for the Cl and Cl* reactions is shown in Fig. 4B. As can be seen, agreement with the predictions of quantum-scattering calculations on both PESs is almost always within the experimental uncertainty limits. Only at the lowest collision energy studied here, ~4.2 kcal/mol, is the excited spin-orbit state more reactive than the ground spin-orbit state.

The excellent overall agreement between our molecular beam experiments and the results of quantum-reactive scattering calculations on two sets of ab initio PESs indicates that the theoretical formulation includes correctly the essential physics governing the nonadiabatic processes of importance in the Cl + H_2 reaction. The degree of agreement, both for this and the F/F*+D_2 reaction (*11*), demonstrates that we can now attain the same level of accuracy in the theoretical modeling of triatomic reactions involving multiple PESs as has been achieved previously for reactions in which only one PES is included (*6*, *10*, *30*, *31*). Ultimately, the success attained here should encourage similarly detailed experimental-theoretical investigations of non-BO effects in more complex chemical reactions (*32*, *33*).

References and Notes

1. T. C. Allison *et al.*, in *Gas-Phase Chemical Reaction Systems: Experiments and Models 100 Years After Max Bodenstein*, J. Wolfrum, H.-R. Volpp, R. Rannacher, J. Warnatz, Eds. (Springer, Heidelberg, Germany, 1996), pp. 113–124.
2. M. Alagia *et al.*, *Science* **273**, 1519 (1996).
3. P. Casavecchia, *Rep. Prog. Phys.* **63**, 355 (2000).
4. K. J. Laidler, *Chemical Kinetics* (Harper and Row, New York, 1987), pp. 14, 288–298.
5. M. H. Alexander, G. Capecchi, H.-J. Werner, *Science* **296**, 715 (2002).
6. D. Skouteris *et al.*, *Science* **286**, 1713 (1999).
7. M. Balucani *et al.*, *Phys. Rev. Lett.* **91**, 013201 (2003).
8. F. Garand, J. Zhou, D. E. Manolopoulos, M. H. Alexander, D. M. Neumark, *Science* **319**, 72 (2008).
9. D. E. Manolopoulos *et al.*, *Science* **262**, 1852 (1993).
10. M. Qiu *et al.*, *Science* **311**, 1440 (2006).
11. L. Che *et al.*, *Science* **317**, 1061 (2007).
12. M. H. Alexander, G. Capecchi, H.-J. Werner, *Faraday Discuss. Chem. Soc.* **127**, 59 (2004).
13. J. M. Bowman, *Science* **319**, 40 (2008).
14. P. J. Dagdigian, M. L. Campbell, *Chem. Rev.* **87**, 1 (1987).
15. G. Li, H.-J. Werner, F. Lique, M. H. Alexander, *J. Chem. Phys.* **127**, 174302 (2007).
16. W. Bian, H.-J. Werner, *J. Chem. Phys.* **112**, 220 (2000).
17. H.-J. Werner, M. Kallay, J. Gauss, *J. Chem. Phys.* **128**, 034305 (2008).
18. S. H. Lee, L.-H. Lai, K. Liu, H. Chang, *J. Chem. Phys.* **110**, 8229 (1999).
19. F. Dong, S.-H. Lee, K. Liu, *J. Chem. Phys.* **115**, 1197 (2001).
20. B. F. Parsons, K. E. Strecker, D. W. Chandler, *Eur. Phys. J.* **38**, 15 (2006).
21. M. H. Alexander, J. Klos, D. E. Manolopoulos, *J. Chem. Phys.* **128**, 084312 (2008).
22. L. Schnieder, K. Seekamp-Rahn, E. Wrede, K. H. Welge, *J. Chem. Phys.* **107**, 6175 (1997).
23. G. Capecchi, H.-J. Werner, *Phys. Chem. Chem. Phys.* **6**, 4975 (2004).
24. M. Qiu *et al.*, *Rev. Sci. Instrum.* **76**, 083107 (2005).
25. Methods are available as supporting material on *Science* Online. See fig. S1 for the REMPI spectrum of the Cl and Cl* atoms, fig. S2 for a comparison of the lowest CW and JX PES in collinear geometry, and fig. S3 for a comparison of the DCSs predicted by the simulations on the CW and JX PESs.
26. M. H. Alexander, D. E. Manolopoulos, H. J. Werner, *J. Chem. Phys.* **113**, 11084 (2000).
27. M. H. Alexander, Y.-R. Tzeng, D. Skouteris, in *Chemical Reaction Dynamics*, G. Lendvay, A. Lagard, Eds. (Kluwer, Amsterdam, 2004), pp. 45–65.
28. K. Stark, H.-J. Werner, *J. Chem. Phys.* **104**, 6515 (1996).
29. D. Skouteris *et al.*, *J. Chem. Phys.* **114**, 10662 (2001).
30. S. Althorpe *et al.*, *Nature* **416**, 67 (2002).
31. F. J. Aoiz, L. Bañares, V. J. Herrero, *Int. Rev. Phys. Chem.* **24**, 119 (2005).
32. W. Hu, G. Lendvay, B. Maiti, G. C. Schatz, *J. Phys. Chem. A* **112**, 2093 (2008).
33. P. Casavecchia *et al.*, *J. Phys. Chem. A* **109**, 3527 (2005).

34. X.Y. and D.H.Z. were supported by the Chinese Academy of Sciences, the National Natural Science Foundation of China, and the Ministry of Science and Technology of China. D.X. was supported by the National Natural Science Foundation of China (20533060 and 20725312). P.C. is grateful to X.Y. and the Dalian Institute of Chemical Physics for a visiting professorship. H.J.W. is grateful to the German Fonds der Chemischen Industrie for financial support.

Supporting Online Material

www.sciencemag.org/cgi/content/full/322/5901/573/DC1
Materials and Methods
Figs. S1 to S3

14 July 2008; accepted 19 September 2008
10.1126/science.1163195

Midbody Targeting of the ESCRT Machinery by a Noncanonical Coiled Coil in CEP55

Hyung Ho Lee,[1] Natalie Elia,[2] Rodolfo Ghirlando,[3] Jennifer Lippincott-Schwartz,[2] James H. Hurley[1]*

The ESCRT (endosomal sorting complex required for transport) machinery is required for the scission of membrane necks in processes including the budding of HIV-1 and cytokinesis. An essential step in cytokinesis is recruitment of the ESCRT-I complex and the ESCRT-associated protein ALIX to the midbody (the structure that tethers two daughter cells) by the protein CEP55. Biochemical experiments show that peptides from ALIX and the ESCRT-I subunit TSG101 compete for binding to the ESCRT- and ALIX-binding region (EABR) of CEP55. We solved the crystal structure of EABR bound to an ALIX peptide at a resolution of 2.0 angstroms. The structure shows that EABR forms an aberrant dimeric parallel coiled coil. Bulky and charged residues at the interface of the two central heptad repeats create asymmetry and a single binding site for an ALIX or TSG101 peptide. Both ALIX and ESCRT-I are required for cytokinesis, which suggests that multiple CEP55 dimers are required for function.

Cytokinesis, the division of the cytoplasm, is the final step of the M phase of the cell cycle. Cytokinesis begins with the formation of the contractile ring, which drives the growth of the cleavage furrow. Vesicle trafficking components, including the exocyst complex and SNAREs (soluble *N*-ethylmaleimide–sensitive factor attachment protein receptors), deliver the additional membrane needed for the cleavage furrow to grow (*1*–*3*). When the extension of the furrow ends, the contractile ring disassembles, and a structure known as the midbody remains as the final tether between the two daughter cells. The last step in cytokinesis, the cleavage of the plasma membrane at the midbody, is referred to as abscission. The mechanism of abscission became clearer with the discovery that the midbody protein CEP55 (*4*–*6*) recruits two key components of the ESCRT machinery (*7*–*11*): the ESCRT-I complex and ALIX (*12*, *13*). The role of ALIX and ESCRT-I in abscission appears to be recruitment of ESCRT-III subunits, which are required for normal midbody morphology (*14*) and are widely believed to have a membrane scission activity (*15*).

Deletion analysis of ALIX mapped the interaction with CEP55 to a putative unstructured Pro-rich sequence near its C terminus (*12*, *13*). Similarly, the TSG101 subunit of ESCRT-I interacts via an unstructured linker between its ubiquitin-binding UEV domain and the region that forms the core complex with other ESCRT-I subunits (*12*, *13*). CEP55 is a predominantly coiled-coil protein that otherwise lacks familiar protein-protein interaction domains. The predicted coiled coil of CEP55 is interrupted near the middle by a ~60-residue region that has been suggested to serve as a hinge between the N- and C-terminal coiled-coil regions (*13*). Remarkably, this putative hinge region is also the locus for binding to the putative unstructured Pro-rich regions of ALIX and TSG101. Because it is very unusual for two unstructured regions from two different proteins to drive spe-

[1]Laboratory of Molecular Biology, National Institute of Diabetes and Digestive and Kidney Diseases, Bethesda, MD 20892, USA. [2]Cell Biology and Metabolism Branch, National Institute of Child Health and Human Development, Bethesda, MD 20892, USA.
*To whom correspondence should be addressed. E-mail: hurley@helix.nih.gov

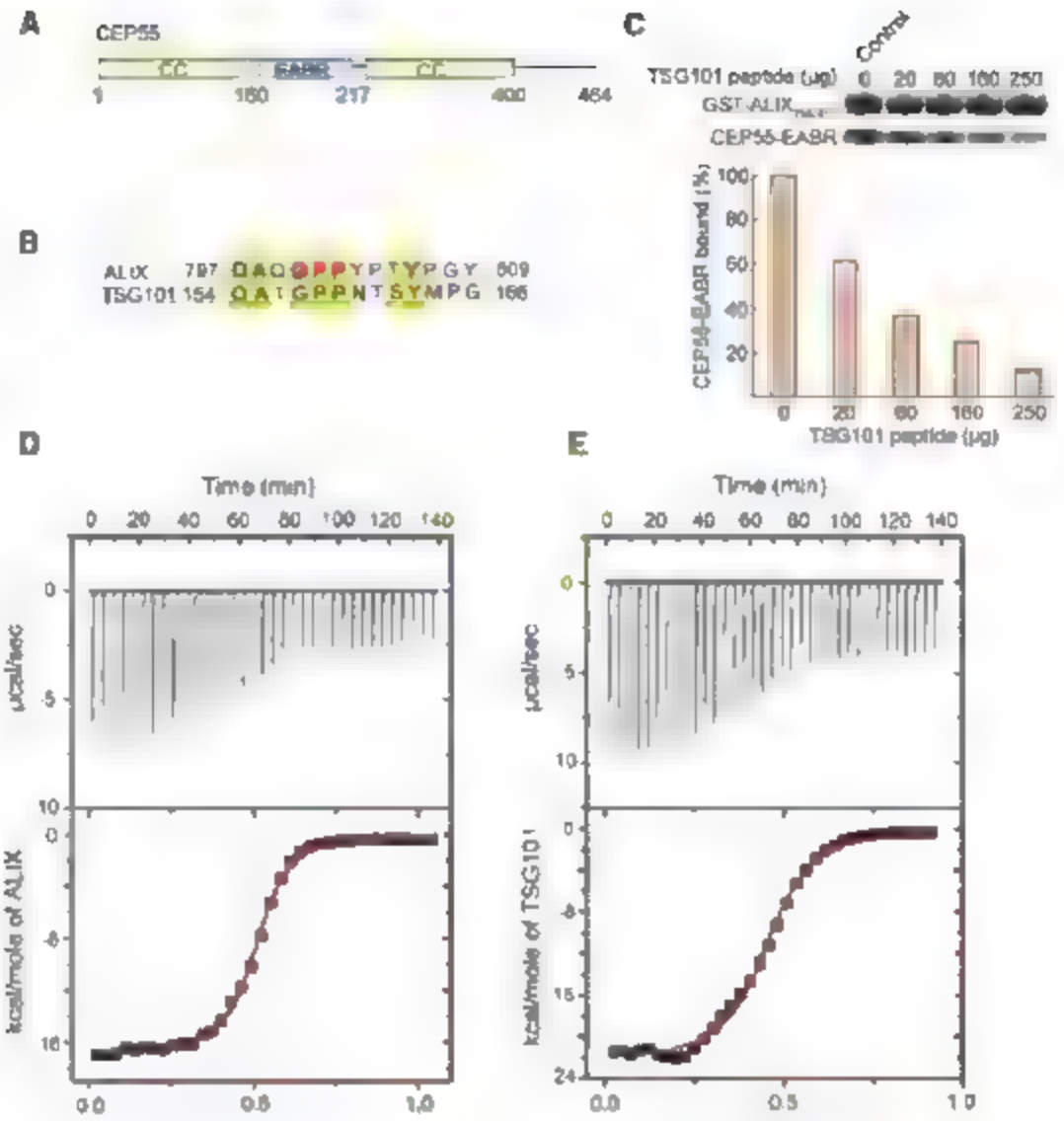

Fig. 1. The CEP55 ESCRT- and ALIX-binding region (EABR) and its interactions. (**A**) Predicted coiled-coil regions (yellow) and the EABR of CEP55 (blue). The region designated EABR corresponds to the region formerly suggested to be a hinge between the N- and C-terminal coiled coils (*13*). (**B**) CEP55 binding sequences of ALIX and the ESCRT-I subunit TSG101. Conserved residues are highlighted in light green; residues shown to be functionally important in ALIX are in bold red type (*21*). (**C**) Pull-down of CEP55-EABR by the GST-ALIX fragment shown, in the presence of the indicated amounts of TSG101 peptide competitor. (**D**) Isothermal titration calorimetry (ITC) of ALIX peptide into CEP55-EABR solution. (**E**) ITC of TSG101 peptide into CEP55-EABR solution.

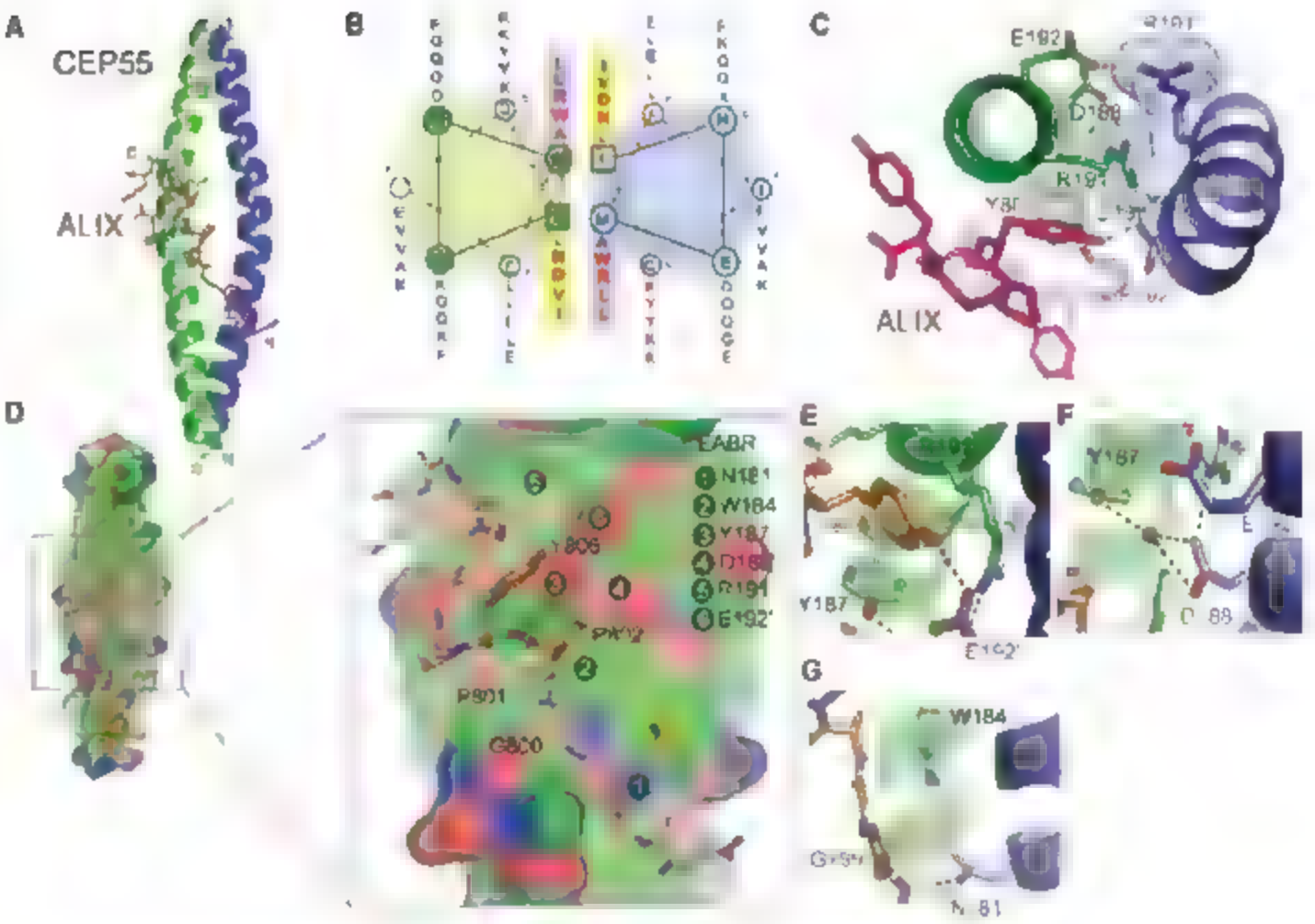

Fig. 2. Structure of the noncanonical CEP55-EABR coiled coil and its complex with ALIX. (**A**) The overall structure of the CEP55-EABR homodimer (green and blue ribbons) in complex with the ALIX peptide (stick model: carbon, orange; oxygen, red; nitrogen, blue). (**B**) Helical wheel analysis of the six heptad repeats of the EABR coiled coil (*21*). (**C**) Charge repulsion between Asp^{189}, Arg^{191}, and Glu^{192} pairs in the homodimer creates asymmetry in the coiled coil and interactions with the ALIX peptide. (**D**) Overview and close-ups of selected regions of the CEP55 surface (carbon, green; oxygen, red; nitrogen, blue), with the ALIX peptide colored as in (A). (**E** to **G**) Molecular interactions in the complex shown in detail and colored as in (A).

cific contacts between them, we pursued a more detailed deletion analysis (fig. S1) with the aim of characterizing binding constants, stoichiometry, and the structural basis of the interaction.

The CEP55 fragment EABR containing residues 160 to 217 (Fig. 1A and fig. S1) bound to a 13-residue peptide based on the Pro-rich sequence of ALIX (residues 797 to 809) (Fig. 1B) with a dissociation constant K_d = 1 μM and a stoichiometry of 2:1 (Fig. 1D). The EABR bound to the related TSG101 peptide (residues 154 to 166) with essentially the same affinity and stoichiometry (Fig. 1E). Various CEP55-EABR:peptide stoichiometric mixtures were subjected to analytical ultracentrifugation (figs. S2 to S4). A 2:1 EABR:ALIX mixture showed the presence of a single complex, whereas all mixtures having a higher proportion of peptide resulted in the 2:1 complex as well as excess free peptide. Similarly, a peptide derived from the Pro-rich region of TSG101 formed a 2:1 CEP55:peptide complex (fig. S2). When the TSG101 peptide was added to a preformed 2:1 CEP55:ALIX peptide complex, a peak corresponding to the equivalent amount of uncomplexed peptide was formed, which suggests that TSG101 and ALIX compete for the same site (fig. S2, bottom panel). Competitive binding experiments (Fig. 1C) confirmed that the two peptides interact with the same site.

To gain further insight into the structural organization of ESCRTs at the midbody, we determined the 2.0 Å resolution structure of CEP55-EABR bound to the ALIX peptide (Fig. 2A, fig. S5, and table S1). The EABR forms a parallel coiled coil over its entire length, comprising a total of six heptad repeats (Fig. 2B). In the two heptad repeats closest to the N and C termini, respectively, there is canonical hydrophobic packing between the two coils. In the two central heptad repeats (repeats 3 and 4), in contrast, there are several nonstandard interactions between the coils (Fig. 2, B and C). In repeat 3, the a position is occupied by Asn[181] and the d position by Trp[184] (Fig. 2B). In repeat 4, Asp[188] and Arg[191] occupy these two positions. Asp and Arg occur at the a and d positions, respectively, of coiled coils with less than 1% of their overall frequency in GenBank (*16*). The effect of placing four disfavored polar and/or bulky residues at both the a and d positions of adjacent heptad repeats is dual. First, the two coils are pushed up to 9 Å apart (fig. S6), versus 6 Å for canonical parallel dimeric coils (*17*). Second, to avoid steric overlap and electrostatic repulsion, the structure

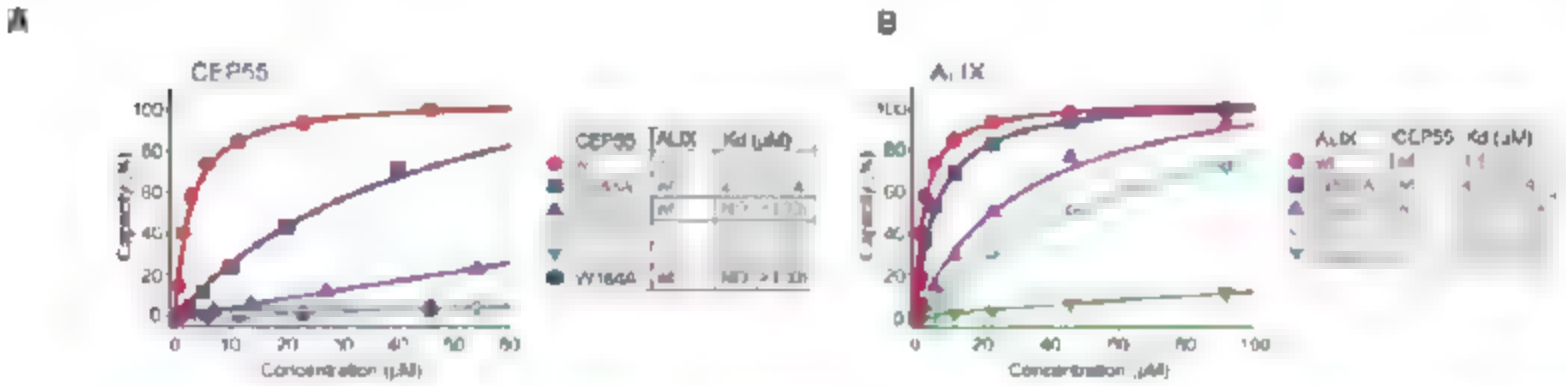

Fig. 3. Point mutations in CEP55 and ALIX abrogate binding and cellular localization. (**A**) Surface plasmon resonance (SPR) analysis of wild-type and mutant CEP55-EABR mutants binding to wild-type ALIX fragment. Binding curves are colored according to affinity in the order red > blue > pink > cyan > green > black in (A) and (B). (**B**) SPR analysis of wild-type and mutant ALIX fragment binding to wild-type CEP55-EABR. (**C**) Midbody localization of wild-type and mutant GFP-ALIX expressed in HeLa cells. Insets show higher magnification of the midbody region. In the middle panels, α-tubulin staining was used to highlight the midbody microtubule structure. (**D**) Live-cell imaging of midbody localization of wild-type mCh-ALIX and wild-type or mutant CEP55 coexpressed in HeLa cells. CEP55 midbody localization was not affected in the mutant (fig. S7). Insets show higher magnification of the midbody region. Scale bars, 10 μm.

becomes asymmetric (Fig. 2C). By pushing apart the two coils in an asymmetric manner, the four noncanonical a- and d-position residues create a single binding site for the ALIX peptide.

The ALIX peptide interacts with CEP55-EABR via its GPP sequence (Gly^{800}, Pro^{801}, Pro^{802}) and Tyr^{806}, which together form the $GPPX_3Y$ motif. The peptide conformation is kinked between the GPP and Tyr^{806}, and wraps around the protruding side chain of CEP55 Tyr^{187} (Fig. 2, D and E). CEP55 Tyr^{187} is essential for the ALIX interaction (Fig. 3A). The GPP sequence makes extensive contacts with CEP55 Trp^{184} and Tyr^{187} and with the aliphatic portions of the Lys^{180} and Gln^{183} side chains (Fig. 2, D to G). Mutation of CEP55 residues Trp^{184} or Tyr^{187} reduces binding to essentially undetectable levels (Fig. 3A). Within the GPP sequence, Pro^{801} makes the most extensive contacts of the three residues of the GPP motif, and its mutation to Ala reduces binding by a factor of ~60 (Fig. 3B). The Gly and the second Pro make correspondingly smaller but still substantial contributions to specificity (Fig. 3B). The second major point of contact involves ALIX Tyr^{806}, which wedges its ring between CEP55 Tyr^{187} and Trp^{184} and forms a short, strong hydrogen bond between its hydroxyl and the side chain of Glu^{192} (Fig. 2, E and F). Mutation of Glu^{192} reduces binding by a factor of ~30 (Fig. 3A), whereas mutation of ALIX Tyr^{806} almost completely abolishes binding (Fig. 3B).

To evaluate the effect of interfering with ALIX-CEP55 interactions on the subcellular localization of ALIX, we tagged full-length ALIX mutants with green fluorescent protein (GFP) and compared their localization to that of wild-type ALIX. Whereas wild-type ALIX strongly localized to midbodies (Fig. 3C, top row) (*12*, *13*), $ALIX^{P801A}$, which had weaker binding affinity in vitro, had reduced midbody localization (Fig. 3C, row 2). Notably, $ALIX^{Y806A}$, which completely blocks binding in vitro, showed no midbody localization above background (Fig. 3C, bottom row). The magnitude of the effect of mutating the ALIX $GPPX_3Y$ motif on localization thus correlates well with the effects on in vitro binding and with the structure.

To further understand the relationship between ALIX and CEP55 in cells, we tested a series of GFP-CEP55 mutants at the corresponding binding residues. Although the localization of CEP55 to midbodies was not affected in any of the mutants (fig. S7), ALIX localization appeared to be impaired. Specifically, cells cotransfected with wild-type mCh-ALIX (mCh, monomeric cherry red fluorescent protein) and any of the CEP55 mutants W184A, Y187A, and R191A showed severely impaired midbody localization of mCh-ALIX relative to wild-type CEP55 (Fig. 3D). This shows that the integrity of CEP55-EABR is important for ALIX to target to this structure. When mCh-TSG101 was cotransfected with CEP55 mutants (fig. S8), a similar CEP55 dependence on TSG101 midbody localization was observed. Taken together, the cellular results strongly corroborate that the interfacial residues observed in both ALIX and CEP55 are responsible for the physiological localization of ALIX by CEP55. Furthermore, the localization of TSG101 is shown to be controlled in cells by the same key EABR residues in CEP55 as for ALIX.

The ESCRT machinery directs a conserved membrane cleavage reaction that is important in multiple cellular processes. At the endosome, the ESCRTs have a dual function in cargo sorting and membrane budding. ESCRTs are targeted to endosomes by multiple low-affinity (K_d > 100 μM) interactions with ubiquitinated membrane proteins and micromolar interactions with 3-phosphoinositides (*7*–*11*). Viruses such as HIV-1, in contrast, appear to self-organize into buds and require the ESCRTs for their final scission from the plasma membrane of the host cell (*18*–*20*). In viral budding, ESCRT targeting is mediated primarily by micromolar-affinity (K_d ~ 5 to 30 μM) interactions with PTAP and YPXL motifs (*21*) and ESCRT-I (*22*) and ALIX (*23*, *24*), respectively. ESCRT targeting to the midbody appears more similar to the situation in viral as opposed to endosomal budding, in that a single, highly specific micromolar binary interaction between $GPPX_3Y$ motifs and CEP55-EABR is key to recruitment. These observations are consistent with a model in which the ESCRTs have a broad-based modular membrane scission activity targeted via the recognition of short peptide motifs, in addition to their endosome-specific, ubiquitin-directed ability to cluster cargo.

In a working model for cleavage of the membrane neck, ESCRT-I and ALIX recruit ESCRT-III components, which are also found at the midbody (*13*). ESCRT-III forms a circular array that is an attractive candidate to drive the closure and cleavage of the membrane neck (*15*). Indeed, an ALIX allele defective in binding the ESCRT-III subunit CHMP4 does not support cytokinesis (*14*). Both ESCRT-I and ALIX are needed for cytokinesis, at least in HeLa cells (*12*, *13*). Our finding that one CEP55 dimer binds to only one copy of ALIX or ESCRT-I indicates that multiple CEP55 dimers are required for function, which suggests that the nucleation of ESCRT-III assembly occurs at a minimum of two sites. The unexpected finding that the region previously thought to form a hinge between the N-terminal and C-terminal coiled coils is, in fact, itself in a coiled-coil conformation and is probably contiguous with the N-terminal coiled coil provides tight constraints on possible models for the organization of CEP55 within the midbody. A possible model that incorporates the characterization of the CEP55-EABR.ALIX complex and related crystallographic (*25*–*27*) and electron

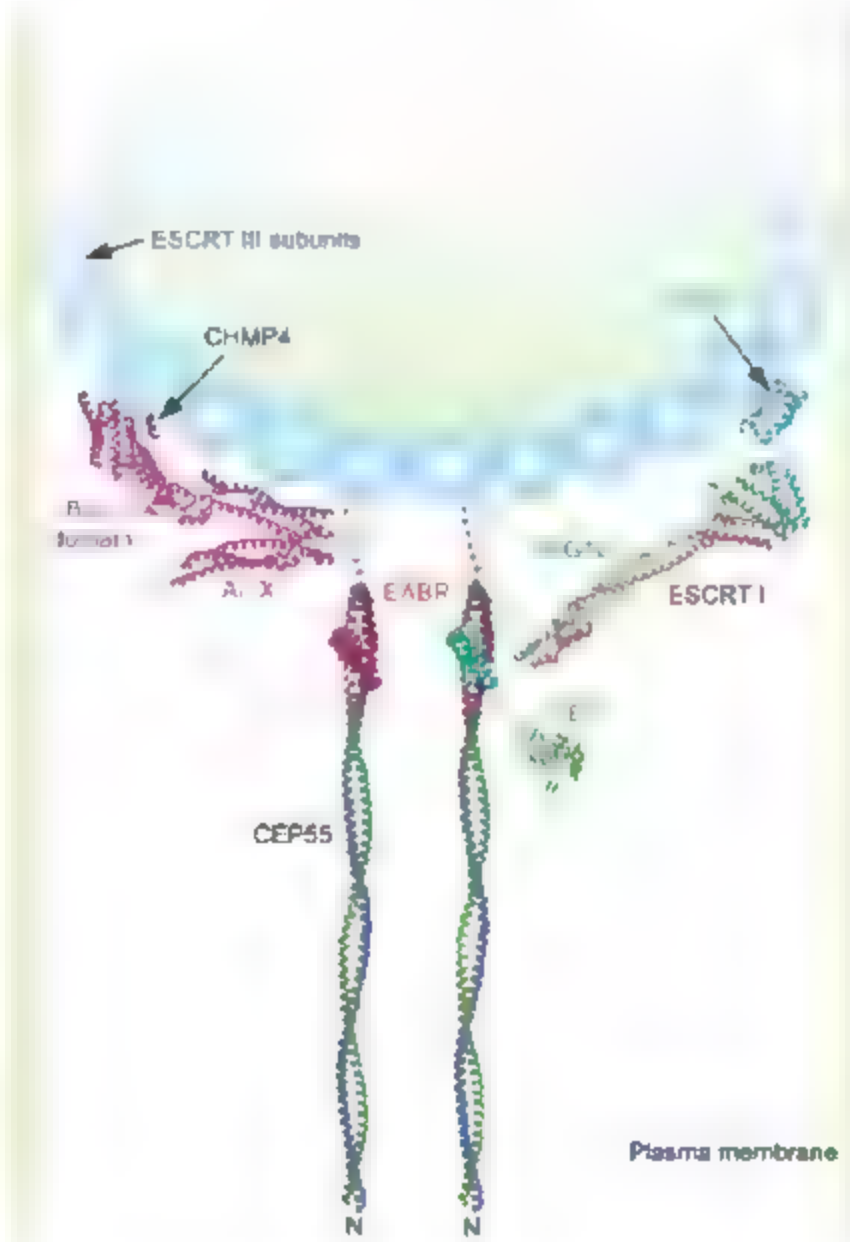

Fig. 4. A model for the organization of CEP55-ESCRT and CEP55-ALIX complexes in the midbody. The model of the N-terminal half of the CEP55 structure docked to the ESCRT-I core (*25*) and UEV domain (*22*) and ALIX (*26*) structures is described in the supporting online material. The crystallized EABR portion of the CEP55 coiled coil is highlighted in red. The structure of the C-terminal domain of the yeast Vps28 subunit of ESCRT-I is shown (*28*) as a putative binding site for Vps20, the yeast ortholog of the human ESCRT-III subunit CHMP6. The binding site on the Bro1 domain of ALIX for the C-terminal helix (blue) of the CHMP4 subunit of ESCRT-III is shown (*27*, *29*). A schematic of an ESCRT-III circular array (*15*) is also shown. The width of the membrane neck is not to scale.

microscopic analyses (*15*) is shown in Fig. 4. Although much remains to be learned about the molecular architecture of the midbody and the precise stereochemistry of cytokinesis, the results and model presented here provide one foothold for furthering such an understanding.

References and Notes

1. M. Glotzer, *Science* **307**, 1735 (2005).
2. F. A. Barr, U. Gruneberg, *Cell* **131**, 847 (2007).
3. R. Prekeris, G. W. Gould, *J. Cell Sci.* **121**, 1569 (2008).
4. W. M. Zhao, A. Seki, G. W. Fang, *Mol. Biol. Cell* **17**, 3881 (2006).
5. I. Martinez-Garay, A. Rustom, H. H. Gerdes, K. Kutsche, *Genomics* **87**, 243 (2006).
6. M. Fabbro *et al.*, *Dev. Cell* **9**, 477 (2005).
7. T. Skagsvold, K. Pattni, L. Malerod, H. Stenmark, *Trends Cell Biol.* **16**, 317 (2006).
8. R. L. Williams, S. Urbe, *Nat. Rev. Mol. Cell Biol.* **8**, 355 (2007).
9. D. P. Nickerson, D. W. Russell, G. Odorizzi, *EMBO Rep.* **8**, 644 (2007).
10. S. Saksena, J. Sun, T. Chu, S. D. Emr, *Trends Biochem. Sci.* **32**, 561 (2007).
11. J. H. Hurley, *Curr. Opin. Cell Biol.* **20**, 4 (2008).
12. J. G. Carlton, J. Martin-Serrano, *Science* **316**, 1908 (2007); published online 6 June 2007 (10.1126/science.1143422).
13. E. Morita *et al.*, *EMBO J.* **26**, 4215 (2007).
14. J. G. Carlton, M. Agromayor, J. Martin-Serrano, *Proc. Natl. Acad. Sci. U.S.A.* **105**, 10541 (2008).
15. P. I. Hanson, R. Roth, Y. Lin, J. E. Heuser, *J. Cell Biol.* **180**, 389 (2008).
16. A. Lupas, M. Van Dyke, J. Stock, *Science* **252**, 1162 (1991).
17. E. K. O'Shea, J. D. Klemm, P. S. Kim, T. Alber, *Science* **254**, 539 (1991).
18. E. Morita, W. I. Sundquist, *Annu. Rev. Cell Dev. Biol.* **20**, 395 (2004).
19. P. D. Bieniasz, *Virology* **344**, 55 (2006).
20. K. Fujii, J. H. Hurley, E. O. Freed, *Nat. Rev. Microbiol.* **5**, 912 (2007).
21. Single-letter abbreviations for amino acid residues: A, Ala; C, Cys; D, Asp; E, Glu; F, Phe; G, Gly; H, His; I, Ile; K, Lys; L, Leu; M, Met; N, Asn; P, Pro; Q, Gln; R, Arg; S, Ser; T, Thr; V, Val; W, Trp; Y, Tyr; X, any amino acid.
22. O. Pornillos, S. L. Alam, D. R. Davis, W. I. Sundquist, *Nat. Struct. Biol.* **9**, 812 (2002).
23. U. M. Munshi, J. Kim, K. Nagashima, J. H. Hurley, E. O. Freed, *J. Biol. Chem.* **282**, 3847 (2007).
24. Q. Zhai *et al.*, *Nat. Struct. Mol. Biol.* **15**, 43 (2008).
25. M. S. Kostelansky *et al.*, *Cell* **129**, 485 (2007).
26. R. D. Fisher *et al.*, *Cell* **128**, 841 (2007).
27. J. Mccullough, R. D. Fisher, F. G. Whitby, W. I. Sundquist, C. P. Hill, *Proc. Natl. Acad. Sci. U.S.A.* **105**, 7687 [illegible].
28. E. Pineda-Molina *et al.*, *Traffic* **7**, 1007 (2006).
29. J. Kim *et al.*, *Dev. Cell* **8**, 937 (2005).

30. We thank B. Beach for generating DNA constructs. E. Freed and K. Kutsche for providing DNAs, T. Alber for discussions, and the staff of SER-CAT for user support at the Advanced Photon Source (APS). Use of the APS was supported by the U.S. Department of Energy, Basic Energy Sciences, Office of Science, under contract W-31 109-Eng-38. Supported by NIH intramural support, NIDDK (J.H.H.), NICHD (J.L.), and IATAP (J.H.H. and J.L.). Crystallographic coordinates have been deposited in the RCSB Protein Data Bank with accession number 3E1R.

Supporting Online Material

www.sciencemag.org/cgi/content/full/322/5901/576/DC1
Materials and Methods
Figs. S1 to S8
Table S1
References

19 June 2008; accepted 10 September 2008
10.1126/science.1162042

Functional Traits and Niche-Based Tree Community Assembly in an Amazonian Forest

Nathan J. B. Kraft,[1] Renato Valencia,[2] David D. Ackerly[1]

It is debated whether species-level differences in ecological strategy, which play a key role in much of coexistence theory, are important in structuring highly diverse communities. We examined the co-occurrence patterns of over 1100 tree species in a 25-hectare Amazonian forest plot in relation to field-measured functional traits. Using a null model approach, we show that co-occurring trees are often less ecologically similar than a niche-free (neutral) model predicts. Furthermore, we find evidence for processes that simultaneously drive convergence and divergence in key aspects of plant strategy, suggesting that at least two distinct niche-based processes are occurring. Our results show that strategy differentiation among species contributes to the maintenance of diversity in one of the most diverse tropical forests in the world.

Explaining the high species diversity of moist tropical forests has proved an enduring challenge to ecologists and has inspired many theories of species coexistence and much debate (*1*–*3*). Current coexistence theories can be divided into two categories: those that invoke a role for meaningful differences in the ecological strategy (niche) of co-occurring species (*2*–*5*), and those that rely on dispersal and stochastic demographic processes that explicitly assume the equivalent per capita fitness of species (*1*). The latter, termed neutral theory, was mainly developed to explain coexistence in diverse tropical forests (*1*), where it seemed implausible that each tree species occupied a unique niche, although it can be applied to a range of communities.

[1]Department of Integrative Biology, University of California, Berkeley, CA 94720, USA. [2]Laboratorio de Ecología de Plantas, Escuela de Ciencias Biologicas, Pontificia Universidad Católica del Ecuador, Aptado. 17-01-2184, Quito, Ecuador

Few large-scale tests of coexistence theories in tropical forests have explicitly examined the ecological strategy of co-occurring species, in part because of difficulties in identifying more than a few discrete plant strategies (such as shade-tolerant, light-demanding pioneer, etc.) (*6*). Recent advances in functional ecology now permit a more precise quantification of woody plant strategy along a number of continuous, often orthogonal, axes of variation related to resource acquisition strategy, regeneration niche, environmental tolerance, and life history (*7*–*10*), opening the door for previously intractable analyses.

Here we present a critical test of neutral and niche-based coexistence theories in one of the most diverse tropical forest plots in the world. The stochastic processes associated with neutral theory assume the equivalence of all individuals, and therefore species, with the result that species co-occurrence patterns should be random with respect to ecological strategy (*1*, *11*). We tested for two niche-based alternatives: (i) that co-occurring species converge in strategy because of establishment and/or survival barriers imposed by the abiotic environment ("environmental filtering") (*4*, *12*, *13*), and (ii) that co-occurring species diverge in strategy as predicted by classic coexistence theory ("niche differentiation") (*5*, *14*). The latter pattern may occur as a result of competition or of enemy-mediated density dependence (*15*) if plant susceptibility (*16*) and overall plant strategy are phylogenetically conserved. A strength of our approach is that we are able to test for both processes (*17*), because environmental filtering should limit the range of strategies found in a community (*12*, *17*), whereas niche differentiation should spread individuals evenly along strategy axes (*14*, *17*). These two features of community-trait distributions can be assessed sequentially.

We tested these predictions in the Yasuní Forest Dynamics Plot (FDP) in eastern Ecuador, a 25-ha plot containing over 150,000 mapped trees ≥1 cm in diameter at breast height (dbh) from over 1100 species (*18*). The ecological strategy for each species was quantified with field-measured estimates of specific leaf area (SLA, leaf area divided by dry mass), leaf nitrogen concentration, leaf size, seed mass, and maximum dbh (used here as a proxy for maximum height), as well as published estimates of wood density (*19*, *20*). We combined this trait information with species co-occurrence data to develop estimates of the community-trait distribution at the 20-by-20–m ("quadrat") scale. Metrics of community-trait structure sensitive to environmental filtering and niche differentiation were compared to a null expectation. We generated our null expectation by creating random communities of equal richness by drawing species from the entire plot weighted by their plot-wide occurrence, irrespective of trait values (*20*).

We predict that if habitat filtering is occurring at the quadrat scale, the range of observed trait

values will be smaller than the null expectation (*12*). The variance may also be reduced by habitat filtering, although this is a more difficult metric to interpret, as it may also be affected by niche differentiation (*17*). Habitat filtering may shift the mean of the quadrat trait distribution relative to the null expectation, although filtering can occur without this effect. Likewise, if niche differentiation is occurring, we predict that the standard deviation (SD) of nearest-neighbor distances (measured along trait axes) will be lower (species spaced more evenly), and the kurtosis of the distribution of trait values will be smaller (fat-tailed distribution) as compared to the null expectation (*14*, *17*).

Trait-based community analysis requires the selection of traits that are critical to the community processes of interest. Our selection of traits (Table 1) connected to the leaves, seeds, wood, and overall life form of each species covers a range of traits frequently deemed essential to woody plant strategy (*8*–*10*). Logistical concerns related to the extremely high diversity of the system limited us to these practical traits that are established proxies for plant strategy, although additional traits such as rooting depth, leaf secondary chemistry, and seedling relative growth rate would be of great interest, if and when data become available.

Our analyses found strong evidence for niche-based processes throughout the FDP (Fig. 1, Tables 1 and 2, and table S1). Across the entire plot, mean trait values varied more among quadrats (Table 2, Fig. 1A, and fig. S1), and trait ranges were significantly smaller within quadrats (Table 1, Fig. 1C, and fig. S2), as compared to expectations from our null model. These patterns are consistent with a role for habitat filtering. The Yasuní FDP contains two principal topographically defined habitats: ridgetops and valley bottoms (Fig. 1A). Prior analyses of species distributions in Yasuní have shown that many species show associations with topographic habitat (*18*) and soil nutrients (*21*), results that agree with our trait-based analysis. Our analyses highlight the fact that the topographic habitats support communities with divergent strategies, in addition to contrasting species identities, despite close physical proximity between the two habitat types. Ridgetops tend to be composed of species with lower average SLA, smaller leaves, heavier seeds, and denser wood as compared to valley communities (Fig. 1A and fig. S1). Comparing our initial results to a null model restricted to topographic habitat reduces the habitat filtering effect in many cases (table S4), suggesting that the two topographic habitats explain some, but not all, of the habitat filtering effect we observe in the plot. Habitat or microsite variation that does not correspond with topographic habitats may be responsible for the remainder.

Against this background of habitat filtering, all traits with the exception of wood density were more evenly distributed than predicted (Table 1), as measured either by the SD of nearest-neighbor

Table 1. Trait coverage, an example of the ecological significance of each trait, and Wilcoxon signed-rank test of plot-wide null model results. The mean test was two-tailed; all other tests were one-tailed. n.s., not significant; NN, nearest neighbor.

Trait	Species sampled (% of plot stems)	Strategy correlation	Mean	Range	SD of NN distance	Kurtosis	Variance
SLA	1088 (99.9%)	Leaf economics-resource capture (*29*)	n.s.	<0.0001	0.012	0.007	<0.0001
Leaf nitrogen concentration	559 (90.5%)	Leaf economics-resource capture (*29*)	n.s.	0.0001	<0.0001	0.604	<0.0001
Leaf size	1084 (99.8%)	Disturbance and nutrient stress strategy (*7*)	n.s.	<0.0001	<0.0001	<0.0001	<0.0001
Seed mass	321 (58%)	Regeneration strategy (*9*)	n.s.	0.825	0.761	0.014	0.186
Wood density	265 (29%)	Allocation to growth versus strength/pathogen resistance (*19*)	n.s.	0.998	0.913	0.233	0.533
Maximum dbh	1123 (100%)	Light capture strategy (*30*)	n.s.	<0.0001	<0.0001	0.011	<0.0001

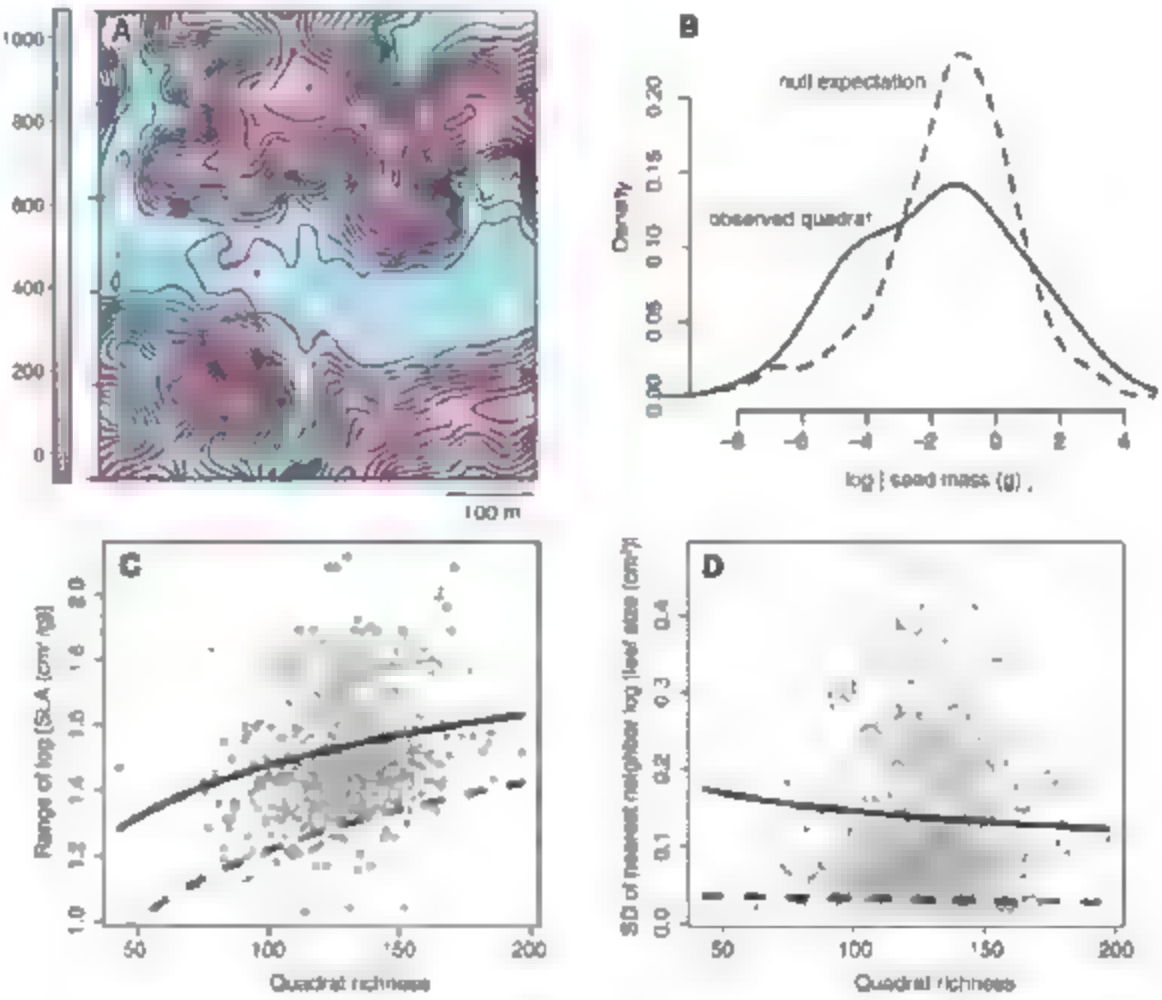

Fig. 1. Examples of community trait patterns at Yasuní. See figs. S1 to S3 for complete results. (**A**) The rank of observed mean SLA in the null distribution for all 625 quadrats. Contours indicate topography within the plot (interval = 2 m); thus, ridgetops have lower than expected SLA and valleys have higher. (**B**) Observed (solid line) and expected (dashed line) distribution of seed masses in one quadrat with significantly low kurtosis. (**C**) Points indicate the observed range of SLA (log-transformed) in each quadrat as a function of quadrat richness. The solid line indicates the expected range value predicted by the null model, and the dashed line indicates the 5% confidence interval of the null distribution used to assess significance in Table 2. Only one interval is indicated because the test is one-tailed. The distribution of observed points is significantly shifted below the null expectation (Table 1), suggesting that in aggregate, quadrat-level SLA ranges are smaller than expected across the forest. (**D**) Same plot for the SD of nearest-neighbor distances for leaf size (log-transformed). The distribution of observed points is significantly shifted below the null expectation (Table 1), indicating that in aggregate, quadrat-level leaf size distributions are more evenly spread than expected.

Table 2. Percentage of individual quadrats in Yasuni significantly deviating from the null model. The mean test was two-tailed; all other tests were one-tailed.

Trait	Mean	Range	SD of NN distance	Kurtosis	Variance
SLA	33.5%	8.2%	5.1%	6.1%	14.1%
Leaf nitrogen concentration	14.6%	5.3%	5.1%	3.8%	7.9%
Leaf size	15.9%	6.1%	6.9%	5.9%	7.2%
Seed mass	9.8%	6.1%	5.0%	6.4%	6.9%
Wood density	10.1%	1.8%	2.7%	3.5%	2.1%
Maximum dbh	10.9%	9.0%	6.9%	6.4%	13.9%

Table 3. Wilcoxon signed-rank test of sapling and adult comparisons. Significant values reflect a shift toward greater departures from the null expectation in adults, relative to saplings. The mean test was two-tailed; all other tests were one-tailed

Trait	Mean	Range	SD of NN distance	Kurtosis	Variance
SLA	0.007	>0.5	>0.5	0.188	>0.5
Leaf nitrogen concentration	<0.0001	<0.0001	0.0037	0.0524	<0.0001
Leaf size	<0.0001	>0.5	>0.5	>0.5	>0.5
Seed mass	<0.0001	>0.5	<0.0001	<0.0001	>0.5
Wood density	<0.0001	>0.5	>0.5	>0.5	>0.5
Maximum dbh	<0.0001	>0.5	>0.5	>0.5	<0.0001

distances (Fig. 1D and fig. S2) or by kurtosis (fig S3), a pattern we attribute to niche differentiation. In ecological terms, a platykurtic distribution (Fig. 1B) indicates that species with a broad distribution of trait values (such as small, medium, and large seeds, or shrub, midcanopy, and emergent growth forms) co-occur more often than predicted, whereas a low SD of nearest-neighbor distances (Fig. 1D) suggests that, on average, co-occurring species are more evenly spaced along the trait axis than predicted. In many cases, these effects were strengthened when habitat-specific species pools were used (table S4). Although many individual quadrats are indistinguishable from the null expectation (Table 2), the presence of detectable, significant, plot-wide niche differentiation effects (Table 1) in such a diverse community is surprising evidence against a purely neutral explanation of species coexistence.

Dispersal, seedling establishment, or post-establishment mortality that is nonrandom with respect to trait values may have produced the patterns we observed. As plants only enter the FDP census once they reach 1 cm in dbh, we cannot test for trait effects at the earliest life stages. On the other hand, we can indirectly examine mortality that occurs during the transition from sapling to adult. We tested the hypothesis that trait patterns became increasingly nonrandom in adults in the community by repeating our analyses for restricted cohorts of co-occurring individuals 1 to 10 cm in dbh (saplings) or >10 cm in dbh (adults) and comparing the sapling assemblage in each quadrat to the adult assemblage (*20*). In many cases, adults in each quadrat exhibited stronger nonrandom patterns than saplings (Table 3), despite a reduction in power to detect nonrandom patterns in the adults that arises in the analysis because of smaller community sizes (*22*). Thus, it appears that at least some of the community-wide pattern is due to post-sapling mortality that is nonrandom with respect to traits.

The evenly distributed trait patterns that we observed may be produced by direct competition (*14*) or by other density-dependent processes. For example, previous studies have shown that density-dependent attack by specialist herbivores or pathogens may be pervasive in tropical forests (*23*) and that the probability of attack by natural enemies for plants has a strong phylogenetic component (*24*). In general, studies have shown that closely related plants have similar ecological strategies (*19*, *25*), including qualitative defenses (*26*). Thus, our results may reflect nonrandom mortality inflicted by natural enemies.

Using a functional trait approach, we have found evidence for niche-based processes known to have stabilizing effects on diversity (*27*) in one of the most species-rich tropical forest assemblages on the planet. Although the magnitude of these processes still needs to be quantified (*28*), their existence indicates that forces included in neutral theory (such as demographic stochasticity and dispersal limitation) may not be sufficient to explain species distributions and the maintenance of diversity in this forest, even though they are occurring. Taken together, our results support a niche-based view of tropical forest dynamics in which subtle but pervasive habitat specialization and strategy differentiation contribute to species coexistence.

References and Notes

1. S. P. Hubbell, *The Unified Neutral Theory of Biodiversity and Biogeography* (Princeton Univ. Press, Princeton, NJ, 2001).
2. J. M. Chase, M. A. Leibold, *Ecological Niches: Linking Classical and Contemporary Approaches* (Univ. of Chicago Press, Chicago, 2003).
3. S. J. Wright, *Oecologia* **130**, 1 (2002).
4. E. Weiher, P. A. Keddy, *Ecological Assembly Rules. Perspectives, Advances, Retreats* (Cambridge Univ. Press, Cambridge, 1999).
5. J. Silvertown, *Trends Ecol. Evol.* **19**, 605 (2004).
6. I. M. Turner, *The Ecology of Trees in the Tropical Rain Forest* (Cambridge Univ. Press, Cambridge, 2001).
7. J. H. C. Cornelissen *et al.*, *Aust. J. Bot.* **51**, 335 (2003).
8. M. Westoby, I. J. Wright, *Trends Ecol. Evol.* **21**, 261 (2006).
9. M. Westoby, D. S. Falster, A. T. Moles, P. A. Vesk, I. J. Wright, *Annu. Rev. Ecol. Syst.* **33**, 125 (2002).
10. L. Poorter *et al.*, *Ecology* **89**, 1908 (2008).
11. Theoretically, tradeoffs among functional and life-history traits can lead to the demographic equivalence of species, thus reconciling species-level variation in ecological strategy with neutral theory, although this would still lead to random patterns in the co-occurrence of species traits.
12. W. K. Cornwell, D. W. Schwilk, D. D. Ackerly, *Ecology* **87**, 1465 (2006).
13. B. M. J. Engelbrecht *et al.*, *Nature* **447**, 80 (2007).
14. W. J. Stubbs, J. B. Wilson, *J. Ecol.* **92**, 557 (2004).
15. D. H. Janzen, *Am. Nat.* **104**, 501 (1970).
16. C. O. Webb, G. S. Gilbert, M. J. Donoghue, *Ecology* **87**, 123 (2006).
17. W. K. Cornwell, D. Ackerly, *Ecol. Monogr.*, 10.1890/07-1134.1, in press.
18. R. Valencia *et al.*, *J. Ecol.* **92**, 214 (2004).
19. J. Chave *et al.*, *Ecol. Appl.* **16**, 2356 (2006).
20. Materials and methods are available as supporting material on *Science* Online.
21. R. John *et al.*, *Proc. Natl. Acad. Sci. U.S.A.* **104**, 864 (2007).
22. N. J. B. Kraft, W. K. Cornwell, C. O. Webb, D. D. Ackerly, *Am. Nat.* **170**, 271 (2007).
23. C. Wills *et al.*, *Science* **311**, 527 (2006).
24. G. S. Gilbert, C. O. Webb, *Proc. Natl. Acad. Sci. U.S.A.* **104**, 4979 (2007).
25. A. Prinzing, W. Durka, S. Klotz, R. Brandl, *Proc. R. Soc. London Ser. B* **268**, 2383 (2001).
26. P. V. A. Fine, I. Mesones, P. D. Coley, *Science* **305**, 663 (2004).
27. P. Chesson, *Annu. Rev. Ecol. Syst.* **31**, 343 (2000).
28. P. B. Adler, J. HilleRisLambers, J. M. Levine, *Ecol. Lett.* **10**, 95 (2007).
29. I. J. Wright *et al.*, *Nature* **428**, 821 (2004).
30. D. S. Falster, M. Westoby, *J. Ecol.* **93**, 521 (2005).

31. N.J.B.K. is grateful to A. Martin, L. Williams, P. Alvia, and L. Dunn for field assistance and to A. Thompson, T. Altanchilians, and M. Piven for help with sample analysis. Leaf trait collection was supported by the Center for Tropical Forest Science and the University of California, Berkeley, Department of Integrative Biology. We benefited from interactions with R. Condit, W. Cornwell, P. Fine, S. Kembel, J. Lake, M. Metz, N. Swenson, and four anonymous reviewers. S. J. Wright and N. Garwood generously provided unpublished seed data from collection efforts supported by NSF grants DEB-614525, DEB-614055, and DEB-614659. R.V. thanks the government of Ecuador (Donaciones de Impuesto a la Renta 2004-2006), Pontificia Universidad Católica del Ecuador, the Mellon Foundation, the Tupper Family Foundation, the Smithsonian Tropical Research Institute, and NSF (grants DEB-0090311 and DEB-9806828) for support of the forest census. This research was possible because of the kind permission of the Ministerio del Ambiente of Ecuador.

Supporting Online Material

www.sciencemag.org/cgi/content/full/322/5901/580/DC1
Materials and Methods
Figs. S1 to S3
Tables S1 to S8
References

19 May 2008; accepted 18 September 2008
10.1126/science.1160662

White Fat Progenitor Cells Reside in the Adipose Vasculature

Wei Tang,[1] Daniel Zeve,[1] Jae Myoung Suh,[1] Darko Bosnakovski,[1] Michael Kyba,[1] Robert E. Hammer,[2] Michelle D. Tallquist,[3] Jonathan M. Graff[1,3,4]*

White adipose (fat) tissues regulate metabolism, reproduction, and life span. Adipocytes form throughout life, with the most marked expansion of the lineage occurring during the postnatal period. Adipocytes develop in coordination with the vasculature, but the identity and location of white adipocyte progenitor cells in vivo are unknown. We used genetically marked mice to isolate proliferating and renewing adipogenic progenitors. We found that most adipocytes descend from a pool of these proliferating progenitors that are already committed, either prenatally or early in postnatal life. These progenitors reside in the mural cell compartment of the adipose vasculature, but not in the vasculature of other tissues. Thus, the adipose vasculature appears to function as a progenitor niche and may provide signals for adipocyte development.

How adipocytes (fat cells) develop is a fundamental biological question with important ramifications for human health and disease (*1*, *2*). Little is known about the identity, localization, or biological characteristics of endogenous adipocyte progenitors (*2*). These progenitors probably reside in the adipose stromal-vascular fraction (SVF), a heterogeneous mixture of cells operationally defined by enzymatic dissociation of adipose depots followed by density separation from adipocytes (*1*, *3*). Peroxisome proliferator-activated receptor gamma (PPARγ), a central regulator of fat formation, is necessary and sufficient for adipogenesis (*4*, *5*). Thus, marking PPARγ-expressing cells in vivo might provide insights into adipose lineage specification.

To mark and perform lineage analyses on PPARγ-expressing cells, we generated PPARγ–tet transactivator (tTA) (*6*) knock-in mice placing tTA under the control of the PPARγ locus (fig. S1) (*7*). We introduced into these PPARγ-tTA mice two additional alleles: (i) a tTA-responsive Cre allele [tetracycline response element-Cre (TRE-Cre)] and (ii) an element that indelibly expresses lacZ in response to the Cre recombinase (ROSA26-flox-stop-flox-lacZ) (*8*, *9*). With these genetic manipulations, we thereby created a PPARγ-reporter strain (PPARγ-R26R, for PPARγ-Rosa26 reporter) in which the endogenous PPARγ promoter/enhancer induces expression of tTA, leading to Cre expression and an indelible lacZ marking of PPARγ-expressing cells and all descendants (fig. S1). The PPARγ-tTA strain functioned as expected, that is, it was active in adipose depots and repressed by doxycycline (Dox), establishing a tool to examine the adipose lineage (Fig. 1A and figs. S1 and S2).

To capture the rapid and dramatic expansion of the adipose lineage that occurs during the first postnatal month (*1*, *10*), we Dox-treated the PPARγ-R26R mice, starting at different days during this crucial window (fig. S3A). We found

[1]Department of Developmental Biology, University of Texas Southwestern Medical Center, Dallas, TX 75390, USA. [2]Department of Biochemistry, University of Texas Southwestern Medical Center, Dallas, TX 75390, USA. [3]Department of Molecular Biology, University of Texas Southwestern Medical Center, Dallas, TX 75390, USA. [4]Department of Internal Medicine, University of Texas Southwestern Medical Center, Dallas, TX 75390, USA.

*To whom correspondence should be addressed. E-mail: jon.graff@utsouthwestern.edu

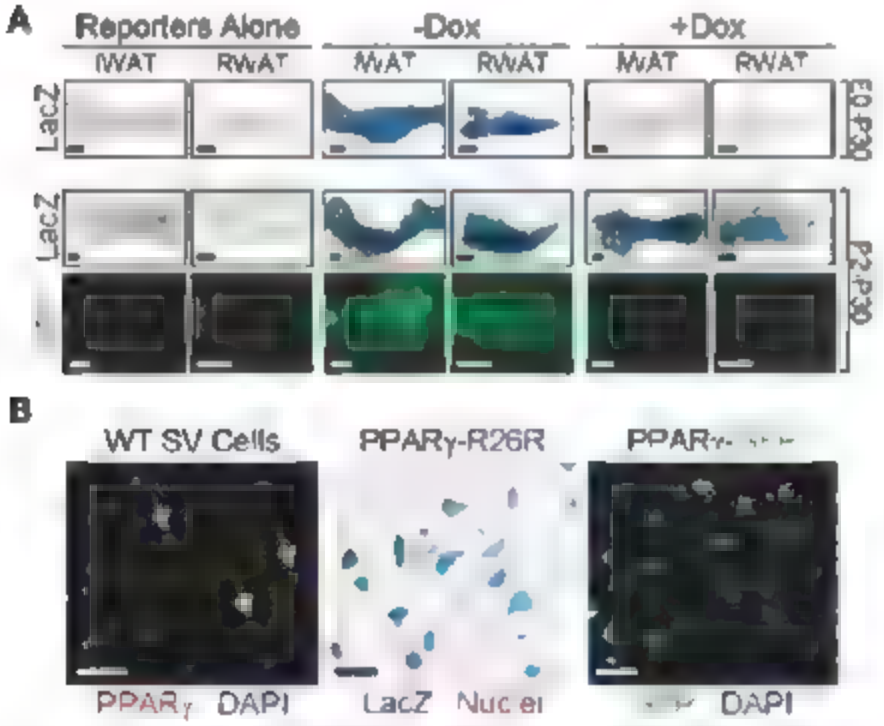

Fig. 1. PPARγ-expressing progenitors proliferate and maintain the precursor pool. (**A**) PPARγ-tTA;TRE-Cre;R26R (PPARγ-R26R) or PPARγ-tTA;TRE-H2B-GFP (PPARγ-GFP) (bottom panels) mice were treated with or without Dox, either from embryonic day 0 (E0) to postnatal day 30 (P30) (top row) or from P2 to P30 (middle and bottom rows), and then inguinal and retroperitoneal white adipose tissues (IWAT and RWAT, respectively) were excised and examined for lacZ (blue) or GFP (green) expression. Left panels show equivalent depots of control mice containing either TRE-Cre;R26R or TRE-H2B-GFP. (**B**) P30 SV cells from wild-type (left), PPARγ-R26R (middle), and PPARγ-GFP (right) WAT were examined for expression of PPARγ (red) with immunocytochemistry (left) or for reporter expression. (Left) Nuclei were stained with 4′,6′-diamidino-2-phenylindole (DAPI) (blue). Yellow arrows indicate cells that express PPARγ (purple). (Middle) lacZ (blue) nuclei counterstained with nuclear fast red (red). (Right) GFP (green) nuclei stained with DAPI (blue). (**C**) Flow cytometry profiles of SV cells of untreated TRE-H2B-GFP (left) or PPARγ-GFP mice treated without (middle) or with Dox (right) from P2 to P30. The *x* axis is GFP fluorescent intensity, and the *y* axis is phycoerythrin (PE) channel to help illustrate the distribution of GFP$^+$ cells. (Inset) The *x* axis is GFP fluorescent intensity, and the *y* axis is the cell count of the GFP$^+$ cells per interval of fluorescent intensity (one unit = 1000). SV cells from TRE-H2B-GFP mice served as a gating control. (**D**) SV cells removed from TRE-Cre;R26R (left) and PPARγ-R26R mice treated as indicated were isolated and stained with X-Gal (blue) and nuclear fast red (red). Dox treatment did not alter the number or percentage of lacZ$^+$ cells based on statistical analysis of more than 2000 cells counted in each group. Scale bars: (A), 2 mm; (B) and (D), 50 μm.

homogenous lacZ expression in postnatal day 30 (P30) adipose depots that was not appreciably altered, even when Dox administration began in the first postnatal days (Fig. 1A and fig. S3). This surprising result indicated that the vast majority of P30 adipocytes derived from a preexisting pool of PPARγ-expressing cells, either adipocytes already present prenatally/early postnatally or proliferating precursors. Both interpretations conflict with previous data, however. The possibility that these cells are pre-formed adipocytes is incompatible with the proliferative increase that occurs over this time frame, whereas the notion that PPARγ-expressing cells are progenitors is inconsistent with cell culture studies (*11*, *12*). To distinguish between the two possible interpretations, we examined the Dox-induced response of another reporter, TRE-H2B-GFP, that is stable in postmitotic cells but, in contrast to the indelible lacZ marker, becomes diluted in proliferating cells after inhibition of the tet system (*13*, *14*). Dox treatment (P2 to P30) markedly reduced adipose depot and adipocyte green fluorescent protein (GFP) expression (Fig. 1A), indicating that PPARγ-expressing cells proliferate. Consistent with these data, ~50% of adipocytes were labeled by bromodeoxyuridine (BrdU) when administered between P10 and P30 (fig. S4). The stability of lacZ marking together with the diminishing GFP expression indicate that adipose lineage cells, already instructed to express PPARγ prenatally, proliferate and are the major source of the spurt of adipocyte development observed in the first month of life.

The adipose SVF (fig. S5) is postulated to contain adipocyte progenitors (*1*, *15*). We therefore investigated this location as a possible source from which the proliferating PPARγ-expressing cells characterized above may originate. We found that a subset of stromal-vascular (SV) cells expressed immunocytochemically detectable levels of PPARγ, as well as the lacZ and GFP reporters (Fig. 1B and fig. S6). These SV resident PPARγ-expressing cells proliferate, as they incorporated BrdU after a brief 2-hour chase, even when the BrdU pulse-chase was initiated after 10 days of Dox pretreatment to ensure that cells containing both GFP and BrdU expressed GFP before initiation of the brief BrdU pulse (fig. S7). In addition, GFP$^+$ SV cells isolated by fluorescence-activated cell sorting (FACS) had considerable proliferative capacity (fig. S8). Further support for the in vivo proliferation of the GFP$^+$ SV cells derives from flow cytometry profiles showing a Dox-induced (P2 to P30) decrease in the number and fluorescent intensity of GFP$^+$ SV cells (Fig. 1C and fig. S9). Dox did not reduce the number or percentage of lacZ$^+$ SV cells, indicating that a pool of PPARγ-expressing cells remains in the SV compartment (Fig. 1D). Together these data indicate that the SV compartment of adipose depots contains PPARγ-expressing cells that divide, are mobilized from and also repopulate the SVF, and behave as an amplifying population that contributes to the adipocyte lineage.

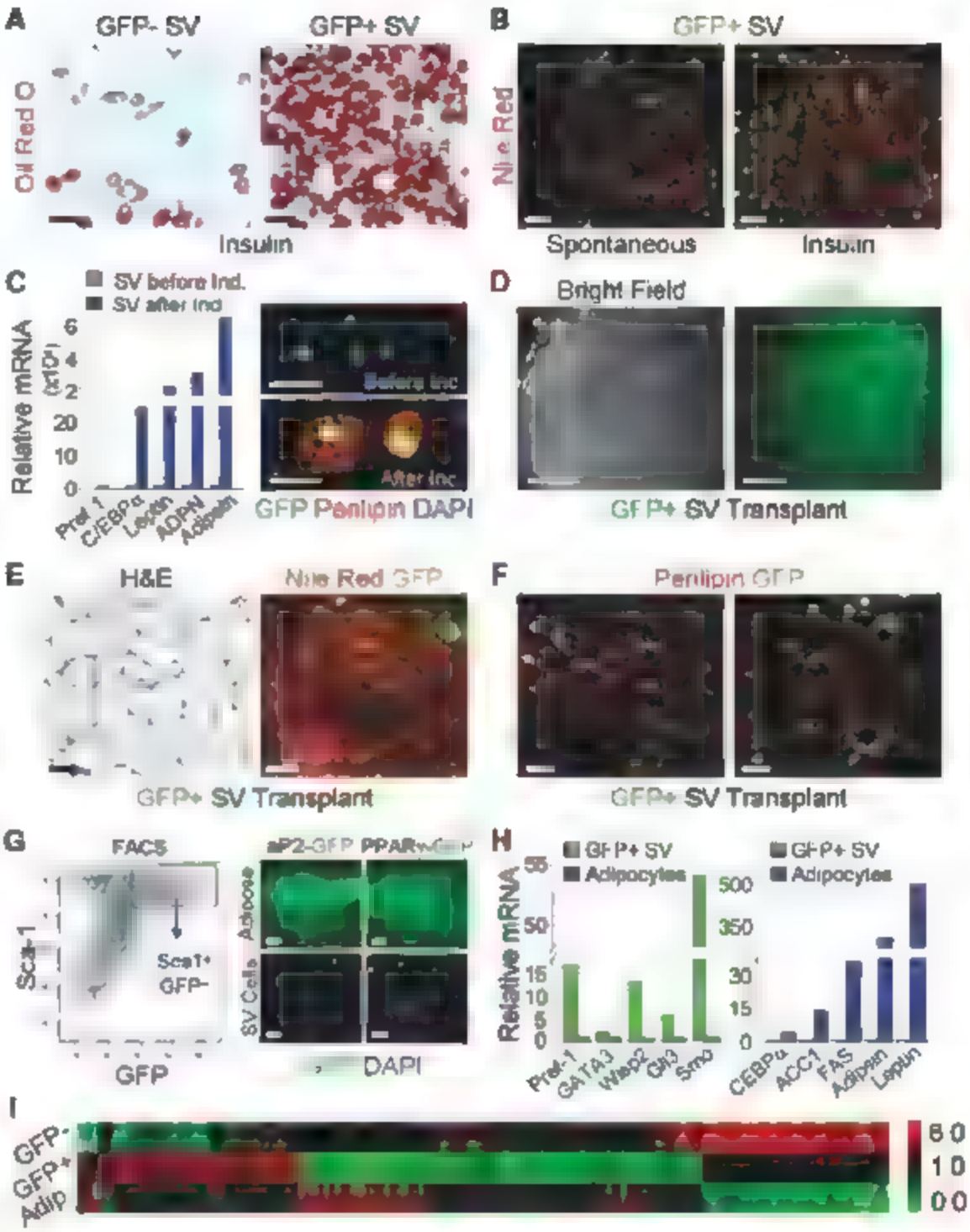

Fig. 2. PPARγ-expressing SV cells are adipogenic and have a unique molecular signature. (**A**) GFP$^-$ and GFP$^+$ SV cells from PPARγ-GFP mice were sorted, plated, cultured to confluence, and insulin-stimulated adipogenesis was examined with the lipid-specific stain Oil Red O (red). (**B**) Sorted GFP$^+$ SV cells were cultured in media or media supplemented with insulin and then stained with Nile red, a lipid-specific fluorescent dye, to simultaneously visualize fat accumulation and GFP expression. (**C**) (Left) Quantitative real-time fluorescence polymerase chain reaction (QPCR) analysis of the indicated markers in sorted GFP$^+$ cells before (green bars) and after (blue bars) insulin-stimulated adipogenesis. C/EBPα is an adipogenic transcription factor; leptin, adiponectin (ADPN), and adipsin are adipokines, and Pref-1 is a preadipocyte marker whose expression inversely correlates with adipogenesis. (Right) SV cells from P30 PPARγ-GFP adipose depots were examined for GFP (green) and perilipin (an adipocyte marker, red) expression both before (top) and after (bottom) adipogenic induction. Nuclei were stained with DAPI (blue). (**D** to **F**) FACS-isolated GFP$^+$ SV cells were implanted into nude mice, and the tissue that formed after 1 month was photographed with bright field [left panel in (D)] and fluorescent microscopy [right panel in (D)] and examined with hematoxylin and eosin (H&E) staining [left panel in (E)], GFP fluorescence and Nile red staining [right panel in (E)], and GFP fluorescence and perilipin immunochemistry (F). (**G**) (Left) P30 PPARγ-GFP adipose depot SV cells were examined for Sca-1 and GFP expression with flow cytometry. The box indicates the Sca1$^+$GFP$^+$ double-positive population. (Right) IWAT (adipose, top) and SV cells (bottom) of aP2-GFP transgenics were analyzed for GFP expression, which was present in adipocytes but not in SV cells. PPARγ-GFP serves as a control. Nuclei were stained with DAPI (blue). (**H**) QPCR analyses of the indicated markers of FACS-isolated GFP$^+$ SV cells (green bars) and floated adipocytes (blue bars). (**I**) GFP$^-$ SV cells, GFP$^+$ SV cells, and adipocytes were subjected to gene-expression profiling. The heat map illustrates 152 genes that differentiate GFP$^+$ SV cells from the other populations. Red depicts a greater-than-or-equal-to twofold increase in gene expression, whereas green depicts a less-than-or-equal-to twofold decrease in gene expression. Scale bars: (A) to (C), (E), and right panel, bottom row of (G), 50 μm; (D) and right panel, top row of (G), 2 mm; (F), 20 μm in confocal images.

We assessed the adipogenic potential (in vitro and after transplantation) of FACS-isolated GFP$^+$ SV cells (fig. S10). In culture, the sorted GFP$^+$ SV cells underwent spontaneous and insulin-stimulated adipogenesis that was enhanced compared with GFP$^-$ SV cells (Fig. 2, A and B, and fig. S11). GFP$^+$ SV adipogenesis mirrored the gene-expression patterns described for preadipocyte cell line adipogenesis, and the induced adipocytes expressed the perilipin protein with the appropriate subcellular distribution (Fig. 2C) (*16*). Moreover, freshly isolated GFP$^+$ P30 SV cells transplanted into nude mice led to formation of an ectopic GFP$^+$ depot, containing lipid-laden adipocytes that coexpressed GFP and perilipin (Fig. 2, D to F). Thus these GFP$^+$ SV cells have the proliferative and adipogenic properties expected of the endogenous progenitor population.

Fig. 3. SVP vessels contain GFP$^+$ precursors that form adipocytes. (**A**) SVP structures from P30 PPARγ-GFP mice were photographed with light (left) and fluorescent (right) microscopy. Arrows indicate an SV tube. (**B**) PPARγ-GFP SVP tubes were isolated and stained with the lipid-specific dye boron-dipyrromethene (BODIPY), either before culture (left) or after 3 days cultured on a petri dish in insulin (right). Arrows indicate an SV tube. (**C**) PPARγ-GFP SVP tubes were cultured in suspension. Formation of adipocytes that derive from the GFP$^+$ tubes was assessed with BODIPY staining (red). GFP is shown in green. Lipid droplets were visualized with confocal microscopy (right). (**D**) SVP isolates of P30 PPARγ-GFP mice were examined for expression of GFP (green) and the indicated endothelial (PECAM, red) and mural cell (SMA and NG2, blue) markers. (**E**) PPARγ-GFP SVP vessel was examined for expression of GFP (green) and the mural cell markers PDGFRβ (red) and SMA (blue). Yellow arrows indicate the position of GFP$^+$ nuclei within mural cells. Scale bars: (A), (B), and left panels of (C), 50 μm; right panels of (C), (D) and (E), 20 μm in confocal images.

To characterize the GFP$^+$ SV progenitors and their relationship to other cells present in the adipose depot, we assessed cell-surface marker expression using flow cytometry and FACS (fig S10). The majority of GFP$^+$ SV cells expressed Sca1 and CD34, but not CD105, CD45, TER-119, or Mac-1 (Fig. 2G and fig. S12). When these markers were used to positively or negatively select cells (and independently of the GFP reporter), we again isolated a subset of SV cells that generated a GFP$^+$ ectopic adipose depot after transplantation (fig. S13). Some GFP$^+$ SV cells could potentially be differentiated adipocytes that had yet to accumulate enough lipid to float during the density-based SV fractionation procedure. However, reporters driven by the promoter/enhancer of aP2 (*17*), a marker of adipocytes and a PPARγ target gene, displayed strong expression in adipose depots and adipocytes but not in SV cells, unlike the PPARγ reporters (Fig. 2G and fig. S14). Immunocytochemical analyses also showed that the GFP$^+$ SV cells did not express perilipin, an adipocyte marker (Fig. 2C). In addition, the FACS-isolated GFP$^+$ SV cells were molecularly distinct from adipocytes, expressing higher levels of the preadipocyte marker Pref-1, the adipogenic inhibitor GATA3, and targets of the anti-adipogenic Wnt (Wisp2) and Hedgehog (Smo, Gli3) pathways and much lower levels of numerous adipocyte markers (e.g., C/EBPα, FAS, leptin, etc.) (Fig. 2H and fig S15A). Gene-expression profiles further defined the GFP$^+$ SV cells as a unique population within adipose tissues (Fig. 2I). Differentially expressed genes include developmental transcription factors (e.g., goosecoid and Twist2), extracellular matrix genes (e.g., MMP3), anti-angiogenic factors (e.g., Stab1), and signaling cascade components (e.g., EGFR and FGF10) (fig. S15B). Thus, GFP$^+$ SV

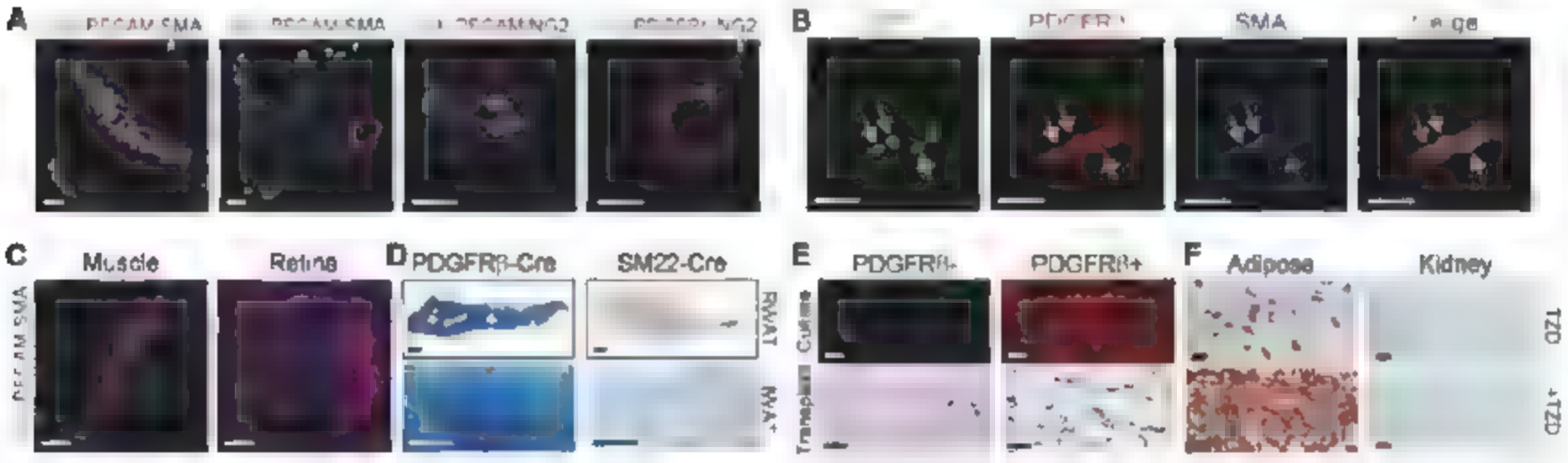

Fig. 4. GFP$^+$ cells are present in adipose depot mural cells. (**A**) P30 PPARγ-GFP WAT was freshly frozen, cryosectioned, and examined with direct fluorescence for GFP and indirect immunofluorescence for the indicated endothelial (PECAM, red) and mural cell (SMA, blue; NG2, blue; PDGFRβ, red) markers. (**B**) Cryosection of a PPARγ-GFP adipose depot showing expression of GFP, PDGFRβ (red), and SMA (blue). Yellow arrows indicate some mural cell nuclei that express GFP. (**C**) Muscle cryosections and retinal whole mount of PPARγ-GFP mice were examined for GFP, PECAM, and SMA as in (A) and (B). GFP was not expressed in mural cells of these tissues. (**D**) RWAT (top, ×5) and IWAT (bottom, ×20) of P30 PDGFRβ-Cre;R26R and SM22-Cre;R26R mice were stained for β-galactosidase expression (blue). (**E**) SV cells were isolated from P30 wild-type mice and sorted with a PDGFRβ antibody. (Top) Confluent PDGFRβ-negative and -positive cells were cultured in insulin, and fat formation was assessed with BODIPY (red). (Bottom) PDGFRβ-negative and -positive cells were transplanted into nude mice, and the resultant tissues were sectioned and H&E stained. (**F**) Adipose SVF and cells dissociated from the kidney were sorted with a PDGFRβ antibody, and PDGFRβ-positive cells were cultured in the absence (top) or presence (bottom) of TZD. Scale bars: (A) to (C), 20 μm in confocal images; (D), 1 mm; (E) and (F), 50 μm.

cells are phenotypically distinct from adipocytes and other SV cells and have a unique molecular signature that allows prospective isolation for transplantation and further lineage analyses.

The local microenvironment (niche) is a crucial determinant of progenitor fate, function, and maintenance (*18*). In part due to the nature of the SV dissociation and isolation method, the anatomical location and neighboring cells of the SV adipocyte precursors are not known. To investigate the architecture of the SV compartment, we developed an SV particulate (SVP) isolation procedure designed to partially maintain the native SV structure while removing adipocytes that obscure visualization of the precursor location (fig. S16). In the SVPs, the majority of GFP^+ cells were arrayed in tubelike structures (Fig. 3A). Based on inspection and lack of lipid staining, the GFP^+ cells present in freshly isolated tubes did not contain lipid droplets (Fig. 3, A and B). Organotypic cultures of SVPs led to formation of lipid-laden GFP^+ adipocytes along the tubes, indicating that the tube-associated SVP GFP^+ cells were adipogenic (Fig. 3, B and C). Because the SVP tubes resembled blood vessels, we stained them with antibodies that recognize constituent cells of the vasculature, including platelet endothelial cell adhesion molecule (PECAM) and three mural cell markers (SMA, PDGFRβ, and NG2) (*19*). The SVP tubes expressed PECAM and were surrounded by cells that expressed SMA, PDGFRβ, and NG2, indicating that they were vessels (Fig. 3, D and E). GFP^+ SVP cells expressed these mural cell markers (Fig. 3, D and E). The notion that PPARγ might be expressed in a subset of mural cells is noteworthy because cultured mural cells, similar to mesenchymal stem cells, are multipotent and can be induced to undergo adipogenesis, chondrogenesis, osteogenesis, and myogenesis and may provide a progenitor reservoir (*19*, *20*).

To investigate the distribution of the GFP^+ progenitors within the mural cell compartment, we immunohistochemically examined sections of freshly frozen PPARγ-GFP P30 adipose depots and other organs. In the adipose vasculature, we again observed colocalization of GFP and mural cell markers (Fig. 4, A and B). The GFP^+ vessels were of various sizes and disseminated throughout the depot (Fig. 4A). However, only a subset of mural cells within a vessel expressed GFP, and some adipose vessels did not appear to harbor GFP^+ progenitors (fig. S17). Mural cells in other examined P30 tissues (including skeletal and cardiac muscles, kidney, retina, pancreas, spleen, lung, etc.) did not express the GFP reporter (Fig. 4C and fig. S18). In older animals (~6 months), we detected GFP in some small caliber PECAM-positive, SMA-negative adult skeletal muscle vessels (figs. S19 and S20). The majority of these adult skeletal muscle GFP^+ cells expressed PECAM, and the cells were not adipogenic (fig. S20). Thus, adipose depots appear to contain a unique population of progenitors present in the adipose depot mural cell compartment.

PDGFRβ marks mural cells and is required for their development (*19*). To explore the possibility that PDGFRβ-expressing cells were part of the adipocyte lineage, we used β-galactosidase (X-Gal) to stain adipose depots of P30 mice that contained both a PDGFRβ-Cre transgene (*21*), which expresses Cre in mural cells and other developing cells, and R26R. As a specificity control, we used SM22-Cre (*22*), a driver construct expressed in a subset of vascular smooth muscle cells. In these Cre-mediated lineage studies, we found that PDGFRβ-Cre generated strong and relatively homogenous lacZ expression throughout adipose depots in adipocytes and mural cells (Fig. 4D). In contrast, SM22-Cre did not, although lacZ was expressed in a distinct subset of adipose depot vessels (Fig. 4D).

To assess the adipogenic potential of PDGFRβ-expressing mural cells, we isolated PDGFRβ-positive and -negative cells from white adipose tissues and other organs by FACS, cultured them in insulin, or transplanted them into nude mice (fig. S21). In both assays, the adipose depot $PDGFRβ^+$ SV cells had higher (and substantially more) adipogenic potential than did PDGFRβ SV cells (Fig. 4E); this adipogenesis was stimulated by thiazolidinediones (TZDs), which are diabetes drugs that activate PPARγ (*23*) (Fig. 4F). In contrast, $PDGFRβ^+$ cells isolated from other organs did not display such potential and were unresponsive to TZDs (Fig. 4F and fig. S22). Although we could identify sections that contained adipocytes in the non-adipose transplants, these adipocytes were GFP-negative (in contrast to adipocytes present in adipose depot SV $PDGFRβ^+$ transplants) (fig. S22), apparently derived or recruited from host tissues. These data are consistent with the possibility that adipocyte progenitors reside as adipose depot mural cells with distinct properties such as adipogenic potential.

The intertwined epidemics of obesity and diabetes have led to a public health crisis that demands an improved understanding of adipocyte biology (*2*, *24*). Yet the identity of the adipocyte progenitors and their precise location has remained elusive. Exploiting genetic reporters, we show that the pool of murine white adipocyte precursors has largely been committed prenatally or just after birth. These precursors divide, maintain the progenitor pool, and produce adipocytes. Some of these progenitors appear to be mural cells that reside in the vasculature of adipose tissue; these results are supported by early electron micrographic studies (*25*, *26*). Thus, the adipose vasculature appears to function as a progenitor niche and may provide signals for adipocyte development.

Several earlier studies have documented an interplay between adipose tissue and the vasculature and shown that this interaction provides possible targets for obesity/diabetes therapies (*27*–*30*). The results described here add a fresh perspective to this interplay. In addition, they provide a foundation for further characterization of the adipose vascular niche and for prospective isolation of the adipocyte progenitors. Such experiments should help to establish whether intervention in adipose lineage formation can be an effective therapeutic approach for obesity and diabetes.

References and Notes

1. G. Ailhaud, P. Grimaldi, R. Negrel, *Annu. Rev. Nutr.* **12**, 207 (1992).
2. S. Gesta, Y. H. Tseng, C. R. Kahn, *Cell* **131**, 242 (2007).
3. S. Klaus, A. M. Cassard-Doulcier, D. Ricquier, *J. Cell Biol.* **115**, 1783 (1991).
4. M. A. Lazar, *Biochimie* **87**, 9 (2005).
5. S. R. Farmer, *Cell Metab.* **4**, 263 (2006).
6. A. Kistner *et al.*, *Proc. Natl. Acad. Sci. U.S.A.* **93**, 10933 (1996).
7. Materials and methods are available as supporting material on *Science* Online.
8. T. S. Yu, M. Dandekar, L. M. Monteggia, L. F. Parada, S. G. Kernie, *Genesis* **41**, 147 (2005).
9. P. Soriano, *Nat. Genet.* **21**, 70 (1999).
10. J. R. Cook, L. P. Kozak, *Dev. Biol.* **92**, 440 (1982).
11. S. Altiok, M. Xu, B. M. Spiegelman, *Genes Dev.* **11**, 1987 (1997).
12. E. D. Rosen, O. A. MacDougald, *Nat. Rev. Mol. Cell Biol.* **7**, 885 (2006).
13. T. Kanda, K. F. Sullivan, G. M. Wahl, *Curr. Biol.* **8**, 377 (1998).
14. T. Tumbar *et al.*, *Science* **303**, 359 (2004), published online 11 December 2003, 10.1126/science.1092436.
15. T. C. Otto, M. D. Lane, *Crit. Rev. Biochem. Mol. Biol.* **40**, 229 (2005).
16. J. M. Ntambi, K. Young-Cheul, *J. Nutr.* **130**, 3122S (2000).
17. R. A. Graves, P. Tontonoz, K. A. Platt, S. R. Ross, B. M. Spiegelman, *J. Cell. Biochem.* **49**, 219 (1992).
18. D. L. Jones, A. J. Wagers, *Nat. Rev. Mol. Cell Biol.* **9**, 11 (2008).
19. A. Armulik, A. Abramsson, C. Betsholtz, *Circ. Res.* **97**, 512 (2005).
20. A. Dellavalle *et al.*, *Nat. Cell Biol.* **9**, 255 (2007).
21. S. S. Foo *et al.*, *Cell* **124**, 161 (2006).
22. P. Boucher, M. Gotthardt, W.-P. Li, R. G. W. Anderson, J. Herz, *Science* **300**, 329 (2003).
23. J. M. Lehmann *et al.*, *J. Biol. Chem.* **270**, 12953 (1995).
24. P. G. Kopelman, *Nature* **404**, 635 (2000).
25. K. Iyama, K. Ohzono, G. Usuku, *Virchows Arch. B Cell Pathol.* **31**, 143 (1979).
26. S. Cinti, M. Cigolini, D. Bosello, P. Bjorntorp, *J. Submicrosc. Cytol.* **16**, 243 (1984).
27. M. A. Rupnick *et al.*, *Proc. Natl. Acad. Sci. U.S.A.* **99**, 10730 (2002).
28. M. G. Kolonin, P. K. Saha, L. Chan, R. Pasqualini, W. Arap, *Nat. Med.* **10**, 625 (2004).
29. L. E. Kuo *et al.*, *Nat. Med.* **13**, 803 (2007).
30. S. Nishimura *et al.*, *Diabetes* **56**, 1517 (2007).

31. We thank S. Kennedy, T. Wang, R. Adams, R. Evans, S. Kerrie, L. Monteggia, M. Osawa, R. Perlingeiro, D. LaPlant, and M. Iacovino, as well as members of the Graf lab. J.M.G. is a founder of Reata Pharmaceuticals, a privately held company designed to address unmet needs in cancer, neurodegenerative, and inflammatory conditions. This work was supported by NIH and the National Institute of Diabetes and Digestive and Kidney Diseases (grants 1R01DK064261 and 1R01DK066556) and the University of Texas Southwestern Medical Center Excellence in Education Fund. W.T., J.M.G., and the University of Texas Southwestern Medical Center may file a patent application related to the work reported here.

Supporting Online Material

www.sciencemag.org/cgi/content/full/1156232/DC1
Materials and Methods
Figs. S1 to S22
References

7 February 2008; accepted 4 September 2008
Published online 18 September 2008;
10.1126/science.1156232
Include this information when citing this paper.

H_2S as a Physiologic Vasorelaxant: Hypertension in Mice with Deletion of Cystathionine γ-Lyase

Guangdong Yang,[1,5] Lingyun Wu,[2]* Bo Jiang,[1] Wei Yang,[1] Jiansong Qi,[1] Kun Cao,[1] Qinghe Meng,[3] Asif K. Mustafa,[4] Weitong Mu,[4,6] Shengming Zhang,[5] Solomon H. Snyder,[4]* Rui Wang[1,5]*

Studies of nitric oxide over the past two decades have highlighted the fundamental importance of gaseous signaling molecules in biology and medicine. The physiological role of other gases such as carbon monoxide and hydrogen sulfide (H_2S) is now receiving increasing attention. Here we show that H_2S is physiologically generated by cystathionine γ-lyase (CSE) and that genetic deletion of this enzyme in mice markedly reduces H_2S levels in the serum, heart, aorta, and other tissues. Mutant mice lacking CSE display pronounced hypertension and diminished endothelium-dependent vasorelaxation. CSE is physiologically activated by calcium-calmodulin, which is a mechanism for H_2S formation in response to vascular activation. These findings provide direct evidence that H_2S is a physiologic vasodilator and regulator of blood pressure.

Nitric oxide (NO) and carbon monoxide (CO) are established physiologic messenger molecules, and NO has an important role as an endothelial cell–derived relaxing factor (EDRF) and regulator of blood pressure (*1*, *2*). Indirect evidence has implicated another endogenous gasotransmitter, hydrogen sulfide (H_2S), in similar functions (*3*–*7*). H_2S can be produced by cystathionine γ-lyase (CSE) or cystathionine β-synthase (CBS) (*3*, *4*), but definitive evidence for either of these enzymes in the physiologic formation of H_2S is lacking.

To investigate the role of H_2S as a physiologic vasorelaxant and determinant of blood pressure, we generated mice with a targeted deletion of the gene encoding CSE (*8*) (fig. S1, A to C). The homozygous ($CSE^{-/-}$) and heterozygous ($CSE^{+/-}$) mutant mice were viable, fertile, and indistinguishable from their control wild-type littermates ($CSE^{+/+}$) in terms of growth pattern. CSE mRNA and protein were absent in heart, aorta, mesenteric artery, liver, and kidneys of $CSE^{-/-}$ mice (fig. S1, D and E). Endogenous H_2S levels in aorta and heart of homozygous mutant male mice ($CSE^{-/-}$) were both decreased by about 80% (Fig. 1A), and H_2S levels in aorta and heart of heterozygous mutant male mice ($CSE^{+/-}$) were both decreased by about 50%. Serum H_2S levels in $CSE^{-/-}$ mice and $CSE^{+/-}$ mice were reduced by about 50 and 20%, respectively (Fig. 1B). Female $CSE^{-/-}$ mice showed a similar decline in H_2S levels (fig. S2, A and B). The residual H_2S in serum may reflect nonenzymatic reduction of elemental sulfur to H_2S or H_2S generated from other tissues that express CBS, another H_2S-generating enzyme (*3*, *5*, *9*).

CSE mutant mice developed age-dependent hypertension. Beginning at 7 weeks of age, both male (Fig. 1C) and female (fig. S2C) $CSE^{-/-}$ mice displayed a higher blood pressure than age-matched wild-type (WT) mice. Blood pressure in the mutant mice peaked at more than 135 mm Hg when the mice were 12 weeks of age; this was almost 18 mm Hg higher than that in control mice. Heterozygous $CSE^{+/-}$ mice also showed elevated blood pressure beginning at 7 weeks of age. The rise in blood pressure was similar in homozygous and heterozygous mice until the mice were 10 weeks of age, after this point, the blood pressure of $CSE^{-/-}$ mice was about 10 mm Hg higher than that of $CSE^{+/+}$ mice. Blood pressure levels assessed by the tail-cuff method were confirmed by direct monitoring of arterial blood pressure through intra-carotid artery catheterization (fig. S3A). Heart rates

[1]Department of Physiology, University of Saskatchewan, Saskatoon, SK S7N 5E5, Canada. [2]Department of Pharmacology, University of Saskatchewan, Saskatoon, SK S7N 5E5, Canada. [3]Department of Pathology, University of Saskatchewan, Saskatoon, SK S7N 5E5, Canada. [4]Departments of Neuroscience, Pharmacology and Molecular Sciences and Psychiatry, Johns Hopkins University School of Medicine, Baltimore, MD 21205, USA. [5]Department of Biology, Lakehead University, Thunder Bay, ON P7B 5E1, Canada. [6]Department of Medicine, Gastroenterology Division, Johns Hopkins University School of Medicine, Baltimore, MD 21205, USA.

*To whom correspondence should be addressed. E-mail: rwang@lakeheadu.ca (R.W.), lily.wu@usask.ca (L.W.), or ssnyder@jhmi.edu (S.H.S.)

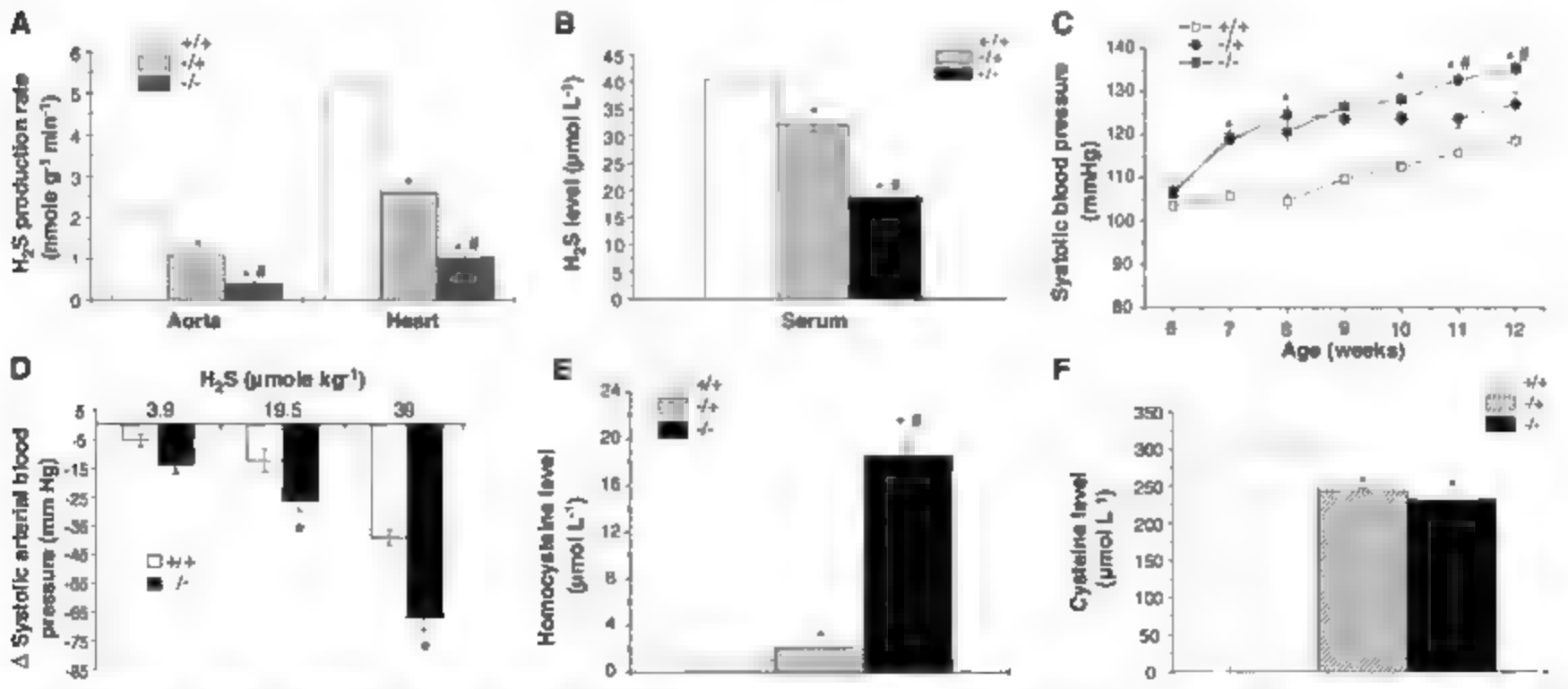

Fig. 1. Phenotype of CSE male knockout mice. (**A**) Reduced H_2S production from aorta and heart tissues in $CSE^{-/-}$ mice and $CSE^{+/-}$ mice. Number of mice are given for each group; $n = 16$. (**B**) Reduced serum H_2S level in $CSE^{-/-}$ mice and $CSE^{+/-}$ mice ($n = 8$ to 10). (**C**) Age-dependent increase in blood pressure of $CSE^{-/-}$ mice and $CSE^{+/-}$ mice ($n = 12$). (**D**) H_2S administration lowers systolic arterial blood pressure in 10-week-old $CSE^{-/-}$ mice ($n = 13$ to 15). (**E**) Increased plasma homocysteine level in $CSE^{-/-}$ mice and $CSE^{+/-}$ mice ($n = 19$). (**F**) Decreased plasma L-cysteine level in $CSE^{-/-}$ mice and $CSE^{+/-}$ mice ($n = 15$). All results are means ± SEM. *$P < 0.05$ versus WT; #$P < 0.05$ versus heterozygote.

were similar in mutant and WT mice. In humans, CSE activity increases rapidly after birth, reaching adult levels when infants are about 3 months of age (*10*, *11*). The age-dependent hypertension of the mutant mice paralleled the ontogeny of CSE in mice, increasing to peak adult levels 3 weeks after birth (*12*). Endogenous H_2S levels in brains from $CSE^{-/-}$ mice were similar to WT mouse values (fig. S3B), consistent with evidence that CSE is not the source of brain H_2S (*3*, *5*, *11*, *12*), and this similarity suggests that the hypertension in the mutant mice is not due to alterations in the central nervous system. In addition, endothelial NO synthase (eNOS) protein was not decreased in $CSE^{-/-}$ mice, which indicated that the hypertension was not due to a loss in NO-mediated vasorelaxation. Kidney architecture was also preserved in the $CSE^{-/-}$ mice, which signifies that the elevation in blood pressure was not caused by renal damage (fig. S4).

H_2S relaxes blood vessels and lowers blood pressure by opening ATP-sensitive K^+ channels in vascular smooth muscle (*4*, *13*, *14*). We explored whether exogenous H_2S could influence the hypertension of $CSE^{-/-}$ animals. Intravenous bolus injections of NaHS, an H_2S donor (*4*, *13*, *15*), elicited dose-dependent transient decreases in systolic blood pressure of both anesthetized $CSE^{-/-}$ and $CSE^{+/+}$ mice (Fig. 1D). The magnitude of decline was greater in mutant versus WT mice, which suggested that the former have a heightened sensitivity to H_2S. NaHS injections did not alter the heart rate of WT or mutant mice. Intravenous bolus injections of ammonium (39 μmol/kg) or pyruvate (39 μmol/kg), the two other products of CSE activity (*3*, *16*), did not influence blood pressure or heart rate. Plasma levels of oxobutanoate, an intermediate in the catabolism of cystathionine by CSE, were similar in $CSE^{-/-}$ and $CSE^{+/+}$ mice (fig. S3C).

CSE deficiency may elicit accumulation of homocysteine and diminished levels of L-cysteine (*17*). In 10-week-old male $CSE^{-/-}$ mice, plasma homocysteine and L-cysteine levels were, respectively, about 18 and 0.8 times the levels seen in age-matched WT mice, whereas the levels in $CSE^{-/+}$ mice were, respectively, about 2.0 and 0.8 times those in WT mice (Fig. 1, E and F). A similar decrease in L-cysteine levels was observed in female $CSE^{-/-}$ mice (fig. S2E). To ascertain whether the hypertension of $CSE^{-/-}$ mice reflects hyperhomocysteinemia (*18*), we administered L-methionine to WT mice in their drinking water for 6 weeks. This intervention augmented plasma homocysteine levels (fig. S3D), but did not alter blood pressure (fig. S3E). Also, while plasma homocysteine levels in male $CSE^{-/-}$ mice were nine times higher than those in male $CSE^{+/+}$ mice (Fig. 1E), blood pressure in the two genotypes was similar (Fig. 1C). Moreover, female and male $CSE^{-/-}$ displayed similar blood pressures (fig. S5A), despite females having six times the plasma homocysteine levels and homocysteine/cysteine ratios seen in males (Fig. 1E and figs. S2D and S5B). Thus, homocysteine is unlikely to be the principal determinant of hypertension in the CSE mutant mice.

We next investigated whether hypertension in the $CSE^{-/-}$ mice reflected alterations in the vascular redox state. Analysis of vascular tissue indicated that the levels of superoxide anion, a

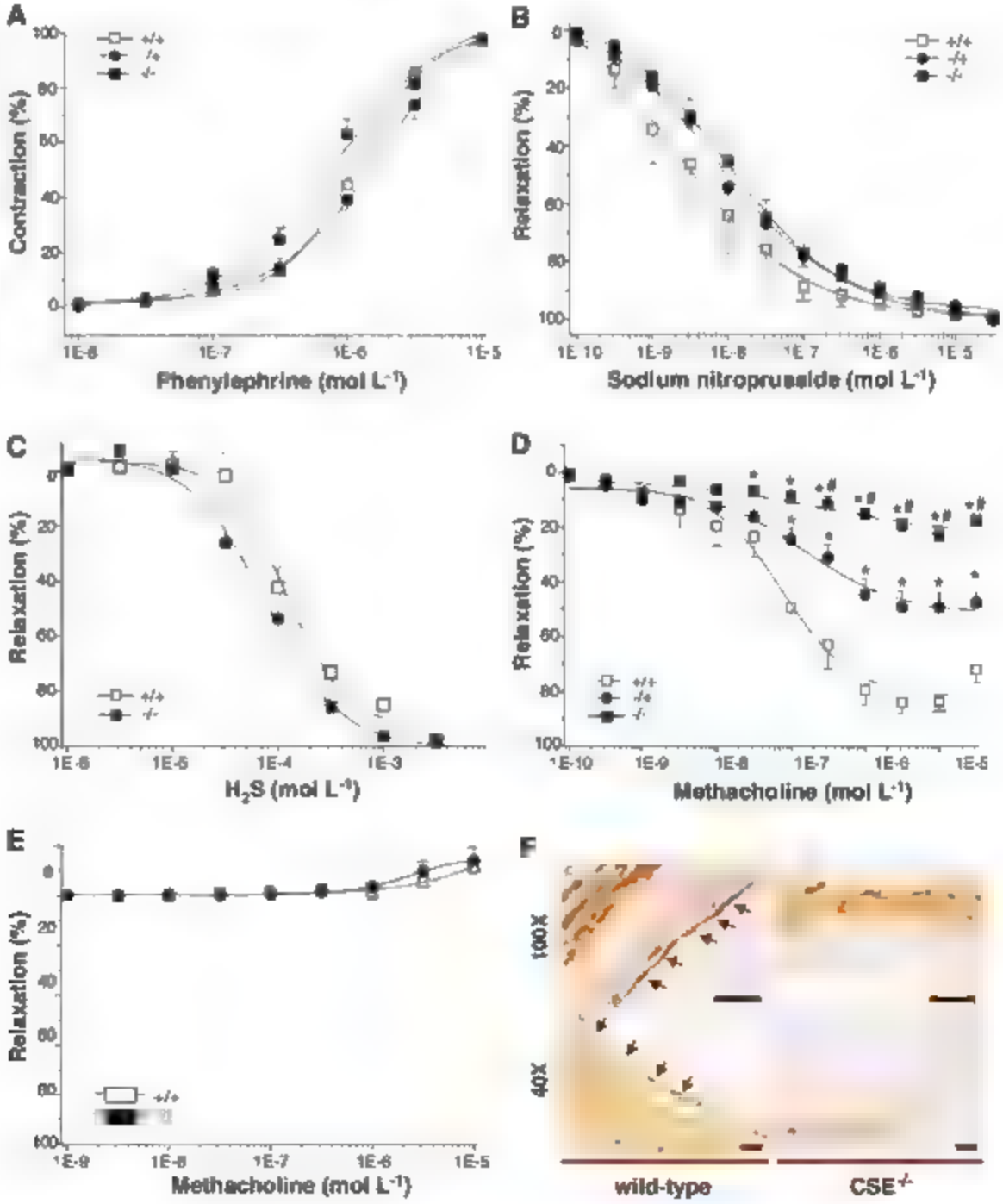

Fig. 2. Impaired endothelial function in CSE mutant mice. Contraction of mesenteric artery evoked by phenylephrine (**A**) and relaxation of mesenteric artery by sodium nitroprusside (**B**), H_2S (**C**), and methacholine (**D**). $n = 15$ for each group. All results are means ± SEM. $^*P < 0.05$ versus WT; $\#P < 0.05$ versus heterozygote. (**E**) Endothelial removal abolishes methacholine-induced relaxation of mesenteric artery. No relaxation occurs in vessels of WT or mutant mice after stripping of the endothelium. For $CSE^{-/-}$ mice, $n = 8$; and for $CSE^{+/+}$ mice, $n = 9$. (**F**) Immunohistochemical localization of CSE to arterial endothelium (black arrows) is abolished in $CSE^{-/-}$ mice. Scale bars, 20 μm.

reactive oxygen species (ROS) that regulates vascular tone, were not significantly different in $CSE^{-/-}$ versus WT mice (fig. S6A). Glutathione (GSH) levels were moderately decreased in the aorta and mesenteric artery beds of the mutant mice (fig. S6B), possibly as a result of the modest decreases seen in L-cysteine levels. As substantially greater decreases of GSH are not associated with hypertension, it is unlikely that GSH plays a major role in the hypertension of CSE mutant mice (*19*).

To investigate mechanisms underlying $CSE^{-/-}$ hypertension, we examined blood vessel responses of the mutant mice. Phenylephrine contracts blood vessels by activating α-adrenoceptors in vascular smooth muscle, whereas H_2S and NO directly relax the muscle (*4*, *20*). By contrast, relaxation after cholinergic stimulation reflects influences on endothelium (*21*). Phenylephrine evoked contraction of mesenteric arteries to a similar extent in WT and $CSE^{-/-}$ mice (Fig. 2A), and the NO donor sodium nitroprusside produced a similar vasorelaxation response in mutant and WT mesenteric arteries (Fig. 2B). H_2S more potently relaxed mesenteric arteries of $CSE^{-/-}$ mice, with a median inhibitory concentration (IC_{50}) of 75 μM, as compared with WT mice (IC_{50} = 120 μM), consistent with supersensitivity associated with diminished formation of endogenous H_2S (Fig. 2C). By contrast, methacholine-induced relaxation of mesenteric arteries that had been constricted by phenylephrine was markedly impaired in mutant mice (Fig. 2D), and endothelial removal abolished methacholine relaxation of both WT and mutant arteries (Fig. 2E). Immunohistochemistry experiments revealed that CSE protein predominantly localized to the endothelium, with faint staining in smooth muscle (Fig. 2F). In an earlier study, we had shown that CSE mRNA is expressed in vascular smooth muscle (*4*). Our reexamination of these data revealed that CSE mRNA is also expressed in the endothelium. Thus, H_2S displays properties characteristic of an EDRF. It is formed in endothelium, and prevention of its synthesis impairs relaxation elicited by a neurotransmitter that acts via the endothelium, but does not impair effects of agents that act directly on smooth muscle. The extent to which H_2S, NO, or CO contribute to EDRF activity in different vascular beds is unclear.

How does endothelial stimulation generate H_2S? eNOS and heme oxygenase-2 (HO-2), the biosynthetic enzymes for NO and CO, respectively, are activated by calcium-calmodulin (*1*, *22*). Thus, endothelial activation by substances such as acetylcholine or bradykinin elicits formation of inositol 1,4,5-trisphosphate, which releases intracellular calcium to stimulate formation of NO or CO. We found a similar mode of regulation for CSE. Using recombinant CSE, we demonstrated its direct binding to calmodulin, which was abolished by the calcium chelator EGTA and the calmodulin antagonist W7 (Fig. 3A). Catalytic activity of pure CSE was increased more than twofold by calcium and calmodulin, but not by either substance alone (Fig. 3B), a level of stimulation similar to the NO- and CO-generating enzymes eNOS (*23*) and HO-2 (*22*). Calcium-dependent regulation of CSE was also evident in endothelial cells, which contain abundant levels of CSE (Fig. 3C). H_2S formation by these cells was markedly augmented by the calcium ionophore A23187, with the increase blocked by the calcium chelator BAPTA [1,2-bis(2-aminophenoxy)ethane-*N*,*N*,*N*′,*N*′-tetraacetic acid] and by W7 (Fig. 3D). These agents markedly reduced basal levels of H_2S, which indicated that H_2S generation by CSE is physiologically regulated by calcium-calmodulin.

Endothelial-dependent vasorelaxation reflects muscarinic cholinergic activation of eNOS (*24*). We demonstrated similar regulation of H_2S formation. Thus methacholine treatment of endothelial cells tripled H_2S levels (Fig. 3E), an effect blocked by the anticholinergic drug atropine. Depletion of CSE by RNA interference markedly diminished the enhancement of H_2S formation by methacholine and A23187 and lowered basal levels of H_2S (Fig. 3F).

In summary, we have established CSE as the physiologic source of H_2S in multiple tissues, especially the vascular system. Mice genetically deficient in this enzyme display marked hypertension, comparable to that of $eNOS^{-/-}$ mice (*24*–*26*). Our findings are consistent with the previous observation that administration of the CSE inhibitor DL-propargylglycine elevates blood pressure (*27*). H_2S has properties in common with physiologic EDRFs. Thus, blood vessel relaxation in response to muscarinic stimulation is profound-

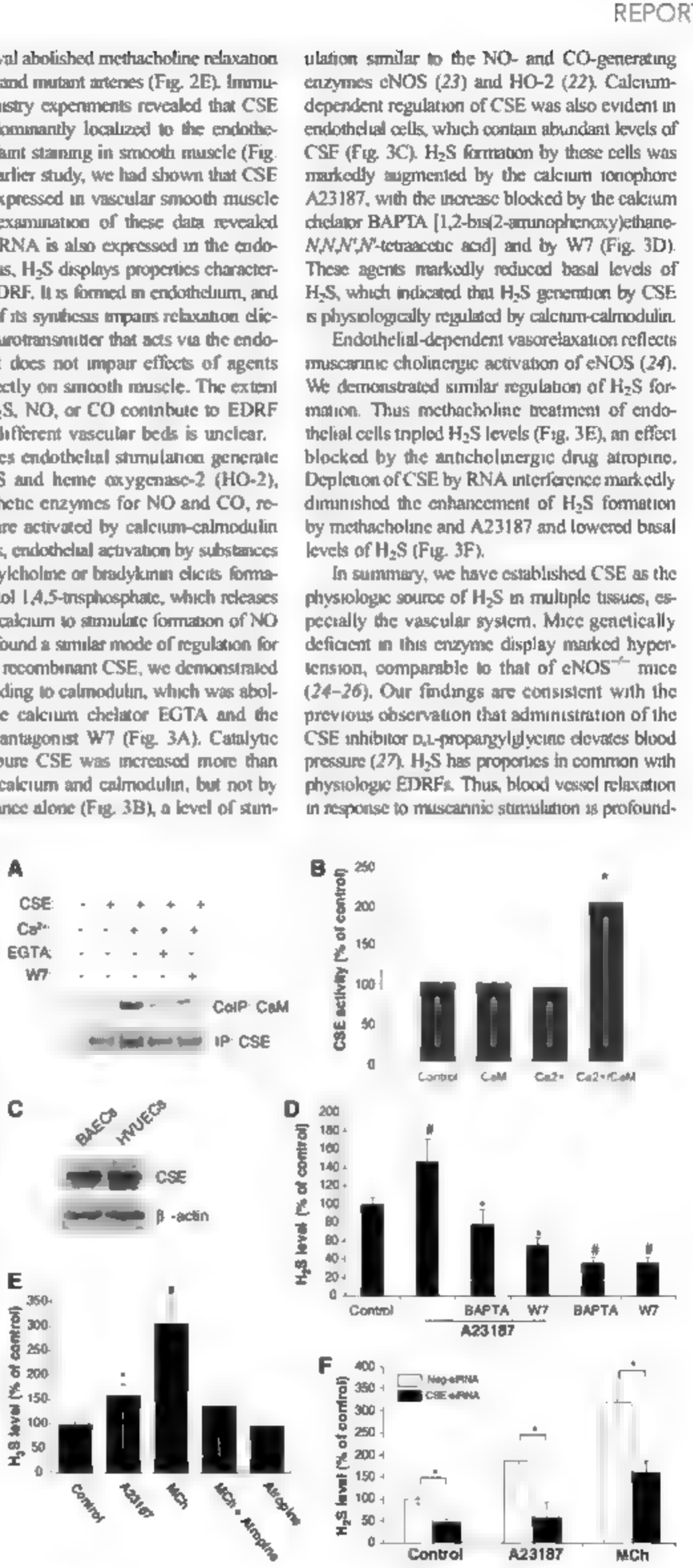

Fig. 3. CSE is activated by calcium-calmodulin upon muscarinic cholinergic stimulation of vascular endothelial cells. **(A)** Calmodulin binds CSE in vitro in the presence of calcium (2 mM). The interaction is diminished by the calcium chelator, EGTA (1 mM), as well as the calmodulin antagonist W7 (100 μM). **(B)** Calcium-calmodulin activates purified CSE in vitro. Calcium (1 mM) or calmodulin (5 μM) separately has no effect on CSE activity. $n = 3$. $^*P < 0.05$ versus the control. **(C)** CSE is endogenously expressed in bovine aortic endothelial cells (BAECs) and human umbilical vein endothelial cells (HUVECs). **(D)** CSE is activated in BAECs treated with the calcium ionophore A23187 (1 μM) for 10 min. Incubation beforehand with the acetoxymethylester of the intracellular calcium chelator BAPTA (BAPTA-AM, 50 μM) or W7 (50 μM) for 30 min prevents CSE activation. $n = 3$. $^*P < 0.05$ versus A23187 treatment; $\#P < 0.05$ versus control. **(E)** CSE is strongly activated in BAECs treated with the muscarinic agonist methacholine (MCh, 1 μM) for 10 min. The activation is twice as much as with similar concentrations of A23187. The stimulatory effect of MCh is abolished by the muscarinic antagonist atropine (50 μM) ($n = 3$ or 4). $^*P < 0.05$ versus control; $\#P < 0.05$ versus all other groups. **(F)** CSE is the endogenous H_2S generator in BAECs. Transfecting cells with 100 nM CSE-specific short interfering RNA (CSE-siRNA) for 48 hours markedly diminishes the enhanced H_2S production observed with A23187 (1 μM) or MCh (1 μM). Western blotting showed that CSE protein is decreased about 60 to 70% by CSE-siRNA ($n = 3$). $^*P < 0.05$.

ly reduced in CSE-deficient mice. Moreover, CSE is predominantly localized to the endothelial layer of blood vessels. The EDRF activity of H_2S reflects muscarinic activation of intracellular calcium release, with calcium-calmodulin physiologically stimulating CSE. NO-mediated EDRF activity arises through a similar mechanism.

Although NO is well established as an EDRF, in numerous vascular beds EDRF activity is only partially diminished by NO synthase inhibitors and in mice lacking the gene for eNOS (*28*, *29*). In our experiments, EDRF activity of murine mesenteric arteries from mutant mice lacking CSE was reduced by about 60%, which suggests that H_2S functions as an EDRF in this vascular bed. The similar elevation of blood pressure in mice with CSE and eNOS knockouts implies that H_2S influences vascular systems underlying peripheral resistance to an extent comparable to the action of NO. A physiologic role for H_2S in regulating blood pressure raises the possibility that pharmacologic enhancement of H_2S formation could be an alternative approach for treatment of hypertension.

References and Notes

1. D. Boehning, S. H. Snyder, *Annu. Rev. Neurosci.* **26**, 105 (2003)
2. J. F. Ndisang, H. E. N. Tabien, R. Wang, *J. Hypertens.* **22**, 1057 (2004)
3. R. Wang, *FASEB J.* **16**, 1792 (2002)
4. W. Zhao, J. Zhang, Y. Lu, R. Wang, *EMBO J.* **20**, 6008 (2001)
5. H. Kimura, *Mol. Neurobiol.* **26**, 13 (2002)
6. Y. Y. Mok *et al.*, *Br. J. Pharmacol.* **143**, 881 (2004)
7. S. Fiorucci *et al.*, *Gastroenterology* **129**, 1210 (2005)
8. Materials and methods are available as supporting material on Science online.
9. D. G. Searcy, S. H. Lee, *J. Exp. Zool.* **282**, 310 (1998)
10. S. H. Zlatkin, G. H. Anderson, *Pediatr. Res.* **16**, 65 (1982)
11. K. Heinonen, *Biochem. J.* **136**, 1011 (1973).
12. I. Ishii *et al.*, *Biochem. J.* **381**, 113 (2004)
13. W. Zhao, R. Wang, *Am. J. Physiol. Heart Circ. Physiol.* **283**, H474 (2002)
14. Y. Cheng, J. F. Ndisang, G. Tang, K. Cao, R. Wang, *Am. J. Physiol. Heart Circ. Physiol.* **287**, H2316 (2004).
15. G. Zhong, F. Chen, Y. Cheng, C. Tang, J. Du, *J. Hypertens.* **21**, 1879 (2003).
16. G. Yang, K. Cao, L. Wu, R. Wang, *J. Biol. Chem.* **279**, 49199 (2004)
17. J. Wang, R. A. Hegele, *Hum. Genet.* **112**, 404 (2003).
18. K. S. McCully, *Nat. Med.* **2**, 386 (1996).
19. C. Iwata, X. Wang, K. Uchida, N. Nakanishi, Y. Hattori, *Life Sci.* **80**, 873 (2007).
20. L. J. Ignarro, *Biosci. Rep.* **19**, 51 (1999)
21. C. L. Cooke, S. T. Davidge, *Cardiovasc. Res.* **60**, 635 (2003)
22. D. Boehning, L. Sedaghat, T. W. Sedlak, S. H. Snyder *J. Biol. Chem.* **279**, 30927 (2004).
23. J. B. Michel, D. Feron, K. Sase, P. Prabhakar, T. Michel, *J. Biol. Chem.* **272**, 25907 (1997).
24. P. L. Huang *et al.*, *Nature* **377**, 239 (1995).
25. K. D. Lake-Bruse *et al.*, *Am. J. Physiol. Heart Circ. Physiol.* **2**, H770 (1999).
26. E. G. Shesely *et al.*, *Proc. Natl. Acad. Sci. U.S.A.* **93**, 13176 (1996)
27. W. Zhao, J. F. Ndisang, R. Wang, *Can. J. Physiol. Pharmacol.* **81**, 848 (2003)
28. M. Feletou, P. M. Vanhoutte, *Ann. Med.* **39**, 495 (2007).
29. R. P. Brandes *et al.*, *Proc. Natl. Acad. Sci. U.S.A.* **97**, 9747 (2000)

30. We thank C. Watkins for experimental and conceptual assistance. Supported by U.S. Public Health Service grant MH18501 and Research Scientist Award DA00074 to S.H.S., and operating grants of Canadian Institutes of Health Research to J.W. and R.W.

Supporting Online Material

www.sciencemag.org/cgi/content/full/322/5901/587/DC1
Materials and Methods
Figs. S1 to S6
References

2 July 2008; accepted 18 September 2008
10.1126/science.1162667

TMEM16A, A Membrane Protein Associated with Calcium-Dependent Chloride Channel Activity

Antonella Caputo,[1] Emanuela Caci,[1] Loretta Ferrera,[1] Nicoletta Pedemonte,[2] Cristina Barsanti,[1] Elvira Sondo,[1] Ulrich Pfeffer,[3] Roberto Ravazzolo,[1] Olga Zegarra-Moran,[1] Luis J. V. Galietta[1,2]*

Calcium-dependent chloride channels are required for normal electrolyte and fluid secretion, olfactory perception, and neuronal and smooth muscle excitability. The molecular identity of these membrane proteins is still unclear. Treatment of bronchial epithelial cells with interleukin-4 (IL-4) causes increased calcium-dependent chloride channel activity, presumably by regulating expression of the corresponding genes. We performed a global gene expression analysis to identify membrane proteins that are regulated by IL-4. Transfection of epithelial cells with specific small interfering RNA against each of these proteins shows that TMEM16A, a member of a family of putative plasma membrane proteins with unknown function, is associated with calcium-dependent chloride current, as measured with halide-sensitive fluorescent proteins, short-circuit current, and patch-clamp techniques. Our results indicate that TMEM16A is an intrinsic constituent of the calcium-dependent chloride channel. Identification of a previously unknown family of membrane proteins associated with chloride channel function will improve our understanding of chloride transport physiopathology and allow for the development of pharmacological tools useful for basic research and drug development.

Electrogenic chloride transport across cellular membranes is mediated by ion channels, which have been classified on the basis of their mechanism of activation. Accordingly, there are Cl^- channels regulated by cyclic adenosine monophosphate (cAMP), Ca^{2+}, cell-volume changes, and membrane potential (*1*). Ca^{2+}-activated Cl^- channels (CaCCs) are involved in important physiological processes such as electrolyte/fluid secretion, smooth muscle excitability, and olfactory perception, but their molecular identity is still unclear and controversial (*2*, *3*). The proteins that have been proposed as main constituents of CaCCs include CLC-3 (*4*), bestrophins (*5*, *6*), and members of the chloride channel, calcium-activated (CLCA) family (*7*, *8*). CLCA proteins are unlikely candidates because they are secreted into the extracellular medium (*9*). CLC-3 and bestrophin gene expression cause the appearance of Cl^- currents that lack the typical voltage dependence of CaCCs (*2*, *3*, *10*, *11*). Therefore, it is likely that the molecular identity of CaCCs remains only partially defined.

[1]Laboratorio di Genetica Molecolare, Istituto Giannina Gaslini, Genova 16148, Italy. [2]Centro di Biotecnologie Avanzate, Genova 16132, Italy. [3]National Cancer Research Institute, Genova 16132, Italy.

*To whom correspondence should be addressed. E-mail: galietta@unige.it

Long-term stimulation of airway epithelial cells with interleukin-4 (IL-4) causes a marked increase in Ca^{2+}-activated Cl^- secretion (*12*) (fig. S1). Because this effect may be caused by increased mRNA levels of the corresponding channel gene, we used this response to identify the proteins constituting the CaCC. Therefore, we performed a microarray-based gene expression analysis on resting and IL-4–treated bronchial epithelial cells and found a large set of proteins whose corresponding mRNA is markedly up-regulated by the cytokine (*13*). These proteins included chemokines, cell adhesion molecules, transcription factors, other regulatory factors, and a group of putative membrane proteins with unknown functions (TMTC3, TSPAN8, KIAA1126, SIDT1, and TMEM16A) that show different levels of stimulation by IL-4 (fig. S1). Up-regulation by IL-4 was confirmed by real-time reverse transcription polymerase chain reaction (RT-PCR). For example, TMEM16A mRNA was increased approximately sevenfold after IL-4 treatment.

To further analyze these candidate channels by gene silencing, we used CFPAC-1, a pancreatic cell line with abundant CaCC activity (*14*), and CFBE41o-, a cell line derived from human bronchial epithelium (*15*). We transfected small pools of small interfering RNA (siRNA) against each of the putative membrane proteins up-regulated by IL-4. siRNA against TMC5, an unknown membrane protein with possible channel function but not affected by IL-4, served as a control. siRNA-transfected CFPAC-1 and CFBE41o- cells were assessed for CaCC activity with an assay based on a halide-sensitive yellow fluorescent protein (YFP) (*16*, *17*). Cells with stable YFP expression were stimulated with uridine 5′-triphosphate (UTP) (100 μM), which elicits a purinergic receptor–mediated increase of intracellular Ca^{2+}. The Ca^{2+} increase triggered a rapid

fluorescence decrease due to a large I^- influx through CaCCs (Fig. 1A). Cells transfected with siRNA against TMEM16A showed a 60 to 70% reduction in Ca^{2+}-dependent I^- influx as compared with cells treated with control siRNA or siRNA against other targets (Fig. 1B and fig. S2). To confirm these results, we transfected CFPAC-1 and CFBE41o– cells with a single siRNA against TMEM16A obtained from a commercial source different from where we obtained the siRNA for the first screening (Fig. 1C and fig. S2). Anti-TMEM16A RNA duplexes caused in both cell types a substantial reduction in CaCC activity. The same degree of inhibition by anti-TMEM16A siRNA was obtained when Ca^{2+}-elevation was triggered with ionomycin (1 μM) instead of UTP, which indicated that TMEM16A silencing affects a step downstream of purinergic receptor activation and cytosolic Ca^{2+} increase. CaCC activity was also unaffected when cells were transfected with siRNA against two TMEM16A homologs, TMEM16F and TMEM16K.

We also measured the activity of CaCCs and the effect of TMEM16A silencing with the short-circuit current technique (*17*). Primary cultures of human bronchial epithelial cells were transfected with nontargeting or anti-TMEM16A single siRNA at the time of plating on porous membranes. After 8 to 10 days, when the cells were differentiated and polarized, they were treated for 24 hours with or without IL-4 (10 ng/ml). Addition of UTP (100 μM) to the apical membrane elicited a transient increase of the current due to Ca^{2+}-dependent Cl^- secretion (Fig. 1D), and this response was up-regulated in cells treated with IL-4 (Fig. 1E). In agreement with data obtained with the YFP assay, the UTP-dependent Cl^- current was significantly reduced in cells previously transfected with anti-TMEM16A siRNA, with or without IL-4 treatment (Fig. 1, D and E). This effect was not due to inhibition of the purinergic-dependent Ca^{2+} signal, because the Ca^{2+} increase triggered by UTP was not diminished after transfection with TMEM16A-specific siRNA as compared with control-transfected cells (fig. S3). This result indicates that TMEM16A is not involved in intracellular Ca^{2+} signaling or homeostasis but is probably more directly involved in Cl^- transport. Silencing of TMEM16A also caused CaCC activity inhibition when the basolateral membrane was permeabilized (fig. S4).

In additional short-circuit current experiments on CFPAC-1 cells, UTP triggered a fast transient current increase due to the activation of apical CaCCs (*14*, *18*). This current was absent in cells transfected with anti-TMEM16A siRNA (fig. S5). The currents in TMEM16A-silenced cells were similar to those of cells treated with niflumic acid, a classical blocker of CaCCs channels (fig. S5).

Whole-cell patch-clamp experiments were carried out on CFPAC-1 cells to further confirm the silencing of CaCCs by anti-TMEM16A siRNA. Using a micropipette (intracellular) solution containing 600 nM free Ca^{2+}, we recorded typical CaCC currents (*14*) with time-dependent activation at positive membrane potentials (Fig. 1F). The steady-state current-voltage relationship showed a strong outward rectification. Returning to the negative holding potential at the end of positive test pulses generated inward tail currents that slowly inactivated. CFPAC-1 cells transfected with anti-TMEM16A siRNA showed a marked reduction of CaCC currents as compared with cells transfected with control siRNA (Fig. 1F). Outward currents at positive voltages, and corresponding tail currents, were inhibited. In fact, membrane currents after

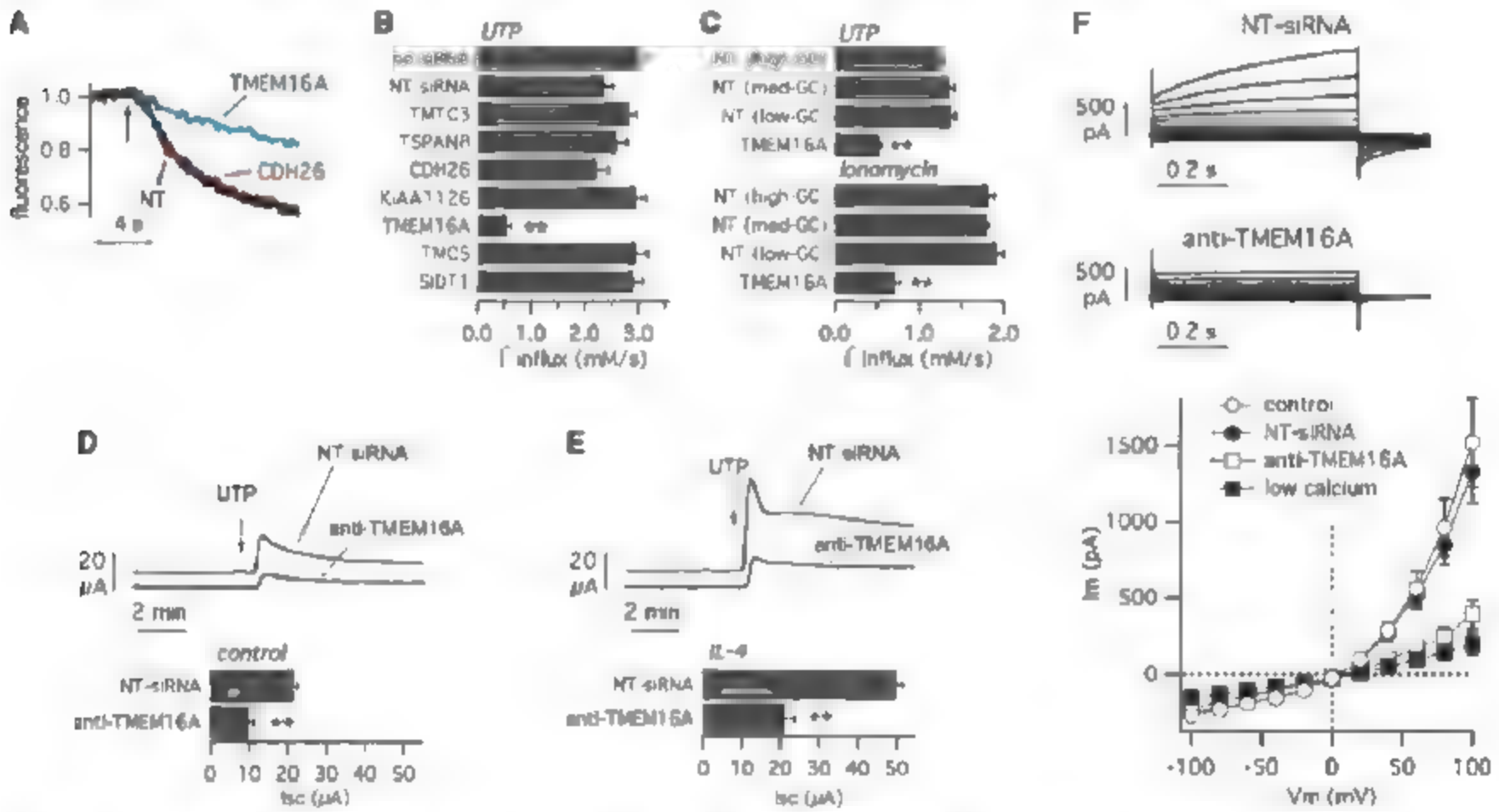

Fig. 1. Down-regulation of Ca^{2+}-dependent anion transport by TMEM16A silencing. (**A** to **C**) CaCC assay based on the halide-sensitive YFP in pancreatic CFPAC-1 cells. (**A**) Representative traces showing cell fluorescence quenching upon the addition of extracellular I^- plus UTP (arrow). (**B**) Summary of Ca^{2+}-activated I^- influx in untreated cells, in cells transfected with non-targeting siRNA (NT-siRNA), or transfected with siRNA pools against the indicated genes (mean ± SEM, $n = 8$ experiments per condition). (**C**) Ca^{2+}-activated I^- influx as in (**B**) but with a single siRNA against TMEM16A versus three nontargeting siRNA with different guanosine and cytosine content (mean ± SEM, $n = 5$ experiments per condition). Cells were stimulated with UTP (100 μM) or ionomycin (1 μM). ** $P < 0.01$ versus nontargeting siRNA. (**D** and **E**) Short-circuit current (I_{sc}) recordings on polarized monolayers of primary human bronchial epithelial cells. Ca^{2+}-dependent Cl^- secretion was triggered with apical UTP (100 μM). Cells were transfected with nontargeting or anti-TMEM16A siRNA and then left in control conditions (D) or incubated with IL-4 (E). (Top) Representative traces. (Bottom) Summary of results (mean ± SEM, $n = 4$ experiments per condition). ** $P < 0.01$ versus nontargeting siRNA. (**F**) Whole-cell membrane currents (I_m) from CFPAC-1 cells. Pipette (intracellular) solution contained 600 nM free Ca^{2+}. (Top) Representative currents elicited at voltages in the −100- to +100-mV range. (Bottom) Membrane currents measured at the end of voltage pulses (I_m) (mean ± SEM, $n = 10$ to 20 experiments) are plotted against the applied membrane potential. Conditions were nontransfected, transfected with non-targeting siRNA, transfected with anti-TMEM16A, and nontransfected but with nominal 0 Ca^{2+} in the intracellular solution. The currents measured in TMEM16A-silenced cells were significantly smaller than those of control-transfected cells at +20 mV ($P < 0.05$) and at +40 to +100 mV ($P < 0.01$).

TMEM16A silencing, were similar to those of nonsilenced cells recorded with a Ca^{2+}-free micropipette solution (Fig. 1F).

In silico gene expression data indicate that TMEM16A is preferentially expressed in exocrine glands and organs rich in glands. In mice (see http://symatlas.gnf.org/SymAtlas/ for tissue distribution), TMEM16A is highly expressed in the mammary glands, prostate, large intestine, lung, trachea, uterus, and vomeronasal organ. We compared expression between CFPAC-1 and 9HTEo- cells. Real-time RT-PCR in CFPAC-1 cells, which have a large CaCC activity (*14*), showed that expression of TMEM16A mRNA was ~200-fold higher than in 9HTEo− cells, a tracheal epithelial cell line in which UTP and other Ca^{2+}-elevating agents induce a small activation of a different channel, the swelling-activated Cl^- channel (*19*).

TMEM16A is alternatively spliced, generating multiple protein isoforms with various combinations of alternative protein segments a, b, c, and d (fig. S6). All isoforms were predicted to maintain a basic structure consisting of eight transmembrane helices with N and C termini lying on the cytosolic side. To determine which isoform is expressed in bronchial epithelial cells, we performed RT-PCR experiments with primers flanking the entire coding sequence. Amplification products were cloned in plasmids, and 22 clones were fully sequenced. We found that bronchial epithelial cells expressed an isoform, TMEM16A(abc), that has 982 amino acids (*13*).

To further validate the involvement of TMEM16A in CaCC function, we transiently cotransfected COS-7 and HEK-293 cells with a plasmid carrying the halide-sensitive YFP and plasmids coding for various TMEM16A isoforms (fig. S6). In both cell types, transfection of TMEM16A cDNAs caused a substantial increase of the halide transport triggered by ionomycin as compared with cells transfected with the YFP alone. The effect was particularly dramatic for isoforms (abcd), (abc), and (ac): Up to 60 to 80% of cell fluorescence was quenched by I^- influx in the first 10 s. Accordingly, Ca^{2+}-dependent I^- influx was 25 to 30 times larger than in mock-transfected cells (fig. S6). Conversely, the Ca^{2+}-dependent halide transport generated by TMEM16A(*0*) was considerably smaller than that generated by transfection with other isoforms.

The correlation between TMEM16A and CaCC channels was further investigated by stable transfection of TMEM16A in Fischer rat thyroid (FRT) cells. Such cells have low endogenous CaCC transport and are able to form tight epithelia, suitable for transepithelial Cl^- current measurements (*16*, *17*). Null FRT cells responded to ionomycin with a small current increase (1 to 2 μA). The pool of FRT cells arising from stable TMEM16A(abc) transfection showed a ninefold increase in ionomycin-induced current (Fig. 2A). Isolation of pure clones from the pool led to the generation of cells with very large ionomycin-induced currents, up to 170-fold larger than in null FRT cells (Fig. 2A). These currents were strongly inhibited by niflumic acid (100 μM). We further studied pharmacological sensitivity by using the YFP assay. TMEM16A-dependent anion transport was highly sensitive to niflumic acid and 5-nitro-2-(3-phenylpropylamino) benzoic acid (NPPB) but not to diphenylamine carboxylate and cystic fibrosis transmembrane conductance regulator inhibitor–172 ($CFTR_{inh}$-172) (fig. S7).

To study the subcellular localization of TMEM16A protein, we introduced by mutagenesis a FLAG epitope in the N terminus of isoform (abc) at the end of segment (a). This construct was transiently transfected and stable-transfected in human embryonic kidney (HEK) 293 and FRT cells, respectively. Immunofluorescence showed a pattern consistent with a plasma membrane localization of the TMEM16A protein (Fig. 2B). The protein with the FLAG epitope was fully functional (fig. S6).

Whole-cell patch-clamp experiments revealed that FRT cells with stable expression of TMEM16A(abc) manifested membrane currents with the typical voltage dependence of CaCC (Fig. 2C). The shape and size of the currents were dependent on the free-Ca^{2+} concentration in the pipette (cytosolic) solution (Fig. 2, C and D). In contrast, none of the null cells showed CaCC-like currents (Fig. 2C). The maximum current, measured at +100 mV in null cells with 600 nM free Ca^{2+} in the pipette solution, was 42 ± 8 pA (n = 10 experiments), a value 25 times smaller than in TMEM16A-transfected cells under identical conditions (n = 16 experiments; $P < 0.01$). TMEM16A-dependent currents were sensitive to extracellular Cl^- concentration. Lowering of extracellular Cl^- by replacement with gluconate from 154 to 4 mM strongly abolished outward currents (Cl^- entering the cell) and shifted the reversal potential by 41.2 ± 4.0.1 mV in the positive direction (n = 5 experiments) (Fig. 2E), the expected shift for a perfectly selective Cl^- channel being 90 mV. Such a difference may indicate that the underlying channel has a small but notable permeability to gluconate (*20*).

We transiently transfected the plasmid carrying the coding sequence for isoform (abcd) in HEK-293 cells for whole-cell patch-clamp analysis. As expected for a transfection with an estimated 20 to 30% efficiency, 18 out of 65 cells showed membrane currents with CaCC biophysical characteristics (Fig. 3A). This current was never observed in 27 mock-transfected cells. After averaging the results from all

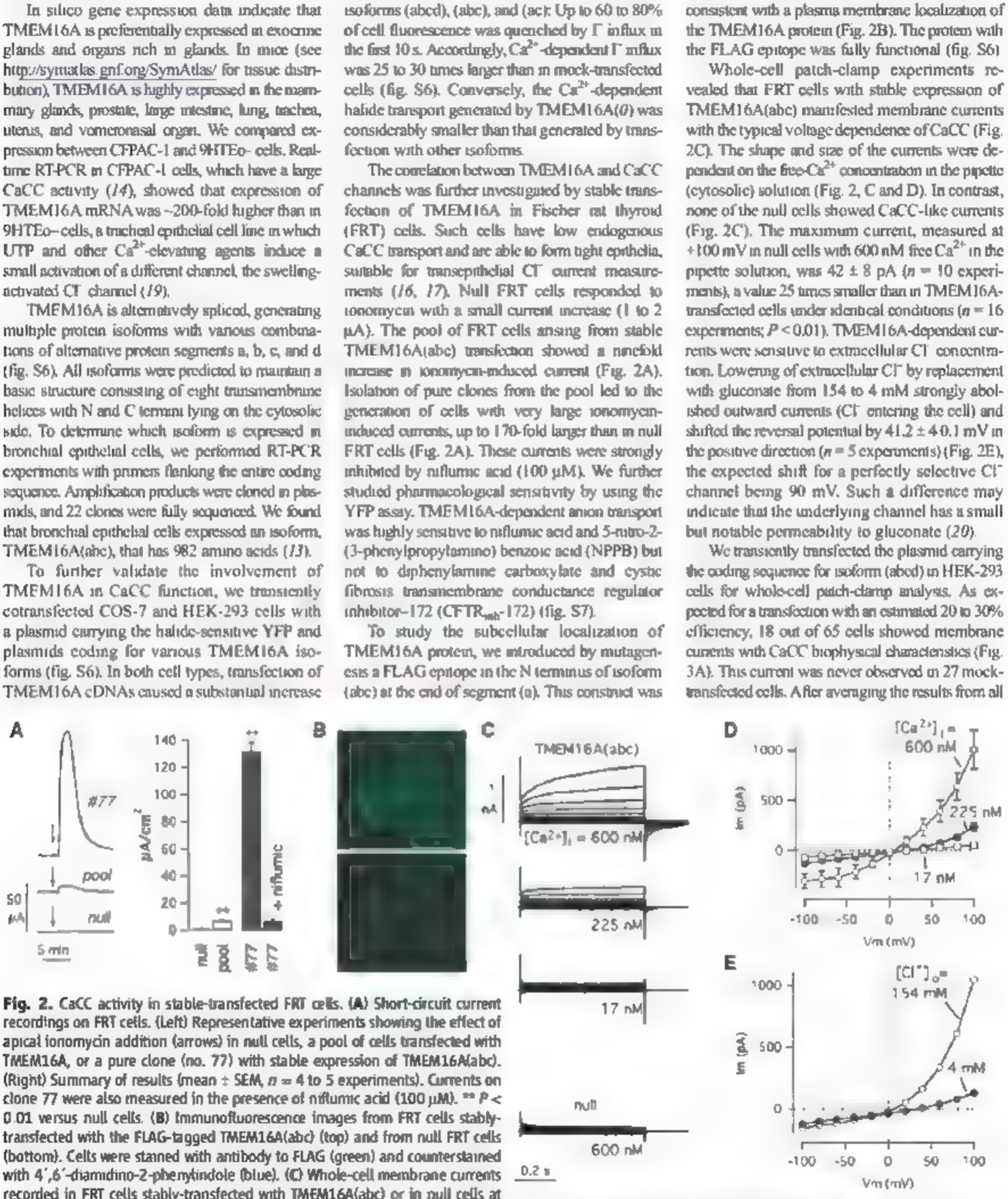

Fig. 2. CaCC activity in stable-transfected FRT cells. (**A**) Short-circuit current recordings on FRT cells. (Left) Representative experiments showing the effect of apical ionomycin addition (arrows) in null cells, a pool of cells transfected with TMEM16A, or a pure clone (no. 77) with stable expression of TMEM16A(abc). (Right) Summary of results (mean ± SEM, n = 4 to 5 experiments). Currents on clone 77 were also measured in the presence of niflumic acid (100 μM). ** $P <$ 0.01 versus null cells. (**B**) Immunofluorescence images from FRT cells stably-transfected with the FLAG-tagged TMEM16A(abc) (top) and from null FRT cells (bottom). Cells were stained with antibody to FLAG (green) and counterstained with 4′,6′-diamidino-2-phenylindole (blue). (**C**) Whole-cell membrane currents recorded in FRT cells stably-transfected with TMEM16A(abc) or in null cells at the indicated intracellular free-Ca^{2+} concentration. (**D** and **E**) Current-voltage relationships for TMEM16A(abc)-expressing cells showing dependence on intracellular free Ca^{2+} (D) or extracellular Cl^- (E). In the latter type of experiments, intracellular Ca^{2+} was 600 nM.

cells, without selecting for the ones having voltage-dependent currents, we found a considerable difference with respect to mock-transfected cells. For example, at +100 mV the currents were approximately fivefold larger in (abcd)-transfected cells (Fig. 3, A and B). Cl^- selectivity of currents evoked by TMEM16A transfection was demonstrated by extracellular Cl^- replacement with gluconate. Under these conditions, outward currents were strongly decreased and the reversal potential was shifted by 32.9 ± 1.5 mV in the positive direction. When we expressed the (0) isoform in HEK-293, we measured currents that lacked the time-dependent activation at positive voltages of (abc) and (abcd) isoforms. Although small, such currents were substantially larger than those of mock-transfected cells (Fig. 3, A and B).

To further validate the relationship of TMEM16A proteins with CaCC currents, we introduced mutations in highly conserved amino acids with predicted localization in transmembrane segments of the (abcd) isoform (fig. S6). We transiently transfected the resulting plasmids in HEK-293 cells and studied whole-cell membrane currents with the patch-clamp technique. Transfection of Lys^{349} → Ala^{349} (K349A) (*21*), K631A, and T830A generated currents that were not markedly different from those of wild-type protein, whereas K636A and R912A elicited very small membrane currents. R563A was associated with CaCC currents with an altered kinetic behavior. The decay of tail currents after returning to the holding potential from positive test pulses was substantially slower (Fig. 3C). Fitting the current decay with a single exponential function gave time constants consistently higher for R563A relative to wild-type protein (Fig. 3D). Q757A caused a marked alteration in voltage dependence. Transfected cells showed membrane currents larger than those in control cells but without time-dependent activation at positive voltages (Fig. 3E). Furthermore, the currents elicited by Q757A expression showed a reduced Cl^- selectivity because extracellular Cl^- replacement with gluconate shifted the reversal potential by only 23.3 ± 1.5 mV (Fig. 3F).

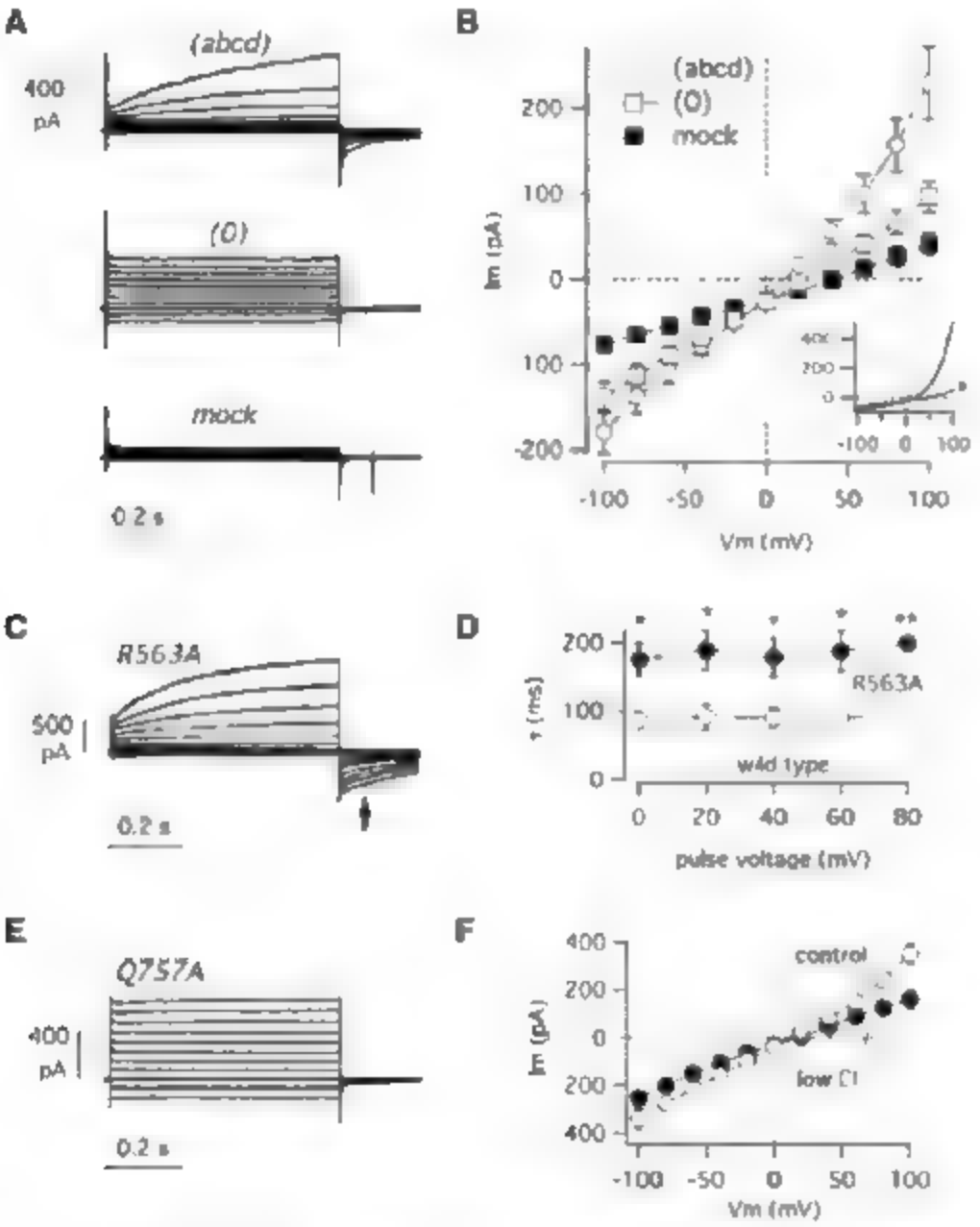

Fig. 3. Induction of Cl^- currents by transient TMEM16A expression. (**A**) Representative membrane currents measured in HEK-293 cells. Each panel is the overlap of currents elicited in a single cell at membrane potentials in the −100 to +100 mV range. Cells were transfected with null plasmids or with plasmids coding for (abcd) or (0) isoforms. (**B**) Current-voltage relationships from experiments as those shown in (A). Each point is the mean ± SEM of currents measured at the end of voltage pulses (n = 27 to 65 experiments). Values for (abcd) and (0) isoforms were significantly larger than those of mock-transfected cells at positive ($P < 0.01$) and negative ($P < 0.05$) membrane potentials). (Inset) Current-voltage relationship for a representative cell transfected with the (abcd) isoform before (no asterisk) and after (asterisk) replacement of extracellular Cl^- with gluconate. (**C**) Membrane currents from a cell transfected with TMEM16A(abcd) carrying the R563A mutation. The arrow shows tail currents with a slower decay as compared with the wild-type protein in (A). (**D**) Time constant values (τ) (mean ± SEM, n = 3 experiments per condition) determined by fitting tail currents of the wild-type protein and the R563A mutant with a single exponential function. Tail currents were measured at −60 mV after stepping the membrane to the indicated voltages. * $P < 0.05$; ** $P < 0.01$. (**E**) Membrane currents from a cell transfected with the Q757A mutant. (**F**) Current-voltage relationship from experiments with the Q757A mutant before and after replacement of extracellular Cl^- with gluconate (mean ± SEM, n = 6 experiments per condition).

The R563A mutation in the first transmembrane segment of TMEM16A(abcd) is homologous to the R515K mutation in the bestrophin-1 protein, which is associated with a form of vitelliform macular dystrophy (*22*). Bestrophin-1 has been proposed to be a Ca^{2+}-activated Cl^- channel (*23*), although this has been questioned (*24*). Our results show that R563A mutation in TMEM16A(abcd) alters the kinetic properties of the channel, which is consistent with the hypothesis that this residue is important for the function of Cl^- channels.

We have obtained evidence that TMEM16A is a membrane protein involved in Ca^{2+}-dependent Cl^- transport. In particular, silencing by siRNA or up-regulation by cDNA transfection leads to the decrease or increase, respectively, of membrane currents whose biophysical properties reproduce those of classical CaCCs found in various cell types. Furthermore, specific mutagenesis of highly conserved amino acids changed intrinsic properties of the channel. TMEM16A belongs to a large family that includes other membrane proteins that may also have an ion channel function. Family members with strong sequence identity to TMEM16A, such as TMEM16B, are also possible CaCCs. Other family members, such as TMEM16F, TMEM16J, or TMEM16K, may represent other types of Cl^- channels with different biophysical properties and mechanisms of regulation.

References and Notes

1. T. Jentsch, V. Stein, F. Weinreich, A. Zdebik, *Physiol. Rev.* **82**, 503 (2002).
2. J. Eggermont, *Proc. Am. Thorac. Soc.* **1**, 22 (2004).
3. C. Hartzell, I. Putzier, J. Arreola, *Annu. Rev. Physiol.* **67**, 719 (2005).
4. F. Huang *et al.*, *J. Biol. Chem.* **276**, 20093 (2001).
5. Z. Qu, R. W. Wei, W. Mann, H. C. Hartzell, *J. Biol. Chem.* **278**, 49563 (2003).
6. H. Sun, T. Tsunenari, K. W. Yau, J. Nathans, *Proc. Natl. Acad. Sci. U.S.A.* **99**, 4008 (2002).
7. R. Gandhi *et al.*, *J. Biol. Chem.* **273**, 32096 (1998).
8. A. D. Gruber, K. D. Schreur, H. L. Ji, C. M. Fuller, B. U. Pauli, *Am. J. Physiol.* **276**, C1261 (1999).
9. A. Gibson *et al.*, *J. Biol. Chem.* **280**, 27205 (2005).
10. B. Nilius *et al.*, *J. Physiol.* **498**, 381 (1997).
11. Z. Qu, R. W. Wei, H. C. Hartzell, *Am. J. Physiol.* **285**, F326 (2003).
12. L. J. V. Galietta *et al.*, *J. Immunol.* **168**, 839 (2002).
13. Materials and methods are available as supporting material on *Science* Online.
14. L. J. V. Galietta *et al.*, *Pflugers Arch.* **426**, 534 (1994).
15. K. Kunzelmann *et al.*, *Am. J. Respir. Cell Mol. Biol.* **8**, 522 (1993).
16. L. J. V. Galietta *et al.*, *J. Biol. Chem.* **276**, 19723 (2001).
17. N. Pedemonte *et al.*, *J. Immunol.* **178**, 5144 (2007).
18. M. A. Caren, X. Yang, C. Schultz, S. B. Shears, *J. Biol. Chem.* **275**, 26906 (2000).
19. L. J. V. Galietta *et al.*, *FEBS Lett.* **304**, 61 (1992).
20. S. Frings, D. Reuter, S. J. Kleene, *Prog. Neurobiol.* **60**, 247 (2000).

21. Single-letter abbreviations for the amino acid residues are as follows: A, Ala; C, Cys; D, Asp; E, Glu; F, Phe; G, Gly; H, His; I, Ile; K, Lys; L, Leu; M, Met; N, Asn; P, Pro; Q, Gln; R, Arg; S, Ser; T, Thr; V, Val; W, Trp; and Y, Tyr.
22. This study was supported by grants from the Telethon Foundation (GGP05103), Cystic Fibrosis Foundation Therapeutics, Comitato Interministeriale per la Programmazione Economica–Regione Liguria 2007 (Drug Discovery and Delivery), and the Italian Cystic Fibrosis Foundation.

Supporting Online Material

www.sciencemag.org/cgi/content/full/1163518/DC1
Materials and Methods
Figs. S1 to S7
References

21 July 2008; accepted 28 August 2008
Published online 4 September 2008;
10.1126/science.1163518
Include this information when citing this paper

Receptor-Like Kinase ACR4 Restricts Formative Cell Divisions in the *Arabidopsis* Root

Ive De Smet,[1,2,4]* Valya Vassileva,[1,2]*† Bert De Rybel,[1,2] Mitchell P. Levesque,[3]‡ Wim Grunewald,[1,2] Daniël Van Damme,[1,2] Giel Van Noorden,[1,2] Mirande Naudts,[1,2] Gert Van Isterdael,[1,2] Rebecca De Clercq,[1,2] Jean Y. Wang,[3] Nicholas Meuli,[5] Steffen Vanneste,[1,2] Jiří Friml,[1,2] Pierre Hilson,[1,2] Gerd Jürgens,[4] Gwyneth C. Ingram,[5] Dirk Inzé,[1,2] Philip N. Benfey,[3] Tom Beeckman[1,2]§

During the development of multicellular organisms, organogenesis and pattern formation depend on formative divisions to specify and maintain pools of stem cells. In higher plants, these activities are essential to shape the final root architecture because the functioning of root apical meristems and the de novo formation of lateral roots entirely rely on it. We used transcript profiling on sorted pericycle cells undergoing lateral root initiation to identify the receptor-like kinase ACR4 of *Arabidopsis* as a key factor both in promoting formative cell divisions in the pericycle and in constraining the number of these divisions once organogenesis has been started. In the root tip meristem, ACR4 shows a similar action by controlling cell proliferation activity in the columella cell lineage. Thus, ACR4 function reveals a common mechanism of formative cell division control in the main root tip meristem and during lateral root initiation.

Unlike animals, plants produce new tissues and organs primarily postembryonically from pluripotent stem cells in the root and shoot meristems. In *Arabidopsis* root tips, the embryonic stem cell niche, a single layer of initial cells surrounding the quiescent center, is well characterized (*1*). However, the branching process in roots depends on the formation of new meristems starting from a limited number of pericycle lateral root founder cells (*2*). The mechanisms underpinning the restriction of formative cell division to a few pericycle cells and the specification of stem cell identity in this process remain unresolved.

To gain insight into this process, we performed live imaging on longitudinal pericycle cell files during lateral root initiation in *Arabidopsis*. Time-lapse recordings revealed a repeated cell division pattern composed of two successive rounds of asymmetric cell divisions, generating a central core of four small cells and two larger flanking cells (Fig. 1, A to D, fig. S1, and movie S1). To achieve this, the original pericycle lateral root founder cells undergo an initial asymmetric division to generate a smaller daughter cell and a larger flanking cell. The latter will undergo another asymmetric division, resulting in a central core of small cells. Hereafter, the process of anticlinal asymmetric cell divisions stops, and the two central cells change their axis of division by 90° and divide periclinally (Fig. 1E and fig. S1). The flanking and the adjacent undivided pericycle cells undergo few or no anticlinal divisions and will only contribute modestly to the flanks of the primordium (*2*).

Exogenous application of the plant hormone auxin induces cell division and results in lateral root initiation in the entire pericycle at the xylem poles in *Arabidopsis* (*3*). Auxin can thus be used to synchronously induce asymmetric cell divisions of cells, facilitating analysis of molecular mechanisms of lateral root formation. To identify molecular components controlling this essential cell division pattern, we characterized the transcript profile of auxin-activated pericycle cells precisely located at the xylem pole using fluorescence-activated cell sorting in combi-

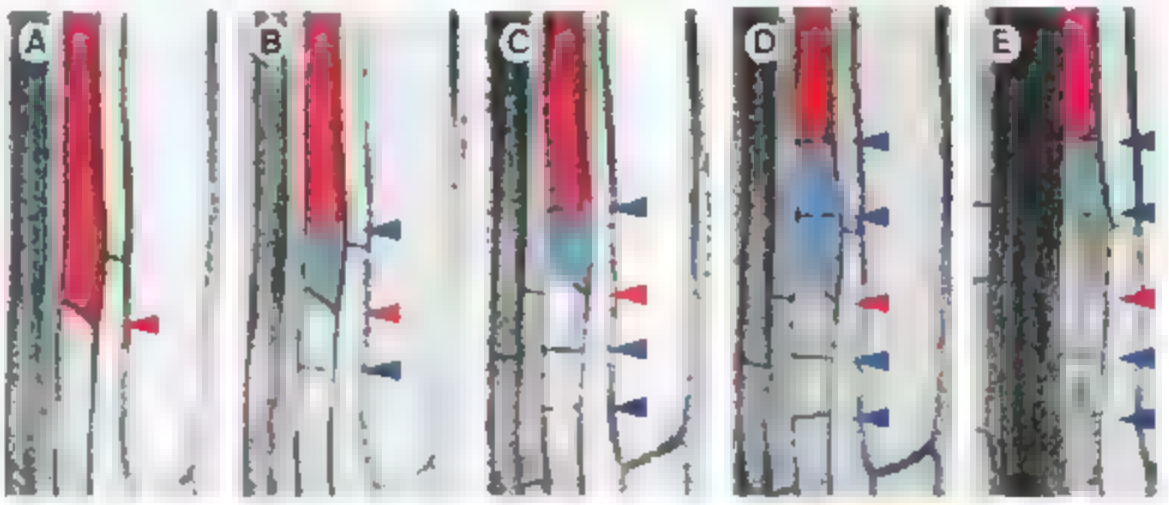

Fig. 1. Identification of asymmetric cell division genes during lateral root initiation. (**A** to **E**) In vivo analysis of consecutive divisions in one file of xylem pole pericycle cells visualized with the plasma membrane marker *p35S::EGFP:1T16a* (black). Arrowheads mark the oblique cell wall between two adjacent pericycle cells (red), consecutive anticlinal asymmetric cell divisions (blue), and first periclinal divisions of the central cells (green). Color code used for the overlay corresponds to fig. S1. (**F**) Diagram depicting the different filters to which the microarray data were subjected to reveal a subset of 15 candidate regulators and the identification of ACR4.

[1]Department of Plant Systems Biology, Flanders Institute for Biotechnology (VIB), B-9052 Ghent, Belgium. [2]Department of Molecular Genetics, Ghent University, B-9052 Ghent, Belgium. [3]Department of Biology and Institute for Genome Sciences and Policy, Center for Systems Biology, Duke University, Box 90338, Durham, NC 27708, USA. [4]Center for Plant Molecular Biology (ZMBP), Auf der Morgenstelle 3, University of Tübingen, D-72076 Tübingen, Germany. [5]Institute of Molecular Plant Science, Rutherford Building, Kings Buildings, University of Edinburgh, Edinburgh, EH9 3JR, UK.

*These authors contributed equally to this work.
†Present address: Academik Metodi Popov Institute of Plant Physiology, Bulgarian Academy of Sciences, Academik Georgi Bonchev Street, Building 21, 1113 Sofia, Bulgaria.
‡Present address: Max Planck Institute for Developmental Biology, Department of Genetics and Genomics, Spemannstrasse 35/III, D-72076 Tübingen, Germany.
§To whom correspondence should be addressed. E-mail: tom.beeckman@psb.ugent.be

nation with a highly synchronized time course (*4*, *5*). We identified 1920 significantly differentially expressed genes (table S1). K-means clustering of the expression patterns leads to the delineation of 10 profiles that show temporal changes in expression levels (fig. S2). The reproducibility of the expression profiles, the resolution of our experimental approach, and the potential involvement in lateral root development were evaluated using quantitative polymerase chain reaction, promoter–*beta-glucuronidase* (GUS) reporters, and mutants, respectively (figs. S3 to S5 and table S2). This combination of synchronized lateral root induction and cell sorting yielded a transcript profile data set reflecting lateral root initiation with high spatial and temporal resolution.

To identify candidate factors involved in regulating the asymmetric cell division pattern, we subjected our data set to several filters (*5*) and identified 15 potential key regulatory genes for the process of asymmetric cell division and cell fate specification during lateral root initiation (Fig. 1F and table S3). One promising candidate, the only gene identified by all of the filter criteria (Fig. 1F and table S3), encodes the membrane-localized receptor-like kinase *ARABIDOPSIS CRINKLY4* (*ACR4*, AT3G59420) (*6*). *ACR4* is transcribed specifically in the small daughter cells after the first asymmetric pericycle cell division. Subsequently, the expression expands to the adjacent small daughter cells from the second asymmetric cell division, resulting in a central core-specific expression pattern (fig. S6, and movie S2).

Because several receptor-like kinases have been demonstrated to regulate patterning, establish cell identities, and specify cell fate (*7*–*10*), we investigated whether the asymmetric expression of ACR4 not only reflects organized pericycle division but also is causal for this process. We determined that *acr4* exhibited a significant increase (19%) in the total number of lateral root meristems (LRMs)/cm, compared with wild-type (Fig. 2A and table S4). Because *ACR4* is a member of the *CRINKLY4* gene family in *Arabidopsis* (*11*), redundancy could be expected. Notwithstanding that the other family members were not identified in the transcript profiling, double- and triple-mutant combinations of *acr4* with mutations in the other four family members (*CRR1*, *CRR2*, *CRR3*, and *CRR4*) exhibited even higher LRM densities (Fig. 2A and table S4). In wild type, LRMs exhibit a left-right alternation with regular spacing of lateral roots (*12*) and are never

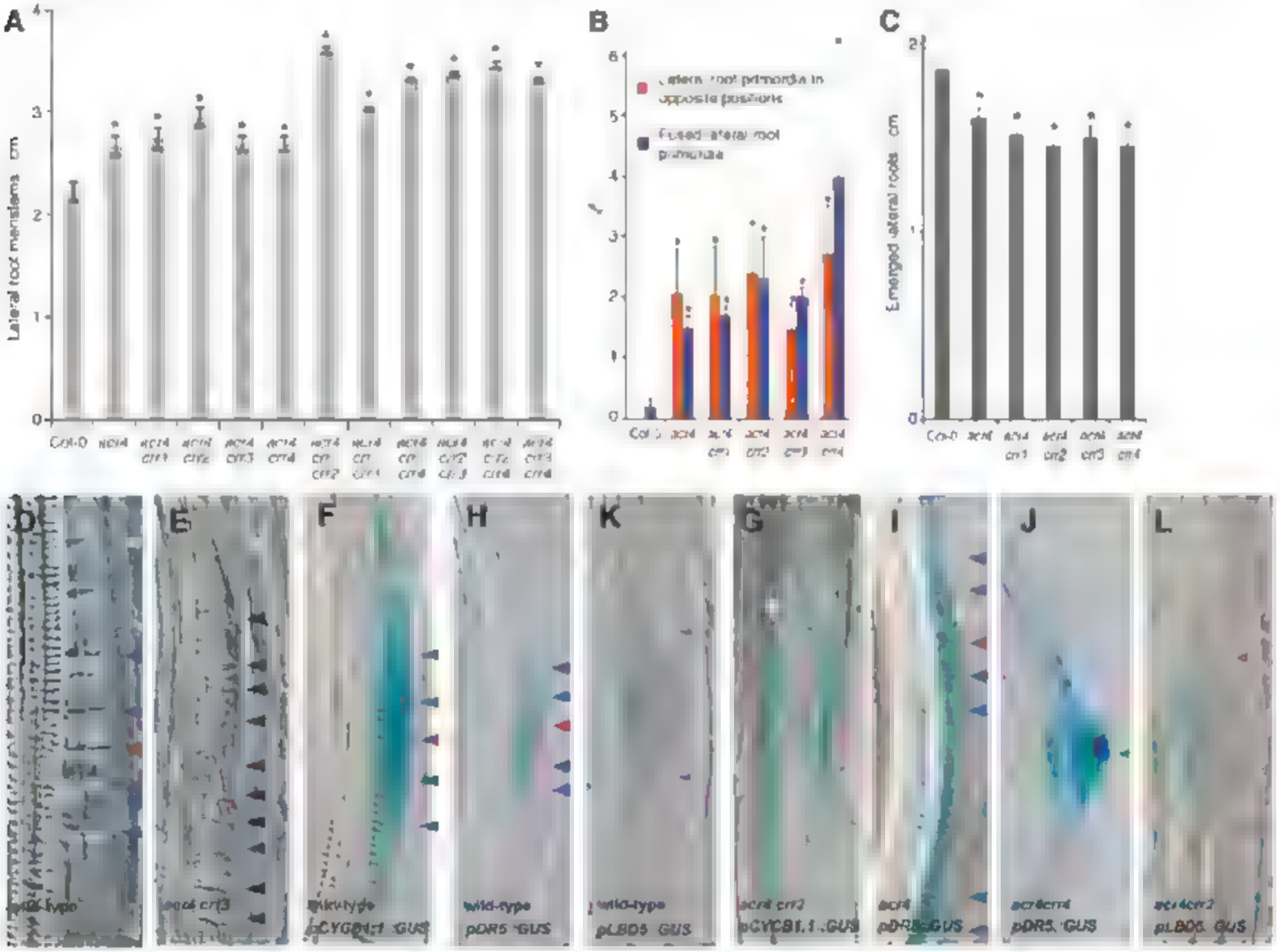

Fig. 2. ACR4 represses pericycle cell divisions in flanking and adjacent cells during lateral root initiation. (**A** to **C**) Lateral root phenotypes of single, double, and triple mutants for five related receptor-like kinases, including ACR4. (A) Lateral root meristem (LRM) densities (including all primordial stages; mean ± SEM). (B) Percentage of aberrant lateral root positioning (mean ± SEM). (C) Lateral root densities, only including emerged lateral roots (mean ± SEM). *, statistically significant differences for values compared with wild type as determined by Student's *t*-test ($P < 0.05$). (**D** to **L**) Division pattern and marker analysis in pericycle cells during lateral root initiation in wild type [(D), (F), (H), and (K)] and representative examples of single or double mutants for five related receptor-like kinases, including ACR4 [(E), (G), (I), (J), and (L)]. Pericycle shows increased cell divisions (black arrowheads); thus, the primordium boundary and central core are not clearly defined in *acr4crr3* (E) compared with wild-type primordium (D). Markers *pCYCB1;1::GUS* [(F) and (G)], *pDR5::GUS* [(H) to (J)], and *pLBD5::GUS* [(K) and (L)] show altered expression patterns in mutants [(G), (I), (J), and (L)] compared with wild type [(F), (H), and (K)]. White, green, and pink arrowheads indicate pericycle cell file [(F) and (G)], opposing primordia (J) and lateral root organ boundaries [(K) and (L)], respectively; broken red line separates two layers of pericycle (E).

initiated opposite each other (Fig. 2, B and D, and table S5). In the mutants of the ACR4 gene family, LRMs were initiated close to one another (fig. S7) and often in the normally excluded opposite positions (Fig. 2, B and J, table S5, and fig. S7). The mutants also had stretches of a two-layered pericycle or fused primordia, both abnormal features (Fig. 2, B and E, and table S5). During lateral root initiation and primordium development, mutant pericycle cells frequently exhibited unusual mitotic activity and auxin response, as visualized by *pCYCB1 1 GUS* (*13*) and *pDR5 GUS* (*14*), respectively (Fig. 2, F to J). At a later stage, boundaries of the wild-type lateral root primordium showed expression of *pLBD5::GUS* (Fig. 2K), but mutant lateral root primordia lacked such clear identification of their borders (Fig. 2L). However, most of the primordia at aberrant positions arrest during development (fig. S7) and do not contribute to the overall root architecture. Hence, when only emerged lateral roots are taken into account, instead of the total number of LRMs, *acr4* has a significantly lower density than wild type (Fig. 2C and table S4). To get better insight in the role of ACR4 during lateral root initiation, we overexpressed ACR4 tissue-specifically in the xylem pole pericycle and could show that this line had a higher density of emerged lateral roots (fig. S8). These observations suggest that ACR4 is required to coordinate pericycle cell divisions during lateral root initiation, where it functions mainly to prevent surrounding cells from dividing but also seems to be involved in the initiation event itself.

In mutants *gnom*^{R5} (*15*) and *slr-1* (*16*), which lack asymmetric pericycle cell divisions and lateral roots, *ACR4* expression was also absent from the pericycle but was normal in the mutant root tips (Fig. 3, A to C). In *slr-1xCYCD3;1*^{OE}, zones of short pericycle cells can be observed (Fig. 3D, inset), but still no lateral roots are formed (*16*). No *ACR4* expression could be detected in the zones of short pericycle cells, whereas root tip expression remained again unchanged (Fig. 3D). In *gnom*^{R5}, auxin induced unstructured proliferation of the pericycle (Fig. 3E, inset) but no organized lateral roots (*15*). *ACR4* was not expressed in the resulting multilayered pericycle of *gnom*^{R5} (Fig. 3E). As in auxin-treated *gnom*^{R5}, wild-type roots, exposed to the vesicle trafficking inhibitor brefeldin A (BFA) and to auxin, showed homogeneous proliferation of the pericycle (*15*) (Fig. 3F) and no *ACR4* expression (Fig. 3G). Thus, ACR4 is correlated with formative divisions and organogenesis, and functions in lateral root formation by suppressing proliferative cell divisions in nearby pericycle cells.

ACR4 is also expressed in the root apical meristem in columella and epidermis/lateral root cap initials and their respective derivatives (*6*) (fig. S9). Therefore, we investigated whether ACR4 has a similar role in mediating formative divisions in the root apex. Differentiation of columella cells can be monitored by lugol staining of the starch grains that are present in columella cells but not in columella initials (*17*). In contrast to wild-type roots, which generally exhibited orga-

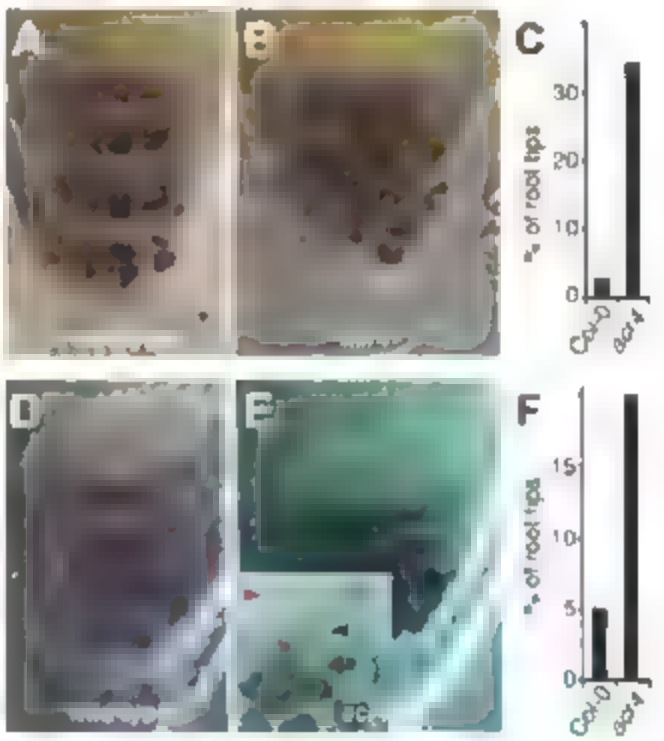

Fig. 4. ACR4 represses irregular divisions in columella stem cell daughter cells in the root apex. (A to F) Root apex at 2 days after germination shows regular columella cell tiers in wild type with one (A) or two layers of undifferentiated cells after a recent division of the columella initial (D) and disorganized columella in *acr4* (B) with up to three undifferentiated cells in one tier (E). Inset in (E) shows an extra cell in the uppermost layer of differentiated columella in *acr4* (black arrowhead). Violet, starch grains; red asterisks, undifferentiated and dividing cells; red arrowhead, quiescent center. [(C) and (F)] Percentage of root tips with disorganized columella (C) and additional columella cell divisions measured by the appearance of additional non-starch staining initials (F).

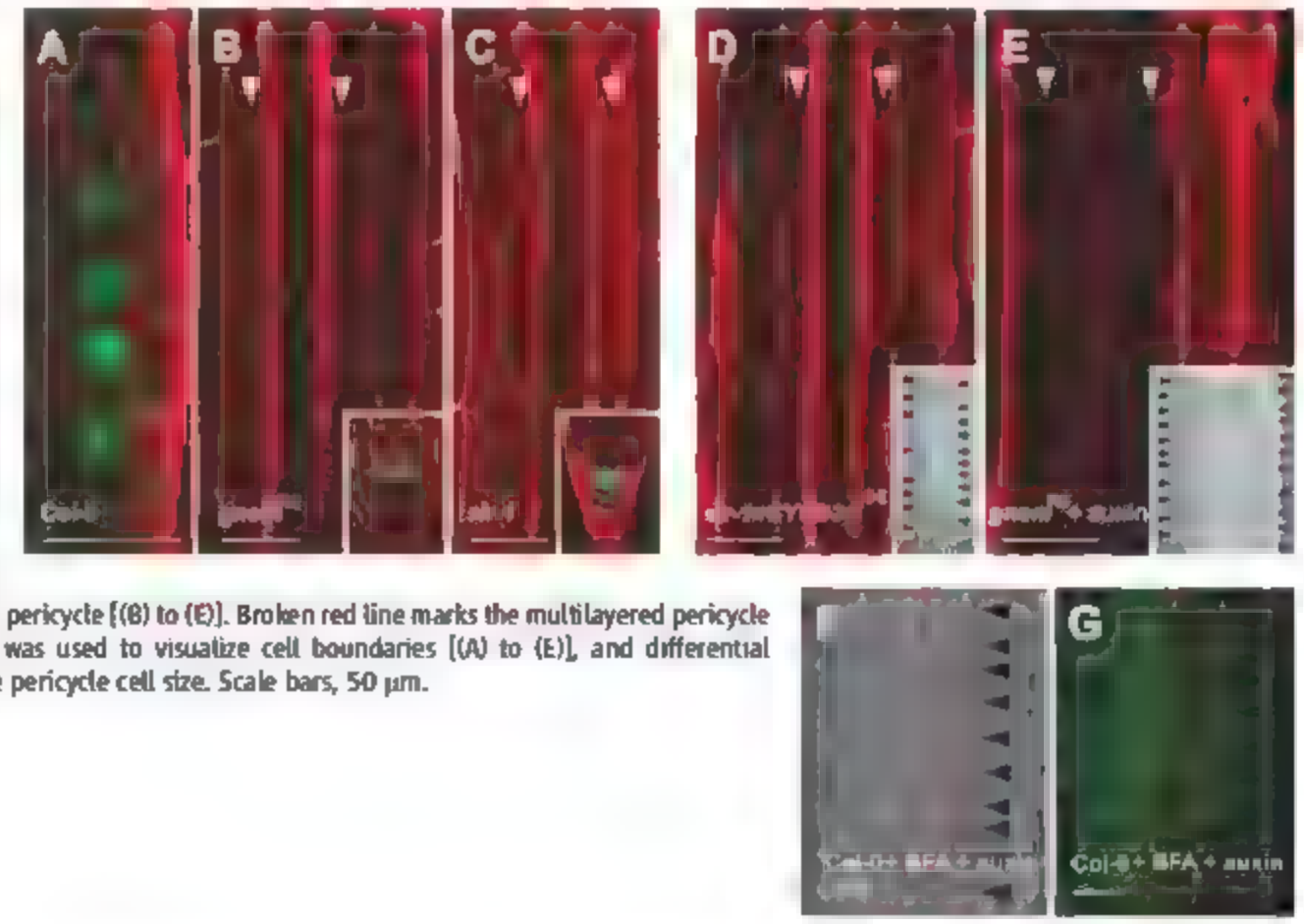

Fig. 3. *ACR4* expression correlates with formative divisions and organogenesis. (A) *pACR4::H2B:YFP* expression (green) in wild-type roots in the central core of the lateral root initiation site. (B to G) *pACR4::H2B:YFP* expression in seedling roots without [(B) to (D)] and with [(E) to (G)] auxin treatment in *gnom*^{R5} [(B) and (E)], *slr-1* (C), *slr-1xCYCD3;1*^{OE} at zone of short pericycle cells (D), and Col-0 treated with BFA [(F) and (G)]. The inset shows the unaltered expression in the main root tip [(B) and (C)], the zone of short pericycle cells (D), or the multilayered pericycle (E) (the last two are recalcitrant to propidium iodide staining). Black arrowheads, uncoordinated cell divisions [(D) to (G)]; white arrowheads, pericycle [(B) to (E)]. Broken red line marks the multilayered pericycle [(F) and (G)]. Propidium iodide (red) was used to visualize cell boundaries [(A) to (E)], and differential interference contrast optics to visualize pericycle cell size. Scale bars, 50 μm.

nized tiers of columella root cap cells (Fig. 4A), the root cap of the *acr4* mutant is frequently distorted (Fig. 4, B and C, and table S6). Wild-type roots display usually one, occasionally two, layer(s) of unstained cells below the quiescent center, resulting from a recent synchronous division of all columella initial cells (Fig. 4, A and D). The *acr4* root tips, however, often displayed additional divisions in cells of the columella cell lineage (Fig. 4, E and F, and table S6), ultimately giving rise to a distorted root cap. In view of the redundancy between members of the ACR4 family, these aberrant divisions occur more often in the triple-mutant combinations (table S6). Therefore, ACR4 function is also required to restrict division activity in daughter cells of columella stem cells in the root apex.

Plants and animals require asymmetric cell divisions, coinciding with the acquisition of the correct cell fate, for growth and reproduction (*18*, *19*). For instance, the asymmetric cell division mechanism is central to the activity of stem cells (*20*), and recent studies have shown a correlation with cancer-like states of the cell when asymmetric cell divisions do not take place (*21*). We have shown that the receptor-like kinase *ACR4* represses supernumerary formative divisions of root cells, both in pericycle cells during lateral root initiation and in the columella in the root apex (fig. S10). Our data suggest that ACR4 signaling is a critical homeostatic mechanism in mediating formative divisions in pluripotent root tissue during organogenesis and might act both cell autonomously and non–cell autonomously. Cell autonomously, ACR4 might be required for correct specification of lateral root primordia cells, as can be deduced from enhanced lateral root formation in the gain-of-function plants and from its strict transcriptional correlation with formative divisions in the pericycle. This is in agreement with ACR4-dependent cell specification that has been proposed for the L1 layer (*6*). Non–cell autonomously, ACR4-signaling might prevent neighboring pericycle cells from becoming triggered for lateral root initiation. Interestingly, a similar dual role for the maize homolog CRINKLY4 was proposed in the L1 layer based on the results of a genetic mosaic analysis (*22*). ACR4 function reveals the common mechanisms for both root apical meristem and developing lateral root primordia and is likely to be mechanistically related to its role in the L1 layer.

In the future, the ACR4 pathway regulating root apical and lateral meristem function may be worth comparing to the CLAVATA receptor-like kinase pathway that functions in the shoot apical meristem to maintain the size of the stem cell pool.

References and Notes

1. J. R. Dinneny, P. N. Benfey, *Cell* **132**, 553 (2008).
2. H. Fukaki, Y. Okushima, M. Tasaka, *Int. Rev. Cytol.* **256**, 111 (2007).
3. K. Himanen *et al.*, *Plant Cell* **14**, 2339 (2002).
4. K. Birnbaum *et al.*, *Science* **302**, 1956 (2003).
5. Materials and methods are available as supporting material on *Science* Online.
6. M. L. Gifford, S. Dean, G. C. Ingram, *Development* **130**, 4249 (2003).
7. S. H. Kwak, J. Schiefelbein, *Dev. Biol.* **302**, 118 (2007).
8. S. H. Kwak, R. Shen, J. Schiefelbein, *Science* **307**, 1111 (2005).
9. E. D. Shpak, J. M. McAbee, L. J. Pillitteri, K. U. Torii, *Science* **309**, 290 (2005).
10. H. Tanaka *et al.*, *Development* **134**, 1643 (2007).
11. X. Cao, K. Li, S. G. Suh, T. Guo, P. W. Becraft, *Planta* **220**, 645 (2005).
12. I. De Smet *et al.*, *Development* **134**, 681 (2007).
13. S. Vanneste *et al.*, *Plant Cell* **17**, 3035 (2005).
14. E. Benkova *et al.*, *Cell* **115**, 591 (2003).
15. M. Geldner *et al.*, *Development* **131**, 389 (2004).
16. H. Fukaki, S. Tameda, H. Masuda, M. Tasaka, *Plant J.* **29**, 153 (2002).
17. C. van den Berg, V. Willemsen, G. Hendriks, P. Weisbeek, B. Scheres, *Nature* **390**, 287 (1997).
18. R. Heidstra, *Prog. Mol. Subcell. Biol.* **45**, 1 (2007).
19. E. Caussinus, F. Hirth, *Prog. Mol. Subcell. Biol.* **45**, 205 (2007).
20. L. Wolpert, *J. Cell Sci. Suppl.* **10**, 1 (1988).
21. H. Clevers, *Nat. Genet.* **37**, 1027 (2005).
22. P. W. Becraft, S. H. Kang, S. G. Suh, *Plant Physiol.* **127**, 486 (2001).

23. We thank B. Scheres, K. Theres, P. Springer, H. Fukaki, and Nottingham Arabidopsis Stock Centre for providing seeds. This work was funded by grants from the Interuniversity Poles of Attraction Program–Belgian Science Policy (PS/13); grants from the U.S. National Science Foundation *Arabidopsis* 2010 program to P.N.B., a fellowship for non–European Union researchers from the Belgian Science Policy (BELSPO) to V.V., long-term fellowships from the European Molecular Biology Organization ALTF 108-2006 to I.D.S. and ALTF 142-2007 to S.V., predoctoral fellowships from the Institute for the Promotion of Innovation by Science and Technology in Flanders to I.D.S. and S.V., from the Bijzonder Onderzoeksfonds van de Universiteit Gent to B.D.R., and from the Gatsby Charitable Foundation to N.M., a travel grant of the Research Foundation of Flanders to I.D.S., and a postdoctoral fellowship of the Research Foundation of Flanders to D.V.D. We are grateful to R. Groß-Hardt, U. Voß, S. Lau, and two anonymous referees for critical comments and suggestions on the manuscript.

Supporting Online Material

www.sciencemag.org/cgi/content/full/322/5901/594/DC1
Materials and Methods
Figs. S1 to S13
Tables S1 to S11
Movies S1 and S2
References

7 May 2008; accepted 10 September 2008
10.1126/science.1160158

Functional Targeting of DNA Damage to a Nuclear Pore–Associated SUMO-Dependent Ubiquitin Ligase

Shigeki Nagai,[1,2]* Karine Dubrana,[2]*† Monika Tsai-Pflugfelder,[1] Marta B. Davidson,[3] Tania M. Roberts,[3] Grant W. Brown,[3] Elisa Varela,[1] Florence Hediger,[2] Susan M. Gasser,[1,2]‡ Nevan J. Krogan[4]

Recent findings suggest important roles for nuclear organization in gene expression. In contrast, little is known about how nuclear organization contributes to genome stability. Epistasis analysis (E-MAP) using DNA repair factors in yeast indicated a functional relationship between a nuclear pore subcomplex and Slx5/Slx8, a small ubiquitin-like modifier (SUMO)–dependent ubiquitin ligase, which we show physically interact. Real-time imaging and chromatin immunoprecipitation confirmed stable recruitment of damaged DNA to nuclear pores. Relocation required the Nup84 complex and Mec1/Tel1 kinases. Spontaneous gene conversion can be enhanced in a Slx8- and Nup84-dependent manner by tethering donor sites at the nuclear periphery. This suggests that strand breaks are shunted to nuclear pores for a repair pathway controlled by a conserved SUMO-dependent E3 ligase.

Nuclear pores have been implicated in a range of cellular processes, including macromolecular transport, transcription, and DNA repair. Recent work in several species argues that the binding of genes at nuclear pores contributes to transcriptional regulation (*1*, *2*). At the same time, mutations in components of a pore subcomplex (Nup84, Nup120, Nup133, and Nup60) rendered yeast cells hypersensitive to DNA damaging agents (*3*–*5*). Moreover, the loss of yeast telomere anchoring reduced DNA repair selectively in subtelomeric regions (*3*), and loss of the Nup84 complex was shown to be synthetic lethal with mutations that impair homologous recombination (*5*, *6*). Such strains accumulated spontaneous damage (*5*, *7*), a phenotype partially suppressed by overexpression of a pore-associated desumoylating enzyme, Ulp1 (*7*, *8*). Although Ulp1 is an essential enzyme whose loss also impairs transport through nuclear pores (*9*), it was suggested that nuclear pores and SUMO metabolism might contribute to DNA repair.

To examine this further, we mapped the subnuclear position and dynamics of a tagged DNA double strand break (DSB) in vivo by using the yeast strain JKM179 (*10*). In this strain, a single cut can be induced at the mating type locus (*MAT*) by galactose-controlled expression of the HO endonuclease (*11*). To a strain lacking donor sequences

[1]Friedrich Miescher Institute for Biomedical Research, Maulbeerstrasse 66, 4058 Basel, Switzerland. [2]Department of Molecular Biology and National Center of Competence in Research Frontiers in Genetics, 30 Quai Ernest Ansermet, 1211 Geneva, Switzerland. [3]Department of Biochemistry, Donnelly Centre for Cellular and Biomolecular Research, University of Toronto, 160 College Street, Toronto, Ontario M5S 3E1, Canada. [4]Department of Cellular and Molecular Pharmacology, California Institute for Quantitative Biomedical Research, University of California, San Francisco, 1700 Fourth Street, San Francisco, CA 94158, USA.

*These authors contributed equally to this work.
†Present address: UMR218, Institut Curie/Section de Recherche, 26 Rue d'Ulm, 75231 Paris, and Institut de Radiobiologie Cellulaire et Moléculaire, CEA, 92265 Fontenay aux Roses, France.
‡To whom correspondence should be addressed. E-mail: susan.gasser@fmi.ch

Fig. 1. Relocation of an irreparable DSB to the nuclear periphery. (**A**) Galactose induces a DSB at *MAT* in a haploid strain that lacks homologous donor loci (*11*), bears lacO sites 4.4 kb from *MATα*, and expresses GFP-LacI and Nup49-GFP fusion proteins (GA-1496). (**B**) Position of the GFP-tagged *MAT* locus was scored relative to the NE (single-plane confocal images detecting Nup49 and *MAT* signals). Ratios of distance from NE and diameter in focal plane are binned into equal concentric zones (*12*). (**C**) Results of scoring *MAT* position in GA-1496 or in strains with either an uncleavable HO site (*mata*^{ho}, GA-1965) or *HM* loci (*HML HMR*; GA-2269). Red bar indicates random distribution, and an asterisk indicates significantly nonrandom. Number of cells analyzed and confidence values for a proportional test between random and experimental distribution are (for *MATα* and 2-hours glucose, 356 and $P = 1.6 \times 10^{-1}$; for *mata*^{ho} 2-hours galactose, 258 and $P = 8.9 \times 10^{-1}$; *MATα* 2-hours galactose, 195 and $P = 4.5 \times 10^{-8}$; and *MATα+HM*, 363 and $P = 3.2 \times 10^{-1}$). (**D**) 250 sequential confocal frames at 1.5-s intervals were aligned by the pore signals for G1 phase cells of the strains used in (C) (*12*), and *MAT* position was marked in each frame. Five-min trajectories are green. Bar indicates 1 μm.

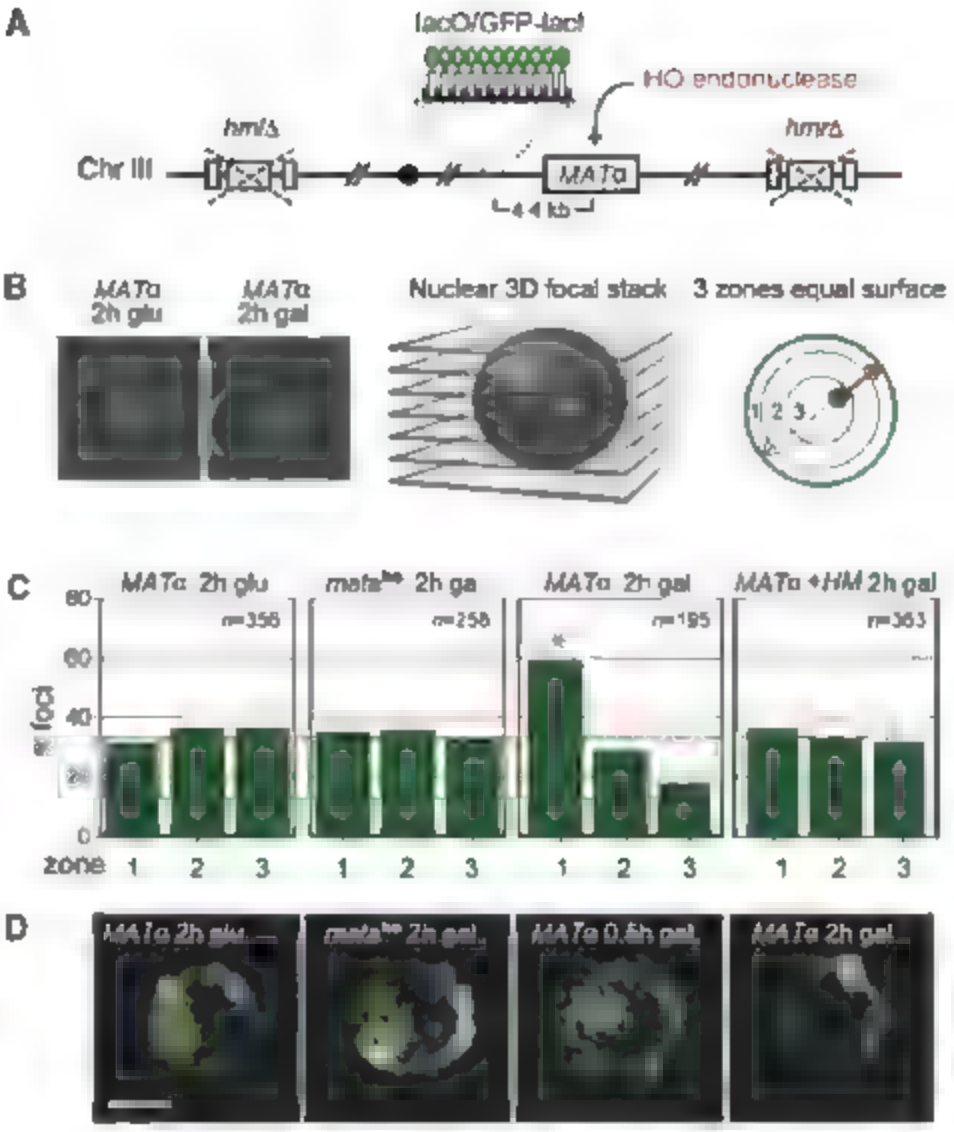

Fig. 2. Collapsed replication forks colocalize with pores. (**A**) Position of LacO-tagged early origin ARS607 (GA-1461) or late origin ARS1412 (GA-2070) was determined as in Fig. 1. (**B**) Exponentially growing GA-1461 cells were incubated ±0.2 M HU 1 or 2 hours. Spot position in S-phase cells was scored as in Fig. 1. Zone 1 enrichment by 2 hours is significant ($P = 8 \times 10^{-5}$). (**C**) Strains as in (A) were synchronized in G1 by α-factor treatment and released into 0.2 M HU ± 0.033% MMS for 1 hour. Zone 1 enrichment of collapsed forks is significant (asterisk indicates $P = 2 \times 10^{-3}$). (**D**) GFP-tagged ARS607 (red) and a CFP-Nup49 fusion (green) were expressed in a *nup133Δ* background expressing nup133Δ 44-236 (*19*). Cells synchronized in G1 phase were released 1 hour in 0.033% MMS plus 0.2 M HU. Deconvolved confocal sections of nuclei were scored for complete GFP-CFP signal overlap.

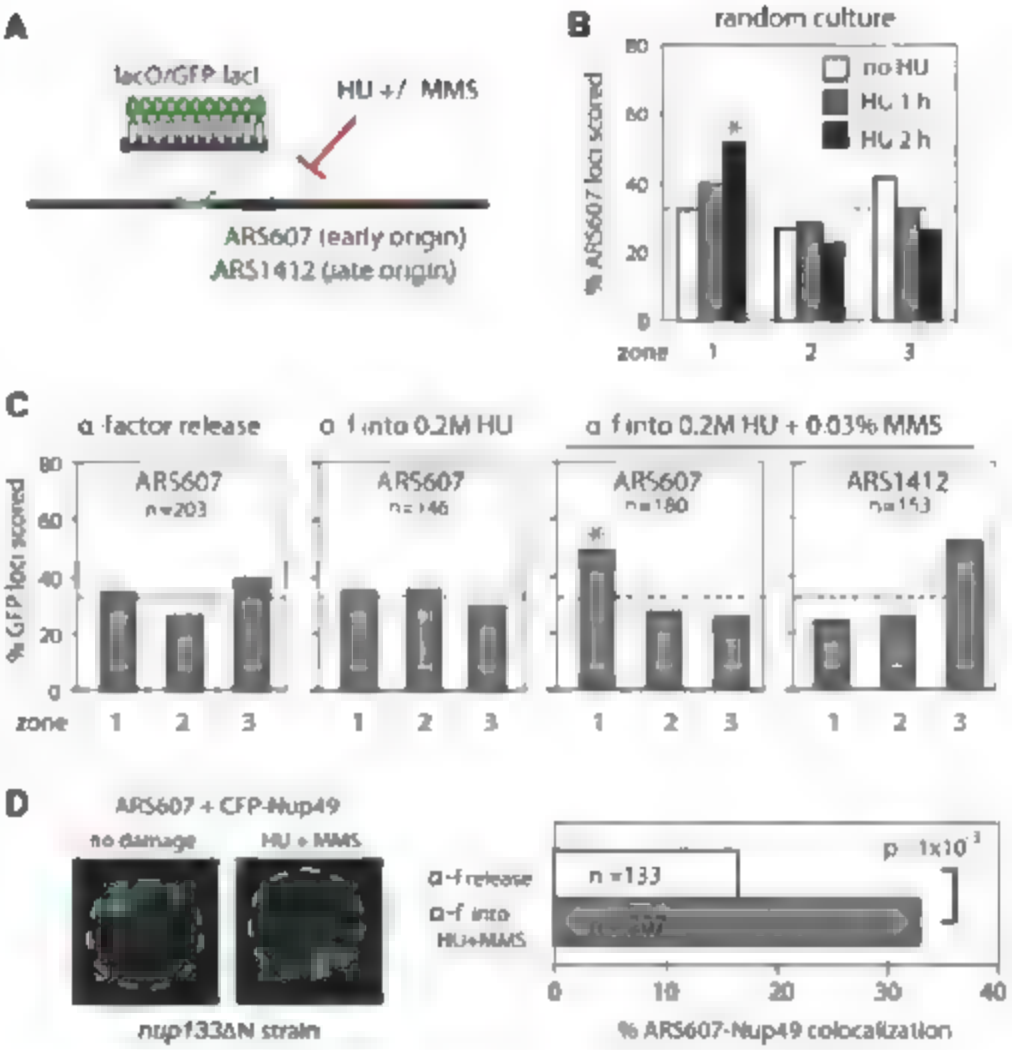

for homologous recombination (HR), we added lacI binding sites (256×lacO) adjacent to *MAT*. Expressing a green fluorescent protein (GFP)–lacI fusion protein enabled tracking of the DSB by live fluorescence microscopy with respect to the nuclear envelope (NE), visualized through a Nup49-GFP fusion (*12*) (Fig. 1A).

To determine the subnuclear localization of a DSB at *MAT*, we acquired 18-step stacks of images of yeast cells growing in agar (Fig. 1B) and scored the position of the GFP-tagged DSB relative to the nearest pore signal. This value was divided by the nuclear diameter in the plane of focus, and ratios were binned into three concentric zones of equal surface, such that a random distribution yields 33% per zone (*12*).

In the absence of HO-induced cleavage (growth in glucose), GFP-*MAT* was randomly distributed throughout the nuclei (Fig. 1C). Yet 2 hours after HO induction, the cleaved *MAT* locus was enriched in the outermost zone (56%; $P = 7.6 \times 10^{-8}$) (Fig. 1C). The *mat*^{ho} locus, bearing an uncleavable HO consensus (Fig. 1C) or unrelated tagged loci (e.g., ARS607; fig. S1) showed no redistribution upon galactose-induced expression of HO.

The relocalization of the HO-induced DSB to the NE was not immediate, occurring between 0.5 and 2 hours after cut induction (fig. S1A), yet it persisted for over 4 hours. The DSB was also readily detected at the NE by immunostaining for ATR kinase, Mec1 (*13*) (fig. S2, A and B). Importantly, when donor sequences for repair of the DSB by HR were present, *MAT* remained randomly distributed despite HO induction (Fig. 1C and fig. S1B).

Live time-lapse imaging of the uncut *MAT* locus shows subdiffusive movement within a radius of about 0.6 μm (*14*). This movement was unchanged after 30 min of HO-endonuclease induction, although by 2 hours the cut site showed highly constrained movement (Fig. 1D). We quantify increased constraint by scoring the frequency of large steps [>0.5 μm/1.5 s (*14*)] and radial movement (fig. S1C). Sequestration at the NE correlated temporally with resection of the DSB and accumulation of Mec1/Ddc2 (*13*) but not with the recruitment of yKu, Rad52, or Mre11 complex (*15*). Importantly, the DSB did not colocalize with telomere clusters at the NE (fig. S2C).

In unperturbed S-phase cells, foci of checkpoint and repair proteins form at spontaneous DNA breaks that arise from dysfunctional replication forks (*16*). Prolonged incubation in hydroxyurea (HU) enhanced the appearance of such foci, as did pretreatment of cells with methylmethane sulfonate (MMS), an alkylating agent that induces nicks (*17*) (fig. S3A). Because DNA polymerases remain fork-associated and able to restart for ~1 hour on HU (*18*), we could ask whether this stalling of polymerases or fork collapse itself provoked the relocation of the lacO-tagged origin ARS607 to the NE (Fig. 2A). In an unsynchronized yeast culture exposed to 0.2 M HU, we could track a shift from random to perinuclear positioning only after prolonged HU treatment [50% zone 1 at 2 hours, $P = 8 \times 10^{-5}$ (Fig. 2B)]. Furthermore, when cells were synchronously released from G1 phase into HU for 1 hour, allowing polymerases to stall, ARS607 remained randomly distributed unless fork breakage

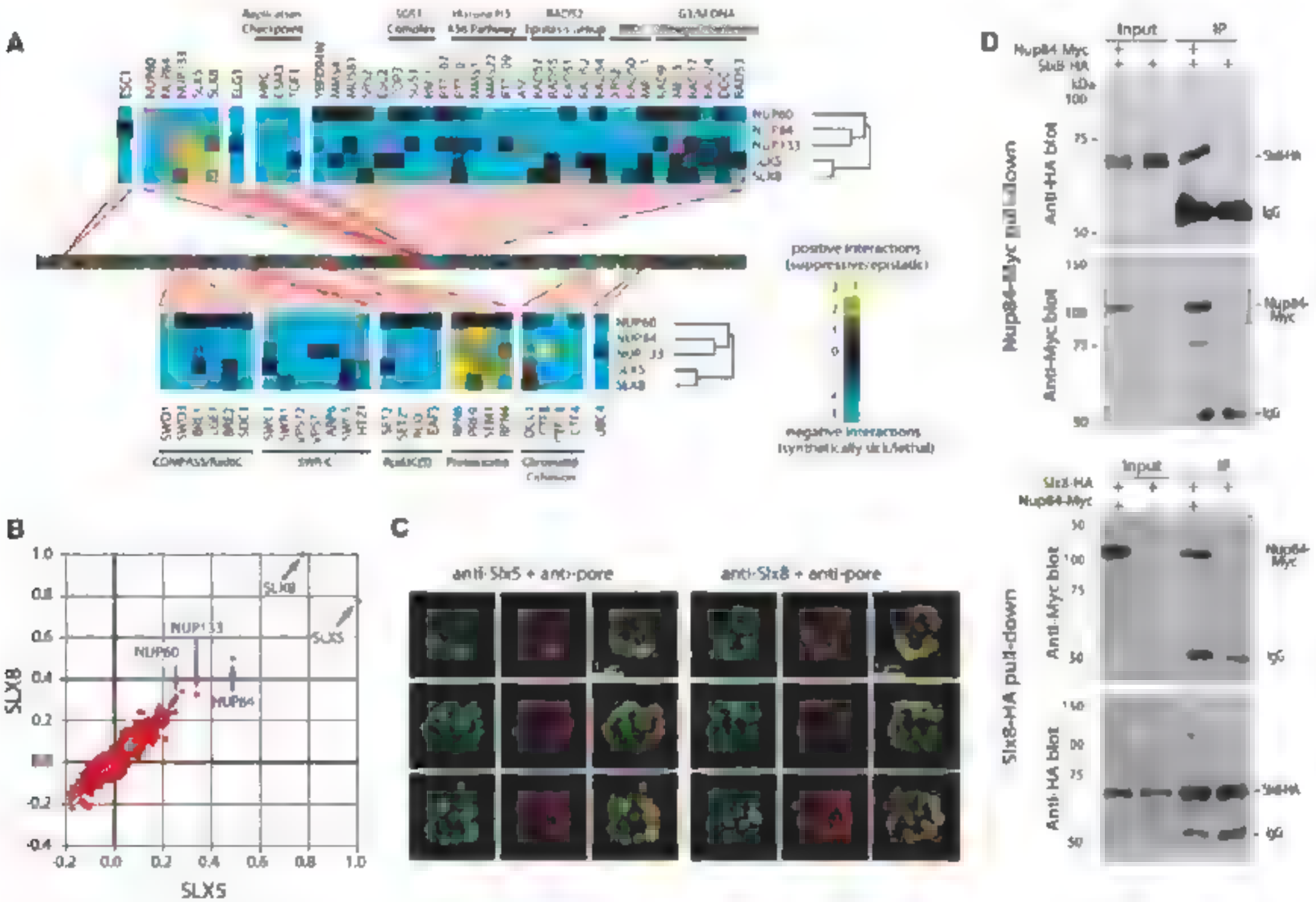

Fig. 3. Nup84 complex and Slx5/Slx8 interact. (**A**) Hierarchical clustering of the nuclear function E-MAP (*21*). Genetic interactions from this map common to *nup60*Δ, *nup84*Δ, *nup133*Δ, *slx5*Δ, and *slx8*Δ are highlighted in blue and yellow. (**B**) Plot of correlation coefficients generated from comparison of the genetic profiles from *slx5*Δ or *slx8*Δ to all other profiles in this E-MAP. (**C**) Rat anti-HA (in green) and mouse anti–nuclear pore (Mab414, in red) colocalized by deconvolved confocal imaging of cells bearing Slx5-HA (GA-3867) or Slx8-HA (GA-3868). (**D**) Coimmunoprecipitation of Slx8 with Nup84 from cells bearing both Slx8-HA and Nup84-Myc (GA-5161) or Slx8-HA alone (GA-3868) (*10*). Westerns of proteins recovered with anti-Myc– or anti-HA–coated magnetic beads were probed with both antibodies. IgG, immunoglobulin G.

was enhanced by treating cells additionally with MMS (Fig. 2C). A late-firing origin (ARS1412) that does not fire under these conditions did not shift (Fig. 2C), nor did origins in cells treated with MMS alone (fig. S1A). We thus conclude that fork-associated breaks, rather than polymerase pausing, triggers relocation to the NE.

To see whether the collapsed forks colocalized with nuclear pores, we introduced an N-terminal deletion of Nup133 [*nup133ΔN* (*19*)] in a strain expressing cyan fluorescent protein (CFP)–Nup49. In this mutant, pores cluster on one side of the nucleus, yet DNA repair and mRNA export are unperturbed (*5*, *19*). In HU and MMS, colocalization of GFP-tagged ARS607 with the clustered CFP-pore signal doubled (Fig. 2D), suggesting that collapsed replication forks may interact with pores.

Further insight into the damage-nuclear pore connection arose from an E-MAP (epistatic-miniarray profile) analysis (*20*), which compiled both negative (e.g., synthetic lethality) and positive (e.g., suppression) interactions between 743 genes involved in nuclear function (*21*). Whereas individual interactions can be difficult to interpret, hierarchical clustering allows the grouping of functionally related genes according to the similarity of their interaction profiles (*20*, *21*). Three nonessential components of the Nup84 nuclear pore complex, *NUP60*, *NUP84*, and *NUP133*, clustered with factors involved in DNA replication and repair, whereas genes for other pore factors, notably Nup82, Nup192, and Nup157, did not.

Intriguingly, deletions of Nup84 complex genes behaved most similarly to deletions of *SLX5* and *SLX8*, genes encoding a heterodimeric complex implicated in DNA repair (Fig. 3, A and B). Slx5 harbors two small ubiquitin-like modifier (SUMO) recognition motifs, and Slx8 bears a RING domain with ubiquitin ligase activity (*22*–*28*). This complex directly binds DNA (*27*), and deletion of either gene leads to an accumulation of sumoylated proteins (*26*). Despite the striking similarity of Slx5 and Slx8 genetic profiles with those of the Nup84 complex, double deletions of *slx5* or *slx8* with *nup84* or *nup60* display negative interactions (Fig. 3A). This suggests that, despite their functional relatedness, their contributions to cell survival do not entirely overlap.

We next tested whether Slx5 and Slx8 colocalize with nuclear pores by double immunostaining for hemagglutinin (HA)–tagged Slx5 or Slx8 and pores. Deconvolution confocal microscopy showed a considerable degree of coincidence of the two signals at the nuclear rim, although anti-Slx5/8 also labels speckles throughout the nucleoplasm (Fig. 3C) (*24*). The overlap of Slx8-HA with nuclear pores was not enhanced by treating cells with zeocin, which induces DSB by chemical insult (fig. S3).

To test whether Slx5 and Slx8 are physically associated with pore complexes, we Myc-tagged Nup84 in strains bearing HA-tagged Slx5 or Slx8 and monitored interaction by reciprocal coimmunoprecipitation. We detected a robust coprecipitation of HA-tagged Slx8 with anti-Myc only in cells bearing the Nup84-Myc fusion (Fig. 3D). Reciprocally, Nup84-Myc was recovered in an anti–Slx8-HA precipitate (Fig. 3D). Neither DNA damage nor formaldehyde fixation altered the efficiency of their interaction (fig. S4), arguing that Nup84 and the Slx5/Slx8 complex interact (*22*, *23*, *27*, *28*).

It remained to be seen whether nuclear pore proteins and/or Slx5/Slx8 associate with an irreparable DSB when it moves to the NE. Chromatin immunoprecipitation (ChIP) on cross-linked then sonicated yeast cells was first performed with a monoclonal antibody (Mab414) that recognizes FG repeat–containing pore components. Indeed, after a 2-hour HO induction, we found significant

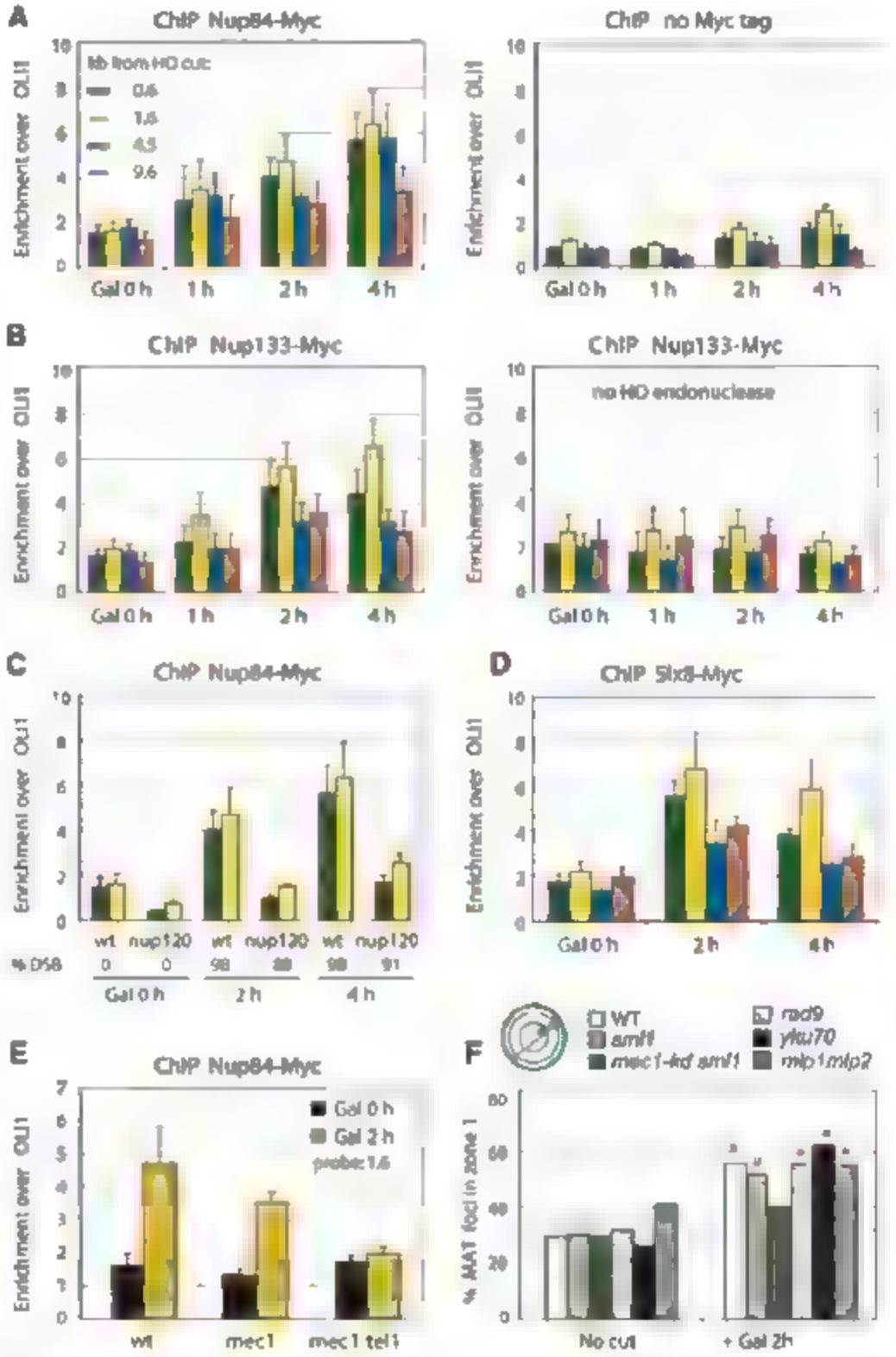

Fig. 4. An irreparable DSB interacts with nuclear pores. (**A** and **B**) ChIP with anti-Myc in JKM179 derivatives with or without Nup84-Myc (GA-4133) or Nup133-Myc, with or without *GAL1*:HO (GA-4135 and GA-4140) at indicated time points on galactose. Primer/probe sets for real-time polymerase chain reaction are 0.6 kb, 1.6 kb, 4.5 kb, and 9.6 kb from the HO cut. For calculation of absolute enrichment over a mitochondrial gene, *OLI1*, see (*10*). (**C**) Anti–Nup84-Myc ChIP in a *nup120Δ* mutant (GA-4861) and a wild-type strain, as in (A). (**D**) Anti-Myc ChIP for Slx8-13Myc in GA-4137, as in (A). (**E**) ChIP for Nup84-Myc was performed in *mec1Δsml1Δ* (GA-4847), *mec1Δtel1Δ sml1Δ*, or wild-type strains. Absolute enrichment of *MAT*+1.6 kb over *OLI1* as in (A). (**F**) The position of cleaved *MAT* was scored as in Fig. 1B in isogenic strains ± 2 hour HO induction. Strains and *n* and *P* values are as follows: WT (GA-1496) no cut: 365, 1.6×10^{-1}; cut: 195, 4.5×10^{-8}; *yku70* (GA-1954) no cut: 118, 6.8×10^{-2}; cut: 117, 2.6×10^{-11}; *mlp1mlp2* (GA-2228) no cut: 174, 3.7×10^{-2}; cut: 184, 5.5×10^{-10}; 148, 5.6×10^{-2}; *mec1-kd1 sml1* (*13*) (GA-2488) no cut: 269, 5.8×10^{-2}; cut: 228, 9.2×10^{-2}; *sml1*(*13*) (GA-2490) no cut: 205, 6.2×10^{-1}, cut: 151, 1.7×10^{-8}; *rad9* (GA-580) no cut: 315, 2.3×10^{-1}; cut: 309, 3.2×10^{-11}.

and selective recovery of *MAT* with pore proteins in a cleavage-dependent manner (fig. S5).

With use of Myc-tagged versions of Nup84 and Nup133, we then monitored the DSB association of the Slx5/Slx8-associated nuclear pore proteins. Both nucleoporins became closely associated with the DSB, peaking 2 to 4 hours after HO induction (Fig. 4, B and C). No enrichment was observed in strains lacking the HO endonuclease or the epitope tag, confirming the association is damage-specific. Pore association of the DSB required an intact Nup84 complex because the DSB-Nup84 interaction was compromised in *NUP120* or *NUP133* deletion strains (Fig. 4C), consistent with these mutants' hypersensitivity to DNA damage (*4*, *5*). We further confirmed that Slx8 binds directly to a DSB by performing ChIP with Slx8-Myc (Fig. 4D). Together with the imaging results, we conclude that DSB association with nuclear pores requires intact Nup84 complex.

The kinetics of the perinuclear shift suggested that end-processing might influence the relocalization of damage. Potential regulators include Mec1/Tel1, the ATR/ATM checkpoint kinases in budding yeast, which are recruited to DSBs to trigger repair and delay cell cycle progression (*13*). Moreover, Mec1-Ddc2 accumulate at resected DSBs with kinetics similar to that of DSB-pore association (*13*). To test whether Mec1 or Tel1 is needed for damage relocalization, we performed Nup84-Myc ChIP in strains lacking Mec1 and/or Tel1, each combined with *sml1Δ* to ensure viability. Whereas the recruitment of Nup84-Myc to *MAT* was only slightly impaired in *mec1sml1* strain, loss of both kinases abolished the association (Fig. 4E).

The effect of Mec1 kinase activity on DSB localization was also monitored by live microscopy of the lacO-tagged HO cut in the *mec1*-kinase dead background (*13*) (Fig. 4F). Relocation of the cleaved *MAT* locus was reduced by *mec1* mutation but was not dependent on the downstream checkpoint response. We detected robust relocation of GFP-tagged *MAT* locus in a *rad9Δ* mutant (Fig. 4F). Importantly, loss of yKu or deletion of genes encoding two pore-associated proteins, Mlp1 and Mlp2, had no effect on DSB relocalization (Fig. 4F). Because Ulp1 protein levels drop dramatically in the *mlp1/2* double mutant (*7*, *8*), it is unlikely that Ulp1 is involved in damage relocalization, although it is possible that Ulp1 regulates downstream repair events. Given that Ulp1 is implicated in the maintenance of genome stability (*7*, *29*) and *slx5/slx8* mutants are synthetically sick with a temperature-sensitive *ulp1* allele (*23*), Slx5/Slx8 may function in parallel to Ulp1.

Further support for a role of Nup84, Slx5, and Slx8 in DNA repair is the significant increase in spontaneous foci of the recombination protein Rad52 or the Mec1 cofactor, Ddc2, in *slx5/8* mutants (Fig. 5A) (*5*, *24*, *25*). We also detect enhanced rates of spontaneous gross chromosomal rearrangement (GCR) (Fig. 5B) (*25*). Lastly, both *nup84* and *nup120* deletion strains fail to efficiently restart replication after prolonged arrest on combinations of HU and MMS (fig. S6). We propose that the Nup84-Slx5/8 complex resolves DNA damage at collapsed forks, leading to the reduced accumulation of damage foci and suppression of inappropriate genomic rearrangements.

Spontaneous gene conversion (GC) events are thought to arise from damage at replication forks. To score these, we exploited a repair system in which heteroallelic mutations in the *lys2* gene are placed on nonhomologous chromosomes. Restoration of a functional *LYS2* gene requires spontaneous GC (*30*), an event allowing for growth without lysine (Fig. 5C). We found that loss of Nup84 or Slx8 leads to a dramatic increase in spontaneous GC events, which is suppressed by plasmid-borne wild-type *NUP84* or *SLX8* (Fig. 5D). This is consistent with increased rates of fork-associated damage in these mutants.

To examine whether artificial recruitment of a locus near nuclear pores enhances GC in a wild-type background, we added four lexA binding sites upstream of the *lys2* allele on ChrII and introduced NE-associated proteins LexA-Yif1 or LexA-Nup84 (Fig. 5C). The binding of such fusion proteins shifts the internal locus to the nuclear periphery (fig. S7).

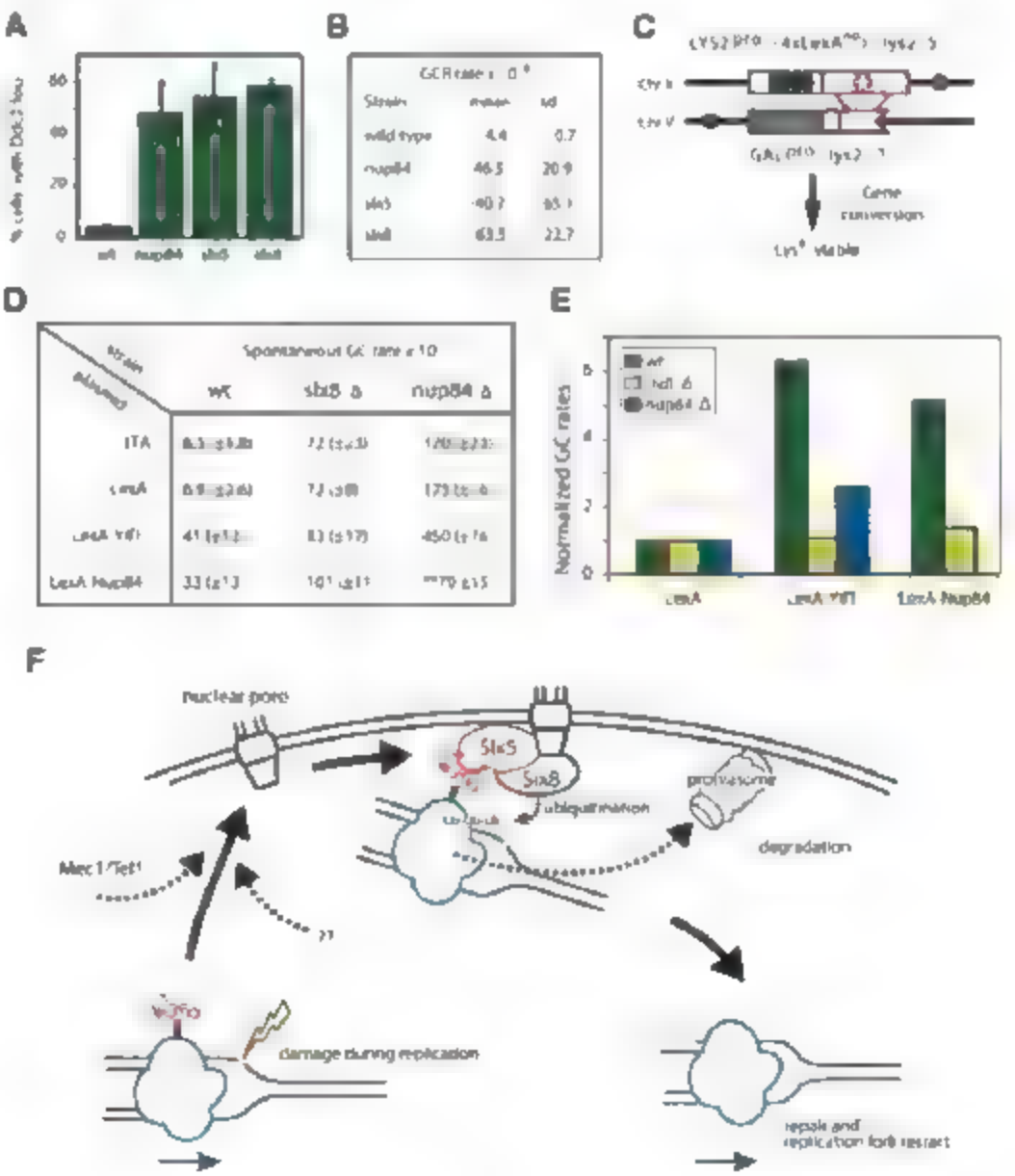

Fig. 5. Slx5/Slx8-Nup84 complex mutants affect recombination and GC rates. (**A**) Percentage cells ($n > 200$) containing Ddc2–yellow fluorescent protein (YFP) foci in strains carrying indicated gene deletions; averaging and standard deviation over three experiments. (**B**) GCR rates (*18*) are enhanced in *nup84Δ* and *slx5Δ* or *slx8Δ* strains; averaging and standard deviations from three fluctuation tests. (**C**) Recombination substrates for GC assays on nonhomologous chromosomes were modified by integrating four LexA sites upstream of the *lys2* frameshift allele (white star;4lexA.*lys2*). ChrV carries 3′ truncated *lys2* allele. GC renders cells Lys+. (**D**) Perinuclear anchoring of 4lexA:*lys2* is achieved by expression of fusions LexA-Yif1 or LexA-Nup84 (fig. S7). Spontaneous GC rates in wild-type or indicated mutants as in (*30*) and (*10*). Double asterisks indicate suppression of *slx8Δ*-enhanced GC rate by LexA-Slx8 expression. (**E**) Rates of GC in (D) were normalized to +LexA values. (**F**) Model of Mec1/Tel1-dependent relocation of damage to Nup84/Slx5/Slx8 complexes that may ubiquitinylate a substrate for proteolysis, enabling fork-associated repair.

The impact of relocalization on GC was then tested by monitoring rates of spontaneous Lys+ colony formation. We found sixfold higher GC rates in the presence of either LexA-Nup84 or LexA-Yif1 compared with LexA (Fig. 5D). This was not associated with loss of viability or altered cell division, although the increase in GC conferred by the perinuclear anchor could reflect either increased damage or increased repair.

To resolve this, we asked whether the enhancement of GC achieved by anchoring required the Nup84-Slx5/Slx8 complex. We monitored GC rates with tethered donor loci in *slx8Δ* or *nup84Δ* and found that the increased GC rate conferred by tethering was lost in the mutants (Fig. 5, D and E). One simple interpretation is that the absence of Slx8 or Nup84 attenuates a repair pathway that requires anchorage at or near nuclear pores.

These data support a functional role for the Nup84 complex as a coordinator of SUMO-dependent repair pathways. There is a remarkable selectivity in the recruitment for irreparable DSBs and collapsed replication forks because we score no shift of stalled replication forks or DSBs reparable by HR. This argues for a specific pathway of repair requiring both the Nup84 complex and the Slx5/Slx8 SUMO-dependent ubiquitin ligase. Given the hypersensitivity of *slx5* and *slx8* mutants to HU (*22*, *25*), we propose that this pathway facilitates collapsed replication fork recovery. Although the translocation of damage to the NE does not require Slx5/Slx8, the enhanced rate of repair conferred by pore association does.

A sumoylated protein may accumulate at collapsed forks or irreparable DSBs, requiring Slx5/Slx8 ubiquitylation and proteasomal degradation to enable appropriate repair. The E-MAP data (Fig. 3A) and the fact that Slx5/Slx8 are physically associated with the proteasome (*31*) support this model (Fig. 5F). Furthermore, the presence of the proteasome at the NE (*32*) provides a rationale for the observed relocalization. Lastly, the proteasome is recruited to DSBs (*33*). Thus, we propose that the Slx5/Slx8 pathway involves targeted degradation of a sumoylated protein bound at collapsed forks or resected breaks (Fig. 5F). The relevant targets of Slx5/Slx8 ubiquitination are unknown, but likely candidates based on E-MAP data include Pol32, Rad27, and Srs2 (Fig. 3) (*21*).

References and Notes

1. R. Schneider, R. Grosschedl, *Genes Dev.* **21**, 3027 (2007).
2. A. Akhtar, S. M. Gasser, *Nat. Rev. Genet.* **8**, 507 (2007).
3. P. Therizols *et al.*, *J. Cell Biol.* **172**, 189 (2006).
4. C. B. Bennett *et al.*, *Nat. Genet.* **29**, 426 (2001).
5. S. Loeillet *et al.*, *DNA Repair* **4**, 459 (2005).
6. X. Pan *et al.*, *Cell* **124**, 1069 (2006).
7. B. Palancade *et al.*, *Mol. Biol. Cell* **18**, 2912 (2007).
8. X. Zhao, C. Y. Wu, G. Blobel, *J. Cell Biol.* **167**, 605 (2004).
9. K. Slade *et al.*, *J. Biol. Chem.* **277**, 49554 (2002).
10. Materials and methods are available as supporting material on Science Online.
11. S. E. Lee *et al.*, *Cell* **94**, 399 (1998).
12. F. Hediger, A. Taddei, F. R. Neumann, S. M. Gasser, *Methods Enzymol.* **375**, 345 (2004).
13. K. Dubrana, H. van Attikum, F. Hediger, S. M. Gasser, *J. Cell Sci.* **120**, 4209 (2007).
14. P. Heun, T. Laroche, K. Shimada, P. Furrer, S. M. Gasser, *Science* **294**, 2181 (2001).
15. X. H. Wang, J. E. Haber, *PLoS Biol.* **2**, E21 (2004).
16. M. Lisby, U. H. Mortensen, R. Rothstein, *Nat. Cell Biol.* **5**, 572 (2003).
17. J. A. Tercero, J. F. Diffley, *Nature* **412**, 553 (2001).
18. J. A. Cobb *et al.*, *Genes Dev.* **19**, 3055 (2005).
19. V. Doye, R. Wepf, E. C. Hurt, *EMBO J.* **13**, 6062 (1994).
20. M. Schuldiner *et al.*, *Cell* **123**, 507 (2005).
21. S. R. Collins *et al.*, *Nature* **446**, 806 (2007).
22. J. R. Mullen, V. Kaliraman, S. S. Ibrahim, S. J. Brill, *Genetics* **157**, 103 (2001).
23. Y. Xie *et al.*, *J. Biol. Chem.* **282**, 34176 (2007).
24. R. C. Burgess, S. Rahman, M. Lisby, R. Rothstein, X. Zhao, *Mol. Cell. Biol.* **27**, 6153 (2007).
25. C. Zhang, T. M. Roberts, J. Yang, R. Desai, G. W. Brown, *DNA Repair* **5**, 336 (2006).
26. Z. Wang, G. M. Jones, G. Prelich, *Genetics* **172**, 1499 (2006).
27. L. Yang, J. R. Mullen, S. J. Brill, *Nucleic Acids Res.* **34**, 5541 (2006).
28. J. Prudden *et al.*, *EMBO J.* **26**, 4089 (2007).
29. C. Soustelle *et al.*, *Mol. Cell. Biol.* **24**, 5130 (2004).
30. J. A. Freedman, S. Jinks-Robertson, *Genetics* **162**, 15 (2002).
31. S. R. Collins *et al.*, *Mol. Cell. Proteomics* **6**, 439 (2007).
32. C. Enenkel, A. Lehmann, P. M. Kloetzel, *Mol. Biol. Rep.* **26**, 131 (1999).
33. N. Krogan *et al.*, *Mol. Cell* **16**, 1027 (2004).

34. We thank J. E. Haber, M. Lisby, S. Jinks-Robertson, R. Kolodner, and R. Rothstein for generously providing strains; M. Shales for artwork; K. Saeturn and V. Kalck for technical help; and C. J. Ingles, J. E. Haber, and our laboratories for discussions. We acknowledge the Novartis Research Foundation, Swiss Cancer League, Swiss National Science Foundation, Sandler Family Foundation, NIH, National Cancer Institute of Canada, and Canadian Cancer Society for support.

Supporting Online Material

www.sciencemag.org/cgi/content/full/322/5901/597/DC1
Materials and Methods
Figs. S1 to S7
Table S1
References

7 July 2008; accepted 16 September 2008
10.1126/science.1162790

Splicing Factors Facilitate RNAi-Directed Silencing in Fission Yeast

Elizabeth H. Bayne,[1] Manuela Portoso,[1]* Alexander Kagansky,[1] Isabelle C. Kos-Braun,[1] Takeshi Urano,[2] Karl Ekwall,[3] Flavia Alves,[1] Juri Rappsilber,[1] Robin C. Allshire[1]†

Heterochromatin formation at fission yeast centromeres is directed by RNA interference (RNAi). Noncoding transcripts derived from centromeric repeats are processed into small interfering RNAs (siRNAs) that direct the RNA-induced transcriptional silencing (RITS) effector complex to engage centromere transcripts, resulting in recruitment of the histone H3 lysine 9 methyltransferase Clr4, and hence silencing. We have found that defects in specific splicing factors, but not splicing itself, affect the generation of centromeric siRNAs and consequently centromeric heterochromatin integrity. Moreover, splicing factors physically associate with Cid12, a component of the RNAi machinery, and with centromeric chromatin, consistent with a direct role in RNAi. We propose that spliceosomal complexes provide a platform for siRNA generation and hence facilitate effective centromere repeat silencing.

RNA interference (RNAi) and related pathways regulate gene expression at both transcriptional and posttranscriptional levels. In fission yeast (*Schizosaccharomyces pombe*), RNAi directs the formation of heterochromatin (*1*, *2*). Analogous to metazoan centromeres, fission yeast centromeres comprise a kinetochore domain flanked by outer repeat (*otr*) sequences that are assembled in heterochromatin. These *otr* regions are transcribed by RNA polymerase II (Pol II) and give rise to double-stranded RNA that is processed into small interfering RNAs (siRNAs) by Dicer (Dcr1). These siRNAs are loaded into Argonaute (Ago1), a component of the RNA-induced transcriptional silencing (RITS) effector complex (*3*). siRNAs target RITS to cognate nascent transcripts, resulting in recruitment of further factors including the RDRC complex (comprising Rdp1, Cid12, and Hrr1) (*4*), and ultimately Clr4, which methylates histone H3 on Lys[9] (H3K9me2). H3K9me2 is bound by the HP1-related protein Swi6, which in turn recruits cohesin, critical for centromere function (*5*).

To further dissect the mechanism of RNAi-directed chromatin modification, we previously performed a screen that identified mutations at 12 loci termed *csp* (centromere suppressor of position effect), which at 25°C alleviate silencing of marker genes inserted in the *otr* of centromere 1 (*6*). Several of the *csp* mutants are alleles of known RNAi components (*7*, *8*). The *csp4* and *csp5* mutants are temperature-sensitive (*ts*) lethal alleles. Complementation and sequencing revealed that *csp4* and *csp5* are alleles of *cwf10* and *prp39*, respectively, both of which encode splicing factors. *csp4*, now denoted *cwf10-1*, creates a missense mutation (C323Y) in the guanosine triphosphate–binding domain of Cwf10.

[1]Wellcome Trust Centre for Cell Biology and Institute of Cell Biology, School of Biological Sciences, University of Edinburgh, 6.34 Swann Building, Edinburgh EH9 3JR, UK. [2]Department of Biochemistry, Shimane University Faculty of Medicine, 89-1 Enya-cho, Izumo 693-8501, Japan. [3]Karolinska Institute, Department of Biosciences and Medical Nutrition, University College Södertörn, Novum 141, 57 Huddinge, Sweden.

*Present address: Institute of Human Genetics, 141 rue de la Cardonille, 34396 Montpellier, France.
†To whom correspondence should be addressed. E-mail: robin.allshire@ed.ac.uk

Cwf10 is the homolog of the *Saccharomyces cerevisiae* U5 small nuclear ribonucleoprotein Snu114 (and of human EFTUD2) that is required for U4/U6 small nuclear RNA (snRNA) unwinding (*9*). *csp5*, now denoted *prp39-1*, makes a nonsense mutation in Prp39 (W550stop). *S. cerevisiae* Prp39 (homologous to human PRPF39) is associated with U1 snRNA and is required for commitment to splicing of pre-mRNA (*10*). Thus, mutations in two distinct essential splicing factors affect silencing at centromeres.

To further investigate possible links between splicing and centromere silencing, we surveyed several additional *ts* lethal splicing mutants for silencing defects at the permissive temperature (*11*–*14*). Only particular splicing mutants affected silencing. Silencing of a centromeric *cen1:ade6*$^+$ marker gene (Fig. 1A) remained intact in the presence of *prp1* (Prp6$^{Sc/Hs}$), *prp2* (U2AF^{Hs}), *prp3* (Prp3^{Sc}/PRPF3^{Hs}), or *prp4* (PRPF4B^{Hs}) mutations (where the superscripts Sc and Hs denotes *S. cerevisiae* and human, respectively). In contrast, mutations in *prp5* (Prp46^{Sc}/PLRG1^{Hs}), *prp8* (Prp2^{Sc}/DHX16^{Hs}), *prp10* (Hsh155^{Sc}/SF3B1^{Hs}), and *prp12* (Rse1^{Sc}/SF3B2^{Hs}), like *cwf10* and *prp39*, alleviated *cen1:ade6*$^+$ silencing (Fig. 1B) and increased *cen1:ade6*$^+$ transcript accumulation (Fig. 1C, *ade6*). Moreover, mutants that alleviated *cen1:ade6*$^+$ silencing also displayed increased levels of noncoding centromeric *otr* transcripts and concomitant reductions in centromeric siRNA accumulation, with *prp10-1* showing the most severe silencing defects (Fig. 1C, *cen-dh* and *cen-dg*, and Fig. 1D). Thus, several specific splicing mutants affect processing of centromeric transcripts into siRNAs and impair centromere silencing.

A mundane explanation for these observations is that impaired splicing of mRNA encoding an RNAi component indirectly affects silencing. However, the silencing and splicing defects observed in these *ts* splicing mutants can be uncoupled. Reverse transcription polymerase chain reaction (RT-PCR) analysis of an mRNA (*tbp1*) that is highly sensitive to splicing defects (*15*) confirmed that these mutants accumulated increased levels of unspliced pre-mRNA at restrictive temperature (36°C). However, at the permissive temperature of 25°C (at which centromeric silencing was alleviated), splicing efficiency was similar to that in wild-type cells (Fig. 2A). Conversely, for mutants that did not alleviate silencing at 25°C, growth at semipermissive temperature impaired splicing of *tbp1* but did not induce increased accumulation of *cen1:ade6*$^+$ or *otr* (*cen-dh*) transcripts, as seen in *prp10-1* (Fig. 2B). Even after prolonged incubation at 36°C, which strongly inhibits splicing (Fig. 2A), centromeric siRNAs were still readily detected in *prp1-1*, *prp2-1*, *prp3-3*, and *prp4-73* (fig. S1). Thus, defective splicing does not inherently perturb the RNAi pathway.

The RNAi genes *ago1*$^+$ and *hrr1*$^+$ contain introns; if their splicing is particularly sensitive to defects, this could explain the observed phenotypes. We therefore constructed strains in which the endogenous *ago1*$^+$ and *hrr1*$^+$ genes were replaced by cDNAs. Even in these strains, the *prp10-1* mutation alleviated silencing as in wild-type cells (Fig. 2C, white colonies). Thus, the silencing defects in *prp10-1* do not result from inefficient splicing of these RNAi components. However, defective splicing of a gene encoding some other, unknown contributory factor cannot be excluded.

Because splicing is generally coupled to transcription (*16*), defective splicing might affect centromeric siRNA production by impairing *otr* transcription. However, in contrast to the *rpb7-G150D* mutation affecting RNA Pol II (*7*), splicing mutants did not affect the abundance or length of centromeric transcripts accumulating in a *dcr1*Δ background (fig. S2). Thus, in these splicing mutants the defect in RNAi-directed silencing lies downstream of *otr* transcription.

Strains lacking RNAi exhibit reduced H3K9 methylation and Swi6 association at centromeric *otr* chromatin (*17*). Chromatin immunoprecipitation (ChIP) revealed that splicing mutants *cwf10-1* and *prp10-1* (but not *prp2-1*) exhibited only a modest decrease in levels of H3K9me2 associated with both centromere repeats and *cen1:ura4*$^+$ (Fig. 3A and fig. S3). Reductions in H3K9me2 in *cwf10-1* and *prp10-1* were greater on *cen1:ura4*$^+$ than on *otr* repeats, and greater still on *cen1:ade6*$^+$ (fig. S4); however, these mutants consistently retained more H3K9me2 than did *dcr1*Δ cells. Levels of centromeric Swi6 were also moderately reduced in *cwf10-1* and *prp10-1* cells (Fig. 3B). Thus, *prp10-1* cells maintain relatively high levels of H3K9me2 and Swi6 at centromeres, even though siRNA generation is severely compromised. This

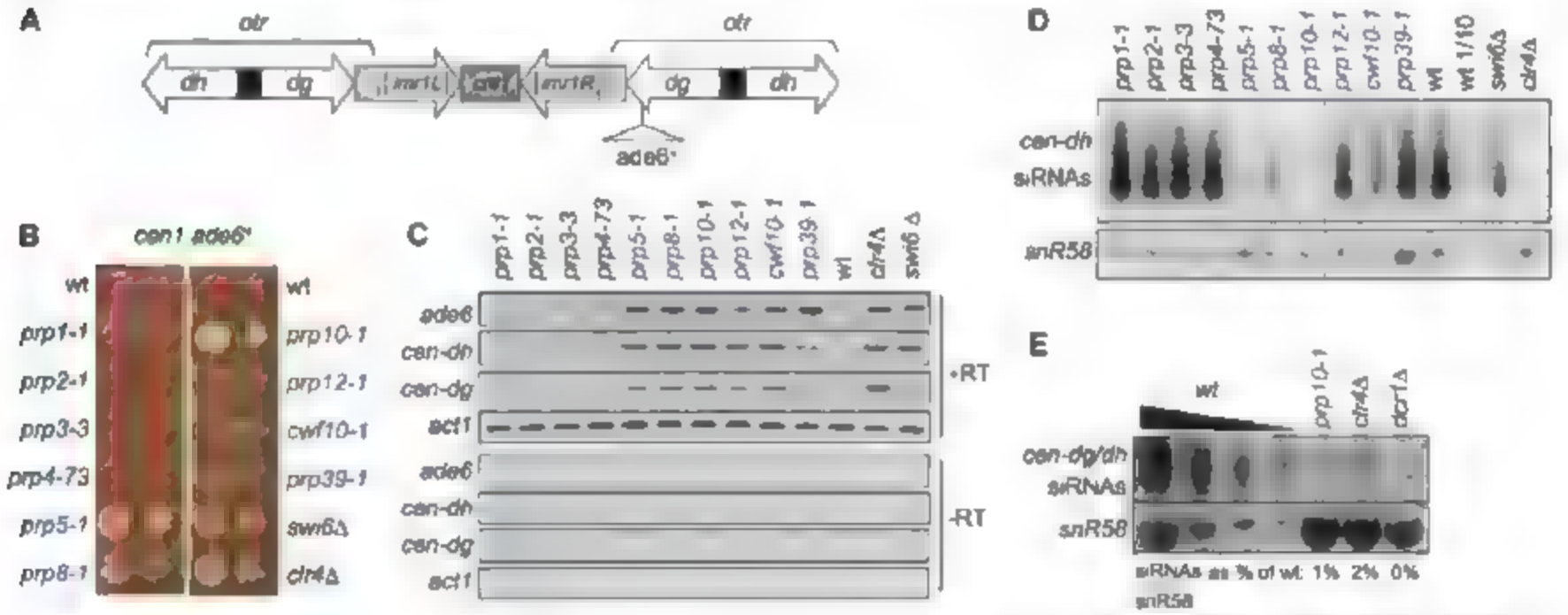

Fig. 1. Specific splicing mutants affect RNAi-directed silencing at centromeres (**A**) Schematic of fission yeast centromere 1, indicating site of integration of *cen1:ade6*$^+$ marker, outer repeat (*otr*) *dg* and *dh* elements, inner repeats (*imr*), and central core (*cnt*). (**B**) Silencing assay on strains bearing *cen1:ade6*$^+$ (red, silent; pink/white, alleviated). (**C**) RT-PCR and quantitative RT-PCR (qRT-PCR) analysis of transcripts from *ade6*, *cen-otr* (*dg* and *dh*), and *act1* control (–RT, no reverse transcriptase). Histograms show transcript levels relative to *act1*, normalized to the wild type. (**D** and **E**) Northern analysis of siRNAs corresponding to *cen-dh* or *dg/dh*. snoRNA58 (snR58) is a loading control.

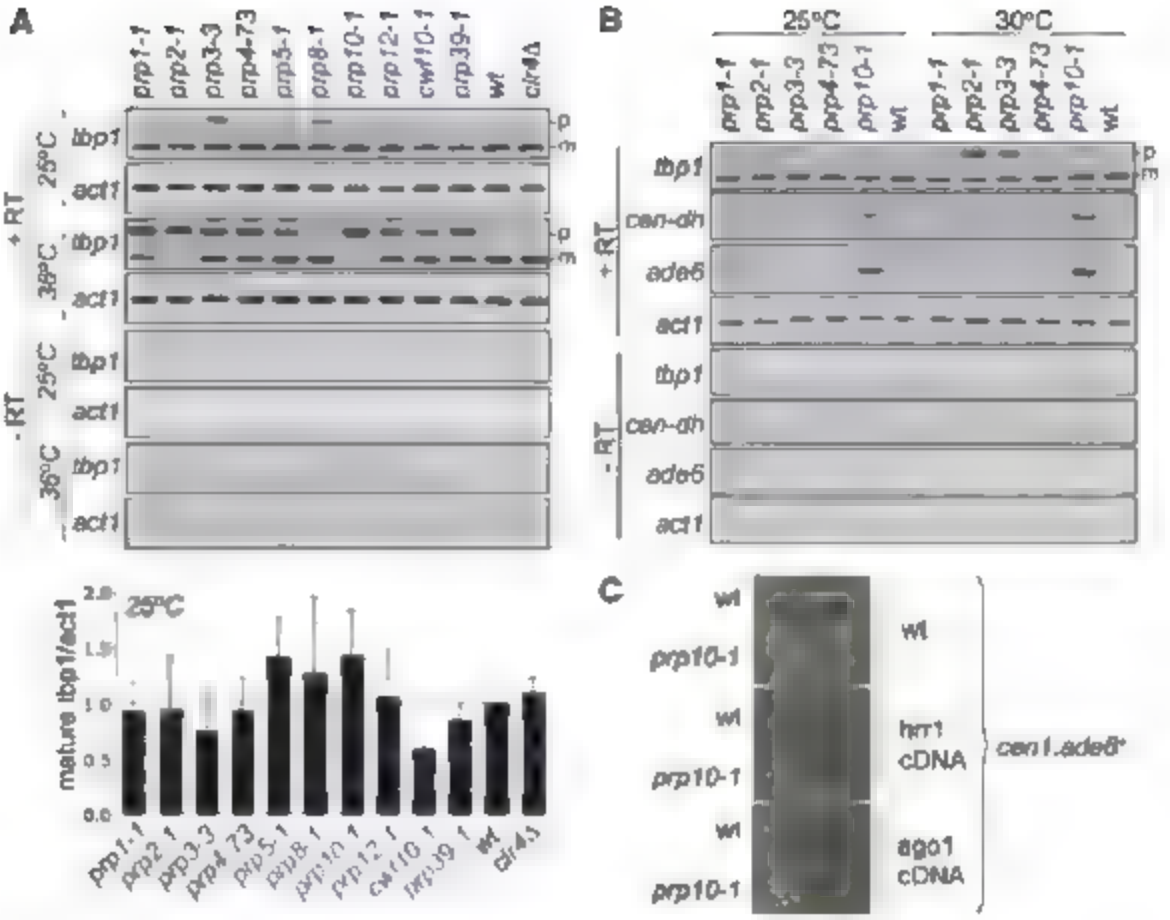

Fig. 2. Defective splicing does not cause defects in centromere silencing. (**A** and **B**) RT-PCR analysis of transcripts from *tbp1*, *ade6*, *cen-dh*, and *act1*. Spliced, mature (m), and unspliced, pre- (p) *tbp1*$^+$ mRNA are indicated. Strains were grown at permissive (25°C) or semipermissive (30°C) temperatures or, for analysis at restrictive temperature, grown at 25°C and then shifted to 36°C for 6 hours. The histogram shows qRT-PCR analysis of *tbp1*$^+$ mature transcript levels relative to *act1*, normalized to the wild type, at 25°C. (**C**) Silencing assay on strains bearing *cen1:ade6*$^+$, with endogenous *ago1*$^+$ or *hrr1*$^+$ replaced by cDNAs.

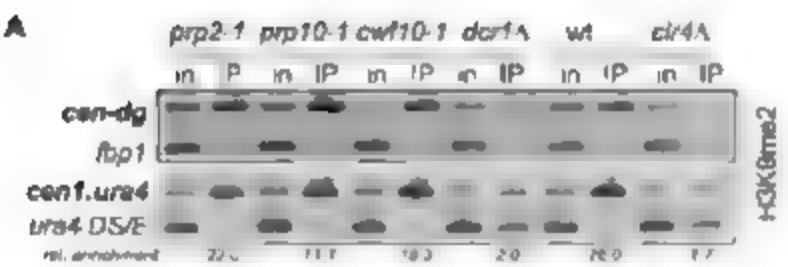

Fig. 3. Splicing mutants disrupt RNAi-dependent heterochromatin. (**A** and **B**) ChIP analysis of H3K9me2 and Swi6 at *cen-dg* or *cen1:ura4*$^+$ relative to a euchromatic control locus (*fbp1* or *ura4 DS/E*, respectively). Representative gels are shown. Relative enrichments were calculated as the ratio of product of interest to control product in immunoprecipitate (IP) relative to input (in). The histogram represents qPCR analysis of four independent experiments; relative enrichments (*cen-dg/fbp1* and *cen1:ura/fbp1*) are shown as a percentage of the wild type. See also fig. S2. (**C**) ChIP analysis of H3K9me2 at *cen-dg* sequences on endogenous centromeres, or on plasmid pH-cc2 [see schematic and (*20*, *27*)]. Plasmid was introduced by transformation and maintained under selection. Primers spanning the *dg*-plasmid backbone junction were used to specifically analyze H3K9me2 on the plasmid.

is similar to cells lacking the polyA polymerase Cid14 (*18*).

siRNAs are absolutely required for establishment, but not maintenance, of H3K9 methylation on centromeric repeats (*19*). To determine whether *cwf10-1* and *prp10-1* affect the establishment of H3K9me2 on naïve repeats, we transformed wild-type or mutant strains with a plasmid bearing part of a *cen1 otr* (*dg*) repeat (*20*). ChIP analysis using plasmid-specific primers confirmed that H3K9me2 was established on the plasmid in wild-type but not in *dcr1*Δ cells. In *prp10-1* cells, H3K9me2 was still established on the plasmid (Fig. 3C, pH-cc2), albeit at a lower level than in wild-type cells, consistent with the lower level of H3K9me2 seen on endogenous centromeric repeats (Fig. 3, A and C, *cen-dg*). This result suggests that *prp10-1* cells must retain a low level of siRNAs, and indeed we detected siRNAs at about 1% of wild-type levels in *prp10-1* cells (Fig. 1F). Thus, very low levels of siRNAs are sufficient to establish H3K9me2 heterochromatin, but high siRNA levels are required to maintain robust heterochromatin, and thus siRNA amplification requires splicing factors such as Prp10 and Cwf10.

Unlike at the centromeres, maintenance of silencing at the mating-type locus does not require RNAi components but does require Cid14 (*18*) and chromatin components such as Swi6 (*21*). Analysis of a *ura4*$^+$ marker inserted within the mating-type locus revealed that, like *dcr1*Δ, none of the tested splicing mutants alleviated mating-type silencing (Fig. 4A). We also tested the effect of the splicing mutants on a *ura4*$^+$ locus silenced by tethering of the RITS component Tas3 to the *ura4* transcript (*22*). As with RNAi mutants (*dcr1*Δ), both *prp10-1* and *cwf10-1* mutants alleviated silencing, whereas *prp2-1* did not (Fig. 4B). Together these observations confirm a specific role for Cwf10 and Prp10 in RNAi-mediated silencing that is downstream of RITS recruitment, consistent with a function related to amplification of the RNAi response.

The phenotypes of splicing mutants suggest that splicing factors may interact with the RNAi

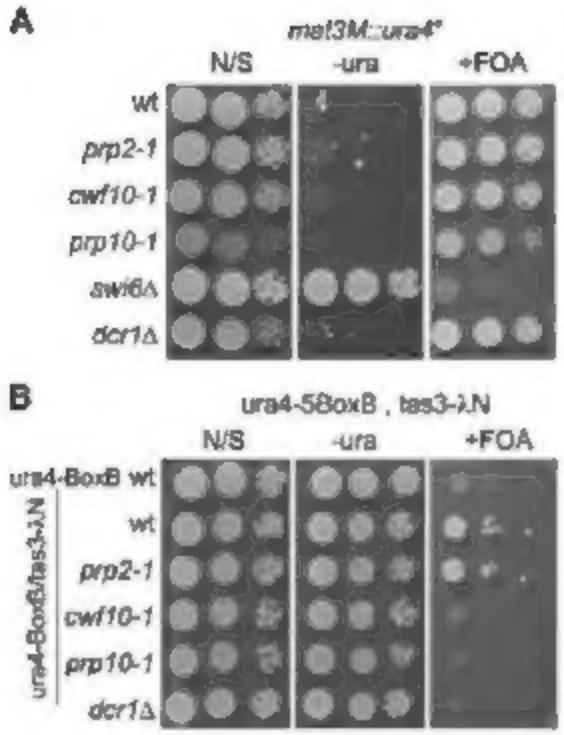

C

Proteins associated with Cid12-FLAG			
H.s.	*S.c.*	*S.p.*	average number of peptides
EFTUD2	Snu114	Cwf10*	20.7
AQR	-	Cwf11	19.7
BRR2	Brr2	Brr2	19.3
CDC5	Cef1	Cdc5	15.7
		Rdp1	**15.3**
		Cid12	**12.7**
PLRG1	Prp46	Prp5*	10.7
SYF1	Syf1	Cwf3	10.0
PRPF45	Prp45	Prp45	8.3
SYF3	Syf3	Cwf4	7.3
PRPF17	Prp17	Prp17	6.7
SPF38	-	Spf38	6.7
SPF27	-	Cwf7	6.0
ECM2	Ecm2	Cwf5	5.3
SYF2	Syf2	Syf2	5.0
		Sum3	5.0
CWF19	BC061.2	Cwf19	4.7
PRPF3	Prp3	Prp3^	4.3
ISY1	Isy1	Cwf12	4.3
U2-A'	Lea1	Lea1	4.0
SF3B2	Rse1	Prp12*	4.0
		Rps402	3.7
		Gpd3	3.7
		Saa1	3.7
PRPF22	Prp22	Prp22	3.7
SRRM2	Cwc21	Cwf21	3.7
		Hsp16	3.0
		Mlo3	3.0
		Rpl26	2.7
		Rad1	2.7
		Bip1	2.7
PRPF43	Prp43	Prp43	2.7
SF3B1	Hsh155	Prp10*	2.3
BUD31	Bud31	Smb1	2.0

*mutant alleles have defective silencing
^mutant allele does not affect silencing

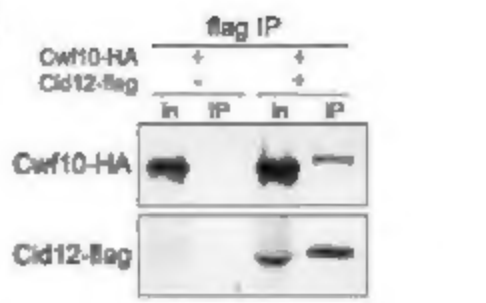

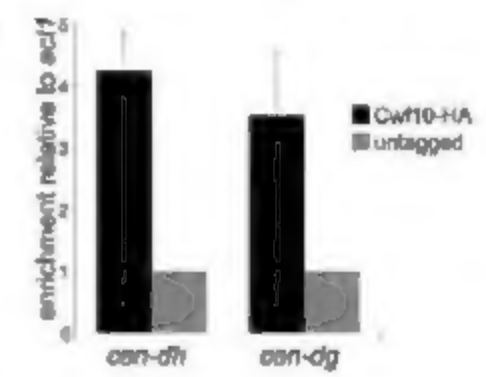

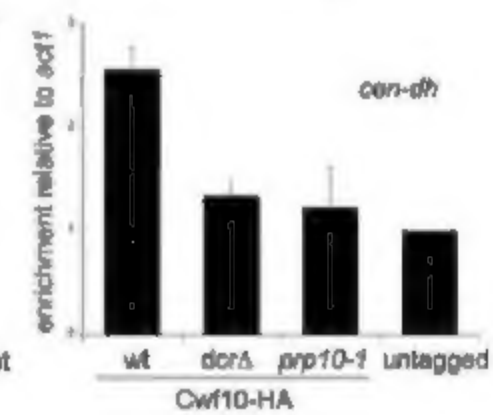

Fig. 4. Splicing factors are specifically required for RNAi-dependent silencing and physically associate with the RNAi machinery and centromere repeats. (**A** and **B**) Assays for silencing of *ura4*$^+$ at mating-type locus [mat3-M::*ura4*$^+$(*21*) (A)] or with tethered Tas3 [*ura4-5BoxB*/*tas3-λN* (*22*) (B)]. Plates are nonselective (N/S), lacking uracil (–ura), or supplemented with FOA (+FOA). (**C**) Proteins specifically associated with Cid12-FLAG, analyzed by LC-MS/MS, as described (*27*). For splicing factors, human (*H.s.*) and budding yeast (*S.c.*) homologs are shown. (**D**) Coimmunoprecipitation of Cwf10-HA with Cid12-FLAG. (**E** and **F**) ChIP analysis of Cwf10 enrichment at *cen-dh* or *cen-dg* relative to a euchromatic, unspliced control locus *act1*$^+$, normalized to an untagged control strain.

machinery. Indeed, in cells lacking Rdp1, spliceosome subunits have been reported to copurify with affinity-selected Cid12 (*4*). To examine this more closely, we analyzed immunoprecipitates of FLAG epitope–tagged Cid12 from wild-type cells by liquid chromatography–mass spectrometry (LC-MS/MS). Many splicing factors were found to specifically associate with Cid12-FLAG. These included Cwf10, Prp10, Prp5, and Prp12, which were required for centromeric silencing, along with splicing factors such as Prp3 that did not affect silencing (Fig. 4C). Splicing factors were rarely identified in immunoprecipitates of numerous other FLAG-tagged proteins, indicating that this interaction is specific. The association of Cwf10 with Cid12 was also verified by coimmunoprecipitation (Fig. 4D). Thus, Cid12 may function in association with a large spliceosomal complex, with particular splicing factor mutants compromising its activity and thereby impairing RDRC-mediated siRNA amplification.

Because splicing factors interact with Cid12, they may (like other RNAi components) associate with centromeric repeats. To test this possibility, we performed ChIP with Cwf10, the splicing factor most strongly represented in Cid12 immunoprecipitates. Hemagglutinin epitope–tagged Cwf10 (Cwf10-HA) was found to be enriched on both *dh* and *dg* centromere repeats, relative to an unspliced control gene, *act1* (Fig. 4E). Prp8-HA was also enriched on centromere repeats, and both Cwf10-HA and Prp8-HA were at least as strongly associated with *cen-dh* as was Cid12-HA (fig. S5). The association of Cwf10-HA with centromere repeats was essentially lost in *dcr1*Δ and *prp10-1* cells, showing it to be linked to a functional RNAi pathway (Fig. 4F). We conclude that splicing factors associate with the RNAi machinery at the centromere to directly facilitate RNAi-mediated centromere silencing.

Processing of transcripts by both the splicing and RNAi machineries is thought to occur cotranscriptionally, implying that generation of siRNAs from centromere transcripts may occur in the context of larger RNA-processing "factories" (*1*, *16*, *22*). We propose that spliceosomal complexes provide a platform that promotes the processing of centromeric transcripts by RDRC, facilitating amplification of homologous siRNAs to high levels. The silencing and chromatin modification defects seen in particular splicing factor mutants are thus explained by disruption of this transcript-to-siRNA processing step, independently of splicing itself. Splicing factors have also been identified in screens for factors affecting RNAi in nematodes and plants (*23*, *24*) and are required for processing of some microRNAs in nematodes, flies, and humans (*25*, *26*). Thus, integration with other RNA processing events may be a conserved feature of RNAi-related pathways.

References and Notes

1. M. Buhler, D. Moazed, *Nat. Struct. Mol. Biol.* **14**, 1041 (2007).
2. S. I. S. Grewal, S. T. Jia, *Nat. Rev. Genet.* **8**, 35 (2007).
3. A. Verdel *et al.*, *Science* **303**, 672 (2004); published online 2 January 2004 (10.1126/science.1093686).
4. M. R. Motamedi *et al.*, *Cell* **119**, 789 (2004).
5. A. L. Pidoux, R. C. Allshire, *Philos. Trans. R. Soc. London Ser. B* **360**, 569 (2005).
6. K. Ekwall, G. Cranston, R. C. Allshire, *Genetics* **153**, 1153 (1999).
7. I. Djupedal *et al.*, *Genes Dev.* **19**, 2301 (2005).
8. T. Volpe *et al.*, *Chromosome Res.* **11**, 137 (2003).
9. C. Bartels, C. Klatt, R. Lührmann, P. Fabrizio, *EMBO Rep.* **3**, 875 (2002).
10. S. R. Lockhart, B. C. Rymond, *Mol. Cell. Biol.* **14**, 3623 (1994).
11. J. Potashkin, D. Kim, M. Fons, T. Humphrey, D. Frendewey, *Curr. Genet.* **34**, 153 (1998).
12. S. Urushiyama, T. Tani, Y. Ohshima, *Mol. Gen. Genet.* **253**, 118 (1996).
13. G. H. Rosenberg, S. K. Alahari, N. F. Kaufer, *Mol. Gen. Genet.* **226**, 305 (1991).
14. J. Potashkin, R. Li, D. Frendewey, *EMBO J.* **8**, 551 (1989).
15. Y. Habara, S. Urushiyama, T. Shibuya, Y. Ohshima, T. Tani, *RNA* **7**, 671 (2001).
16. D. L. Bentley, *Curr. Opin. Cell Biol.* **17**, 251 (2005).
17. T. A. Volpe *et al.*, *Science* **297**, 1833 (2002); published online 22 August 2002 (10.1126/science.1074973).
18. M. Buhler, W. Haas, S. P. Gygi, D. Moazed, *Cell* **129**, 707 (2007).
19. M. Sadaie, T. Iida, T. Urano, J. Nakayama, *EMBO J.* **23**, 3825 (2004).
20. H. D. Folco, A. L. Pidoux, T. Urano, R. C. Allshire, *Science* **319**, 94 (2008).
21. I. M. Hall *et al.*, *Science* **297**, 2232 (2002); published online 5 September 2002 (10.1126/science.1076466).
22. M. Buhler, A. Verdel, D. Moazed, *Cell* **125**, 873 (2006).
23. J. K. Kim *et al.*, *Science* **308**, 1164 (2005); published online 24 March 2005 (10.1126/science.1109267).

24. A. J. Herr, A. Molnar, A. Jones, D. C. Baulcombe, *Proc. Natl. Acad. Sci. U.S.A.* **103**, 14994 (2006).
25. S. Guil, J. F. Caceres, *Nat. Struct. Mol. Biol.* **14**, 591 (2007).
26. P. Goymer, *Nat. Rev. Mol. Cell Biol.* **8**, 597 (2007).
27. See supporting material on *Science* Online.
28. We thank J. Beggs, E. S. Choi, A. Pidoux, F. Simmer, I. Stancheva, and D. Tollervey for comments; N. Kaufer, D. Moazed, and T. Tani for materials; and the Allshire lab for support. Supported by Epigenome Network of Excellence (EC-FP6/Contract/LSHG-CT-2004-503433), of which R.C.A. and K.E. are members (E.B.); UK Medical Research Council grant G0301153/ID:69173 (A.K.); Wellcome Trust Prize Studentship 067844 (M.P.); Marie Curie Excellence Grant MEXT-CT-014171 from the European Commission (J.R.); and Wellcome Trust Principal Research Fellowship grant 065061/Z (R.C.A.).

Supporting Online Material
www.sciencemag.org/cgi/content/full/322/5901/602/DC1
Materials and Methods
Figs. S1 to S5
Tables S1 and S2
References

31 July 2008; accepted 18 September 2008
10.1126/science.1164029

Experiencing Physical Warmth Promotes Interpersonal Warmth

Lawrence E. Williams[1]* and John A. Bargh[2]

"Warmth" is the most powerful personality trait in social judgment, and attachment theorists have stressed the importance of warm physical contact with caregivers during infancy for healthy relationships in adulthood. Intriguingly, recent research in humans points to the involvement of the insula in the processing of both physical temperature and interpersonal warmth (trust) information. Accordingly, we hypothesized that experiences of physical warmth (or coldness) would increase feelings of interpersonal warmth (or coldness), without the person's awareness of this influence. In study 1, participants who briefly held a cup of hot (versus iced) coffee judged a target person as having a "warmer" personality (generous, caring); in study 2, participants holding a hot (versus cold) therapeutic pad were more likely to choose a gift for a friend instead of for themselves.

Ever since Solomon Asch's (*1*) original demonstration of the transformational power of "warm" and "cold" as personality traits in first impressions of individuals, the concept of psychological warmth has been prominently featured in research on social perception and interpersonal liking (*2*–*4*). The warm-cold dimension has emerged as one of two main components of the first impressions (along with competence) we quickly form of other people (*2*, *5*); together they account for a large proportion (82%) of the variance in people's evaluations of social behaviors (*6*). Notably, the warmth and competence dimensions have been found to be the principal ones underlying every group stereotype studied across dozens of countries (*2*, *5*). Of these two fundamental dimensions, warmth is primary, as "people are more sensitive to warmth information than to competence information" (*5*, p. 79) and make trustworthiness judgments of faces faster than for other traits, including competence (*7*).

What does it mean, exactly, to perceive someone as a "warm" versus a "cold" person? According to recent theory and research in social cognition, interpersonal warmth refers to a constellation of traits related to perceived favorability of the other person's intentions toward us, including friendliness, helpfulness, and trustworthiness (*5*). The warm-cold assessment is the social perceiver's immediate "first-pass" as to whether the target individual (or social group) can be trusted as a friend (*7*), or at least as a "non-foe" (i.e., warm), or is instead a potential foe who might attempt to interfere with one's ongoing goal pursuits (i.e., cold). [The competence assessment is then a "second-pass" evaluation of whether the newly encountered individual (or group) has the capacity to act on those perceived intentions (*5*).] This assessment appears to be an automatic and obligatory evaluation that does not require the perceiver's intent to make it.

Why, then, do we speak so naturally of "warm" and "cold" individuals (and not "friend" or "foe," or "trustworthy" and "not trustworthy")? Asch (*1*) gave no rationale to support his hypothesis that warm and cold would be uniquely "central traits" in impression formation, other than his own intuitions. However, in subsequent theorizing he offered a clue, arguing that most abstract psychological concepts are metaphorically based on concrete physical experiences (*8*). Contemporary cognitive linguists have advanced similar arguments that people conceptualize their internal, mental worlds by analogy to the physical world (*9*–*13*). Applied to the question of how warm objects can produce the same affective states as a "warm" person, embodiment theorists have noted how objects and events that produce the same quality of affective response are associated (categorized) together in memory (*14*). In this way, the feelings of warmth when one holds a hot cup of coffee or takes a warm bath might activate memories of other feelings associated with warmth (trust and comfort), because of early experiences with caretakers who provide warmth, shelter, safety, and nourishment.

Harry Harlow (*15*), in his classic studies on maternal-infant bonding in nonhuman primates, demonstrated that macaque monkeys preferred to stay close to a cloth surrogate mother rather than a wire mother. This preference held even when the wire mother was the infant's source of food (a bottle was attached to the wire) and the cloth mother was not. Tellingly, the cloth and the wire mothers differed in another important respect: The cloth (but not the wire) mother was a source of warmth for the infant monkey (a 100-W light bulb had been placed behind the cloth). As Harlow (*15*) concluded, contact comfort with the mother was a very important factor to the infant monkey, over and above her meeting nourishment needs; moreover, monkeys "raised" by the warm cloth mother showed relatively normal social development as adults, in stark contrast to the infants left alone with the wire mother.

In agreement with Harlow's findings, the seminal attachment theorist John Bowlby (*16*) also posited an innate need for direct physical contact with the caretaker, over and above the caretaker's satisfaction of the infant's primary needs of hunger and thirst. Bowlby, as had Lorenz (*17*) before him, argued that maintaining closeness to caretakers during infancy, a period of relative helplessness, is critical for the survival of many animals.

Because of these frequent early life experiences with the trustworthy caregiver, a close mental association should develop between the concepts of physical warmth and psychological warmth. Indeed, recent research on the neurobiology of attachment has added further support for the proposed link between tactile temperature sensation and feelings of psychological warmth and trust (*18*). This research has revealed that the insular cortex is implicated in processing both the physical and the psychological versions of warmth information (*19*). First, the dorsal posterior insula is active during both temperature and touch sensation (*20*, *21*). For example, activity in the right anterior insular cortex was strongly correlated with normal participants' reported perceptions of the thermal intensity of stimuli (*20*), and warm thermal stimulation with a fomentation pack (as compared to neutral thermal stimulation) produced an increase in activation of the contralateral insular cortex, among other regions (*21*).

The insula is also involved in feelings of trust, empathy, and social emotions of guilt and embarrassment. Indeed, there appear to be specialized neurons for these social functions that have been observed in only two regions of the brain, one of which is the frontoinsular cortex (*22*). The insula is more highly activated after social exclusion or rejection than after social inclusion and acceptance (*23*, *24*), and heightened activity in the anterior insular cortex was associated with the rejection of unfair offers in an economic trust game (*25*). Recently, the severe mental illness of borderline personality disorder, characterized by a profound

[1]Leeds School of Business, University of Colorado at Boulder, UCB 419, Boulder, CO, 80309-0419, USA. [2]Department of Psychology, Yale University, Post Office Box 208205, New Haven, CT 06520-8205, USA.

*To whom correspondence should be addressed. E-mail: lawrence.williams@colorado.edu

inability to cooperate with others, has been linked to a lack of differential responsiveness in the anterior insula to trustworthy versus untrustworthy behavior in economic game partners (*19*, *26*).

For these theoretical and empirical reasons, we hypothesized that mere tactile experiences of physical warmth should activate concepts or feelings of interpersonal warmth. Moreover, this temporarily increased activation of interpersonal warmth concepts should then influence, in an unintentional manner, judgments of and behavior toward other people without one being aware of this influence. Such priming or construct accessibility effects, in which concepts activated in one context are residually active for a short time thereafter and exert influence on judgment and behavior in subsequent contexts without the person's awareness, are a staple of contemporary social psychological research (*27*). We recruited 41 undergraduates, modally white and female, with an average age of 18.5 years. Participants were assigned to one of two temperature priming conditions. Participants were primed with temperature by briefly holding either a cup of hot coffee, or a cup of iced coffee. To do this, a confederate blind to the study's hypotheses met participants in the lobby of the psychology building, carrying a cup of coffee, a clipboard, and two textbooks. During the elevator ride to the fourth-floor laboratory, the confederate casually asked participants if they could hold the coffee cup for a second while she recorded their name and the time of their participation. After the confederate wrote down the information, she took back the coffee cup. The temperature of the coffee cup (hot versus iced) was the only between-subjects manipulation (*28*).

When participants arrived at the experimental room, they received a packet containing a personality impression questionnaire, following the same procedure as in Asch's original study (*1*). Participants read that "Person A" was intelligent, skillful, industrious, determined, practical, and cautious. They then rated the target person on 10 personality traits using bipolar scales anchored by a trait and its opposite. Half of the personality traits were semantically related to the warm-cold dimension, and half were unrelated, again following Asch's procedure.

As hypothesized, people who had briefly held the hot coffee cup perceived the target person as being significantly warmer (mean = 4.71; 1 = cold, 7 = warm) than did those who had briefly held the cup of iced coffee [mean = 4.25, $F(1, 39) = 4.08$, $P = 0.05$]. The coffee manipulation did not affect ratings on traits unrelated to the warm-cold dimension [$F(1, 39) = 0.67$, not significant], replicating the findings of Asch (*1*) and Kelley (*3*) in their original demonstrations of the warm-cold effect on impression formation. The effect of the coffee manipulation was specific to feelings of interpersonal warmth and was not a general mood or "halo" effect. Thus, a brief warm or cold physical experience influenced participants' subsequent interpersonal judgments of a target person in the same way that presenting the words "warm" or "cold" was found to affect judgments of the target person in Asch's original study; moreover, participants in the present study showed no awareness of the impact of the physical experience on their judgments (*28*).

The second study had two aims. First, whereas the experimenter in the initial study had been blind to hypotheses, she was of course aware of the participant's experimental condition (as she herself held the hot versus iced coffee), and so could have inadvertently treated participants in the two conditions differently. In the second study this potential issue was eliminated through the use of Icy Hot therapeutic pads retrieved directly by the participant after receiving an instructional packet; the experimenter was blind to the experimental condition before handing participants the instructional packet, and did not interact with participants again until all dependent measures had been completed. Second, we sought to extend the initial findings from the domain of interpersonal judgment to that of the participant's own behavior. In line with research demonstrating the direct behavioral consequences of concepts automatically activated during social perception [e.g., (*29*)], we expected the primed feelings of interpersonal warmth to affect not only judgments of another person but one's behavior toward others as well.

We asked a separate group of 53 participants to briefly hold either the hot or cold therapeutic pad under the guise of a product evaluation. After participants rated the effectiveness of either the hot or cold pad, they were given a choice of reward for participating in the study. This choice constituted the dependent variable of the study. Participants were asked to choose either a Snapple beverage, or a $1 gift certificate to a local ice cream shop. These rewards were framed either as a prosocial gift to "treat a friend," or as a personal reward for the participants themselves. The framing condition was counterbalanced such that half of participants chose between a Snapple reward for themselves and a gift certificate reward for a friend, and the other half chose between a Snapple reward for a friend and a gift certificate reward for themselves.

We hypothesized that participants who evaluated the hot pad would be more likely to choose the interpersonally warmer option of a reward for a friend, whereas participants who evaluated the cold pad would be more likely to choose the reward for themselves. Consistent with this prediction, a significant interaction was obtained between pad temperature and framing conditions (logistic regression $B = 2.85$, $P < 0.05$), such that regardless of type of gift (Snapple or ice cream), participants primed with physical coldness were more likely to choose the gift for themselves (75%) than the gift for a friend (25%), whereas those primed with physical warmth were more likely to choose the gift for a friend (54%) than the gift for themselves (46%). There were no main effects of either temperature condition or framing condition on gift preference.

In summary, experiences of physical temperature per se affect one's impressions of and prosocial behavior toward other people, without one's awareness of such influences. The findings are in agreement with emerging knowledge about the role played by the insula in both the sensation of one's physiological state (such as skin temperature) and the detection of the trustworthiness of others (*19*), and thus provide support for Bowlby's (*16*) contention that early childhood experiences of physical warmth from caregivers are critical for the normal development of interpersonal warmth detection and behavior in adults. A half century after Asch's original intuitions, we are beginning to learn just why the warm-cold dimension is so central to interpersonal perception and behavior.

References and Notes

1. S. Asch, *J. Abnorm. Soc. Psychol.* **41**, 258 (1946).
2. A. J. C. Cuddy, S. T. Fiske, P. Glick, *Adv. Exp. Soc. Psychol.* **40**, 61 (2008).
3. H. H. Kelley, *J. Pers.* **18**, 431 (1950).
4. R. Nisbett, T. Wilson, *J. Pers. Soc. Psychol.* **35**, 250 (1977).
5. S. T. Fiske, A. Cuddy, P. Glick, *Trends Cogn. Sci.* **11**, 77 (2007).
6. B. Wojciszke *et al.*, *Pers. Soc. Psychol. Bull.* **24**, 1251 (1998).
7. J. Willis, A. Todorov, *Psychol. Sci.* **17**, 592 (2006).
8. S. Asch, in *Person Perception and Interpersonal Behavior*, R. Taguiri, L. Petrullo, Eds. (Stanford Univ. Press, Stanford, 1958), pp. 86–94.
9. J. Mandler, *Psychol. Rev.* **99**, 587 (1992).
10. E. Sweetser, *From Etymology to Pragmatics: Metaphorical and Cultural Aspects of Semantic Structure* (Cambridge Univ. Press, New York, 1990).
11. M. Johnson, *The Body in the Mind: The Bodily Basis of Meaning, Imagination, and Reasoning* (Univ. Chicago Press, Chicago, 1987).
12. L. Talmy, *Cogn. Sci.* **12**, 49 (1988).
13. H. H. Clark, in *Cognitive Development and the Acquisition of Language*, T. E. Moore, Ed. (Academic Press, San Diego, 1973), pp. 27–63.
14. P. M. Niedenthal, J. B. Halberstadt, A. H. Innes-Ker, *Psychol. Rev.* **106**, 337 (1999).
15. H. Harlow, *Am. Psychol.* **13**, 673 (1958).
16. J. Bowlby, *Attachment and Loss* (Hogarth Press, London, 1969).
17. K. Lorenz, *On Aggression* (Harcourt, Brace, and World, New York, 1966).
18. T. R. Insel, L. J. Young, *Nat. Rev. Neurosci.* **2**, 129 (2001).
19. A. Meyer-Lindenberg, *Science* **321**, 778 (2008).
20. A. D. Craig, K. Chen, D. Bandy, E. Reiman, *Nat. Neurosci.* **3**, 184 (2000).
21. E.-J. Sung *et al.*, *Int. J. Neurosci.* **117**, 1011 (2007).
22. M. Balter, *Science* **315**, 1208 (2007).
23. N. Eisenberger, M. Lieberman, K. Williams, *Science* **302**, 290 (2003).
24. E. Kross, T. Egner, K. Ochsner, J. Hirsch, G. Downey, *J. Cogn. Neurosci.* **19**, 945 (2007).
25. A. Sanfey, J. Rilling, J. Aronson, L. Nystrom, J. Cohen, *Science* **300**, 1755 (2003).
26. B. King-Casas *et al.*, *Science* **321**, 806 (2008).
27. E. T. Higgins, in *Social Psychology: Handbook of Basic Principles*, E. Higgins, A. Kruglanski, Eds. (Guilford, New York, 1996), pp. 133–168.
28. Materials and methods available as supporting material on *Science* Online.
29. A. Dijksterhuis, J. A. Bargh, *Adv. Exp. Soc. Psychol.* **33**, 1 (2001).

30. We thank P. Bloom, J. Gray, F. Keil, E. Morsella, A. Poehlman, P. Winkielman, S. Gottlieb, K Connolly, S. Hennessey, and funding from National Institute of Mental Health (grant MH-R01-60767), a NSF Graduate Research Fellowship, and a Yale International Center for Finance Whitebox Fellowship.

Supporting Online Material

www.sciencemag.org/cgi/content/full/322/5901/606/DC1
Materials and Methods
SOM Text

30 June 2008; accepted 16 September 2008
10.1126/science.1162548

New Products

Microbalances and Ultramicrobalances

New analytical balances have been added to the Excellence Plus and Excellence lines. The XP6U and XP2U ultramicrobalances and XP6 microbalances offer up to 6 g capacity and 0.1 µg or 1 µg readability. The Excellence XS3DU microbalance offers weighing performance in an 800-mg fine range with 1-µg readability. The XP6U ultramicrobalance has a 61-million-digit resolution. The XP2U ultramicrobalance has a 21-million-digit resolution. The instruments offer all the other Excellence Plus features, such as colored touch-screen display, customized screen programming, intelligent user guidance, and hands-free infrared draft shield.

Mettler Toledo
For information 614-438-4733
www.mt.com

Protein Immunoblot Imaging and Analysis

The FluorChem Q Imaging System provides the sensitivity of chemiluminescence and the quantitative power of fluorescence in one easy-to-use instrument. Designed with fast-lens technology, a peltier-cooled camera captures high-resolution images with a linear dynamic range that outperforms film, and with speeds 10 times faster than a laser scanner. Equipped with three integrated excitation sources for multicolor blots, the FluorChem Q is compatible with Cy dyes, Alexa dyes, Q dots, and chemiluminescent protein immunoblotting kits. This versatile system can also image fluorescent DNA and protein gels. The system comes with intuitive software that automatically stores all experimental imaging protocols as well as channel and filter settings.

Alpha Innotech
For information 510-483-9620
www.alphainnotech.com

Competent Cells

The Multiple-Deletion Strain 42 (MDS42) features competent cells that have been completely sequenced and analyzed by genome. A series of deletions have also been performed to remove nonessential genetic elements, which has improved the transformation efficiencies and improved protein expression. With 15 percent of nonessential regions of the genome removed, the MDS42 competent cells contain no insertion sequence elements, phage and prophage elements, recombination regions, or endonuclease A.

Scarab Genomics
For information 888-513-7075
www.scarabgenomics.com

UV-Visible Spectrophotometers

The new Helios Zeta double-beam and Helios Omega single-beam ultraviolet-visible spectrophotometers are designed for research, routine quality control, and teaching. They are cost-effective instruments that offer excellent throughput and affordable analysis of liquid and solid samples. The systems offer unlimited method and data storage using USB memory devices. Integrated software provides control for a multitude of laboratory requirements from fixed wavelength measurements and quantitative analysis to wavelength scanning and multicomponent analysis.

ThermoFisher Scientific
For information 800-532-4752
www.thermo.com/uv-vis

Chiral Chromatography Columns

Lux columns are a new line of polysaccharide-based columns for the identification and resolution of enantiomers. They are offered with two chiral stationary phases, both of which make use of coated derivatized cellulose as the chiral selector. The two phases combine to create a dependable screening set with a wide range of selectivity. The columns are offered in 3 µm and 5 µm particle sizes.

Phenomenex
For information 310-212-0555
www.phenomenex.com

Tissue Culture Products

The Iwaki range of tissue culture products consists of standard nontreated and tissue culture–treated ware, along with an extensive range of substrate-coated products designed to combat problems associated with in vitro cell culture. The Iwaki coated-ware range has significant benefits over noncoated tissue culture products. In addition, Iwaki products offer considerable time savings compared with "home-made" products. The culture substrates available in the Iwaki range include collagen type 1, fibronectin, gelatin and poly-L-lysine, polyethylene imine, and a unique collagen gel membrane. The range also includes a unique selection of glass-based dishes, multiwell plates, and chamber slides offering high optical clarity for complex cell biology research.

Sterilin
For information +44-(0)-844-844-3737
www.sterilin.co.uk

Live Cell Imaging Chamber

The CV-30 Live Cell Imaging Chamber is a closed-bath chamber that incorporates special features for imaging. It is compatible with any microscope stage capable of accepting a multiwell plate and any stage having a standard microscope slide adapter. The chamber features a user-defined bath geometry and volume, and presents a large viewing area. A glass coverslip forms the top of the chamber, while a 1-mm-thick round coverslip forms the chamber bottom. The CV-30 is compatible with the CytoViva High Resolution Imaging System. This low-profile imaging chamber can be used for simultaneous observation of fluorescent and nonfluorescent samples.

Warner Instruments
For information 800-599-4203
www.warnerinstruments.com

Electronically submit your new product description or product literature information! Go to www.sciencemag.org/products/newproducts.dtl for more information.

Newly offered instrumentation, apparatus, and laboratory materials of interest to researchers in all disciplines in academic, industrial, and governmental organizations are featured in this space. Emphasis is given to purpose, chief characteristics, and availability of products and materials. Endorsement by *Science* or AAAS of any products or materials mentioned is not implied. Additional information may be obtained from the manufacturer or supplier.